



HAL
open science

Hierarchically Porous Silica Materials for the Encapsulation of Molecules of Interest

Philippe Riachy

► **To cite this version:**

Philippe Riachy. Hierarchically Porous Silica Materials for the Encapsulation of Molecules of Interest. Other. Université de Lorraine, 2016. English. NNT : 2016LORR0013 . tel-01752225

HAL Id: tel-01752225

<https://hal.univ-lorraine.fr/tel-01752225>

Submitted on 29 Mar 2018

HAL is a multi-disciplinary open access archive for the deposit and dissemination of scientific research documents, whether they are published or not. The documents may come from teaching and research institutions in France or abroad, or from public or private research centers.

L'archive ouverte pluridisciplinaire **HAL**, est destinée au dépôt et à la diffusion de documents scientifiques de niveau recherche, publiés ou non, émanant des établissements d'enseignement et de recherche français ou étrangers, des laboratoires publics ou privés.



AVERTISSEMENT

Ce document est le fruit d'un long travail approuvé par le jury de soutenance et mis à disposition de l'ensemble de la communauté universitaire élargie.

Il est soumis à la propriété intellectuelle de l'auteur. Ceci implique une obligation de citation et de référencement lors de l'utilisation de ce document.

D'autre part, toute contrefaçon, plagiat, reproduction illicite encourt une poursuite pénale.

Contact : ddoc-theses-contact@univ-lorraine.fr

LIENS

Code de la Propriété Intellectuelle. articles L 122. 4

Code de la Propriété Intellectuelle. articles L 335.2- L 335.10

http://www.cfcopies.com/V2/leg/leg_droi.php

<http://www.culture.gouv.fr/culture/infos-pratiques/droits/protection.htm>



UNIVERSITÉ
DE LORRAINE



Collégium SCIENCES ET TECHNOLOGIE
Pôle scientifique Chimie Physique Moléculaires
Ecole Doctorale Lorraine de Chimie et Physique Moléculaires

Thèse de doctorat
Présentée pour l'obtention du titre de
Docteur de l'Université de Lorraine en Chimie

Présentée par
Philippe RIACHY

Hierarchically Porous Silica Materials for the
Encapsulation of Molecules of Interest

Soutenue le 14 mars 2016

Membres du Jury

Rapporteurs	Mme Isabelle PEZRON	Professeur Université de Technologie Compiègne
	Mme Maria-José GARCIA CELMA	Professeur Département de Pharmacie et Technologie Pharmaceutique, Université de Barcelone
Examineurs	Mme Conxita SOLANS	Professor Investigacio IQAC – CSIC Barcelone
	Mme Isabelle CHEVALOT	Professeur INPL-ENSAIA Université de Lorraine
	Mme Marie-José STEBE	Directrice de Recherches Emérite CNRS SRSMC Université de Lorraine
Directeur de thèse	M Jean-Luc BLIN	Professeur SRSMC Université de Lorraine

*“It is good to have an end to journey toward, but
it is the journey that matters in the end.”*

- *Ursula K. Le Guin in *The Left Hand of Darkness**

Remerciements

Ce travail a été réalisé au sein de l'équipe-projet NANO, au Laboratoire Structure et Réactivité des Systèmes Moléculaires Complexes, Unité Mixte de Recherche n°7565 du CNRS et de l'Université de Lorraine.

Mes premiers remerciements vont à mon directeur de thèse Jean-Luc Blin, professeur à l'Université de Lorraine, ainsi qu'à Marie-José Stébé, directrice de recherche CNRS, pour m'avoir permis de continuer mes études en thèse et accueilli dans leur équipe, où j'ai pu trouver un environnement à la fois intellectuellement stimulant et humainement enrichissant.

J'exprime ma gratitude à Isabelle Pezron, professeur à l'Université de Compiègne, et Maria-José García-Celma, Professeur à l'Université de Barcelone, pour avoir accepté d'évaluer ce travail en tant que rapporteurs.

J'exprime ma reconnaissance à Conxita Solans, Professor Investigació à l'IQAC-CSIC, et Isabelle Chevalot, professeur de l'Université de Lorraine, pour avoir accepté de faire partie de mon jury de thèse.

Je remercie Philippe Gros, professeur à l'Université de Lorraine et directeur du laboratoire SRSMC, ainsi que Xavier Assfeld, professeur à l'université de Lorraine et directeur de l'École Doctorale SESAMES pour m'avoir accueilli au sein de leurs institutions respectives.

En outre, j'adresse ma profonde gratitude pour l'équipe Physico-Chimie des Colloïdes pour avoir financé ma thèse pendant trois ans. J'exprime aussi ma reconnaissance au laboratoire SRSMC et à l'école doctorale SESAMES ainsi qu'au cadre Européen COST-STSM pour les soutiens financiers nécessaires pour les missions et les congrès auxquels j'ai eu l'opportunité de participer.

Je tiens à remercier également Mélanie Emo, ingénieure d'études et responsable du SAXS, pour les nombreuses analyses et modélisations qui ont été cruciales pour l'achèvement de ce travail. Ensuite, j'adresse mes remerciements à Stéphane Parant, ingénieur d'études et gestionnaire du parc d'instruments d'analyses physico-chimiques du SRSMC, pour son aide lors de l'utilisation de la spectrophotométrie UV-Vis. Un grand merci aussi à Cédric Carteret, professeur à l'Université de Lorraine, pour m'avoir formé et aidé lors de la réalisation des expériences de spectroscopie infrarouge ainsi que pour ses conseils. Je tiens à remercier également Jordi Esquena, chef du « Department of Chemical and Biomolecular Nanotechnology » pour m'avoir offert l'opportunité de faire un stage au sein de son laboratoire, ainsi que Ferran Roig, doctorant à l'IQAC-CSIC, pour m'avoir formé et aidé durant ce stage. J'adresse mes remerciements à Bénédicte Lebeau, professeur à l'université de Haute Alsace et responsable de l'équipe Matériaux à Porosité Contrôlée, pour les analyses RMN qu'elle a accepté de faire ainsi que l'imagerie MET et MEB. Je tiens à remercier aussi Stéphane Delaunay, maître de conférences à l'INPL-ENSAIA, ainsi que Léna Dettori, doctorante à l'équipe BioProMo, pour les manipes de production d'acylases et de l'acylation de la lysine qu'ils ont fait. Enfin,

je souhaite adresser mes remerciements à Fabien Lachaud, responsable du service commun de spectrométrie de masse et chromatographie, pour m'avoir formé et aidé à l'utilisation de la GC-MS.

Je suis également reconnaissant à toutes les personnes que j'ai eu le plaisir de côtoyer lors de mon séjour au laboratoire, en particulier Andreea, Nadia, Jonathan, Sanghoon, Carine, Issam, Lionel, Dominique, Laurent, Fernanda, Ileana, Sijin, Imène, Guillaume, Marie, Edyta, Violetta, Sahar et Robin.

Au-delà de la science, il y a des hommes et des femmes qui étaient à mes côtés tout au long de ma thèse. Mes parents, Joseph et Mimoe, d'abord, que je remercie très chaleureusement ici ainsi que mes frères Marc et Fadi et ma sœur Maria. Je tiens à remercier aussi tous mes amis surtout Raji et Georges pour leurs soutiens, et bien sûr Lara pour ses sourires et son réconfort lorsque j'en avais le plus besoin.

Table of Contents

Chapter I

1	Surfactant systems	20
1.1	Properties of surfactant molecules	20
1.1.1	Molecular structure	20
1.1.2	Hydrophilic-lipophilic balance (HLB) system.....	21
1.1.3	Organized molecular assemblies	22
1.2	Emulsions	25
1.3	Nano-emulsions.....	27
2	Porous Silica Materials.....	31
2.1	Sol-gel process	31
2.2	Mesoporous Materials.....	32
2.2.1	Cooperative templating mechanism – CTM	33
2.2.2	Liquid crystal/emulsion templating	34
2.3	Hierarchically porous materials	34
2.3.1	Meso-macroporous materials.....	34
2.3.2	Bimodal mesoporous materials	38
3	Application fields	40
3.1	Drug administration systems.....	40
3.1.1	Effects of porous silica materials properties on drug loading and release	40
3.1.2	Hybrid materials as carriers of active ingredients	41
3.1.3	Active ingredient: Ketoprofen	42
3.2	Porous silica materials as biocatalysts	43
3.2.1	Lipase	43
3.2.2	Catalytic mechanism of the lipase	44
3.2.3	Enzyme immobilization on porous silica materials	46
3.2.4	Effect of the properties of porous material.....	47
4	Aim of this thesis.....	48

5	References	48
---	------------------	----

Chapter II

1	Materials	60
1.1	Surfactants	60
1.2	Oils	60
1.3	Silica source	61
1.4	Enzymes.....	62
2	Methods.....	62
2.1	Phase Diagram	62
2.1.1	Polarized light microscopy	63
2.2	Nano-emulsion formation	64
2.2.1	Phase Inversion Composition – PIC.....	64
2.2.2	Phase Inversion Temperature – PIT	65
2.2.3	Conductivity measurements.....	65
2.2.4	Dynamic light scattering.....	66
2.2.5	Nanoparticle Tracking Analysis – NTA.....	67
2.3	Silica material synthesis.....	68
2.4	Drug release	70
2.5	Transesterification.....	70
2.5.1	Enzyme physisorption on silica substrates.....	70
2.5.2	Adsorption isotherm.....	71
2.5.3	Transesterification of Colza oil	72
2.5.4	Purification of the transesterification reactions products.....	72
2.5.5	Gas chromatography	73
2.5.6	Yield calculation of the transesterification reaction.....	74
3	Characterization methods	76
3.1	Small angle X-ray scattering - SAXS.....	76
3.1.1	Lamellar phase	77
3.1.2	Hexagonal phase.....	77

3.1.3	Mesoporous material	78
3.2	Nitrogen sorption analysis.....	79
3.2.1	Type II isotherm	80
3.2.2	Type IV isotherm.....	80
3.3	Mercury Porosimetry.....	81
3.4	Electronic microscopy	82
3.4.1	Scanning Electronic Microscopy – SEM.....	82
3.4.2	Transmission Electronic Microscopy – TEM.....	82
3.5	Fourier Transform Infrared spectroscopy – FTIR	82
4	References	83

Chapter III

	Detailed investigation of nano-emulsions obtained from the Remcopal 4/decane/water system.....	91
	Nano-emulsions as imprints for the design of hierarchical porous silica through a dual templating mechanism.....	99
	Hybrid hierarchical porous silica templated in nano-emulsions for drug release	109
1	Biocompatible nano-emulsions	134
1.1	Formulation.....	134
1.2	Characterization.....	135
1.3	Release Experiment of the Ketoprofen from the Biocompatible Nano-emulsions	136
1.4	Silica materials templating	136
2	References	137

Chapter IV

1	Introduction.....	143
2	Thermal stability of the hierarchically porous the silica material	144
2.1	Thermal stability of the meso-macroporous silica material	144
2.2	Thermal stability of the dual-mesoporous silica materials.....	146
3	Hydrothermal stability of the hierarchically porous silica material	148
3.1	Hydrothermal stability of the meso-macroporous silica material	148
3.2	Hydrothermal stability of dual-mesoporous silica material.....	153

3.3	Comparison and discussion	156
4	<i>Mucor miehei</i> Lipase immobilization.....	157
4.1	Meso-macroporous biocatalyst	157
4.1.1	Adsorption isotherm	157
4.1.2	Characterization of the meso-macroporous biocatalyst.....	158
4.2	Dual-mesoporous biocatalyst.....	159
4.2.1	Adsorption isotherm	160
4.2.2	Characterization of the dual-mesoporous biocatalyst.....	161
5	Transesterification reaction of colza oil	162
5.1	Recycling of the catalysts.....	164
6	Discussion	164
7	Conclusion	169
8	References	170
9	Acylases immobilization	175
9.1	Immobilization of the acylases	175
9.2	Adsorption isotherm	176
9.3	Conclusion	178
10	References.....	178

Table of Figures

Chapter I

Figure 1-1: Schematic representation of the curvature of the surfactant film. ³	21
Figure 1-2: Schematic drawing of the multiconnected membrane in the L_3 structure with ξ as the sponge pore size and δ as the surfactant bilayer thickness ¹²	23
Figure 1-3: Schematic model of a lamellar phase to the left, and its texture under polarized light microscopy to the right. ¹⁸	23
Figure 1-4: Schematic model of an hexagonal phase to the left, and characteristic texture under polarized light microscopy to the right. ¹⁸	24
Figure 1-5: Schematic models of a bicontinuous cubic liquid crystal to the left and a micellar liquid crystal to the right. ¹⁹	25
Figure 1-6: Schematic representation of the O/W emulsion (left) and W/O emulsion (right). 26	
Figure 1-7: Micrographs of droplets of multiple emulsions. ²⁹	27
Figure 1-8: Schematic representation of the mechanism of the “Ouzo effect”. During the dilution the cosurfactant diffuses into the aqueous medium making the microemulsion thermodynamically unstable thus creating the nano-emulsions. ³	28
Figure 1-9: Schematic representation of the mechanism of the formation of nano-emulsions by the PIC method. ³	29
Figure 1-10: Droplet diameter as a function of addition rate and mixing rate of the Water/Span20-Tween20/Paraffin system. ⁴⁴	29
Figure 1-11: Schematic representation of the mechanism of formation of the nano-emulsions by the PIT method ³ . A) Represents the phases at the phase inversion temperature, B) the structure for a temperature above the PIT and C) the structure for a temperature below the PIT.	30
Figure 2-1 Polymerization behavior of aqueous silica. In a basic solution (B) particles grow in size with decrease in number, in acidic solution or in the presence of flocculating salts (A) particles aggregate into three-dimensional networks and for gels ⁵¹	32
Figure 2-2: Schematic representation of the cooperative templating mechanism and the liquid crystal templating mechanism. ⁵³	33
Figure 2-3: Schematic representation of the CTM mechanism. ⁵⁶	33
Figure 2-4: General synthesis scheme for periodic macroporous solids and the corresponding scanning electron micrographs for a Polystyrene/Silica system prepared with TEOS ⁷²	36
Figure 2-5: TEM micrograph (left) and SEM micrograph (right) of a meso-macroporous silica material prepared from a fluorinated emulsion in the presence of fluorinated microemulsion ⁷⁵	37

Figure 2-6: SEM micrographs of heat-treated gel samples prepared with varied trimethylbenzene concentrations, from left to right: 0.3;0.35;0.4 unit/g ⁸⁵	38
Figure 2-3: TEM micrographs of the bimodal mesoporous material prepared from a mixture of Pluronic P123 and R ^F ₈ (EO) ₉ at a 10:90 ratio ¹⁰⁵	39
Figure 3-1: Release profiles of resveratrol-loaded (▲) from surfactant-loaded silica material, (■) mesoporous silica material ¹¹⁸	42
Figure 3-2: Molecular structure of ketoprofen	43
Figure 3-2 : The structure of the lipase, the A and C represent the closed structure while the B and D represent the open structure (A and B are the lateral vu, and C and D are the vu from above). The catalytic triad is represented in yellow and the structural elements characteristic of all the Lipases (β-sheets and α helices), only after the opening of the lid that the triad becomes accessible to the substrate (D). ¹³⁰	44
Figure 3-3: Catalytic mechanism of the Lipase ¹³¹	45
Figure 3-4: Different methods for immobilizing enzymes (CLEA = cross-linking enzyme aggregates) ¹³⁴	46
Chapter II	
Figure 1-2: Sol stability: relationship between log(gel time) and pH ⁴	61
Figure 2-1: Schematic of a polarized light microscopy ⁶	63
Figure 2-2: Textures of lamellar and hexagonal phases under the polarization microscopy. (a) The L _α phase, texture "Maltese Cross" (b) The L _α phase, oily streaks and "Maltese cross" (c) Hexagonal phase, fanlike texture, (d)Hexagonal phase H ₁ coexisting with a phase L _α	64
Figure 2-3: Conductivity profile as a function of the temperature for the Water/Decane/Remcopal 4 system (O/S = 3, Φ _W = 0.866)	65
Figure 2-4: Schematic of a Dynamic Light Scattering apparatus	67
Figure 2-5: Schematic of the optical configuration used in NTA.	68
Figure 2-4: Schematic representation of the different steps of the formation and the preparation conditions of mesoporous material with a hexagonal structure	69
Figure 2-5: Calibration curve of the lipase for the dual-mesoporous material (black) and the meso-macroporous material (red)	71
Figure 2-6: Photo of the GC-MS Shimadzu QP2010 SE apparatus	73
Figure 2-7: Temperature cycle (A) and a typical chromatogram obtained by GC-MS(B)	74
Figure 2-8: Calibration curve of the methyl esters.	75
Figure 3-3: Schematic of an X-ray tube (A), and of a SAXS apparatus (B)	76
Figure 3-4: Schematic representation and a typical diffractogramm of a lamellar liquid crystal. ¹³	77

Figure 3-5: Schematic representation and a typical diffractogram of a hexagonal liquid crystal.¹³ 78

Figure 3-6: Schematic representation and typical diffractogram of a mesoporous material with a hexagonal structure (A) and wormlike structure (B). 79

Figure 3-7: Type II and Type IV adsorption/desorption isotherms..... 80

Chapter III

Figure 1-1: Ternary phase diagram of the Water/Cremophor EL/Isopropyl Myristate at 30°C. I: monophasic isotropic liquid phase; O_m: reverse micellar solution or W/O microemulsion; L_α: lamellar liquid crystalline phase; II: two-liquid isotropic phases; M: multiphase region; M(OM): multiphase region with an upper W/O microemulsion phase.¹ 134

Figure 1-2: The release profile of ketoprofen from the nano-emulsion..... 136

Figure 1-3: A) SAXS diffractogram for the silica material and B) the nitrogen sorption isotherm and pore size distribution..... 137

Chapter IV

Figure 2-1: Calcination profile of the meso-macroporous silica materials. 144

Figure 2-2: Comparison between the ethanol cleaned material and the calcined material, A) SAXS pattern, B) mercury intrusion porosimetry, C) nitrogen sorption isotherm and D) pore size distribution. 145

Figure 2-3: Comparison of the materials calcined at different temperatures and the initial material, A) SAXS pattern, B) Nitrogen sorption isotherm and C) Mean pore size distribution. 147

Figure 3-1: SAXS patterns evolution as a function of time in boiling water of A) the meso-macroporous material and B) the calcined meso-macroporous material. 149

Figure 3-2: Nitrogen sorption analysis as a function of time in boiling water of the initial meso-macroporous material, A) isotherms and B) pore size distribution of the samples taken at regular intervals. 149

Figure 3-3: Evolution of nitrogen sorption analysis as a function of time in boiling water of the calcined meso-macroporous material, A) isotherm and B) pore size distribution of the samples taken at regular intervals..... 150

Figure 3-4: Graphs showing the evolution of the surface area and pore volume as a function of time in boiling water for A) the initial meso-macroporous material and B) for the calcined meso-macroporous material..... 151

Figure 3-5: Evolution of mercury intrusion porosimetry as a function of time in boiling water of (A) the initial material and of (B) the calcined material..... 151

Figure 3-6: Evolution of the FTIR spectra as a function of time in boiling water of A) the initial meso-macroporous material and B) the calcined material and C,D) the peaks at 4370 cm^{-1} for the materials, respectively.....	152
Figure 3-7: SAXS pattern evolution as a function of time in boiling water of the dual mesoporous silica material.....	153
Figure 3-8: Nitrogen sorption analysis as a function of time in boiling water (A) isotherms and (B) pore size distribution of the dual-mesoporous silica material.	154
Figure 3-9: (A) surface area and pore volume evolution as a function of time in boiling water, and (B) the pore size evolution of the dual-mesoporous silica material.	154
Figure 3-10: A) FTIR analysis of the dual-mesoporous silica material and B) the peak at 4370 cm^{-1} as a function of time in boiling water.....	155
Figure 4-1: Adsorption isotherm of the Mml immobilized at pH6 on the calcined meso-macroporous material.	157
Figure 4-2: FTIR spectra of the adsorbed Mml on the meso-macroporous material (red) and the initial material (black).	158
Figure 4-3: Meso-macroporous biocatalyst characterization before and after enzyme adsorption. A) SAXS pattern, B) pore size distribution, C) Nitrogen sorption isotherm and D) Mercury intrusion porosimetry.	159
Figure 4-4: Adsorption isotherm of the Mml immobilized at pH6 on the dual meso-porous material.....	160
Figure 4-5: FTIR spectra of the dual-mesoporous biocatalyst (red) and the initial material (black).....	160
Figure 4-6: Dual-mesoporous biocatalyst characterization before and after enzyme adsorption. A) SAXS patter, B) pore size distribution and C) Nitrogen sorption isotherm. .	161
Figure 5-1: Methyl esters yield as a function of time for the A) meso-macroporous catalyst, and B) for the dual-mesoporous catalyst.....	162
Figure 5-2: "Turnover number" of the two types of catalysts.....	163
Figure 5-3: Recyclability of the meso-macroporous and the dual-mesoporous catalysts...	164
Figure 6-1: Adsorption isotherms of Mml on A) SBA-15 and B) MMMTE.....	166
Figure 6-2: Recyclability of the SBA-15, MMMTE, meso-macroporous and dual-mesoporous catalysts.....	167
Figure 6-3: The Γ_{max} evolution of the different matrixes in correlation with the pore volume of the matrices.	168
Figure 6-4: the correlation between the mesopore size and A) the initial speed of the formation of methyl esters and B) the turnover number.	168
Figure 6-5: The closed and open conformation of the lipase molecule ²⁸	168

Introduction Générale

Au cours des dernières années les matériaux poreux silicatés sont devenus des matériaux attractifs due à leurs propriétés contrôlables, qui leurs confèrent une adaptabilité aux diverses conditions imposées par des applications diverses. Etant biocompatibles et inertes chimiquement, leurs domaines d'applications peuvent aller de la pharmacie, la cosmétique jusqu'à la catalyse. Ce n'est que récemment, que les matériaux silicatés à porosité hiérarchisée se sont développés à cause de leurs propriétés spécifiques, qui permettent d'améliorer les performances, des matériaux ayant une seule porosité, dans différents domaines d'applications.

De façon générale, des systèmes de vectorisation de principes actifs qui améliorent la biodisponibilité et offrent un contrôle sur la libération, sont recherchés et les matériaux silicatés à porosité hiérarchisée et/ou matériaux hybrides sont des solutions possibles à ces exigences. Leur capacité potentielle à encapsuler une quantité importante de principe actif et leur aptitude à contrôler leur libération, que ce soit par des stimuli externes (UV, champ magnétique) ou internes (pH, oxydo-réduction) confèrent à ce type de matériau les propriétés requises pour répondre aux critères imposés par les applications visées.

De plus, les matériaux à porosité hiérarchisée peuvent servir de support pour des enzymes, dans le but de préparer des catalyseurs hétérogènes. Les catalyseurs hétérogènes permettent de remédier aux inconvénients des catalyseurs homogènes, comme les températures élevées, la difficulté de récupération du catalyseur à la fin de la réaction aboutissant à une consommation importante d'énergie et de matériaux et enfin le coût élevé de production.

Pour synthétiser des matériaux à porosité hiérarchisée il faut associer différents empreintes pour générer plusieurs classes de pores. Emulsions, SLN (Solid Lipid Nanoparticles), billes de polymère sont souvent utilisés. En revanche les nano-émulsions ont été très peu exploitées et ces systèmes possèdent les propriétés nécessaires pour générer des macropores de taille homogène et facilement modulable.

Ce travail porte sur la synthèse d'un nouveau matériau à porosité hiérarchisée en associant des nano-émulsions à des micelles, qui servent d'empreinte. Ce matériau a servi de support pour d'une part, encapsuler un principe actif (kétoprofène) et d'autre part, pour adsorber une enzyme (la lipase Mml).

Le premier chapitre est consacré à une introduction aux Systèmes Moléculaires Organisés en décrivant plus en particulier les méthodes de formation des nano-émulsions ainsi que leurs propriétés. Ensuite, l'utilisation des différents SMO pour la synthèse de matériaux silicatés

poreux est décrite et finalement les applications potentielles de ces matériaux dans le domaine pharmaceutique et en tant que biocatalyseur sont présentées.

Le second chapitre rassemble les modes opératoires employés ainsi que les techniques de caractérisation utilisées.

Le troisième chapitre est consacré à la préparation des matériaux silicatés à porosité hiérarchisée pour examiner leurs capacités d'immobilisation et de libération d'un principe actif. Dans la première partie la formation de nano-émulsions à partir du système Remcopal 4/décane/eau ainsi que leur caractérisation sont étudiées. La seconde partie porte sur la mise au point du matériau silicaté à porosité hiérarchisée ainsi qu'à la compréhension de leur mécanisme de formation. Finalement, dans la troisième partie ces matériaux poreux ainsi que les matériaux hybrides correspondant ont été utilisés pour étudier l'encapsulation d'un principe actif hydrophobe modèle, le kétoprofène, ainsi que sa libération dans différentes conditions.

Le quatrième chapitre est dédié à l'évaluation de la stabilité thermique et hydrothermale de matériaux méso-macroporeux et de matériaux à double mésoporosité, mise au point auparavant au laboratoire. Après cette évaluation, ces matériaux ont servi de support pour l'immobilisation de la *Mucor miehei* lipase (Mml). L'activité catalytique et la recyclabilité ont été examinées. Finalement, les résultats sont comparés à ceux obtenus auparavant dans le groupe avec des matériaux mésoporeux de type SBA-15 et des matériaux méso-macroporeux préparés à partir d'émulsions concentrées.

Introduction

1 Surfactant systems

Surface active agents (usually referred to as surfactants) are amphiphilic molecules that consist of a moiety that have an affinity towards polar compounds, and a moiety that have an affinity towards nonpolar compounds. The hydrophilic moiety is referred to as the “head group”, and is covalently bonded to the hydrophobic moiety, called the “tail group”.

1.1 Properties of surfactant molecules

1.1.1 Molecular structure

The head and the tail moieties of the surfactant molecule can be a wide variety of chemical species which offers numerous variations of the surfactant structure. The hydrophobic group can be a single, double, straight or branched hydrocarbon chain, but it may also be a fluorocarbons, siloxane chain, and it may contain aromatic groups. The hydrophilic group can be ionic or nonionic, small and compact in size or a polymeric chain. Surfactant classification is based on the hydrophilic group type as follow:

- *Anionic*: the head moiety bears a negative charge;
- *Cationic*: the head moiety bears a positive charge;
- *Zwitterionic*: the head moiety bears both positive and negative charges.

Finally *Nonionic* surfactants, which are the main surfactants used in this work. They are interesting due to their several properties such as being resistant to pH variations and the hardness of water. There are several classes of nonionic surfactants such as alcohol ethoxylates, alkyl phenol ethoxylates, fatty acid ethoxylates, monoalkaolamide ethoxylates, sorbitan ester ethoxylates, fatty amine ethoxylates, and ethylene oxide–propylene oxide copolymers. We will discuss in more detail two classes of nonionic surfactants:

- Alcohol ethoxylates

The surfactants of this class are generally produced by ethoxylation of a fatty chain alcohol. The chemical formula of such surfactants is $C_nH_{2n+1}(OC_2H_4)_mOH$ (designated as C_nE_m or C_nEO_m). The solubility of those surfactants depends both on the alkyl chain length and the number of ethylene oxide units in the molecule.

- Ethylene oxide – propylene oxide co-polymers

This class is also known as polymeric surfactants. They are commonly known by their two commercial names “Pluronic” and “Poloxamer”. As their name suggests they have long polymeric hydrophobic chains (PO) and hydrophilic chains (EO). The chemical formula of those surfactants is $(EO)_x(PO)_y(EO)_x$.

1.1.2 Hydrophilic-lipophilic balance (HLB) system

Since a nonionic surfactant's hydrophilic or lipophilic character affects its behavior in water. A numerical value can be assigned in order to classify them according to this behavior. This number is called the Hydrophilic-Lipophilic Balance (HLB).

The experimental procedure for the determination of this value was introduced by Griffin^{1,2}. He made under similar conditions several emulsions with different surfactants but with the same oil. The stability of the emulsion was determined and an HLB value was attributed to the surfactant used for the emulsion. The reference surfactants are the oleic acid as the most hydrophobic one (assigned HLB = 1) and potassium oleate as the most hydrophilic one (assigned HLB = 20). The intermediate HLB values represent the stability of emulsions made using mixtures of the two reference surfactants. This technique proved to be long and laborious. So an empirical formula was established to evaluate the HLB value of a given surfactant by Griffin¹. Nonionic surfactants combine hydrophilic and lipophilic moieties in one molecule and that the ratio between the weight percentages of these two groups is an indication of the behavior that may be expected.

$$HLB = 20 \times \frac{M_{Hydrophile}}{M_{Surfactant}}$$

Where $M_{Hydrophile}$ is the molecular weight of the hydrophilic moiety, and $M_{Surfactant}$ is the molecular weight of the surfactant molecule. Nonionic surfactants containing propylene oxide, butylene oxide, nitrogen, sulfur, etc. exhibit a behavior that is not related to the composition.¹ Griffin² also found that for a mixture of two or more nonionic surfactants, the HLB value has two variables, the HLB value of each individual surfactant (HLB_i), and their weight fraction (X_i^w).

$$HLB_{mixture} = \sum_i X_i^w \times HLB_i$$

- Phase Inversion Temperature (PIT)

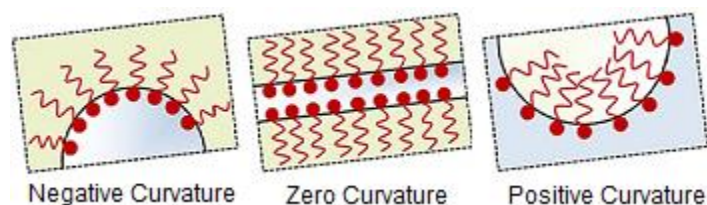


Figure 1-1: Schematic representation of the curvature of the surfactant film.³

For nonionic surfactants, the temperature is a crucial parameter in the surfactant behavior. An increase in the temperature can cause a change in the curvature of the surfactant layer causing its character to evolve from hydrophilic to hydrophobic. This phenomena was studied extensively by Tiddy *et al.*⁴, who showed that the surface area of the hydrophilic moiety

decreases with the increase of temperature. This observation is the consequence of the dehydration of the ethylene oxide chains that increases the hydrophobic character of the surfactant thus causing the transition from a positive curvature to a negative curvature (Figure 1-1).

Several empirical relationships were determined in order to calculate the PIT values of nonionic systems^{5,6}. The Phase Inversion Temperature (PIT) is the temperature at which the curvature of the surfactant changes from positive to negative or vice-versa³. Ravey *et al.*⁷ studied the relationship between the surfactant HLB, the aliphatic alkane number of carbons (ACN) or its equivalent in the case of other oils and the PIT, and showed that:

$$T_{PIT} = -A + 15.5 HLB + 1.8 ACN$$

Where A is a constant equal to 160°C.

1.1.3 Organized molecular assemblies

Many surfactants are water soluble. When the concentration is low, they keep as separate monomers in solution, or they are located at the air-water interface depending on the structure of the molecule. When the concentration reaches a certain value known as Critical Micelle Concentration (CMC) they form aggregates usually called micelles or supramolecular structures. Above this concentration monomers and micelles coexist in solution. The CMC value depends on the hydrophilic/hydrophobic character of the surfactant, the more hydrophobic it is the smaller the value of the cmc. It is worthy to note that some surfactants does not form micelles and in this case they accumulate in the form of aggregates and the concentration at which those aggregates start to appear is called Critical Aggregation Concentration (CAC).

Micelles formed in water are direct micelles (L₁), but there exists also micelles in the oily phase, they are of the reverse type (L₂). The moiety on the surface, whether it is hydrophilic or hydrophobic, forms a screen, especially with ionic surfactants, to prevent the interaction between the medium and the core that is incompatible. Both the direct and reverse micelles are transparent solutions and optically isotropic.

Some surfactants have the capacity to assemble into a bicontinuous disordered phase. This phase is known as the bicontinuous phase (designated as L₃) or sponge phase, or anomalous phase⁸⁻¹⁰. In this phase the medium forms two intertwined continuous networks separated by a bilayer of surfactant molecules (Figure 1-2). This phase is fluid and usually shows shear birefringence when examined by polarized light¹¹.

The formation of liquid crystals, is considered the next step in the aggregation process that takes place when the surfactant concentration is increased. Those liquid crystals have long

range patterns. The structure of the liquid mesophases can be mono-dimensional, two-dimensional and three-dimensional.

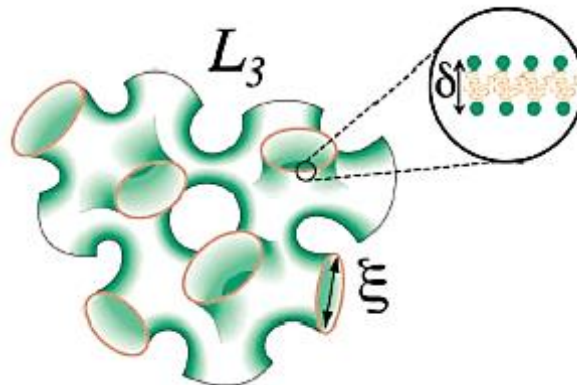


Figure 1-2: Schematic drawing of the multiconnected membrane in the L_3 structure with ξ as the sponge pore size and δ as the surfactant bilayer thickness¹².

❖ Lamellar phase - L_α

The lamellar phase (designated as L_α) consists of surfactant bilayers alternated by water layers. For most surfactants, the swelling by water is limited, but for some surfactants an extreme swelling phenomenon can be observed. In this case the dilution doesn't destroy the phase, but it causes its swelling up to several times the spacing in the lamellar crystal¹³⁻¹⁷. This phase is translucent and optically anisotropic. Through a polarized light microscope can be identified from its typical Maltese cross or oily streaks (Figure 1-3). It can also be identified using X-ray scattering (SAXS), this phase is identified with a peak sequence of 1:2:3:4... and with a repetition distance (d) equal to $2\pi/q$, with q as the wave vector that corresponds to the first order peak.

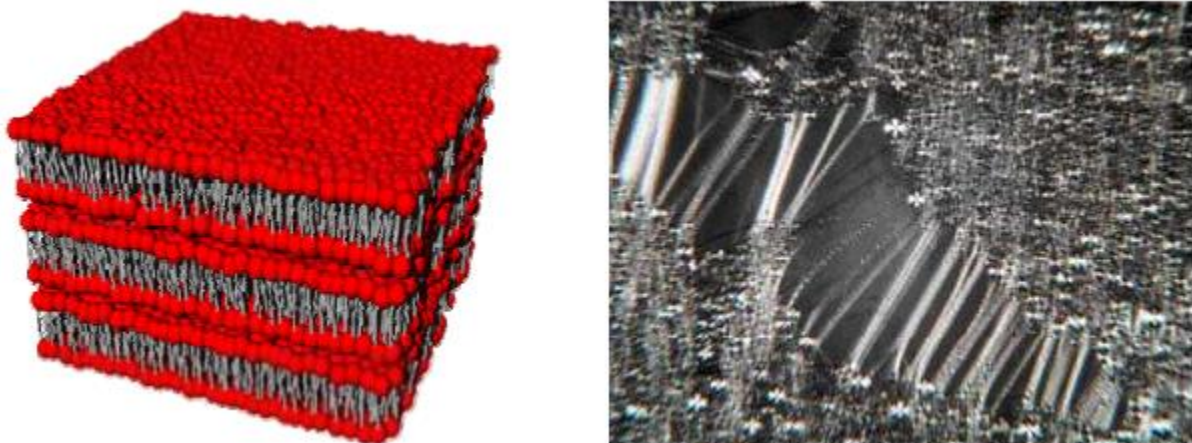


Figure 1-3: Schematic model of a lamellar phase to the left, and its texture under polarized light microscopy to the right.¹⁸

❖ Hexagonal phase - H

A hexagonal liquid crystal consists of cylindrical micelles on a two-dimensional hexagonal ordering. If the surfactant molecules in the structure have their heads towards the continuous medium they are called direct hexagonal phase (H_1), if the tails are towards the continuous medium they are reverse hexagonal phase (H_2). Those phases are transparent and optically anisotropic. They have a mosaic structure when observed through a polarized light microscope.

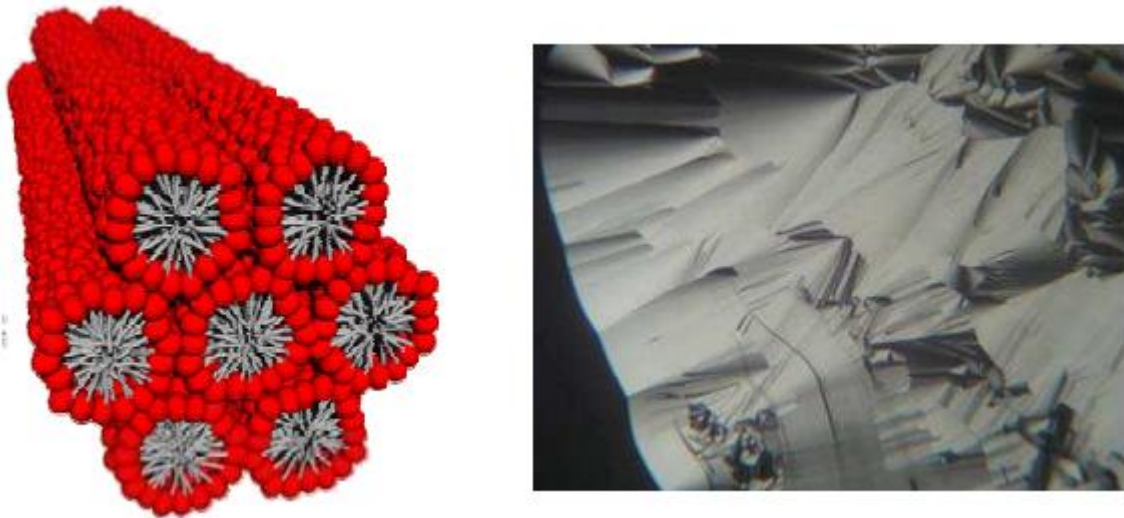


Figure 1-4: Schematic model of an hexagonal phase to the left, and characteristic texture under polarized light microscopy to the right.¹⁸

❖ Cubic phase

The cubic liquid crystals are formed by spherical, cylindrical aggregates or bilayers adopting an isotropic three-dimensional structure. If they are formed by spherical micelles they are cubic micellar phase (I_1, I_2) and they can be organized along a primary, face-centered or body-centered symmetry ($Pm3m, Fd3m, Im3m$). The micelles are separated by a layer of continuous medium. Otherwise, there exist the bicontinuous cubic phases (V_1, V_2) are, as their name suggests, two intertwining continuous networks separated by a bilayer of surfactant (Figure 1-5). Those phases can have three different symmetries $Ia3d, Pn3m$ and $Im3m$. These liquid crystals are highly viscous, transparent and isotropic (undetectable using polarized light microscopy). They are identified using SAXS and the distance that separates the different peaks depends on the type of symmetry they adopt.

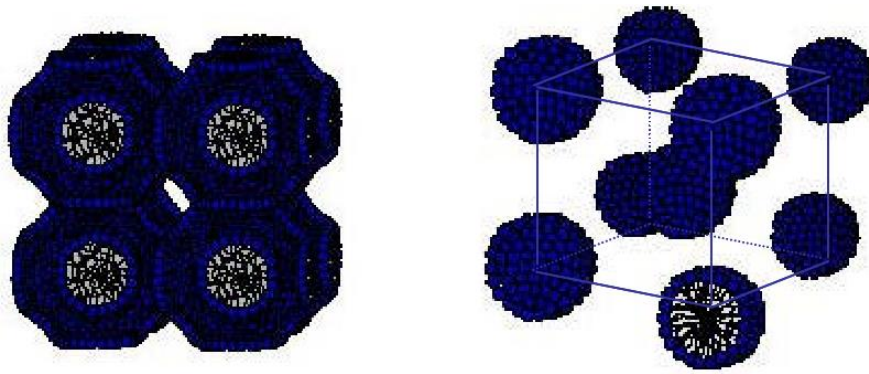


Figure 1-5: Schematic models of a bicontinuous cubic liquid crystal to the left and a micellar liquid crystal to the right.¹⁹

1.1.3.1 Oil in water or water in oil solubilisation

Since the surfactant molecular direct assemblies can form a layer that separates a hydrophilic medium from a hydrophobic core, a third hydrophobic component such as oils or lipids can be solubilized in this hydrophobic environment. The same molecular assemblies can be conserved in, but they show a swelling consistent with the quantity of hydrophobic compounds added. For the micellar structures (L_1), the solubilisation of oil leads to “swollen micelles “ or “microemulsion”²⁰ depending on whether or not an oily core can exist.

On the other hand, when the continuous medium is an oil, the surfactant forms L_2 micelles that can solubilize water in its core.

As for the lamellar, hexagonal and cubic liquid crystals and the L_3 phase, they can solubilize oily or aqueous compounds while preserving their structure. The repetition distance increases with the swelling.

1.2 Emulsions

Emulsions are by definition a mixture of two immiscible liquids, typically oil and water, homogeneous at macroscopic scale, but heterogeneous at microscopic scale. Since the mixtures of oil and water are not stable, usually a surfactant is added to stabilize the mixture. The surfactant’s role is to lower the surface tension between the dispersed and the continuous phase, thus favoring the formation of kinetically stable emulsion droplets. There exist two types of emulsions known as oil in water (O/W) emulsions which is formed by oil droplets in a water continuous medium and water in oil (W/O) emulsions which are formed by water droplets in an oil continuous medium (Figure 1-6).

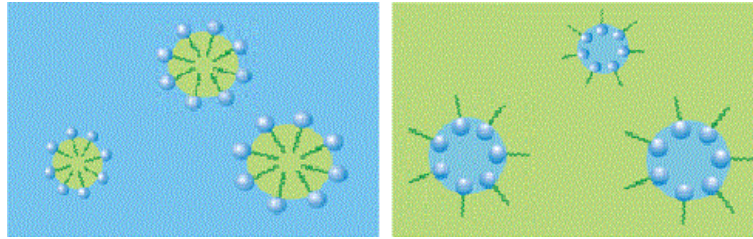


Figure 1-6: Schematic representation of the O/W emulsion (left) and W/O emulsion (right).

The dispersed volume fraction (water or oil) can vary between 0.01 to more than 0.97, in the latter case it is called a concentrated emulsion^{21,22}. As emulsions are kinetically stable, changes of the properties will occur; the slower those changes happen the more stable the emulsions. Because the droplets are constantly moving, whether it is the Brownian motion, gravity or mechanical agitation, the droplets will often collide with each other, this collision will either result in an aggregate or the droplets will move apart. There are two types of aggregation: flocculation and coalescence. Flocculation is the aggregation of droplets without altering their physical properties (size, shape) and can be reversible, while coalescence is the aggregation of droplets that merge together to form larger droplets, this process is irreversible²³. In the case that one of the liquids is slightly soluble in the other, a third aging process might take place, the Ostwald ripening, it is the process of gradual growth of the larger droplets at the expense of smaller ones due to mass transport of soluble dispersed phase into the continuous phase²⁴⁻²⁶, this process is accelerated when the droplets are initially polydisperse.

In most cases the droplets and the continuous medium have different densities, if the droplets' density is lower than the medium, they will tend to go up and form a layer of emulsion droplets at the top of the emulsion in a phenomenon known as creaming, if the droplets have higher densities they will go to the bottom and the phenomenon is known as sedimentation. The creaming velocity of a single droplet that is not subject to deformation is given by the Stokes' law:

$$v = \frac{2gr^2(\rho_{cont} - \rho_{disp})}{9\eta_{cont}}$$

Where g is the acceleration due to gravity, r is the radius of the droplets, ρ_{cont} and ρ_{drop} are the densities of the continuous phase and the dispersed phase respectively, and η_{cont} the viscosity of the continuous phase. It should be noted that this relationship is applicable to dilute emulsions.

So in order to reduce the creaming several parameters can be changed such as choosing a dispersed liquid and a continuous medium with similar densities, or a continuous medium with high viscosity. But those parameters limit the choice of liquids or require additives such as co-surfactants or solid particles. The only parameter that can be changed without influencing the

nature and properties of the components is the radius of the droplets. This parameter can be changed by increasing the emulsification energy, or using the physico-chemical properties of the surfactant (this is further discussed in section 1.3).

These compounds are used to provide long term stability in emulsions by increasing the continuous phase viscosity or producing a yield strength in the system that reduces motion. These stabilizers are usually macromolecules that are not surface active but only soluble in the continuous phase such as Xanthan gum which forms a network of emulsion droplets and stabilizes the emulsion against creaming²⁷.

Another way to stabilize emulsions with solid particles. The particles have a certain affinity for both phases without being soluble in any of them. The type of emulsion formed depends on the contact angle in both liquids. The energy to remove these particles from the interface is much larger than for smaller molecules and therefore they are very efficient at stabilizing interfaces. Those kinds of emulsions are known as “Pickering emulsions”²⁸. And finally, more complex kinds of emulsions also exist such as multiple emulsions where a droplet of water is entrapped in a droplet of oil which is dispersed in an aqueous continuous medium (Figure 1-7).



Figure 1-7: Micrographs of droplets of multiple emulsions.²⁹

1.3 Nano-emulsions

Nano-emulsions known also as mini-emulsions, ultrafine emulsions, submicron emulsions are a specific kind emulsions that have sub-micrometer droplet size³⁰ and a high monodispersity. Generally the droplets of a nano-emulsion have a size smaller than 200 nm³¹. Due to their characteristic size, nano-emulsions have a transparent or bluish aspect and are extremely stable against sedimentation or creaming because it is prevented by the brownian motion of their droplets.

Nano-emulsions, being kinetically stable systems, require energy input in order to be formed, either from mechanical devices or from the intrinsic physicochemical potential of the components. The methods using mechanical energy are called dispersion or high-energy emulsification methods³² while those making use of the chemical energy stored in the components are referred to as condensation or low-energy emulsification methods³³.

1.3.1.1 High energy methods

The droplets are generated by high-shear mixing or by sonication. Those systems are obtained with a large array of surfactants, and for a large water/oil/surfactant composition range. The droplet size can be tuned by varying the amount of energy input (rotation speed³², frequency³⁴) and can be scaled to an industrial level. On the other side this energy can generate heat which is unfavorable in the presence of volatile oils or thermally fragile components^{35,36}. Other techniques such as microfluidic flow focusing and membrane emulsification also exist, even though they are better adapted for industrial production, they require special equipment and are prone to coalescence³⁷.

1.3.1.2 Low energy methods

Another way to generate nano-emulsions with a low energy input is to take advantage of the intrinsic physicochemical properties of the components of a system³⁸. There are two classes of low energy approaches: the self-emulsification and phase inversion

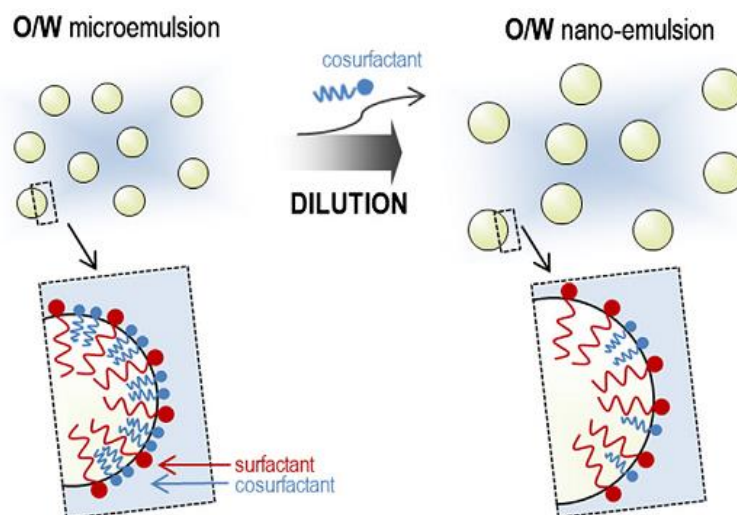


Figure 1-8: Schematic representation of the mechanism of the “Ouzo effect”. During the dilution the cosurfactant diffuses into the aqueous medium making the microemulsion thermodynamically unstable thus creating the nano-emulsions.³

. The self-emulsification method also known as the “Ouzo effect” is the transformation of a microemulsion (thermodynamically stable system) into a nano-emulsion (kinetically stable system) by reducing the surfactant’s concentration via a simple dilution. It consists of an initial solution of oil, surfactant and a co-surfactant (such as ethanol) that is also soluble in the

aqueous medium^{39,40}. Then the simple addition of water will reduce the surfactant's concentration (thus increasing the surface tension above 10^{-4} N.m⁻¹ which is the upper limit for thermodynamic stability³³) and generating an O/W emulsion in one step (Figure 1-8).

The phase inversion methods depend on the phase transitions of a system to generate nano-emulsions. Those phase transitions are associated with the ability of the surfactant to change its curvature during the emulsification process.

The curvature of the surfactant is negative when it forms a W/O emulsion, zero when it forms a planar film and positive when it forms an O/W emulsion (Figure 1-1). In the case of phase inversions mainly nonionic surfactants are used, their curvature can be changed by the modification of the hydration grade of the polar head in the surfactants molecules. The hydration grade can be controlled by modifying the temperature or the composition.

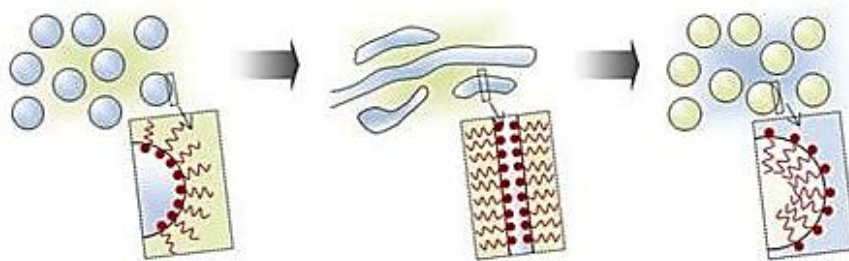


Figure 1-9: Schematic representation of the mechanism of the formation of nano-emulsions by the PIC method.³

The first approach in the phase inversion to form nano-emulsions consists of the progressive addition of water to an oil/surfactant mixture and is known as Phase Inversion Composition.

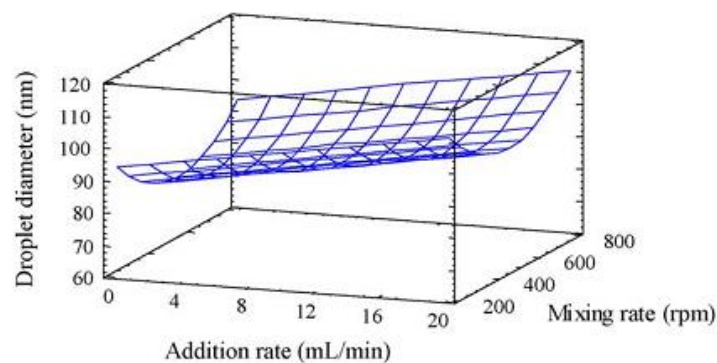


Figure 1-10: Droplet diameter as a function of addition rate and mixing rate of the Water/Span20-Tween20/Paraffin system.⁴⁴

The whole process takes place at constant temperature. The system consists initially of a reverse micelles phase which evolves into a W/O microemulsion upon addition of water. When the fraction of the continuous phase is increased, the spontaneous curvature from negative to

positive curvature. At the final composition oil droplets are formed in an aqueous continuous phase.

In this approach the formulation variables such the surfactant type are crucial, although polyoxyethylene surfactants are not required for this method, they have been used extensively for the preparation of O/W nano-emulsions⁴¹⁻⁴⁴ and W/O nano-emulsions⁴⁵.

Also the variables such as the addition and the stirring rates play a major role. Several researchers^{44,46} have studied the effect of those two variables on the nano-emulsions and concluded that the slower the addition rate the smaller the final nano-emulsions. Likewise for the stirring rate there exist an optimal value because on one hand it enhances the homogenization and on the other it can favor coalescence (Figure 1-10).

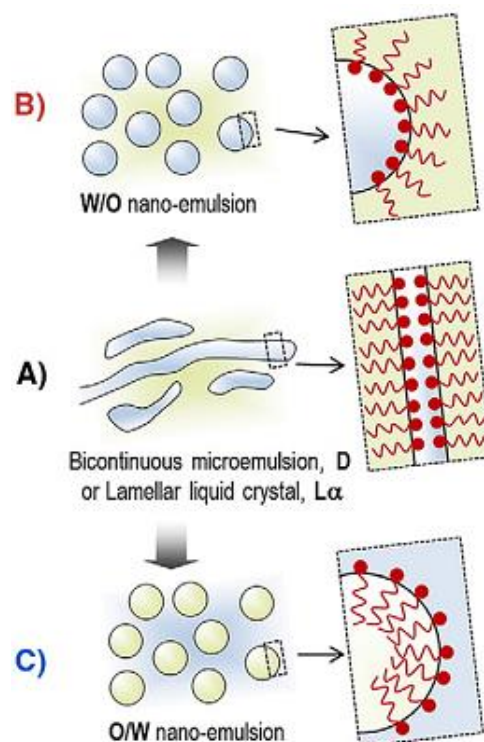


Figure 1-11: Schematic representation of the mechanism of formation of the nano-emulsions by the PIT method³. A) Represents the phases at the phase inversion temperature, B) the structure for a temperature above the PIT and C) the structure for a temperature below the PIT.

On the other hand, the PIT approach consists of the changing of the curvature of the surfactant by changing the temperature. It was first introduced by Shinoda *et al.*⁴⁷ with nonionic surfactants. The nonionic surfactants change their curvature with temperature, at low temperature their curvature is positive and at high temperature their curvature is negative. The temperature at which the curvature is zero is called the phase inversion temperature. This method takes advantage of the low interfacial tensions achieved at the phase inversion temperature, around 10^{-2} - 10^{-5} mN.m⁻¹³³. In such conditions droplets with a very small diameter can be formed. But at such a temperature the surfactant's curvature is close to zero which

increases the coalescence rates. Consequently the cooling process must be fast in order to form small droplets while avoiding any coalescence. Depending on the composition of the system, a bicontinuous microemulsion or a lamellar phase or a mixture of both is present around the phase inversion temperature, a transition through one or more of these phases is necessary in order to form the nano-emulsions (Figure 1-11).

For both phase inversion approaches, the amount of surfactant present in the system influence the size of the droplets formed, the more surfactant present the smaller the size. It should be noted that a nano-emulsion requires much less surfactant than a microemulsion. The properties of the nano-emulsions makes them suitable for applications in drug delivery, cosmetics, pesticides and oil recovery.

2 Porous Silica Materials

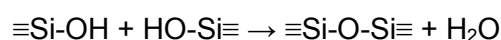
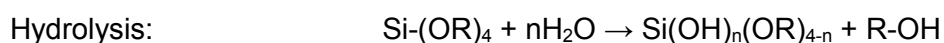
Porous inorganic materials with tunable, hierarchical pore structures are becoming more and more important as a class of solid materials because of their wide variety of applications such as support for catalysts⁴⁸, or biomedical applications such as drug delivery^{49,50}. Their importance comes from their properties such as a large surface area (around 1000 m²/g), their big pore volume, and the presence of pores that allows the control of the diffusion. The use of adapted templates for the preparation of the materials permits the tuning of the pore sizes as well as the other properties in order to meet the requirements of any application.

In this study we will focus on the mesoporous and hierarchically porous silica materials, sol-gel process was employed because of its simplicity.

2.1 Sol-gel process

The sol gel process is based on the ability of silica alkoxides to polymerize and form a network which will then grow into bigger particles called “Sols” or to form a three-dimensional network called “Gel” depending on the reaction parameters as shown in Figure 2-1.

Silicate gels are synthesized by hydrolyzing monomeric tetrafunctional alkoxide precursors, thus the sol-gel process consists of three reactions:



The hydrolysis reaction can be catalyzed by either mineral acids or bases. In most environments the condensation reactions start before the hydrolysis reaction is complete. the condensation reactions form the silica clusters, which depending on the pH, salinity and

temperature either grow to form large particles, or aggregate and form a three dimensional network.

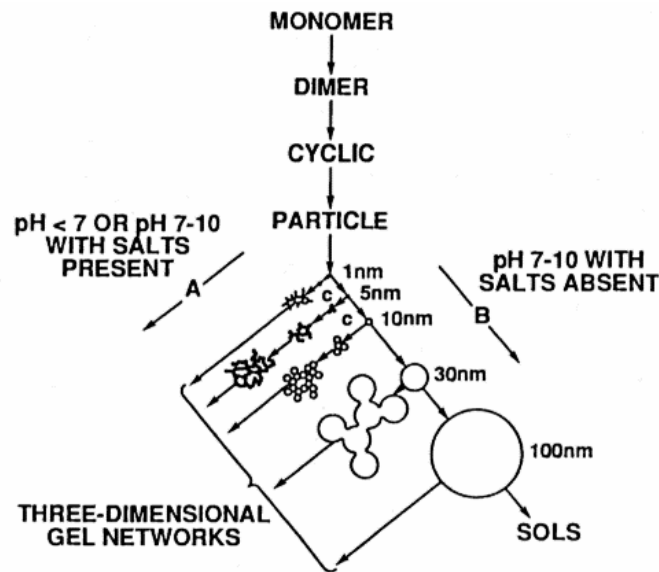


Figure 2-1 Polymerization behavior of aqueous silica. In a basic solution (B) particles grow in size with decrease in number, in acidic solution or in the presence of flocculating salts (A) particles aggregate into three-dimensional networks and for gels ⁵¹.

The most common tetrafunctional alkoxides used in the sol-gel process are the tetraethoxysilane (TEOS) and tetramethoxysilane (TMOS), other precursors exist but are seldom used such as tetra-n-propoxysilane, tetra-n-butoxysilane and tetrakis(2-methoethoxy)silane.

2.2 Mesoporous Materials

Mesoporous materials are materials with pore size between 2 and 50 nm according to the IUPAC nomenclature ⁵². Their main characteristic is their high surface area and their big pore volume. This provides sites where adsorption can occur for molecules such as catalysts or drug molecules. They offered a relatively large pore size compared with the zeolites which allowed the diffusion of larger molecules.

In 1992, scientists at Mobil Corporation synthesized ordered mesoporous material from a template of surfactant micelles⁵⁴. They called this family of mesoporous material the “M41S”. Nowadays there exist several families of mesoporous material synthesized using different surfactant templates and have several textures and pore size and ordering.

Regarding the mechanisms of formation of the mesoporous material there exist two main mechanisms, the cooperative templating mechanism (CTM) and the liquid crystal templating (LCT). Both mechanisms require the presence of an organized Molecular System and the LCT mechanism consist on the transcribing of a liquid crystal already present whereas the CTM

mechanism produces a material with an ordering resulting from the interactions between the silica precursor and a micellar phase (Figure 2-2).

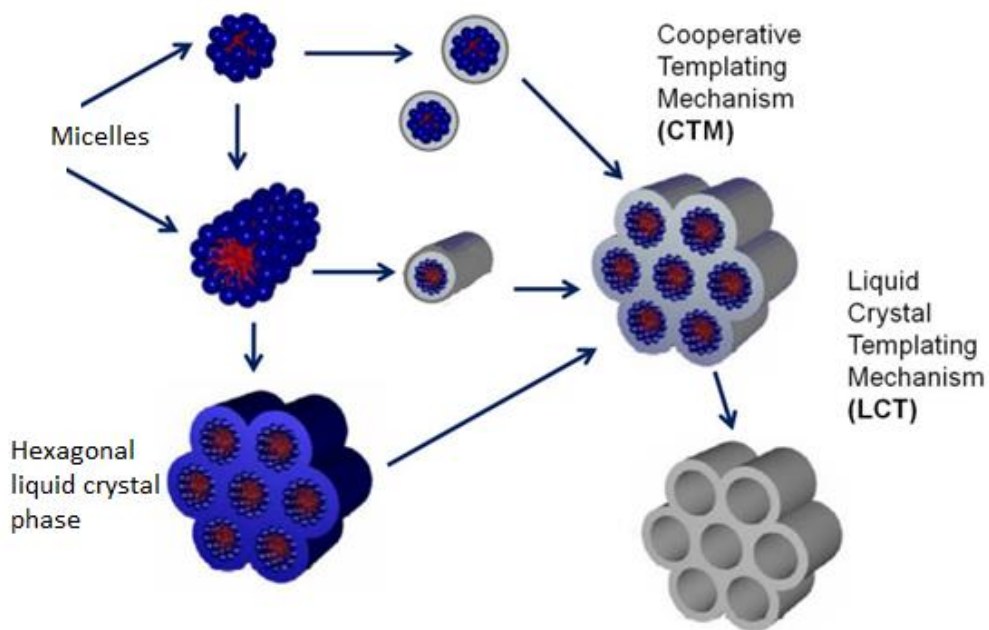


Figure 2-2: Schematic representation of the cooperative templating mechanism and the liquid crystal templating mechanism.⁵³

In the work presented in this thesis, the CTM was used for the templating of the mesopores.

2.2.1 Cooperative templating mechanism – CTM

This mechanism requires the presence of a micellar solution and a silica source.

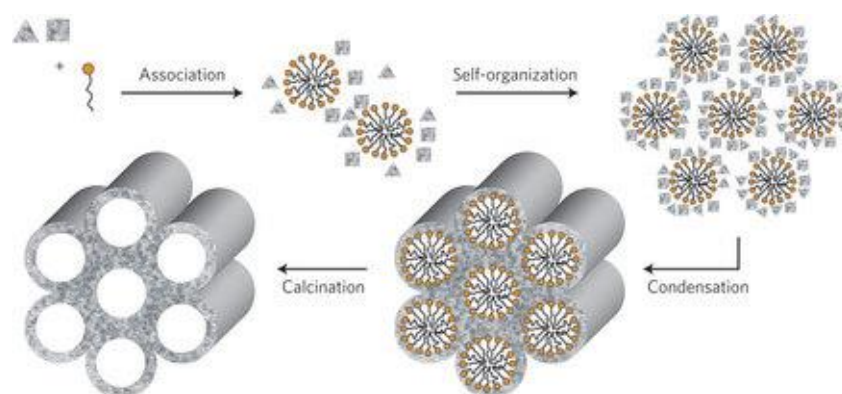


Figure 2-3: Schematic representation of the CTM mechanism.⁵⁶

The silica source polymerizes around the micelles according to the sol-gel process and the pre-formed silica oligomers interact with the surfactant micelles, and the curvature shift induces a change from a micellar solution to an ordered packing forming a surfactant silica hybrid mesophase (hexagonal, cubic or lamellar)⁵⁵.

The first step consists of the polymerization of the inorganic precursor around the micelles, or intra-micellar polymerization, which is the result of the interaction between the polar heads of the surfactants and the precursor. The interactions can be hydrogen bonds if the surfactant is nonionic. The second step is the intermicellar condensation, in which the micelles self-assemble into a close-packed structure, usually hexagonal, and is designated as a hybrid mesophase. In order to complete the process and to ensure the complete condensation of the inorganic matrix, a hydrothermal treatment is used. Finally the final material is obtained after the removal of the surfactant via calcination or Soxhlet extraction using ethanol (Figure 2-3).⁵⁷

2.2.2 Liquid crystal/emulsion templating

This mechanism requires the presence of an initial macromolecular structure which will serve as an organic template. Those templates can be liquid crystals⁵⁸, or emulsions⁵⁹ or solid particles⁶⁰. The silica precursor is added to the template, which condenses and polymerizes directly around the template. Finally, after the elimination of the template, the silica material assumes the shape and the organization of the organic template.

2.3 Hierarchically porous materials

Porous materials have found wide applications in many fields of chemistry such as catalysis, adsorption, electronics and environmental technology because of their high surface area coupled with many other physical and chemical properties⁶¹⁻⁶⁴. Recent developments in research fields such as photonics, bioengineering and nanotechnology increased the need for a well-defined structural, interfacial, compositional and morphological properties which can only be offered in a material having a porosity at multiple scales. In catalysis, it has been reported that a hierarchal combination of pores reduces transport limitations and blockage, resulting in higher activities and better control over selectivity⁶⁵.

2.3.1 Meso-macroporous materials

The increased demand for the encapsulation and release of large molecules with a big molecular weight such as proteins drove the researchers to develop porous silica materials with a large pore size (30 nm)^{66,67}. These applications require porous materials with hierarchical pore structure at different scales in order to achieve highly organized functions and improve the diffusion of large molecules. The development of hierarchical porous materials at multiple scales was the subject of interest over the last few years. The presence of mesopores in the walls of the macropores is more interesting and useful for the catalysis and drug delivery systems. From an application viewpoint, drugs or catalysts can be loaded

in the mesopores and in the micropores while the macropores enhance the mass transfer and reduce the transport limitations. This is particularly beneficial in the case of large molecules or in viscous systems where diffusion rates are low. For the sake of large performance improvement, such materials should possess adjustable and well-defined macropores and tunable mesopores in the macropore walls. On all length scales, the bigger pores should be connected via smaller pores. Thus it remains a challenge to synthesize hierarchically bimodal mesoporous-macroporous materials with controlled individual pore sizes and pore structures, although several methods have been reported that combine the individual process techniques of mesopore and macropore synthesis, for example, by dual templating of surfactant systems and colloids⁶⁸.

In the synthesis of hierarchical meso-macroporous inorganic materials, self-assembled molecular aggregates or supramolecular assemblies are generally employed as the structure-directing systems of meso-structures. Meanwhile, a lot of techniques can be employed for the design of the macroporous network.

2.3.1.1 Polymer spheres templating

A general procedure of synthesis to generate the macroporous network requires the use of polymer spheres as templates. Colloidal polymer spheres, with a narrow size distribution, are left to aggregate in an organized manner. These colloidal spheres are submerged with the inorganic precursor and a micellar solution, then a condensation process is put in place. The surfactants and the spheres are either removed by calcination or solvent extraction. This leads to the formation of a three-dimensional ordered meso-macroporous material (3DOM)⁶⁹⁻⁷¹.

Tiddy *et al.*⁶⁰ synthesized a series of hierarchically ordered porous silica composites with ordering on three different scales of pore size by using polystyrene spheres for the macropores and a mixture of triblock copolymers (pluronic F127 and P123) as templates in the presence of co-surfactants (*n*-alcohols) in an acidic medium. The silica materials consists of three-dimensional ordered macropores (200 – 800 nm) with interconnecting, uniform sized (70-130 nm) windows and the walls of these macropores consist of mesostructured pores (3 – 8 nm), as well as a significant microporosity presenting a macro-meso-microporous structure with a three-dimensional interconnectivity. The formation of windows is due to the close-packed arrangement of the spheres (touching points) (Figure 2-4). The meso- and microporosity are generated by the micelle formation of the block copolymers in the presence of the co-surfactant butanol or pentanol. The surface area and mesopore volume of the materials were low (46 m²/g and 0.053 cm³/g) when the latex spheres are removed by direct calcination at 550°C, while a high total surface area of 531 m²/g was obtained after extraction of the latex spheres using toluene which is then followed by a calcination at 450°C.

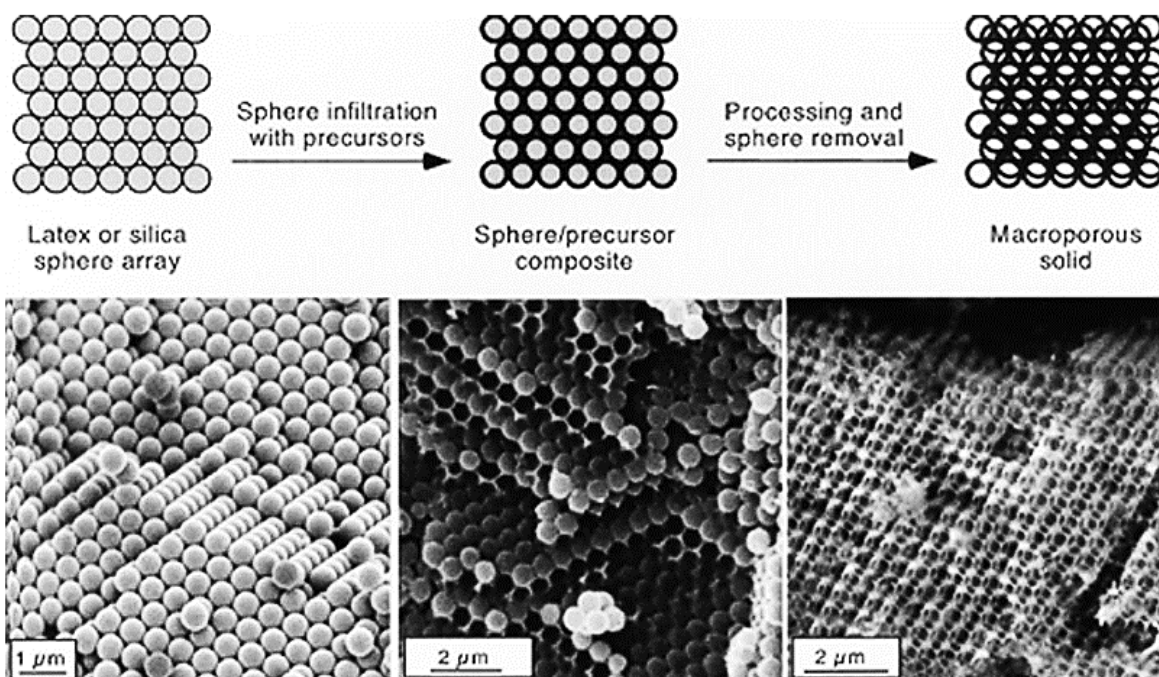


Figure 2-4: General synthesis scheme for periodic macroporous solids and the corresponding scanning electron micrographs for a Polystyrene/Silica system prepared with TEOS⁷².

2.3.1.2 Emulsion templating

The emulsion templating method is probably the most commonly used to obtain macroporous material⁵⁹, it has been used to produce macroporous silica, titania and zirconia with pore sizes starting from 50 nm till several micrometers, although most of the reported cases are disordered macroporous solids. Because the emulsions droplets are deformable, macroscopic samples are able to accommodate stress that arises during the gelation and shrinkage. Samples made using rigid spheres, by contrast, tend to break into small pieces that are seldom larger than a few hundred micrometers. In addition, emulsification conditions can be adjusted to produce droplets with different sizes which are typically in the micrometer range. Moreover, this can be done to a large extent independently of the self-assembling block copolymer species used to direct the structure of the mesopores. This allows direct and independent control of macro- and mesopore dimensions. So the final pore structures can be tailored to different diffusion and reaction criteria⁶⁷.

The introduction of mesopores in the macroporous structure has been done using a surfactant emulsion mediated synthesis. The formation of macro-cellular foams is explained based on a natural phenomenon of O/W emulsion known as “creaming”. This synthesis was carried out using cetyltrimethylammonium bromide as surfactant and trimethylbenzene as oil. The obtained material has a high surface area (800 m²/g) with a narrow pore size distribution centered at 4 nm. It has been also demonstrated that mesoporous silica could be obtained by

using a low oil (mesitylene) concentration, meanwhile under the faster stirring, meso-cellular silica foams was produced. However the mesoporous walls adopt a worm-hole like structure. Cooper *et al.*⁷³ reported the synthesis of hierarchically porous emulsion-templated polymer/silica composite beads by sedimentation polymerization of a high internal phase emulsion (HIPE). High surface area silica beads with an average diameter of 1.3 mm, a high pore volume of 5.7 cm³/g and an interconnected macropore structure were obtained by calcination of the composites structures. The HIPE structure was retained in the silica spheres and the material has a high surface area (422 m²/g). This semi-continuous synthetic procedure could be scaled up to allow the synthesis of significant quantities of beaded materials with a narrow particle size distribution. Carn *et al.*⁷⁴ reported the preparation of hierarchical inorganic porous monoliths with a double template, i.e. direct emulsion at the macroscale and micellar templates at the mesoscale. The monolithic materials had typical polymerized high internal phase emulsion (poly-HIPE)-type interconnected macroporous network with polydisperse cell and window sizes within the micrometer range. These material show interconnected macropores with disordered structures. The mesopores sizes vary between 1.2 to 4 nm. As shown by the examples aforementioned, the synthesis of well-defined macroporous silica with highly ordered mesopores is difficult to perform. However, it has been developed in our group⁷⁵ that the use of O/W fluorinated emulsions allows the design meso-macroporous silica with a well ordered array matrix of mesopores. The emulsion is constituted of fluorocarbon droplets stabilized by the fluorinated surfactant molecules and dispersed in an O/W fluorinated microemulsion (Figure 2-5). The mesopore size distribution is narrow and centered at about 7.5 nm whereas the size of macropores varies from 1 to 3 μm.

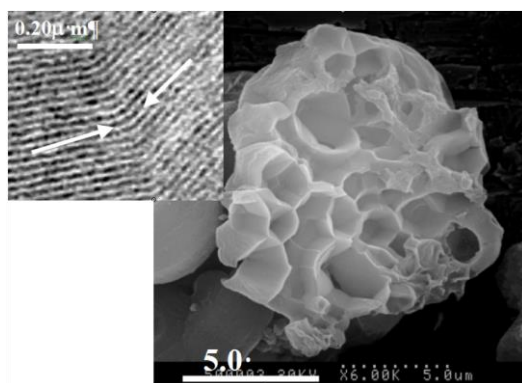


Figure 2-5: TEM micrograph (left) and SEM micrograph (right) of a meso-macroporous silica material prepared from a fluorinated emulsion in the presence of fluorinated microemulsion⁷⁵.

In another way, nano-emulsions have emerged as a new kind of template due to their unique properties^{30,76,77}. They are easy to produce, and the size of the droplets is easy enough to control and the size distribution is narrow. In recent years the interest in nano-emulsions as a template for the design of porous materials started to increase. Prouzet *et al.*^{78,79} reported the synthesis of porous silica from nano-emulsions prepared by phase inversion composition

(PIC). The authors have used the oil phase of the nano-emulsion as a nanoreactor for the preparation of magnetic- γ -Fe₂O₃ nanoparticles. Mou *et al.*⁸⁰ have also used the nano-emulsion templating approach for the synthesis of silica nanoparticles with compartmentalized hollow structure via ultrasound-assisted sol-gel method.

2.3.1.3 Polymerization induced phase separation in the presence of polymers

Another route to the synthesis of mesoporous silica material with interconnected macropores is the application of chemically induced liquid-liquid phase separation⁸¹. This technique is based on the hydrolysis and condensation of inorganic precursors in the aqueous domain, derived from the self-assembly phase of the template used. The earlier the phase separation takes place in the sol-gel transition, the larger the characteristic size of pores and gel skeletons become. A wide variety of water soluble block copolymers, such as polyoxyethylene surfactants, has been used to control the phase separation/gelation kinetics in the preparation of monolithic silica exhibiting both interconnected macropores and textual mesopores. With the use of various silica precursors such as tetramethoxysilane, tetraethoxysilane and bis(trimethoxysilyl)-ethane, amorphous or disordered mesopores can be integrated in gel networks which constitute a co-continuous macroporous structure^{82,83}.

Nakanishi *et al.*^{84,85} synthesized monolithic silica gels with a hierarchical meso-macroporous structure via a spontaneous sol-gel process and yielded materials with highly ordered hexagonal arrays of mesopores (Figure 2-6). The authors explain that the monolithic body with well-defined interconnected macropores is a result of concurrent phase separation and sol-gel transition induced by the polymerization reaction, whereas the mesopores are templated by the cooperative self-assembly of inorganic species and the assembly directing agent polyethylene oxide-block-poly-polypropylene oxide-block-polyethylene oxide.

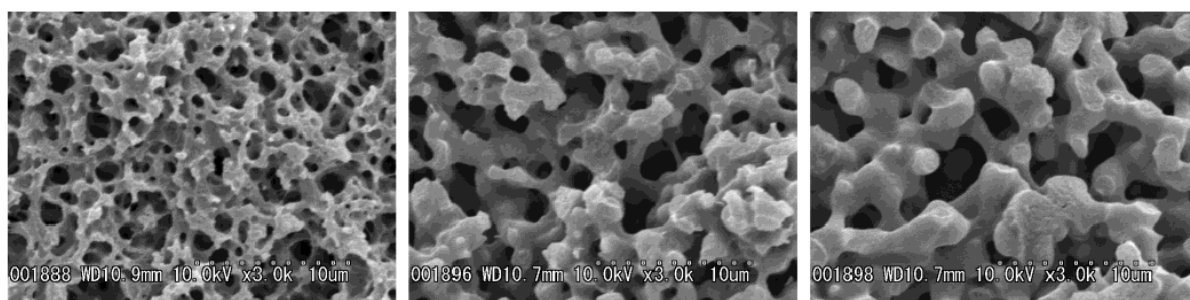


Figure 2-6: SEM micrographs of heat-treated gel samples prepared with varied trimethylbenzene concentrations, from left to right: 0.3;0.35;0.4 unit/g⁸⁵.

2.3.2 Bimodal mesoporous materials

Many papers can be found in the literature focusing on the synthesis of meso-macro, micro-macro or micro-mesoporous materials^{60,75,83,86-90}. However only a few deal with bimodal systems having two types of mesopores^{67,91-95}. In addition, the final material has either a

disordered bimodal mesopore arrangements or ordered mono-modal mesopore with small size template molecular systems embedded in larger entities.

One of the strategies to prepare bimodal mesoporous material consist in using mixtures of templates^{93–99}. For example Chen *et al.*⁹⁸ employed mixtures of micellar solutions of nonionic surfactants including Pluronic, Brij and Tetronic types as templates for synthesizing porous silica materials having mixed pore sizes. Depending on the surfactant mixture, ordered uniform pore size arrangements, partially ordered complex bimodal structures or totally disordered non-mesoporous structures were obtained. Among the surfactant mixtures, the ones of fluorinated and hydrogenated surfactants are useful in specific practical applications, so these mixtures in aqueous systems have been widely investigated using different techniques such as light scattering, NMR and small-angle neutron scattering (SANS)^{100–103}. In these systems, either mixed micelles containing both surfactants in a well-defined proportion, or two kinds of micelles enriched in one of the two components can be formed. In fact, fluorinated surfactants have chemical and physical properties that are different from the hydrogenated ones. Due to the difference in polarities between the fluorocarbon and hydrocarbon chains nonideal net repulsive interactions can occur.

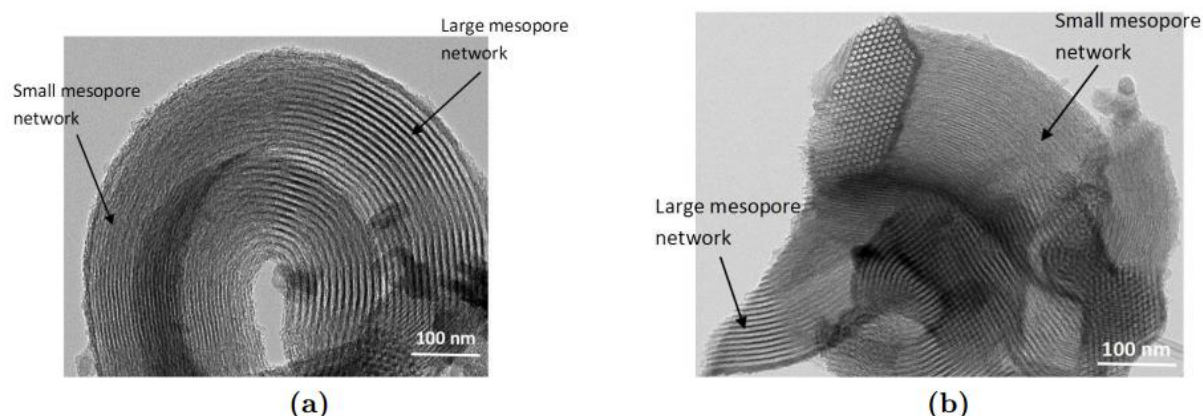


Figure 2-7: TEM micrographs of the bimodal mesoporous material prepared from a mixture of Pluronic P123 and $R^F_8(EO)_9$ at a 10:90 ratio¹⁰⁵.

Xing *et al.*⁹⁴ adopted this methodology to synthesize bimodal mesoporous silica by the cooperative assembly of hydrolyzed tetraethoxysilane (TEOS) with a mixture of ionic fluorinated and hydrogenated surfactants. Although the authors succeeded in tailoring the bimodal pore size by adding lipophilic or fluorophilic oils, disordered worm-hole like pores were formed. Antonietti *et al.*¹⁰⁴ have also reported the synthesis, from mixed micellar solutions of non-miscible fluorinated and hydrogenated surfactants, of mesoporous silica monoliths with bimodal pore size distribution via the nanocasting process. In our Laboratory¹⁰⁵ a mixture of hydrocarbon surfactant (Pluronic P123) and a fluorocarbon surfactant ($R^F_8(EO)_9$) have been used to synthesize a bimodal silica material with two ordered mesopore networks and two mesopore sizes centered at 3.7 and 9.7 nm (Figure 2-7).

3 Application fields

The high melting point, tailored electronic and magnetic properties, corrosion and wear resistance, low thermal conductivity, controlled permeability, high surface area and pore volume, and the low density, make those material suitable for a very large array of applications such as the removal of heavy metals, photoluminescence, lithium batteries, proton conductivity, protective coatings, sensors. In this work we are only interested in the applications in drug administration, enzyme immobilization and catalysis.

3.1 Drug administration systems

Presently, commercial drug administration systems, usually based on polymer technology, are used mainly for implants, oral, transdermal and injectable routes amongst many others, but one of the major drawbacks of such systems is the loss of the activity of the loaded active ingredient before it reaches its target due to premature degradation or release. One way of dealing with this problem is by using stimuli-responsive systems where the release kinetics are controlled either by external stimuli (magnetic field, UV light) or internal stimuli (pH, redox reactions). Those types of systems require a more complex design than the currently available ones in order to meet those criteria. The most important requirement is the biocompatibility of the system since it will be in contact with at least one physiological environment, this implies that the carrier matrix should be chemically inert while maintaining its ability to release the drug when and where it is needed. Recently porous silica materials attracted the attention of researchers as a potential solution for this problem^{106,107}. Lai *et al.*¹⁰⁸ demonstrated in their article the biocompatibility of silica nano-spheres when interacting with cellular systems by encapsulating adenosine triphosphate or antibiotics such as vancomycin in MCM-41 type mesoporous silica nano-spheres and blocking the pores with CdS nanoparticles that can be chemically removed by using various disulfide-reducing agents and testing them in cellular cultures from neonatal rat cerebral cortex.

3.1.1 Effects of porous silica materials properties on drug loading and release

The drug loading and release from porous silica materials can help overcome some of the main problems in this field. This is due to their textural properties which can be adjusted to suit different requirements and needs. The influence of those properties depends on the pore size and the textural properties of the matrix.

- Influence of the porosity on drug loading and release

Drug molecules have different sizes and molecular weights, thus with the appropriate pore size the adsorption can become selective and the release of several active ingredients is consecutive instead of simultaneous. Alongside the control of the order of the active ingredients' release, the pore size controls the flux of the release medium thus controlling also the release rate. Horcajada *et al.*¹⁰⁹ showed that the pore size controls the release rate by modifying the pore size of MCM-41 type materials by increasing the length of the hydrophilic chain of the CTAB surfactant and studying the release of ibuprofen, they determined that the maximal released amount for a pore size of 2.5 nm is 40% while it reaches 68% for a pore size of 3.6 nm.

Furthermore, the association of macropores with mesopores can improve the efficiency of mesoporous materials as they enhance mass transport and reduce diffusion limitations^{70,110}. In these materials the macropores act as channels to facilitate the transport of molecules that have to be adsorbed in the mesopores. It has been demonstrated that hierarchical materials containing both interconnected macroporous and mesoporous structures have enhanced properties when compared with materials with uniform pores¹¹¹.

- Effects of the textural properties on the drug immobilization

Once inside the pores (especially the mesopores and the micropores) the molecules of the active ingredient have two types of interactions. The first one is between the molecule and the surface, this interaction depends on the surface area of the matrix and controls the loaded quantity of the active ingredient. Vallet-Regi *et al.*¹¹² were able to corroborate this theory by comparing the maximum loading capacity of alendronate onto SBA-15 matrix (1157 m²/g) to the one of MCM-41 (719 m²/g) and obtained 139 mg/g and 83 mg/g, respectively.

The second type of interactions is between the molecules themselves, and this type of interactions depends on the pore volume. It has been proven by Devoisselle *et al.*¹¹³ that the intermolecular interactions between the molecules of the active ingredients influence the packing and can result in better drug loading. Those interactions can be facilitated by increasing the pore volume

3.1.2 Hybrid materials as carriers of active ingredients

In recent years, research into organic/inorganic hybrid materials has become an important subject of study for materials and biomaterials sciences. Hybrid materials are materials formed by two components, an organic component and an inorganic one. Generally the behavior of hybrid materials is dependent on the nature and relative content of the constitutive inorganic and organic components, with a close dependence on the experimental conditions¹¹⁴. The silica-ordered mesoporous materials can be functionalized and thus can contain a very large array of guest molecules (ranging from hydrophilic to hydrophobic)¹¹⁴⁻¹¹⁶ and an adjuvant that

facilitates and controls the release rates^{117,118} (Figure 3-1). The adjuvant is usually the surfactant used as template of the mesopores but is not eliminated after the synthesis of the material. There are very few reports in the literature that uses this methodology¹¹⁷⁻¹²¹.

One of the challenges to which the hybrid material can constitute a solution is the use of the mesopores as reservoirs that can be opened and closed as a response to an external stimulus, giving rise to the so-called “stimuli responsive drug delivery systems”. Drugs can be confined into the mesoporous cavities and then locally delivered when and where needed. There are several triggers that can activate the release of the guest molecules such as pH, temperature, magnetism, chemicals, light or ultrasound.

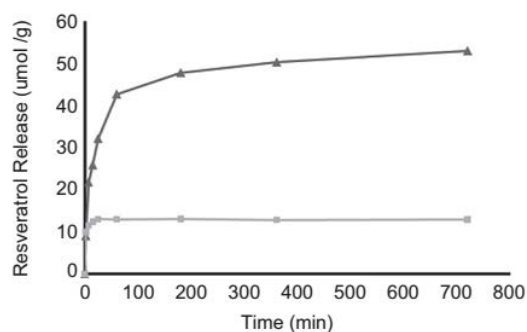


Figure 3-1: Release profiles of resveratrol-loaded (▲) from surfactant-loaded silica material, (■) mesoporous silica material¹¹⁸.

3.1.3 Active ingredient: Ketoprofen

The poor water solubility of many drugs is a limiting factor for their bioavailability which reduces their therapeutic efficiency. In order to face this obstacle, researchers have developed different techniques to enhance the drug dissolution by linking them to a hydrophilic molecule, or by enlarging the surface area which increases the dissolution rate and enhances the dissolution in the body¹²².

Ketoprofen, a potent non-steroidal anti-inflammatory drug (NSAID) possesses also analgesic and antipyretic properties¹²³ has a very low water solubility (0.0213 mg/ml). It is considered a model hydrophobic drug because of its simple metabolism and broad therapeutic window¹²⁴. The main administration route of ketoprofen is orally but it has been associated with systemic adverse events and in particular gastrointestinal disorders¹²³, so other routes has been developed such as topical, transdermal in order to avoid those events. Prescription ketoprofen is used to relieve tenderness, swelling, and stiffness caused by osteoarthritis (arthritis caused by a breakdown of the lining of the joints) and rheumatoid arthritis (arthritis caused by swelling of the lining of the joints). Ketoprofen capsules are also used to relieve pain, including menstrual pain (pain that occurs before or during a menstrual period). It works by stopping the body's production of prostaglandin a substance that causes pain, fever, and inflammation.

Ketoprofen belongs to the propionic acid class, its structure is shown in Figure 3-2. It is highly hydrophobic (water solubility equal to 0.014 %¹²⁵). It has a pKa between 4.2 and 4.4¹²⁶, a logP of 3.12 and a molecular weight of 254.9 g/mol.

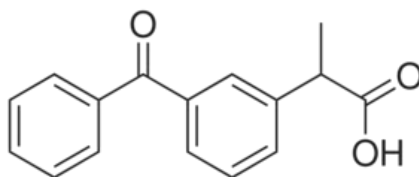


Figure 3-2: Molecular structure of ketoprofen.

Canal *et al.*¹²⁵ used macroporous polystyrene solid foams as a carrier for the ketoprofen and showed that this system have a delayed release with short lag-time. On the other hand, Smirnova *et al.*¹²² showed that the ketoprofen deposited on a hydrophilic silica aerogel matrix by adsorption from supercritical CO₂ is released rapidly (reaches 100% in less than 50 min). This reflects the importance of the carrier on the bioavailability of the active ingredient.

3.2 Porous silica materials as biocatalysts

The immobilization of molecules on porous silica materials is not limited to active ingredients, enzymes can also be immobilized in order to form a biocatalyst. The definition of a biocatalyst is the substance needed to initiate and/or accelerate a biochemical reaction. Enzymes are catalysts of biological origin that have an important catalytic power and a high degree of specificity. Most of the enzymes are proteins found in living organisms with complex structures. Enzymes offer a distinct advantage over other kinds of catalysts due to their specificity: chemo-, regio- and stereo-selectivity, the mild conditions for their reactions, and their eco-friendliness. Their catalytic activity depends on the integrity of their native protein conformation. If an enzyme is denatured or dissociated into subunits, its catalytic activity is lost. The separation of enzyme from solutions is very difficult which makes the recycling almost impossible. Free enzymes are labile and are not always sufficiently stable under operational condition and one time usage, as catalyst is costly. These disadvantages could be overcome by the use of immobilized enzymes¹²⁷. There exist many classes and families of enzymes that can be used to catalyze a large number of reactions. In this work we chose the lipase which is the enzyme needed for the catalysis of the transesterification reaction of triglycerides for the production of biodiesel.

3.2.1 Lipase

Lipases (triacylglycerol acylhydrolases, E.C. 3.1.1.3) are a group of water-soluble enzymes. They play a crucial role in metabolism and fat digestion. They are recognized as one of the

most important group of enzymes in biotechnology, with applications in food, detergent, pharmaceutical, leather, textile, cosmetic and paper industries¹²⁸. Lipases are a sub group of esterases and are also called serine hydrolases. One of the reactions they catalyze is the hydrolysis of triacylglycerol to glycerol and free fatty acids in aqueous media. In organic media they catalyze the reverse reaction, where esters are synthesized.¹²⁹

In this work we were interested in the lipase originating from the *Mucor miehei* (Mm-L) which is extracted from the *Aspergillus oryzae*. It is constituted of 269 amino acids and has a molar mass of 31 600 Da and an isoelectric point at 3.8. It has a spherical shape with a hydrodynamic radius of 4-5 nm. The morphology of the lipase is shown in the Figure 3-3.

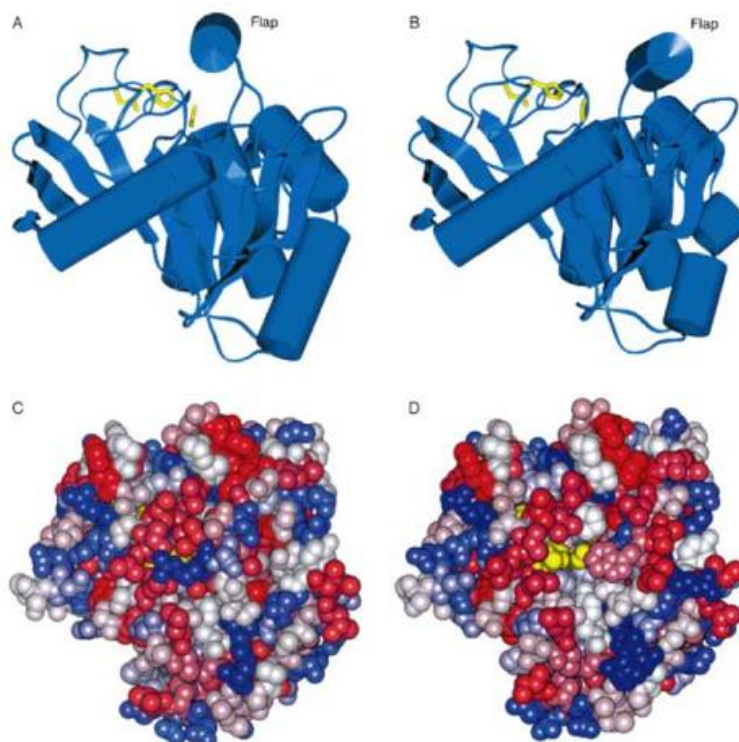


Figure 3-3 : The structure of the lipase, the A and C represent the closed structure while the B and D represent the open structure (A and B are the lateral vu, and C and D are the vu from above). The catalytic triad is represented in yellow and the structural elements characteristic of all the Lipases (β -sheets and α helices), only after the opening of the lid that the triad becomes accessible to the substrate (D).¹³⁰

The active site is protected by a helical shape formed by 15 amino acids, the enzyme is activated when this helicon is moved, and a space of 800 Å² is opened. This activation occurs only when the enzyme is present on the water/oil interface.

3.2.2 Catalytic mechanism of the lipase

The catalytic mechanism of the esterification reaction can be described by four consecutive steps as shown in Figure 3-4.

- The first step is the fixation of the substrate on the enzyme via the activation of the C=O group by the substrate/aspartic acid hydrogen bond, which is then attacked by the serine.
- The second step is the acylation where a covalent bond is created between a carbon atom from the substrate and an oxygen from the serine, causing a charge rearrangement with the neighboring amino acids in order to maintain electrical neutrality.
- The third step is the acyl-enzyme complex, where an alcohol group is liberated because the creation of C=O is more favorable than the creation of O-C-O.
- The fourth step is the nucleophilic attack, where the process continues with a nucleophilic attack, in fact, the C=O oxygen interacts with methanol, activated and coordinated by the one from the aspartic acid. Finally, the creation of the bond between oxygen of the methanol and the carboxyl group causes the release of the ester.

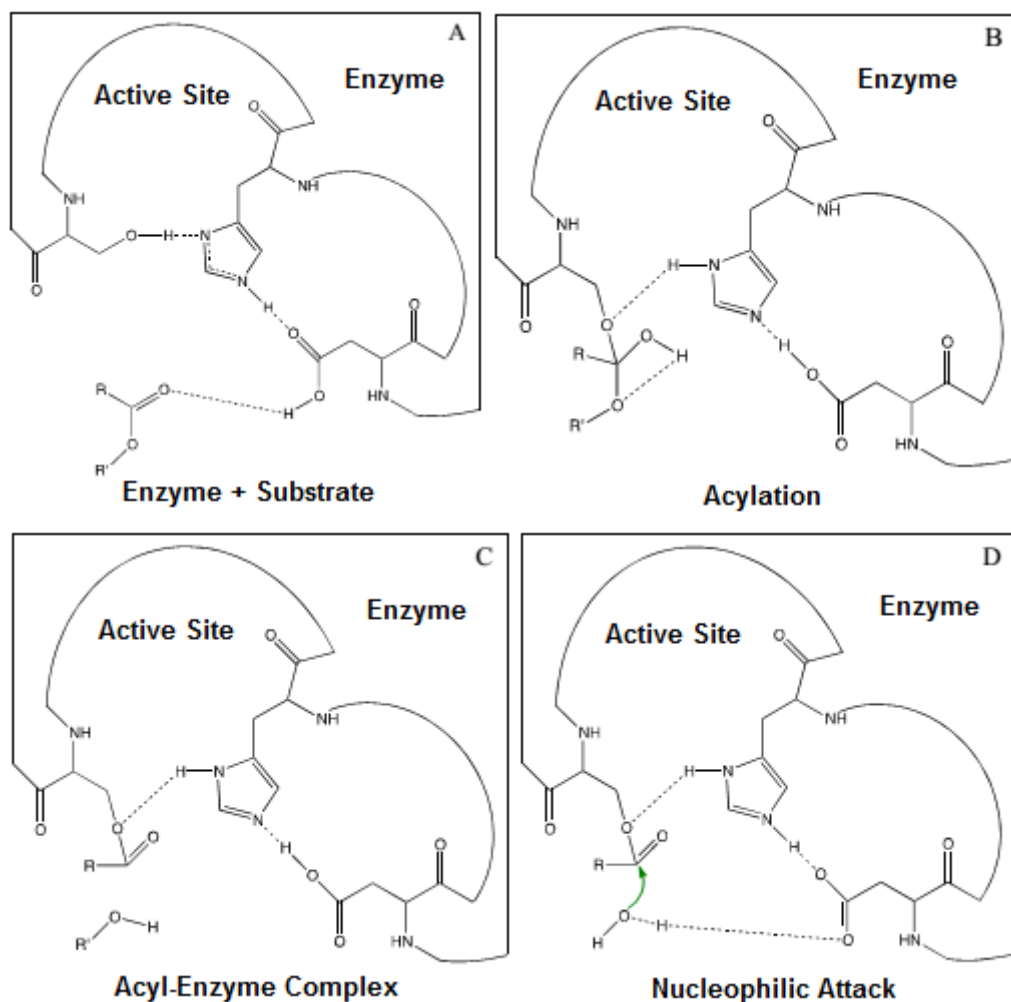


Figure 3-4: Catalytic mechanism of the Lipase¹³¹.

This reaction has also five variables that must be controlled in order for it to be complete: the type of alcohol used, the alcohol/oil molar ratio, the oil contents, and the time and temperature of the reaction.

3.2.3 Enzyme immobilization on porous silica materials

Knowing that the lipase synthesis is slow and very expensive and the final product is highly biodegradable. It is necessary to find a carrier that can encapsulate the enzyme without affecting its activity, and also protect it during the recycling process in order to increase its longevity. There exist three methods for the immobilization of an enzyme, the binding to a carrier¹³², entrapment (encapsulation)¹³³ and cross-linking¹³⁴ as shown in Figure 3-5.

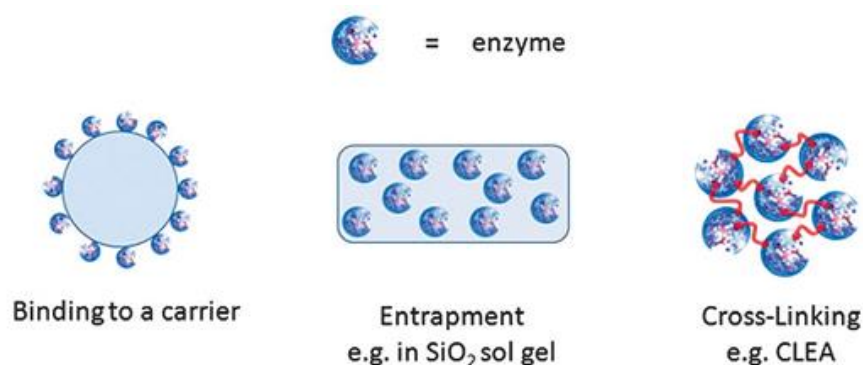


Figure 3-5: Different methods for immobilizing enzymes (CLEA = cross-linking enzyme aggregates)¹³⁴.

The enzyme can be immobilized by physisorption where only weak bonds such as hydrogen bonds or Van Der Waals bonds are used. This is the simplest technique since it requires the dipping of the carrier in an enzyme solution at the appropriate concentration and for the appropriate time. The success of such a process depends on the isoelectric point of both the silica and the enzyme. Also the enzyme can be immobilized by chemisorption, where a covalent bond is created between the substrate and the enzyme directly or via another molecule. More often than not, the surface of the silica is functionalized with a molecule that will later create a covalent bond with the enzyme, thus increasing its stability against leaching, and its longevity against recycling compared with the physisorbed enzymes.

The technique of encapsulation based on the irreversible physisorption of the enzyme according to Sheldon *et al.*¹³⁴ with the only difference that for the encapsulation, the substrate is synthesized in the presence of the enzyme. The limitations of this technique are the synthesis conditions and solvents that may influence badly the activity of the enzyme. Finally the immobilization can be realized by reticulation or cross-linking, the enzyme molecules are linked together by a second molecule via covalent bonding. There exist two type of cross linking the CLEA (cross linking enzyme aggregates) and the CLEC (cross linking enzyme crystals). The cross-linking is a good immobilization technique since the quantity of enzyme can be elevated and the production costs are low. The CLEA type consists of the addition of salts, or water miscible organic solvents or non-ionic polymers, to aqueous solutions of enzymes which leads to their precipitation as physical aggregates of enzyme molecules, held together by non-

covalent bonding without perturbation of their tertiary structure that is without denaturation. Subsequent cross-linking of these physical aggregates renders them permanently insoluble while maintaining their pre-organized superstructure, and, hence their catalytic activity. On the other hand, the CLEC type is prepared by allowing the enzyme to crystallize from aqueous buffer at the optimum pH and then adding a bifunctional reagent, usually glutaraldehyde, to cross link the crystals. The resulting product is robust, highly active particles of controllable particle size, varying from 1 to 100 nm. Those methods only require that the enzymes can be aggregated or precipitated without being denatured¹³⁴.

There is no best immobilization technique, each enzyme and each application requires a suitable immobilization method depending on the work parameters and environments¹³¹.

Table 1: Summary of the advantages and drawbacks of the different immobilization methods

Immobilization methods		Advantages	Drawbacks
Adsorption	Physisorption	<ul style="list-style-type: none"> • Simple to implement • Low risk of denaturation • Cheap 	<ul style="list-style-type: none"> • Reversible, risk of leaching • When adsorbed in multilayer, the catalytic activity is inhibited
	Chemisorption	<ul style="list-style-type: none"> • More efficient • Higher recyclability 	<ul style="list-style-type: none"> • Can be expensive • Can decrease the enzymatic activity
Encapsulation		<ul style="list-style-type: none"> • Lower risk of desorption 	<ul style="list-style-type: none"> • The high temperature of the synthesis and the use of solvents can deteriorate the enzyme
Cross-linking	CLEA	<ul style="list-style-type: none"> • High enzymatic activity • Enzymes are well protected • Cheap 	<ul style="list-style-type: none"> • Enzyme must form crystals or aggregates
	CLEC		

3.2.4 Effect of the properties of porous material

The size of the pores plays a major role in the quantity of adsorbed enzymes. In general, any pore size less than 5 nm is detrimental to the adsorbed quantity of any enzyme that is bigger than 40 000 Da. Any material that have pores that are the same size as the enzymes shows less leaching. Furthermore, the pore connectivity plays a major role. The pores that are unidimensional showed less activity than the interconnected pores in a three-dimensional structure. Basically the best morphology for pores is the silica hollow sphere with the largest pore diameter and pore volume¹³⁵. And finally the surface of the silica porous material plays also a role in the enzyme adsorption. It has been reported by Takahashi *et al.*¹³⁶ that the materials prepared using alkyltrimethylammonium salts as templates adsorbed much more

cationic molecules than the materials prepared using a nonionic surfactant. The surface can also be modified by the pH of the enzyme solution, and in other cases some authors have reported that the adsorption was better when the surface contained aluminum atoms ¹³⁷.

In a previous work in our group done by Jonathan Jacoby¹³¹, the Mml was immobilized onto porous silica materials for biodiesel production from colza oil. In his work, he used an SBA-15 materials and meso-macroporous material with a hexagonal arrangement of the mesopores were investigated. The enzyme immobilization was done by two methods, the first one is by physisorption and consists of submerging the material in an enzyme solution, and the second one is by chemisorption by linking the enzyme to the functionalized surface by urea covalent bonds. Furthermore, Mml was encapsulated in materials from double emulsions and SLNs. All the biocatalysts were evaluated by performing a transesterification reaction in the presence of methanol. The methanolysis parameters were optimized with an experimental design.

4 Aim of this thesis

This work falls under the general scope adopted by the group several years ago. This scope aims to elaborate and understand the function of structured porous materials in relation with organized molecular assemblies used for the preparation of silica, titania and zirconia. Emulsions were used in order to control the size of the macropores in the hierarchically porous materials, moreover they present advantages over other templates such as the capacity to dissolve large amounts of hydrophobic molecules. The application domains are essentially drug delivery and catalysis. In this work we chose the nano-emulsions because their interesting properties. So at first the goal was to determine the best conditions for the formation of nano-emulsions as well as an in depth characterization of their physicochemical properties. Then the effects of the addition of hydrogenated micelles on the stability of nano-emulsions has been studied in order to use those systems to template hierarchically porous silica materials. These materials were prepared in order to design on one hand a new drug delivery system and on the other hand a new biocatalyst.

The drug delivery system has been achieved by encapsulating a model drug molecule "Ketoprofen" and *in vitro* study of the release profile has been engaged. A comparative study has been done with hybrid materials.

The biocatalyst is prepared from hierarchically porous silica materials by encapsulating the lipase in order to better understand the effect of the pore size on the enzyme activity.

5 References

- (1) Griffin, W. Calculation of HLB Values of Non-Ionic Surfactans. *J. Soc. Cosmet. Chem.*

- 1954**, 249–256.
- (2) Griffin, W. Classification of Surface-Active Agents by“ HLB.” *J. Soc. Cosmet. Chem.* **1946**, 311–326.
 - (3) Solans, C.; Solé, I. Nano-Emulsions: Formation by Low-Energy Methods. *Curr. Opin. Colloid Interface Sci.* **2012**, 17 (5), 246–254.
 - (4) Mitchell, D. J.; Tiddy, G. J. T.; Waring, L.; Bostock, T.; McDonald, M. P. Phase Behaviour of Polyoxyethylene Surfactants with Water. Mesophase Structures and Partial Miscibility (Cloud Points). *J. Chem. Soc. Faraday Trans. 1* **1983**, 79 (4), 975.
 - (5) Bourrel, M.; Salager, J. .; Schechter, R. .; Wade, W. . A Correlation for Phase Behavior of Nonionic Surfactants. *J. Colloid Interface Sci.* **1980**, 75 (2), 451–461.
 - (6) Kunieda, H.; Ishikawa, N. Evaluation of the Hydrophile-Lipophile Balance (HLB) of Nonionic Surfactants. II. Commercial-Surfactant Systems. *J. Colloid Interface Sci.* **1985**, 107 (1), 122–128.
 - (7) Ravey, J. Solubilization Properties of Nonionic Surfactants I . Evolution of the Ternary Phase Diagrams with Temperature , Salinity , HLB , and ACN L Effect of the Purity Grade of the Surfactant. *J. Colloid Interface Sci.* **1983**, 91 (828), 20–33.
 - (8) Lindman, B.; Shinoda, K.; Olsson, U.; Anderson, D.; Karlström, G.; Wennerström, H. On the Demonstration of Bicontinuous Structures in Microemulsions. *Colloids and Surfaces* **1989**, 38 (1), 205–224.
 - (9) Appell, J.; Porte, G.; Khatory, a.; Kern, F.; Candau, S. J. Static and Dynamic Properties of a Network of Wormlike Surfactant Micelles (Cetylpyridinium Chlorate in Sodium Chlorate Brine). *J. Phys. II* **1992**, 2 (5), 1045–1052.
 - (10) Schwarz, B.; Mönch, G.; Ilgenfritz, G.; Strey, R. Dynamics of the “Sponge”(L3) Phase. *Langmuir* **2000**, No. 8, 8643–8652.
 - (11) Anderson, D.; Wennerstroem, H.; Olsson, U.; Wennerstrom, H. Isotropic Bicontinuous Solutions in Surfactant-Solvent Systems: The L3 Phase. *J. Phys. Chem.* **1989**, 93 (10), 4243–4253.
 - (12) Honours Projects for 2004
http://sydney.edu.au/science/chemistry/~warr_g/hons2003.html.
 - (13) Appell, J.; Bassereau, P.; Marignan, J.; Porte, G. Extreme Swelling of a Lyotropic Lamellar Liquid Crystal. *Colloid Polym. Sci.* **1989**, 267 (7), 600–606.
 - (14) Nallet, F.; Roux, D.; Prost, J. Hydrodynamics of Lyotropic Smectics : A Dynamic Light Scattering Study of Dilute Lamellar Phases. *J. Phys.* **1989**, 50 (20), 3147–3165.
 - (15) Nallet, F.; Roux, D.; Prost, J. Dynamic Light Scattering Study of Dilute Lamellar Phases. *Phys. Rev. Lett.* **1989**, 62 (3), 276–279.
 - (16) Strey, R.; Schomacker, R.; Roux, D.; Nallet, F.; Olsson, U. Dilute Lamellar and L3 Phases in the Binary water/C12E5 System. *J. Chem. Soc. Faraday Trans.* **1990**, 86 (12), 2253.
 - (17) Roux, D.; Knobler, C. M. Dynamics of Phase Separation between a Lyotropic Dilute

- Lamellar Phase and an Isotropic Phase. *Phys. Rev. Lett.* **1988**, 60 (4), 373–376.
- (18) Du, N. Investigation of Hydrogenated and Fluorinated Surfactant Based-Systems for the Design of Porous Silica Materials, Thèse de l'Université de Lorraine, 2010.
- (19) Bleta, R. Systèmes Fluorés Pour La Conception de Matériaux Poreux . Matrices Pour La Physisorption de Biomolécules, Thèse de l'Université de Lorraine, 2007.
- (20) Tiddy, G. J. T. Surfactant-Water Liquid Crystal Phases. *Phys. Rep.* **1980**, 57 (1), 1–46.
- (21) Lissant, K. J. The Geometry of High-Internal-Phase-Ratio Emulsions. *J. Colloid Interface Sci.* **1966**, 22, 462–468.
- (22) Lissant, K. J.; Mayhan, K. G. A Study of Medium and High Internal Phase Ratio Water/polymer Emulsions. *J. Colloid Interface Sci.* **1973**, 42 (1), 201–208.
- (23) Taylor, P. Ostwald Ripening in Emulsions. *Colloids Surfaces A Physicochem. Eng. Asp.* **1995**, 99 (2-3), 175–185.
- (24) Taylor, P. Ostwald Ripening in Emulsions. *Adv. Colloid Interface Sci.* **1998**, 75 (2), 107–163.
- (25) Kabalnov, a. S.; Makarov, K. N.; Pertzov, a. V.; Shchukin, E. D. Ostwald Ripening in Hydrocarbon Emulsions : Experimental Verification of Equation for Absolute Rates. *J. Colloid Interface Sci.* **1990**, 138 (1), 98–104.
- (26) Kabalnov, A. S.; Shchukin, E. D. Ostwald Ripening Theory: Applications to Fluorocarbon Emulsion Stability. *Adv. Colloid Interface Sci.* **1992**, 38, 69–97.
- (27) Zhao, Q.; Zhao, M.; Yang, B.; Cui, C. Effect of Xanthan Gum on the Physical Properties and Textural Characteristics of Whipped Cream. *Food Chem.* **2009**, 116 (3), 624–628.
- (28) Simovic, S.; Heard, P.; Hui, H.; Song, Y.; Peddie, F.; Davey, A. K.; Lewis, A.; Rades, T.; Prestidge, C. a. Dry Hybrid Lipid-Silica Microcapsules Engineered from Submicron Lipid Droplets and Nanoparticles as a Novel Delivery System for Poorly Soluble Drugs. *Mol. Pharm.* **2009**, 6 (3), 861–872.
- (29) Blin, J.-L.; Jacoby, J.; Kim, S.; Stébé, M.-J.; Canilho, N.; Pasc, A. A Meso-Macro Compartmentalized Bioreactor Obtained through Silicalization of “green” Double Emulsions: W/O/W and W/SLNs/W. *Chem. Commun.* **2014**, 50 (80), 11871–11874.
- (30) Solans, C.; Izquierdo, P.; Nolla, J.; Azemar, N.; Garcia-Celma, M. J. Nano-Emulsions. *Curr. Opin. Colloid Interface Sci.* **2005**, 10 (3-4), 102–110.
- (31) Forgiarini, a.; Esquena, J.; González, C.; Solans, C. Formation of Nano-Emulsions by Low-Energy Emulsification Methods at Constant Temperature. *Langmuir* **2001**, 17 (7), 2076–2083.
- (32) Meleson, K.; Graves, S.; Mason, T. G. Formation of Concentrated Nanoemulsions by Extreme Shear. *Soft Mater.* **2004**, 2 (2-3), 109–123.
- (33) Hidalgo-Alvarez, R. *Structure and Functional Properties of Colloidal Systems*, Surfactant.; Schick, M., Hubbard, A., Eds.; CRC press: New York, 2010.
- (34) Leong, T. S. H.; Wooster, T. J.; Kentish, S. E.; Ashokkumar, M. Minimising Oil Droplet

- Size Using Ultrasonic Emulsification. *Ultrason. Sonochem.* **2009**, *16* (6), 721–727.
- (35) Wooster, T. J.; Golding, M.; Sanguansri, P. Impact of Oil Type on Nanoemulsion Formation and Ostwald Ripening Stability. *Langmuir* **2008**, *24* (22), 12758–12765.
- (36) Abismaïl, B.; Canselier, J. P.; Wilhelm, a. M.; Delmas, H.; Gourdon, C. Emulsification by Ultrasound: Drop Size Distribution and Stability. *Ultrason. Sonochem.* **1999**, *6* (1-2), 75–83.
- (37) Fryd, M. M.; Mason, T. G. Advanced Nanoemulsions. *Annu. Rev. Phys. Chem.* **2012**, *63* (1), 493–518.
- (38) Anton, N.; Vandamme, T. F. Nano-Emulsions and Micro-Emulsions: Clarifications of the Critical Differences. *Pharm. Res.* **2011**, *28* (5), 978–985.
- (39) Vitale, S. a.; Katz, J. L. Liquid Droplet Dispersions Formed by Homogeneous Liquid-Liquid nucleation: “The Ouzo Effect.” *Langmuir* **2003**, *19* (10), 4105–4110.
- (40) Nazarzadeh, E.; Anthonypillai, T.; Sajjadi, S. On the Growth Mechanisms of Nanoemulsions. *J. Colloid Interface Sci.* **2013**, *397*, 154–162.
- (41) Sajjadi, S. Nanoemulsion Formation by Phase Inversion Emulsification: On the Nature of Inversion. *Langmuir* **2006**, *22* (13), 5597–5603.
- (42) Sadurní, N.; Solans, C.; Azemar, N.; García-Celma, M. J. Studies on the Formation of O/W Nano-Emulsions, by Low-Energy Emulsification Methods, Suitable for Pharmaceutical Applications. *Eur. J. Pharm. Sci.* **2005**, *26* (5), 438–445.
- (43) Fernandez, P.; André, V.; Rieger, J.; Kühnle, A. Nano-Emulsion Formation by Emulsion Phase Inversion. *Colloids Surfaces A Physicochem. Eng. Asp.* **2004**, *251* (1-3), 53–58.
- (44) Pey, C. M.; Maestro, a.; Solé, I.; González, C.; Solans, C.; Gutiérrez, J. M. Optimization of Nano-Emulsions Prepared by Low-Energy Emulsification Methods at Constant Temperature Using a Factorial Design Study. *Colloids Surfaces A Physicochem. Eng. Asp.* **2006**, *288* (1-3), 144–150.
- (45) Usón, N.; Garcia, M. J.; Solans, C. Formation of Water-in-Oil (W/O) Nano-Emulsions in a Water/mixed Non-ionic Surfactant/oil Systems Prepared by a Low-Energy Emulsification Method. *Colloids Surfaces A Physicochem. Eng. Asp.* **2004**, *250* (1-3 SPEC. ISS.), 415–421.
- (46) Solè, I.; Maestro, A.; González, C.; Solans, C.; Gutiérrez, J. M. Optimization of Nano-Emulsion Preparation by Low-Energy Methods in an Ionic Surfactant System. *Langmuir* **2006**, *22* (20), 8326–8332.
- (47) Shinoda, K.; Saito, H. The Effect of Temperature on the Phase Equilibria and the Types of Dispersions of the Ternary System Composed of Water, Cyclohexane, and Nonionic Surfactant. *J. Colloid Interface Sci.* **1968**, *26* (1), 70–74.
- (48) Taguchi, A.; Schüth, F. Ordered Mesoporous Materials in Catalysis. *Microporous Mesoporous Mater.* **2005**, *77* (1), 1–45.
- (49) Manzano, M.; Vallet-Regí, M. New Developments in Ordered Mesoporous Materials for Drug Delivery. *J. Mater. Chem.* **2010**, *20* (27), 5593.

- (50) Arruebo, M. Drug Delivery from Structured Porous Inorganic Materials. *Wiley Interdiscip. Rev. Nanomedicine Nanobiotechnology* **2012**, 4 (1), 16–30.
- (51) Iler, R. K. *The Chemistry of Silica: Solubility, Polymerization, Colloid and Surface Properties, and Biochemistry*; John Wiley and Sons, Inc., 1979.
- (52) Sing, K. S. W.; Everett, D. H.; Haul, R. a. W.; Moscou, L.; Pierotti, R. a.; Rouquérol, J.; Siemieniewska, T. REPORTING PHYSISORPTION DATA FOR GAS / SOLID SYSTEMS with Special Reference to the Determination of Surface Area and Porosity. *Pure Appl. Chem.* **1985**, 57 (4), 603–619.
- (53) Michaux, F. Contribution Des Tensioactifs Fluorés À La Synthèse de Matériaux Mésoporeux., Thèse de l'Université de Lorraine, 2009.
- (54) Kresge, C. T.; Leonowicz, M. E.; Roth, W. J.; Vartuli, J. C.; Beck, J. S. Ordered Mesoporous Molecular Sieves Synthesized by a Liquid-Crystal Template Mechanism. *Nature* **1992**, 359 (6397), 710–712.
- (55) Meynen, V.; Cool, P.; Vansant, E. F. Verified Syntheses of Mesoporous Materials. *Microporous Mesoporous Mater.* **2009**, 125 (3), 170–223.
- (56) Tolbert, S. H. Mesoporous Silica: Holey Quasicrystals. *Nat. Mater.* **2012**, 11 (9), 749–751.
- (57) Blin, J. L.; Impéror-Clerc, M. Mechanism of Self-Assembly in the Synthesis of Silica Mesoporous Materials: In Situ Studies by X-Ray and Neutron Scattering. *Chem. Soc. Rev.* **2013**, 42 (9), 4071–4082.
- (58) Vartuli, J. C.; Kresge, C. T.; Leonovicz, M. E.; Chu, a S.; McCullen, S. B.; Johnson, I. D.; Sheppard, E. W. Synthesis of Mesoporous Materials: Liquid-Crystal Templating versus Intercalation of Layered Silicates. *Chem. Mater.* **1994**, 6 (11), 2070–2077.
- (59) Imhof, A.; Pine, D. J. Ordered Macroporous Materials by Emulsion Templating. *Nature* **1997**, 389 (October), 948–951.
- (60) Sen, T.; Tiddy, G. J. T.; Casci, J. L.; Anderson, M. W. Synthesis and Characterization of Hierarchically Ordered Porous Silica Materials. *Chem. Mater.* **2004**, 16 (11), 2044–2054.
- (61) Wakeman, R. J.; Bhungara, Z. G.; Akay, G. Ion Exchange Modules Formed from Polyhipe Foam Precursors. *Chem. Eng. J.* **1998**, 70 (2), 133–141.
- (62) Cundy, C. S.; Cox, P. a. The Hydrothermal Synthesis of Zeolites: History and Development from the Earliest Days to the Present Time The Hydrothermal Synthesis of Zeolites: History and Development from the Earliest Days to the Present Time. *Chem. Rev.* **2003**, 103 (February), 663–702.
- (63) Hentze, H. P.; Antonietti, M. Template Synthesis of Porous Organic Polymers. *Curr. Opin. Solid State Mater. Sci.* **2001**, 5 (4), 343–353.
- (64) Schüth, F. Endo- and Exotemplating to Create High-Surface-Area Inorganic Materials. *Angew. Chemie - Int. Ed.* **2003**, 42 (31), 3604–3622.
- (65) Keshavaraja, A.; Ramaswamy, V.; Soni, H. S.; Ramaswamy, A. V; Ratnasamy, P. Synthesis, Characterization, and Catalytic Properties of Micro-Mesoporous,

- Amorphous Titanosilicate Catalysts. *J. Catal.* **1995**, *157*, 501–511.
- (66) Fan, J.; Yu, C.; Lei, J.; Tu, B.; Zhang, Q.; Li, T.; Zhou, W. Low Temperature Strategy to Synthesize Highly Ordered Mesoporous Silicas with Very Large Pores. *J. Am. Chem. Soc.* **2005**, *127* (31), S1–S7.
- (67) Yuan, Z.-Y.; Su, B.-L. Insights into Hierarchically Meso–macroporous Structured Materials. *J. Mater. Chem.* **2006**, *16* (7), 663.
- (68) Yang, P. D.; Zhao, D. Y.; Margolese, D. I.; Chmelka, B. F.; Stucky, G. D. Generalized Syntheses of Large-Pore Mesoporous Metal Oxides with Semicrystalline Frameworks. *Nature* **1998**, *396* (6707), 152–155.
- (69) Petkovich, N. D.; Stein, A. Controlling Macro- and Mesostructures with Hierarchical Porosity through Combined Hard and Soft Templating. *Chem. Soc. Rev.* **2013**.
- (70) Su, B. L.; Vantomme, A.; Surahy, L.; Pirard, R.; Pirard, J. P. Hierarchical Multimodal Mesoporous Carbon Materials with Parallel Macrochannels. *Chem. Mater.* **2007**, *19* (13), 3325–3333.
- (71) Wang, M.; Sun, Z.; Yue, Q.; Yang, J.; Wang, X.; Deng, Y.; Yu, C.; Zhao, D. An Interface-Directed Coassembly Approach to Synthesize Uniform Large-Pore Mesoporous Silica Spheres. *J. Am. Chem. Soc.* **2014**, *136* (5), 1884–1892.
- (72) Stein, A. Sphere Templating Methods for Periodic Porous Solids. *Microporous Mesoporous Mater.* **2001**, *44-45*, 227–239.
- (73) Zhang, H.; Hardy, G. C.; Rosseinsky, M. J.; Cooper, A. I. Uniform Emulsion-Templated Silica Beads with High Pore Volume and Hierarchical Porosity. *Adv. Mater.* **2003**, *15* (1), 78–81.
- (74) Carn, F.; Colin, A.; Achard, M.-F.; Deleuze, H.; Sellier, E.; Birot, M.; Backov, R. Inorganic Monoliths Hierarchically Textured via Concentrated Direct Emulsion and Micellar templates Electronic Supplementary Information (ESI) Available: XRD Profiles, Nitrogen Physisorption Data and Pore Size Distribution Calculated from Density Functiona. *J. Mater. Chem.* **2004**, *14* (9), 1370.
- (75) Blin, J. L.; Bleta, R.; Ghanbaja, J.; Stébé, M. J. Fluorinated Emulsions: Templates for the Direct Preparation of Macroporous-Mesoporous Silica with a Highly Ordered Array of Large Mesopores. *Microporous Mesoporous Mater.* **2006**, *94* (1-3), 74–80.
- (76) Mason, T. G.; Wilking, J. N.; Meleson, K.; Chang, C. B.; Graves, S. M. Nanoemulsions: Formation, Structure, and Physical Properties. *Journal of Physics: Condensed Matter*. 2006, pp R635–R666.
- (77) Koroleva, M. Y.; Yurtov, E. V. Nanoemulsions: The Properties, Methods of Preparation and Promising Applications. *Russ. Chem. Rev.* **2012**, *81* (1), 21–43.
- (78) Hessien, M.; Singh, N.; Kim, C.; Prouzet, E. Stability and Tunability of O/W Nanoemulsions Prepared by Phase Inversion Composition. *Langmuir* **2011**, *27* (6), 2299–2307.
- (79) Hessien, M.; Léone, P.; Suchaud, M.; LeBeau, B.; Nouali, H.; Guari, Y.; Prouzet, E. Nanocrystalline Iron Oxide Synthesised within Hierarchical Porous Silica Prepared by Nanoemulsion Templating. *Chem. Commun.* **2012**, *48* (80), 10022.

- (80) Wu, S. H.; Hung, Y.; Mou, C. Y. Compartmentalized Hollow Silica Nanospheres Templated from Nanoemulsions. *Chem. Mater.* **2013**, *25* (3), 352–364.
- (81) Nakanishi, K. Pore Structure Control of Silica Gels Based on Phase Separation. *J. Porous Mater.* **1997**, *4* (2), 67–112.
- (82) Sato, Y.; Nakanishi, K.; Hirao, K.; Jinnai, H.; Shibayama, M.; Melnichenko, Y. B.; Wignall, G. D. Formation of Ordered Macropores and Templated Nanopores in Silica Sol-Gel System Incorporated with EO-PO-EO Triblock Copolymer. *Colloids Surfaces A Physicochem. Eng. Asp.* **2001**, *187-188* (2001), 117–122.
- (83) Nakanishi, K.; Kobayashi, Y.; Amatani, T.; Hirao, K.; Kodaira, T. Spontaneous Formation of Hierarchical Macro-Mesoporous Ethane-Silica Monolith. *Chem. Mater.* **2004**, *16* (19), 3652–3658.
- (84) Nakanishi, K.; Sato, Y.; Ruyat, Y.; Hirao, K. Supramolecular Templating of Mesopores in Phase-Separating Silica Sol-Gels Incorporated with Cationic Surfactant. *J. Sol-Gel Sci. Technol.* **2003**, *26* (1-3), 567–570.
- (85) Nakanishi, K.; Kobayashi, Y.; Amatani, T.; Hirao, K.; Kodaira, T. Spontaneous Formation of Hierarchical Macro-Mesoporous Ethane- Silica Monolith. *Chem. Mater.* **2004**, *16* (19), 3652–3658.
- (86) Sel, O.; Kuang, D.; Thommes, M.; Smarsly, B. Principles of Hierarchical Meso- and Macropore Architectures by Liquid Crystalline and Polymer Colloid Templating. *Langmuir* **2006**, *22* (5), 2311–2322.
- (87) Blin, J.-L.; Léonard, A.; Yuan, Z.-Y.; Gigot, L.; Vantomme, A.; Cheetham, A. K.; Su, B.-L. Hierarchically Mesoporous/Macroporous Oxide Templated from PolyethyleneOxide Surfactant Assemblies. *Angew. Chemie* **2003**, *115* (25), 2978–2981.
- (88) Holland, B.; Blanford, C.; Do, T.; Stein, A. Synthesis of Highly Ordered, Three-Dimensional, Macroporous Structures of Amorphous or Crystalline Inorganic Oxides, Phosphates, and Hybrid Composites. *Chem. Mater.* **1999**, No. 17, 795–805.
- (89) Blanford, C. F.; Yan, H.; Schrodin, R. C.; Al-Daous, M.; Stein, a. Gems of Chemistry and Physics: Macroporous Metal Oxides with 3D Order. *Adv. Mater.* **2001**, *13* (6), 401–407.
- (90) Mori, H.; Uota, M.; Fujikawa, D.; Yoshimura, T.; Kuwahara, T.; Sakai, G.; Kijima, T. Synthesis of Micro-Mesoporous Bimodal Silica Nanoparticles Using Lyotropic Mixed Surfactant Liquid-Crystal Templates. *Microporous Mesoporous Mater.* **2006**, *91* (1-3), 172–180.
- (91) Bagshaw, S. a. Bimodal Pore Systems in Non-Ionically Templated [Si]-MSU-X Mesoporous Silica through Biomimetic Synthesis in Weakly Ionic Solutions. *Chem. Commun.* **1999**, No. 18, 1785–1786.
- (92) Sun, J. H.; Shan, Z.; Maschmeyer, T.; Coppens, M. O. Synthesis of Bimodal Nanostructured Silicas with Independently Controlled Small and Large Mesopore Sizes. *Langmuir* **2003**, *19* (20), 8395–8402.
- (93) Groenewolt, M.; Antonietti, M.; Polarz, S. Mixed Micellar Phases of Nonmiscible Surfactants: Mesoporous Silica with Bimodal Pore Size Distribution via the Nanocasting Process. *Langmuir* **2004**, *20* (18), 7811–7819.

- (94) Xing, R.; Lehmler, H. J.; Knutson, B. L.; Rankin, S. E. Synthesis and Tuning of Bimodal Mesoporous Silica by Combined Hydrocarbon/fluorocarbon Surfactant Templating. *Langmuir* **2009**, *25* (11), 6486–6492.
- (95) Wang, X.; Dou, T.; Xiao, Y. Synthesis of Double-Mesopore Silica Using Aqueous Ammonia as Catalyst. *Chem. Commun.* **1998**, No. 9, 1035–1036.
- (96) Michaux, F.; Blin, J. L.; Stébé, M. J. Design of Ordered Bimodal Mesoporous Silica Materials by Using a Mixed Fluorinated–Hydrogenated Surfactant-Based System. *Langmuir* **2007**, *23* (4), 2138–2144.
- (97) Blin, J. L.; Henzel, N.; Stébé, M. J. Mixed Fluorinated–Hydrogenated Surfactant-Based System: Preparation of Ordered Mesoporous Materials. *J. Colloid Interface Sci.* **2006**, *302* (2), 643–650.
- (98) Chen, L.; Xu, J.; Zhang, W. H.; Holmes, J. D.; Morris, M. a. Syntheses of Complex Mesoporous Silicas Using Mixtures of Nonionic Block Copolymer Surfactants: Understanding Formation of Different Structures Using Solubility Parameters. *J. Colloid Interface Sci.* **2011**, *353* (1), 169–180.
- (99) Chen, L.; Zhang, W. H.; Xu, J.; Tanner, D. a.; Morris, M. a. Mesopore Constrictions Derived from the Substitutionally Co-Packed SBA-15. *Microporous Mesoporous Mater.* **2010**, *129* (1-2), 179–188.
- (100) Almgren, M.; Garamus, V. M.; Nordstierna, L.; Luc-Blin, J.; Stébé, M. J. Nonideal Mixed Micelles of Fluorinated and Hydrogenous Surfactants in Aqueous Solution. NMR and SANS Studies of Anionic and Nonionic Systems. *Langmuir* **2010**, *26* (8), 5355–5363.
- (101) Almgren, M.; Wang, K.; Asakawa, T. Fluorescence Quenching Studies of Micellization and Solubilization in Fluorocarbon–Hydrocarbon Surfactant Mixtures. *Langmuir* **1997**, *7463* (2), 4535–4544.
- (102) Ravey, J. C.; Gherbi, A.; Stébé, M. J. Fluorinated and Hydrogenated Nonionics in Aqueous Mixed Systems. *Colloid Polym. Sci.* **2011**, *79*, 173–178.
- (103) Amato, M. E.; Caponetti, E.; Martino, D. C.; Pedone, L.; Fisica, C.; Uni, V.; Scienze, V.; Palermo, I.; Doria, V. a; Catania, I.-. ¹⁹F and NMR Investigation on Mixed Hydrocarbon - Fluorocarbon Micelles. *J. Phys. Chem. B* **2003**, *107*, 10048–10056.
- (104) Zhou, Y.; Antonietti, M. A Novel Tailored Bimodal Porous Silica with Well-Defined Inverse Opal Microstructure and Super-Microporous Lamellar Nanostructure. *Chem. Commun. (Camb)*. **2003**, No. 20, 2564–2565.
- (105) May, A.; Stébé, M. J.; Gutiérrez, J. M.; Blin, J. L. Coexistence of Two Kinds of Fluorinated Hydrogenated Micelles as Building Blocks for the Design of Bimodal Mesoporous Silica with Two Ordered Mesopore Networks. *Langmuir* **2011**, *27* (23), 14000–14004.
- (106) Korteso, P.; Ahola, M.; Karlsson, S.; Kangasniemi, I.; Yli-Urpo, a; Kiesvaara, J. Silica Xerogel as an Implantable Carrier for Controlled Drug Delivery--Evaluation of Drug Distribution and Tissue Effects after Implantation. *Biomaterials* **2000**, *21* (2), 193–198.
- (107) Radin, S.; El-Bassyouni, G.; Vresilovic, E. J.; Schepers, E.; Ducheyne, P. In Vivo Tissue Response to Resorbable Silica Xerogels as Controlled-Release Materials. *Biomaterials* **2005**, *26* (9), 1043–1052.

- (108) Lai, C. Y.; Trewyn, B. G.; Jeftinija, D. M.; Jeftinija, K.; Xu, S.; Jeftinija, S.; Lin, V. S. Y. A Mesoporous Silica Nanosphere-Based Carrier System with Chemically Removable CdS Nanoparticle Caps for Stimuli-Responsive Controlled Release of Neurotransmitters and Drug Molecules. *J. Am. Chem. Soc.* **2003**, *125* (15), 4451–4459.
- (109) Horcajada, P.; Rámila, A.; Pérez-Pariente, J.; Vallet-Regí, M. Influence of Pore Size of MCM-41 Matrices on Drug Delivery Rate. *Microporous Mesoporous Mater.* **2004**, *68* (1-3), 105–109.
- (110) Ying, J. Y.; Mehnert, C. P.; Wong, M. S. Synthesis and Applications of Supramolecular-Templated Mesoporous Materials. *Angew. Chemie Int. Ed.* **1999**, *38* (1-2), 56–77.
- (111) Santamaría, E.; Maestro, a.; Porras, M.; Gutiérrez, J. M.; González, C. Controlled Release of Ibuprofen by Meso-Macroporous Silica. *J. Solid State Chem.* **2014**, *210* (1), 242–250.
- (112) Vallet-Regí, M.; Balas, F.; Colilla, M.; Manzano, M. Drug Confinement and Delivery in Ceramic Implants. *Drug Metab. Lett.* **2007**, *1* (1), 37–40.
- (113) Azaïs, T.; Tourné-Péteilh, C.; Aussenac, F.; Baccile, N.; Coelho, C.; Devoisselle, J.-M.; Babonneau, F. Solid-State NMR Study of Ibuprofen Confined in MCM-41 Material. *Chem. Mater.* **2006**, *18* (26), 6382–6390.
- (114) Vallet-Regí, M.; Colilla, M.; González, B. Medical Applications of Organic–inorganic Hybrid Materials within the Field of Silica-Based Bioceramics. *Chem. Soc. Rev.* **2011**, *40* (2), 596–607.
- (115) Vasiliev, P. O. Functionalization and Processing of Porous Powders into Hierarchically Porous Monoliths., Thesis of the Stockholm University, 2009.
- (116) Moritz, M.; Łaniecki, M. SBA-15 Mesoporous Material Modified with APTES as the Carrier for 2-(3-Benzoylphenyl)propionic Acid. *Appl. Surf. Sci.* **2012**, *258* (19), 7523–7529.
- (117) Kerkhofs, S.; Saïdi, F.; Vandervoort, N.; Van den Mooter, G.; Martineau, C.; Taulelle, F.; Martens, J. a. Silica Capsules Enclosing P123 Triblock Copolymer Micelles for Flurbiprofen Storage and Release. *J. Mater. Chem. B* **2015**.
- (118) Tsai, C. H.; Vivero-Escoto, J. L.; Slowing, I. I.; Fang, I. J.; Trewyn, B. G.; Lin, V. S. Y. Surfactant-Assisted Controlled Release of Hydrophobic Drugs Using Anionic Surfactant Templated Mesoporous Silica Nanoparticles. *Biomaterials* **2011**, *32* (26), 6234–6244.
- (119) Clifford, N. W.; Iyer, K. S.; Raston, C. L. Encapsulation and Controlled Release of Nutraceuticals Using Mesoporous Silica Capsules. *J. Mater. Chem.* **2008**, *18* (2), 162.
- (120) Tyner, K. M.; Schiffman, S. R.; Giannelis, E. P. Nanobiohybrids as Delivery Vehicles for Camptothecin. *J. Control. Release* **2004**, *95* (3), 501–514.
- (121) He, Q.; Shi, J.; Chen, F.; Zhu, M.; Zhang, L. An Anticancer Drug Delivery System Based on Surfactant-Templated Mesoporous Silica Nanoparticles. *Biomaterials* **2010**, *31* (12), 3335–3346.
- (122) Smirnova, I.; Suttiruengwong, S.; Seiler, M.; Arlt, W. Dissolution Rate Enhancement by Adsorption of Poorly Soluble Drugs on Hydrophilic Silica Aerogels. *Pharm. Dev. Technol.* **2005**, *9* (4), 443–452.

- (123) Coaccioli, S. Ketoprofen 2.5% Gel: A Clinical Overview. *Eur. Rev. Med. Pharmacol. Sci.* **2011**, *15* (8), 943–949.
- (124) Kantor, T. G. Ketoprofen: A Review of Its Pharmacologic and Clinical Properties. *Pharmacother. J. Hum. Pharmacol. Drug Ther.* **1986**, *6* (3), 93–102.
- (125) Canal, C.; Aparicio, R. M.; Vilchez, a.; Esquena, J.; García-Celma, M. J. Drug Delivery Properties of Macroporous Polystyrene Solid Foams. *J. Pharm. Pharm. Sci.* **2012**, *15* (1), 197–207.
- (126) Bui, T. X.; Choi, H. Adsorptive Removal of Selected Pharmaceuticals by Mesoporous Silica SBA-15. *J. Hazard. Mater.* **2009**, *168* (2-3), 602–608.
- (127) George, R. Catalysis by Enzymes Immobilized on Tuned Mesoporous Silica, Thesis of Cochin University of Science and Technology, 2013.
- (128) Sharma, R.; Chisti, Y.; Banerjee, U. C. Production, Purification, Characterization, and Applications of Lipases. *Biotechnol. Adv.* **2001**, *19* (8), 627–662.
- (129) Gustafsson, H. Enzyme Immobilization in Mesoporous Silica, Thesis of Chalmers University of Technology, 2012.
- (130) Sarda, L.; Desnuelle, P. Action de La Lipase Pancréatique Sur Les Esters En Émulsion. *Biochim. Biophys. Acta* **1958**, *30* (3), 513–521.
- (131) Jacoby, J. Lipase Mucor Miehei Immobilisée Dans Des Matériaux Poreux Silicatés : Bioréacteurs Pour La Synthèse D'esters Méthyliques À Partir D'huiles Végétales, Thèse de l'Université de Lorraine, 2013.
- (132) Hoffmann, F.; Cornelius, M.; Morell, J.; Fröba, M. Silica-Based Mesoporous Organic-Inorganic Hybrid Materials. *Angew. Chemie - Int. Ed.* **2006**, *45* (20), 3216–3251.
- (133) Carlsson, N.; Gustafsson, H.; Thörn, C.; Olsson, L.; Holmberg, K.; Åkerman, B. Enzymes Immobilized in Mesoporous Silica: A Physical–chemical Perspective. *Adv. Colloid Interface Sci.* **2014**, *205*, 339–360.
- (134) Sheldon, R. a; van Pelt, S. Enzyme Immobilisation in Biocatalysis: Why, What and How. *Chem. Soc. Rev.* **2013**, *42* (15), 6223–6235.
- (135) Liu, J.; Li, C.; Yang, Q.; Yang, J.; Li, C. Morphological and Structural Evolution of Mesoporous Silicas in a Mild Buffer Solution and Lysozyme Adsorption. *Langmuir* **2007**, *23* (13), 7255–7262.
- (136) Takahashi, H.; Li, B.; Sasaki, T.; Miyazaki, C.; Kajino, T.; Inagaki, S. Catalytic Activity in Organic Solvents and Stability of Immobilized Enzymes Depend on the Pore Size and Surface Characteristics of Mesoporous Silica. *Chem. Mater.* **2000**, *12* (11), 3301–3305.
- (137) Vinu, a.; Murugesan, V.; Tangermann, O.; Hartmann, M. Adsorption of Cytochrome c on Mesoporous Molecular Sieves: Influence of pH, Pore Diameter, and Aluminum Incorporation. *Chem. Mater.* **2004**, *16* (16), 3056–3065.

Materials and Methods

1 Materials

1.1 Surfactants

In this work nonionic surfactants were used exclusively. The hydrophilic moiety consists of ethylene oxide groups. On the other hand for the hydrophobic part, we used hydrogenated, fluorinated, and siloxinated chains. Table 1-1 contains the list of the surfactants used as well as their physicochemical properties.

Table 1-1: Physico-chemical properties of the used surfactants

Label with lot number	Chemical formula	ρ (g.ml ⁻¹)	M (g.mol ⁻¹)	V_{mol} (cm ³ .mol ⁻¹)	HLB
[Remcopal 4]	C ₁₂ H ₂₄ (OC ₂ H ₄) ₄ OH	0.95	362	381	9.7
Pluronic P123	HO-(C ₂ H ₄ O) ₂₀ -(C ₃ H ₆ O) ₇₀ - (C ₂ H ₄ O) ₂₀ -OH	1.04	5800	5577	7-9
R ^F ₈ (EO) ₉ [Lot 125 – LX]	C ₈ F ₁₇ C ₂ H ₄ (OC ₂ H ₄) ₉ OH	1.39	870	626	9.6

The Remcopal 4 was provided by CECA. It is a technical grade surfactant. Its hydrophobic moiety consists of a chain of 12 carbons, and its hydrophilic moiety consists of 4 ethylene oxide groups. It should be noted that those numbers represent the average number of groups in each chain. There are no literature concerning the toxicity of Remcopal 4, but in general, the commercial grade C₁₂EO₄ is not toxic, and is used widely as excipient in cosmetics, the only effect is moderate irritation when in contact with the eyes¹.

The Pluronic P123 was provided by Sigma-Aldrich. It is a triblock copolymer formed by three branches, two hydrophilic parts linked to each other by a hydrophobic group. The toxicity of this surfactant is very low, and is considered safe for use for cosmetic applications².

The fluorinated surfactant, R^F₈(EO)₉ is provided by Dupont de Nemours. The hydrophobic chain is formed by fluorinated alkyl groups. Since it is technical grade, the number of groups also represents an average value. It should be noted that the fluorinated alkyl chain is linked to the hydrophilic moiety by a spacer consisting of two ethylene group.

1.2 Oils

Linear alkane was used in this work. A summary of the different properties of the oil is shown in Table 1-2.

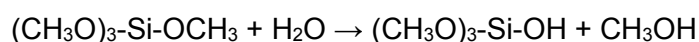
This oil is used mainly in the formation of nano-emulsions, and to dissolve the hydrophobic drug for the drug administration system. Decane is a carcinogenic compound³.

Table 1-2: Physico-chemical properties of the used hydrogenated oils

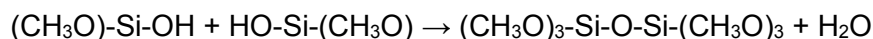
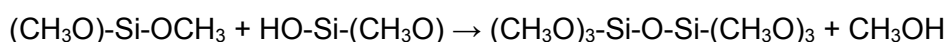
Chemical Formula	M (g.mol ⁻¹)	ρ (g.ml ⁻¹)	Grade	Supplier
Decane C ₁₀ H ₂₂	142	0.73	>95 %	Sigma-Aldrich

1.3 Silica source

The silica precursor used for this work is the tetramethoxysilane (TMOS). As mentioned in the first chapter the polymerization mechanism involves two reactions. The first one is the initiation reaction or the hydrolysis which leads to the formation of hydroxyl groups (Si-OH).



Then, the condensation, leads to the formation of oxygen bridges between silicon atoms.



The polymerization can take up from a few hours to several weeks, but can be accelerated by varying the pH. In particular, the condensation reactions are strongly pH dependent⁴. Figure 1-1 shows the behavior of the silicic acid for different pH values as well as the stability of the colloidal silica.

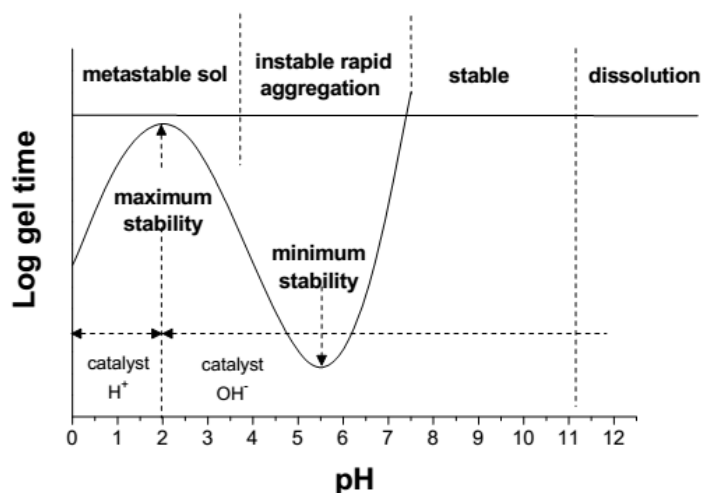


Figure 1-1: Sol stability: relationship between log(gel time) and pH ⁴.

For a pH between 6 and 7 and in the absence of soluble salts, silica bears a negative charge which slows the formation of a gel. But for a pH between 5 and 6 the gelling is accelerated leading to the formation of hydrated amorphous silica gels [SiO₂.xH₂O]. For a pH between 2 and 5, the silica charge is null, so presumably the molecules can readily collide. However in this pH span the concentration of hydroxyl ions governs the condensation of the polysilicic acid molecules, making the OH⁻ ions as the catalyst for the condensation reaction. For a pH

equal to 2 there is a maximum in stability which means that the system has enough time to finish the hydrolysis of the precursor. For pH values lower than 2 the gelling increases with the decrease of the pH, and the catalyst in this case is the H⁺ ions.

1.4 Enzymes

For the bioreactor experiments, the lipase extracted from the fungus *Mucor miehei* was used. It was provided by Sigma-Aldrich.

This enzyme has a molecular mass of 40 000 Da. The radius of the lipase, assuming a spherical shape, is 2 nm thus the calculated external volume of the molecule is 33.5 nm³. Its catalytic activity is 1.39 U/mg.

2 Methods

2.1 Phase Diagram

The surfactant's behavior in water and in the presence of oil were studied by establishing phase diagrams. Precise amounts of surfactant, oil or water are introduced into well closed glass vials. They were homogenized using a vortex or by centrifugation and heat when necessary. The mixture water/surfactant are plotted against the temperature for binary diagrams. The temperature was controlled by a thermostatic water bath, and the samples were kept at a given temperature for 30 minutes till a few hours to reach thermodynamic stability. Once the samples are stable, they are examined and the number of phases is noted along with their optical properties. If the samples are anisotropic, they are examined using a light polarizing microscope to identify the anisotropic phases by their characteristic textures. Further analysis of the samples is carried using SAXS, which allows the verification of the structure and the determination of the structural parameters. The systemic measurement of the Bragg distance allows the quantification of the water swelling of the liquid crystals, and when this swelling is saturated it means that the phase limit has been reached, the addition of further water causes the appearance of a second phase. Therefore a precise delimitation of a phase domain is made. Micellar solutions and microemulsions are identified visually, they form transparent and optically isotropic solutions. The size of the globules is determined by DLS (section 2.2.4). The structure of those globules is determined by using models in the GIFT software

For ternary diagrams, binary mixtures of surfactants and oil or water are initially prepared. Then the third component is added successively. The samples investigated in the same

manner as in the case of binary diagrams. The different domains are reported on a triangular diagram, where each of the vertices represents 100 % of a component.

2.1.1 Polarized light microscopy

While determining the phase diagram, one of the preliminary techniques used in the identification of the different phases is the polarized light microscopy with an Olympus BX 50 microscope equipped with polarizers. This technique is based on the fact that light waves are omnidirectional and will vibrate out at an angle perpendicular from the direction in which the beam is transmitted. There are two polarizing filters in a polarizing microscope - the polarizer and analyzer. The polarizer is situated below the specimen stage usually with its permitted vibration direction fixed, although this is usually rotatable through 360 degrees. The analyzer, usually aligned perpendicularly to the polarizer, is sited above the objectives and can be moved in and out of the light path as required. When both the analyzer and polarizer are in the optical path, their permitted vibration directions are positioned at right angles to each other. In this configuration, the polarizer and analyzer are said to be crossed, with no light passing through the system and a dark field of view present in the eyepieces⁵.

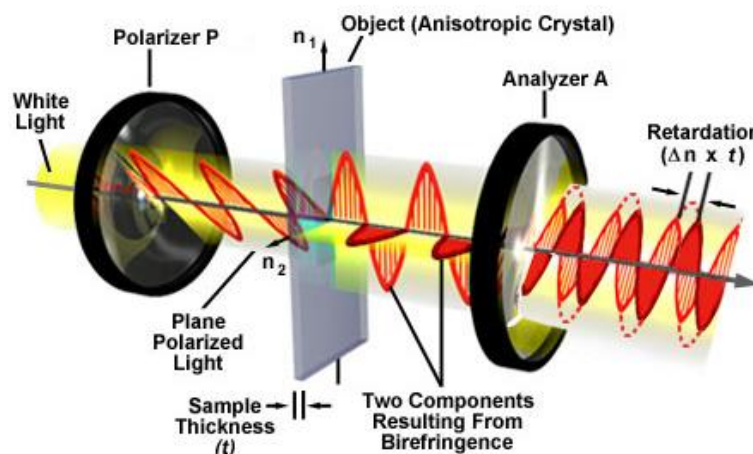


Figure 2-1: Schematic of a polarized light microscopy⁶.

An optically isotropic sample does not change the vibrational direction and the transmitted light is blocked by the analyzer, but when the sample is optically anisotropic the polarized light is split into two different beams at different polarizations and speeds (Figure 2-1). This phenomenon is known as “Birefringence”, which is due to the difference in the refraction index of the compound where the optical properties depend on the propagation direction of the light. The analyzer, placed after the sample is oriented perpendicularly to the polarizer, allows the merge of the two light beams and the image obtained is the result of interference between two beams having different propagation speeds.

Liquid crystals are birefringent due to their anisotropic nature, and therefore they are observable with a polarized light microscope. Each kind of liquid crystals has its own characteristic textures that are due to the defects in the structures (Figure 2-2). The liquid nature of those structures leads to the accumulation of the defects at regular intervals at the micrometer scale.

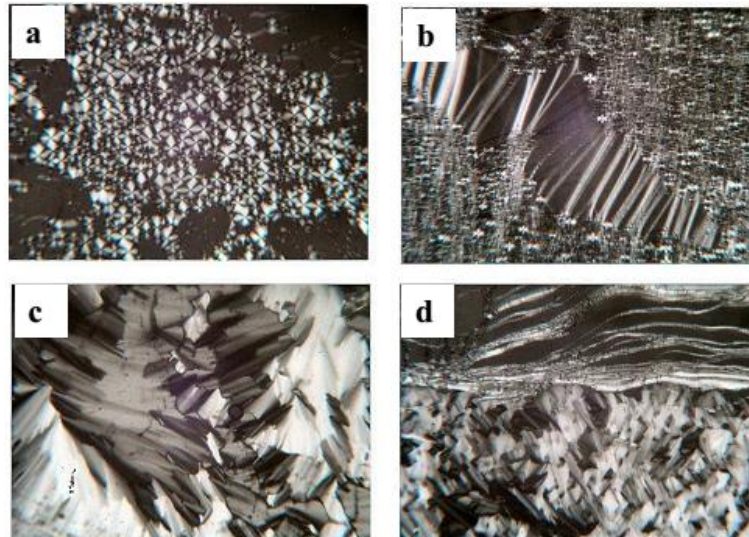


Figure 2-2: Textures of lamellar and hexagonal phases under the polarization microscopy. (a) The L_{α} phase, texture "Maltese Cross" (b) The L_{α} phase, oily streaks and "Maltese cross" (c) Hexagonal phase, fanlike texture, (d) Hexagonal phase H_1 coexisting with a phase L_{α} .

2.2 Nano-emulsion formation

In this work, the nano-emulsions were formed using two low energy methods, the Phase Inversion Composition and the Phase Inversion Temperature⁷. Those two techniques are based on the capacity of the surfactants to change their curvature thus modifying the continuous medium. Polyethoxylated nonionic surfactants with a hydrophobic character are suitable because of their ability to invert phases and go from a water-in-oil emulsion to an oil-in-water emulsion.

2.2.1 Phase Inversion Composition – PIC

With this method, mixtures of the oil and surfactant with different oil/surfactant (O/S) ratios are prepared at first. Then for each sample a peristaltic pump injects the right amount of water very slowly and a constant rate with a volume of 40 μl per cycle. The mixture is stirred continuously using a magnetic stirrer at 700 rpm. The experiments were conducted at 20°C.

2.2.2 Phase Inversion Temperature – PIT

As for the PIT, mixtures of oil, surfactant and water, are prepared with different O/S ratios inside sealed tubes. The samples are placed at temperature of 10 degrees above the PIT (which is determined by conductivity measurements) and then they are quenched at 5°C. The bluish or gray aspect of the isotropic solution is a characteristic of the presence of the nano-emulsions.

2.2.3 Conductivity measurements

The conductivity of the samples was measured as a function of temperature in order to determine the phase inversion temperature, sodium chloride was added to the aqueous phase in order to do the measurements. When the system is an O/W type, the continuous medium is constituted of an electrolyte aqueous solution and the medium becomes conductive. But after the phase inversion, the system becomes a W/O type in which the continuous medium is the oil which a non-conductive medium. The phase inversion is a fast process that happens in the span of a couple of degrees. The phase inversion temperature is identified by the inflexion point of the conductivity curve (Figure 2-3).

In this work a radiometer analytical CDM210 conductivity meter apparatus equipped with a CDC641T conductivity cell was used. The samples were prepared using an electrolyte solution ($\text{NaCl } 10^{-2} \text{ mol.L}^{-1}$). The sample and the conductivity probe are placed in a thermostatic container. The conductivity was measured as a function of the temperature and depending on the sample, the speed of the temperature increase speed was varied by increments of 1–5°C. For each increase of temperature, the conductivity was measured after the equilibrium of the sample is reached. The equilibrium time varied from 10 to 30 min.

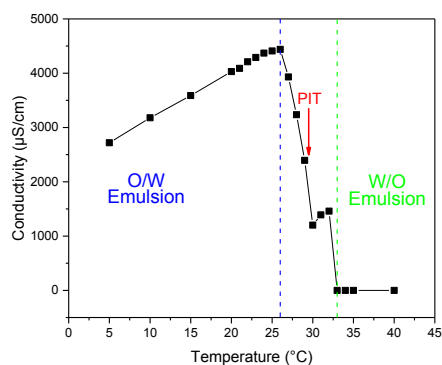


Figure 2-3: Conductivity profile as a function of the temperature for the Water/Decane/Remcopal 4 system ($O/S = 3$, $\Phi_W = 0.866$)

2.2.4 Dynamic light scattering

Dynamic Light Scattering (DLS), sometimes referred to as Photon Correlation Spectroscopy or Quasi-Elastic Light Scattering, is a technique classically used for measuring the size of particles typically, in the sub-micron region, dispersed in a liquid. It is based on the measurement of the Brownian movement. The larger the particle, the slower its Brownian movement is. This movement depends also on the viscosity of the dispersing liquid which change with the temperature.

So in order to detect the Brownian movement, an incident laser beam pass through a cell containing the dispersed particles. Those particles scatter the laser beam and thus fluctuating its intensity. Since those particles are in a perpetual movement the exiting beam's intensity fluctuates as a function of time. These fluctuations are detected and quantified using a detector, which then sends the signal to a correlator. The correlator works as a signal comparator that compares the signal at a given time (t) to the signal at time 0 (t_0) and calculates the correlation between them. This correlation decays through time till it becomes null. The decaying time is a function of the particle size, the smaller the particle the faster it is for the correlation to decay. The correlator used in a DLS instrument will construct the correlation function $G(\tau)$ of the scattered intensity:

$$G(\tau) = \frac{I(t_0)I(t_0 + \tau_0)}{I(t_\infty)^2}$$

with τ as the sample time.

For a large number of monodisperse particles in Brownian motion, the correlation function is an exponential decaying function of the correlator time delay t:

$$G(\tau) = A[1 + B \exp(-2\Gamma\tau)]$$

where A is the baseline of the correlation function, B is the intercept of the correlation function and Γ is the decay rate calculated with:

$$\Gamma = D_t q^2$$

where D_t is the translational diffusion coefficient and q is the wave vector:

$$q = \left(\frac{4\pi n}{\lambda_0}\right) \sin\left(\frac{\theta}{2}\right)$$

Where n is the refractive index of dispersant, λ_0 is the wavelength of the laser (633 nm) and θ is the scattering angle.

Hydrodynamic diameter is obtained from the correlation function using various algorithms using the Stokes-Einstein law:

$$D_H = \frac{kT}{6\pi\eta D_t}$$

were k is the Boltzmann constant, T the absolute temperature, η the viscosity of the continuous medium.

There are two approaches that can be taken: if the curve corresponds to an exponential to the correlation function to obtain the mean size (z-average diameter) and an estimate of the width of the distribution (polydispersity index) (this is called the Cumulants analysis) or multiple exponential to the correlation function to obtain the distribution of particle sizes (such as Non-negative least squares (NNLS) or CONTIN. The size distribution obtained is a plot of the relative intensity of light scattered by particles in various size classes and is therefore known as an intensity size distribution.

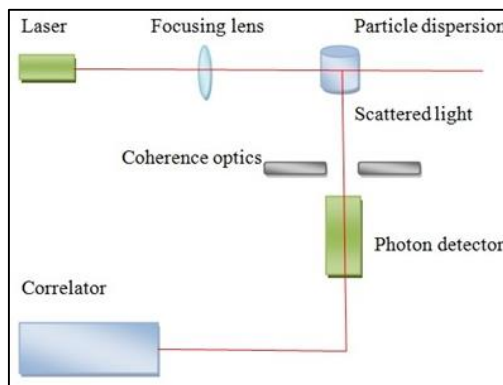


Figure 2-4: Schematic of a Dynamic Light Scattering apparatus

In this work we used a Malvern Zetasizer 3000HSa apparatus equipped with a He-Ne laser (633 nm, 5 mW) as shown in

Figure 2-4: Schematic of a Dynamic Light Scattering apparatus

, its detection range is from 2 nm to a few micrometers. The samples are prepared with demineralized water filtered using a surfactant free cellulose filter (pore size = 0.45 μ m). The samples are injected in disposable polystyrene cells. To confirm the results, every sample was analyzed three times at three different dilutions. The analysis was done at constant a temperature equal to 25°C unless stated otherwise.

2.2.5 Nanoparticle Tracking Analysis – NTA

This technique is based on the same principles as the DLS. It uses both the light scattering and the Brownian motion in order to obtain the particle size in liquid suspensions. The apparatus is equipped with a laser source (635 nm), a sample chamber, and x20 magnification microscope objective fitted on a conventional microscope onto which is mounted a CCD camera as shown in Figure 2-5. The role of the camera is to enable the visualization and recording of the nanoparticle Brownian motion within a field of view of 100 μ m x 80 μ m x 10

μm . Once the sample is injected into the chamber, the CCD camera captures a video of the particles moving under Brownian motion. The NTA software then locates and follows the center of each particle and measures the average distance it travels per frame. Then those measurements are converted into particle size and the plots are accumulated as a particle size distribution profile.

The NTA measurements were performed with a NanoSight NS300 of Malvern. The samples are diluted approximately 10^6 times and were injected in the sample chamber using syringes. The size measurements were done on video recordings of 90s. The detection range of this technique is from 10 nm to 2 μm .

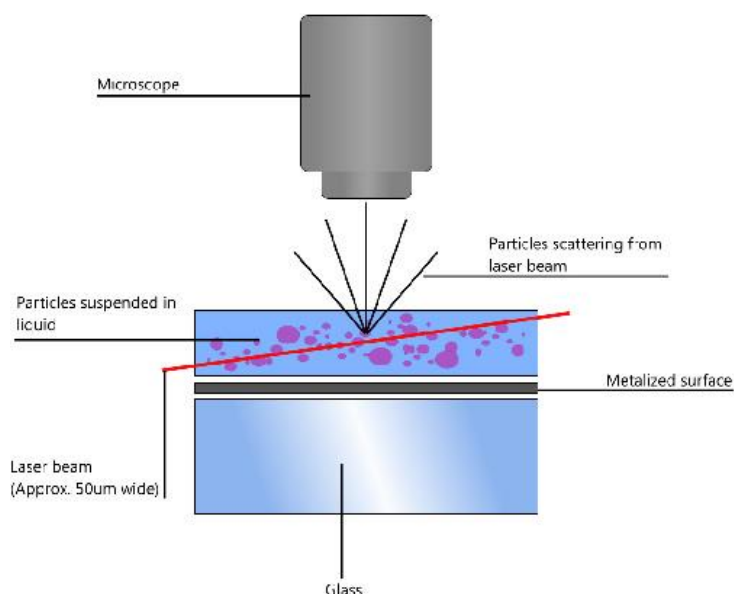


Figure 2-5: Schematic of the optical configuration used in NTA.

2.3 Silica material synthesis

In this work, mesoporous material were synthesized by cooperative templating mechanism (CTM). Micelles of a surfactant are dissolved in an aqueous medium. The pH is adjusted using HCl. Once the surfactant is fully dissolved, the right amount of TMOS is added dropwise to the solution and stirred for one hour. The amount of TMOS varies from one surfactant to another, it is calculated from the surfactant/TMOS molar ratio, a summary of the conditions is reported in Table 2-1. Then the solution is transferred to a Teflon autoclave, and undergo a hydrothermal treatment which can depending on the sample vary between 40°C and 100°C.

Table 2-1: Hydrothermal and TMOS molar ratio for the surfactants used in this work.

Surfactant	Concentration (wt-%)	R	pH	Temperature/Time
Pluronic P123	2,5	0.017	0	40°C/24h → 100°C/48h
$R^F_8(EO)_9$	10	0.5	2	80°C/24h

The different steps of the preparation of the mesoporous materials are presented in Figure 2-6.

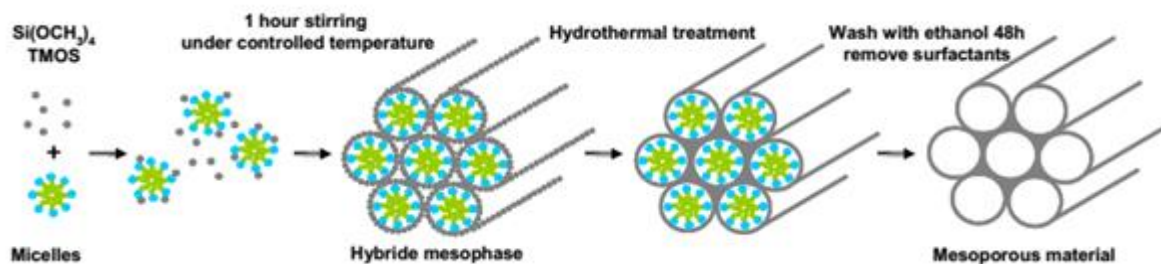


Figure 2-6: Schematic representation of the different steps of the formation and the preparation conditions of mesoporous material with a hexagonal structure.

For the dual-mesoporous material, the P123/ $\text{R}^{\text{F}}_8(\text{EO})_9$ surfactant couple was used. For the P123/ $\text{R}^{\text{F}}_8(\text{EO})_9$ system, the aqueous solution prepared from 1% of P123 and 9% of $\text{R}^{\text{F}}_8(\text{EO})_9$. The pH is stabilized at 0.3 using HCl. The surfactant/TMOS ratio is 0.1. The TMOS is added dropwise to the solution and stirred for 1 hour. Then the solution is transferred to an autoclave which undergoes a hydrothermal treatment at 80°C for 24 hours⁸.

The meso-macroporous material were prepared by “Dual Templating”, the template for the macropores are nano-emulsions. The nano-emulsions are prepared by the PIT method. A mixture containing 20% decane, 6.6% of Remcopol 4 and water at pH 0 is done, then the nano-emulsions are formed by PIT. As for the mesopores, a micellar solution of 5% of P123 at pH 0 is prepared. Finally the nano-emulsions and the micellar solution are mixed with a ratio of 1:1 for 30 seconds. The TMOS is added dropwise for a molar ratio of 0.0025. The mixture is stirred for 1 hour then transferred to an autoclave which undergoes a hydrothermal treatment at 40°C for 24 hours, then at 100°C for 48 hours.

Once the hydrothermal treatment is completed, the organic components are eliminated using ethanol in a Soxhlet device for 48 hours. The recovered powder was dried at room temperature. The characterization of the materials such as the structure, texture and morphology is determined by different techniques. The structure is determined by SAXS, the textural properties are obtained by nitrogen sorption analysis. The morphology is observed through electronic microscopy, and the macropore diameter is measured by mercury porosimetry.

The hybrid materials are prepared by the same manner as for the meso-macroporous materials with minor modifications. The active ingredient which is the ketoprofen is dissolved in the decane/Remcopol 4 mixture before adding of the water. The nano-emulsions are formed by PIT, and mixed with a P123 micellar solution with a 50:50 ratio. The TMOS is added dropwise for a molar ratio of 0.0025. The hydrothermal treatment is done at 40°C for 24 hours, then at 70°C for 48 hours. The final powder is dried at 40°C for 48 hours.

2.4 Drug release

The release profile of ketoprofen from bare silica material and from the hybrid material was studied. The bare silica was loaded with ketoprofen. This operation is done by dissolving an amount of 3.2 % of the drug in a hydroalcoholic solution (70:30 water/ethanol ratio) and the silica material was added and the mixture is stirred for 30 minutes. Then the mixture was filtered using a Buchner filtration system and a filtering paper (5-8 μm pore size). Then the powder is dried at 40°C for 24 h. After analysis, the final material (bare silica or hybrid) contained 2.5 % ketoprofen which is the commercial concentration found in the prescription drugs. This experiment was limited for the meso-macroporous material and its hybrid homologue.

The release experiments were conducted in 3 replicas. 0.3 g of the material was added to 150 ml of a medium solution in a beaker, so that the sink conditions (the volume of the medium should be at least 10 times the drug saturation volume) were respected. During the whole period of the experiment, the samples were stirred using a magnetic stirrer at 100 rpm at room temperature. Samples of 4 ml are extracted at regular time intervals and replaced with 4 ml of fresh medium solution as for to keep the release medium volume constant. The additions that dilute the release medium are accounted for in the calculations. The aliquots are then analyzed using UV-Visible spectrophotometer at $\lambda = 260 \text{ nm}$.

2.5 Transesterification

For the transesterification experiments. The enzyme is adsorbed by physisorption on the silica substrate. So in order to establish the optimal experimental conditions, an adsorption isotherm is required.

2.5.1 Enzyme physisorption on silica substrates

The enzyme immobilization is done by dissolving a certain amount of enzyme (for the lipase 0 to 50 $\text{mg}\cdot\text{ml}^{-1}$) is dissolved in a tris(hydroxymethyl)aminomethane - TRIS/HCl - (25 mM, pH 6) buffer solution. Finally 25 mg of a material is added to the solution. The mixture is agitated using a vibrating table at 150 rpm in order to avoid enzyme degradation. Since each material has different physicochemical properties, the equilibrium can be different. For the meso-macroporous material the lipase maximal adsorption is achieved at 50 min as for the dual-mesoporous material it is 80 min. Finally, the product is filtered using a Buchner filtration system and a filtering paper (5-8 μm pore size), this final product is washed with a fresh buffer solution.

2.5.2 Adsorption isotherm

For the adsorption isotherm, a calibration curve is needed in order to quantify the amount of enzymes adsorbed. For this, several known amounts of enzymes are mixed mechanically with silica and analyzed using an FTIR. The quantity of adsorbed enzyme is calculated by measuring the enzyme's amide II vibrations at 1530 cm^{-1} . The area values of this band are normalized with the corresponding area of a silica band located between 720 and 860 cm^{-1} , which is considered as an internal standard. A calibration curve was established for each type of material used as shown in Figure 2-7. For each sample, the quantity of the adsorbed enzyme is determined at first by calculating the ratio between the amide II band and the silica band, then with the support of the calibration curve which gives the concentration in milligrams of enzymes per milligram of material is known.

The adsorption isotherm representing the quantity of adsorbed enzymes (Γ) on a material is plotted as a function of the concentration of the enzyme left in the solution at adsorption equilibrium ($[C]_{eq}$). The curves are fitted according to the Langmuir equation:

$$\Gamma = \frac{\Gamma_{max}[C]_{eq}}{[C]_{eq} + K_L}$$

The determination of the maximal concentration allows the preparation of catalysts. For this, 25 mg of the material are submerged in 4 ml TRIS/HCl (25 mM, pH 6) that contains the maximal concentration of dissolved enzyme. The adsorption is considered total at equilibrium time.

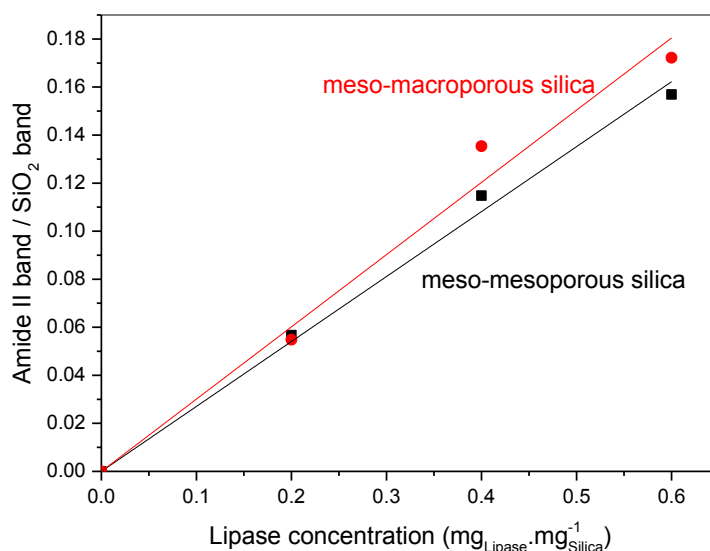


Figure 2-7: Calibration curve of the lipase for the dual-mesoporous material (black) and the meso-macroporous material (red).

2.5.3 Transesterification of Colza oil

For the reaction of the transesterification of colza oil, the catalyst is prepared for the maximal concentration determined from the adsorption isotherm. The reaction of transesterification is done in the conditions determined in our group⁹ which allows the obtaining of 100% yield.

These conditions are: Molar ratio (methanol/oil) = 1

- Water = 2.5%
- Reaction temperature = 24°C
- Stirring = 250 rpm
- Catalyst = 20 mg

The role of the water in this reaction is to create a water/oil interface which facilitates the enzymes activity, but a large quantity of water causes the yield to drop because the triglyceride hydrolysis by lipase^{10,11}.

By definition, the yield is ratio between the quantity of the final product obtained experimentally and the maximal quantity that can be theoretically obtained. For a methanol/oil molar ratio equal to 1, the methanol is the limiting reagent, and the yield is calculated by doing the ratio of the mole number of methyl esters (n_{ME}) and the mole number of methanol in the reaction (n_{MeOH}).

$$Yield (\%) = \frac{n_{ME}}{n_{MeOH}} \cdot 100$$

Since the samples are analyzed by gas chromatography coupled with a mass spectrometer, we can determine the volume of the methyl esters present in the sample from the calibration curve:

$$n_{ME} = \frac{V_{ME} \cdot \rho_{ME}}{M_{ME}}$$

With $\rho_{ME} = 0.87 \text{ g.ml}^{-1}$, and $M_{ME} = 292 \text{ g.mol}^{-1}$.

2.5.4 Purification of the transesterification reactions products

For the study of the transesterification reaction kinetics, aliquots were taken at regular time intervals. These aliquots were purified before the analysis process to eliminate the fatty acids. Using SPE (solid phase extraction) cartridges were, because this system rapid, simple and efficient. It works by adsorbing the compounds to be separated in a stationary phase (already in the cartridge). Then the wanted compounds are recuperated by elution using a specific solvent such as acetonitrile. The solid phase is made from silica (surface area = $500 \text{ m}^2.\text{g}^{-1}$). The silica is functionalized with octadecyl molecules that improves the adsorption of the compounds. The protocol to separate the fatty acids from the methyl esters was optimized in our group⁹:

- Conditioning: the activation of the solid phase and its conditioning are done by injecting 1 ml of acetonitrile, which is then evacuated while keeping the solid phase wet
- Sample injecting: a 100 μ L sample aliquot is injected in the cartridge along with a 100 μ L of an acetonitrile solution containing 0.4% methyl laurate (internal standard).
- Elution process: the methyl esters are recuperated by injecting 9 mL of acetonitrile in the cartridge.
- Finally, 1 mL of acetonitrile is added to the solution.

The acetonitrile was chosen because of its capacity to dissolve methyl esters without dissolving the fatty acids. The internal standard and the aliquot are injected together to make sure that the purification process does not influence the reaction yield.

2.5.5 Gas chromatography

Gas chromatography is a technique that allows the separation of molecules forming a complex mixture. It can be used on compounds that are easily evaporated by heating, without being destroyed. The apparatus used in this work is presented in Figure 2-8, it is a gas chromatography apparatus coupled with a mass spectrometer.



Figure 2-8: Photo of the GC-MS Shimadzu QP2010 SE apparatus.

The machine is constituted of two main components, the “separation” component and the “detection” component. The separation component includes a column (DB5-MS UI) inside a furnace, an injector and a detector. The detection component is the mass spectrometer. The sample is injected and ionized and goes through the detector via a quadrupole that separates the ions. This quadrupole consists of four parallel metal rods, a positive voltage is applied in two opposing rods and a negative voltage applied in the others as well as a radio frequency. The use of gas chromatography coupled with a mass spectrometer allows not only the separation of the different species in a mixture but also the identification of those species via a database, without the need to inject reference samples.

The product of a transesterification process contain multiple ethyl esters that have each a different fusion point. So in order to analyze the entirety of the esters and present them on the same chromatogram, the temperature cycle has been optimized Figure 2-9A.

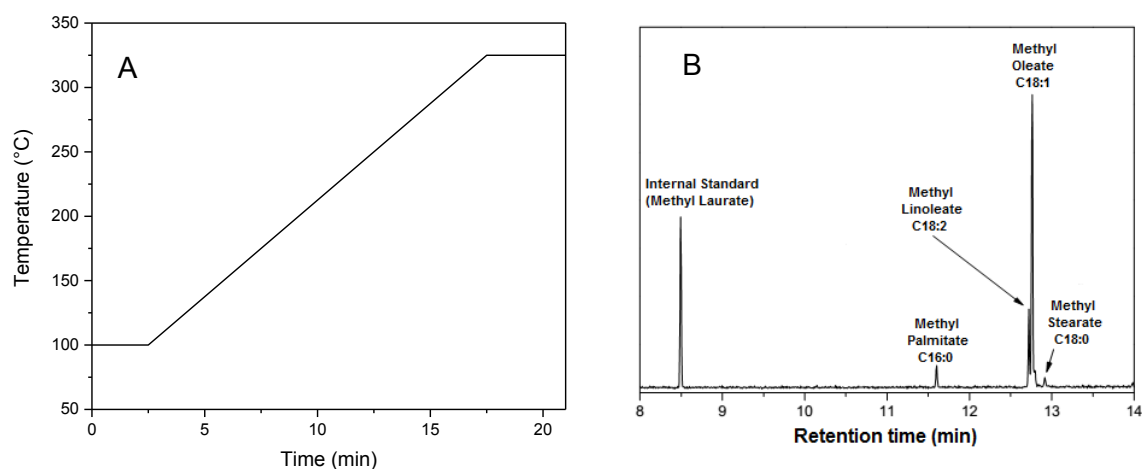


Figure 2-9: Temperature cycle (A) and a typical chromatogram obtained by GC-MS(B)

When a sample is analyzed, it is ionized and all the ions are detected at the same time. The chromatogram where all those ions are presented is called “TIC” or total ion chromatogram. It is then possible to study each ion and to choose the ions that represent best each compound. This finishing step refines the chromatogram and makes it more selective and precise.

The samples are purified so that only methyl esters are preserved, because the transesterification process produce a mixture of fatty acids and esters. Figure 2-9B shows a typical chromatogram obtained by GC-MS. Methyl Laurate was chosen as the internal standard and it has been added to the methyl esters mixture for quantification purposes. Its retention time is shorter than the others.

2.5.6 Yield calculation of the transesterification reaction

The efficacy of a catalyst is evaluated by calculating the yield of the reaction. For this, a 100 μ L of the products of a reaction are diluted in acetonitrile containing 0.004% methyl laurate acting as the internal standard. The internal standard role is to quantify the methyl esters by calculating the ratio between the area of the peak of each methyl ester and the area of the peak of the internal standard. In order to improve the quantification process, a calibration curve is done beforehand. To make this calibration curve only methyl esters are needed. Those esters are obtained by chemical transesterification of the colza oil according to process done by Freedman *et al.*¹². In this experiment, 13 g of methanol are mixed with 60 g of colza oil and heated at 60°C. Then 0.39 g of potassium methoxide is added to the mixture. The reaction is linked to a condenser and protected by a CaCl_2 tube to prevent water.

The reaction lasts 24 hours, then the solution is filtered on a Buchner filter system using filtering paper (0.45 μm). In order to eliminate the glycerol, petroleum ether is added to the mixture as well as sodium sulfate to trap the water already present in the mixture. Then another filtration step as described above is necessary. The use of a rotary evaporator extracts the excess methanol and the petroleum ether.

For the calibration curve, the yield of the transesterification reaction is represented by the quantity of the pure methyl esters present in the solution. For this, it was considered that for a yield of 100%, an acetonitrile solution (10 mL) should contain 100 μL of pure methyl esters along with 100 μL of the internal standard; for a yield of 75%, an acetonitrile solution (10 mL) should contain 75 μL of pure methyl esters along with 100 μL of internal standard; etc. By analyzing 1 μL of each sample using GC-MS, it was possible to measure the area of the methyl ester peaks as well as the area of the internal standard. The calibration curve presented in Figure 2-10 is the ratio of the methyl ester peak area over the peak area of the internal standard plotted against the methyl ester yield.

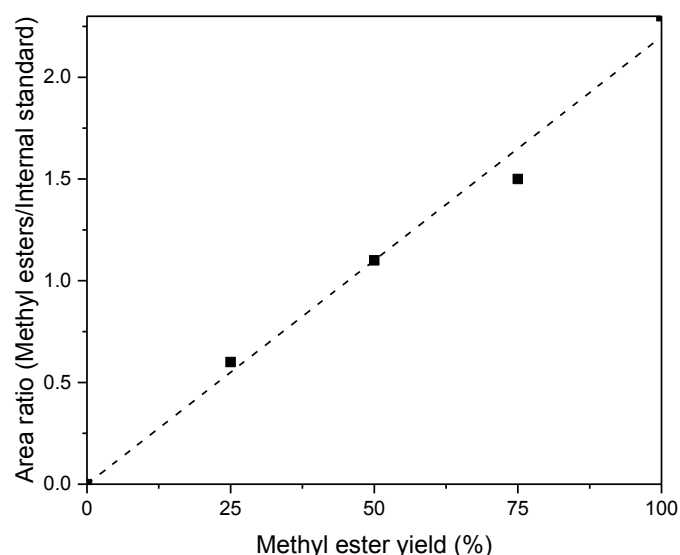


Figure 2-10: Calibration curve of the methyl esters.

In the case of colza oil methanolysis, the stoichiometric molar ratio between methanol and colza oil is 3. If the molar ratio is lesser than 3, the methanol is the limiting reagent and if the ratio is more than 3 then the limiting reagent is the oil. Based on previous works⁹ a molar ratio of 1 gives a 100 % yield and it has been used in this work.

Since for a molar ratio equal to 1, the limiting reagent is the methanol, thus the yield corresponds to the ratio between the number of moles of methyl esters and the number of moles of ethanol used in the reaction.

$$Yield (\%) = \frac{n_{ME}}{n_{MeOH}} \cdot 100$$

3 Characterization methods

3.1 Small angle X-ray scattering - SAXS

It is the method of choice for the characterization of colloidal systems like the organized molecular assemblies. This technique is based on the differences between the electronic densities of the diffusing structures and the continuous medium. The diffusion intensity curves $I(q)$ is represented as a function of the wave vector (q).

$$q = \frac{4\pi \sin \theta}{\lambda}$$

where 2θ is the diffraction angle between the vectors \vec{K} and \vec{K}' (the angle between the incident X-ray beam and the detector), and λ is the X-ray beam wavelength.

From these curves we can determine for example the structure of micelles by using theoretical models. The theoretical curves and experimental ones are confronted and the best fit allows the determination of the most probable structural characteristics. For samples with periodical organization, like the liquid crystals, the X-ray diffraction on the different planes of a structure leads to the observation of Bragg peaks which are characteristic of the system geometry. The repetition distance between the diffraction planes are calculated using Bragg's law:

$$2d_{h,k,l} \sin \theta = n\lambda \Rightarrow d = \frac{2\pi}{q}$$

$d_{h,k,l}$: repetition distance ; θ : diffraction semi-angle ; n : reflection order ; λ : X-ray wavelength.

The ratios between the different peaks are characteristic of a given structure.

The SAXS apparatus at the laboratory is an Anton Paar SAXSess mc². It is constituted from:

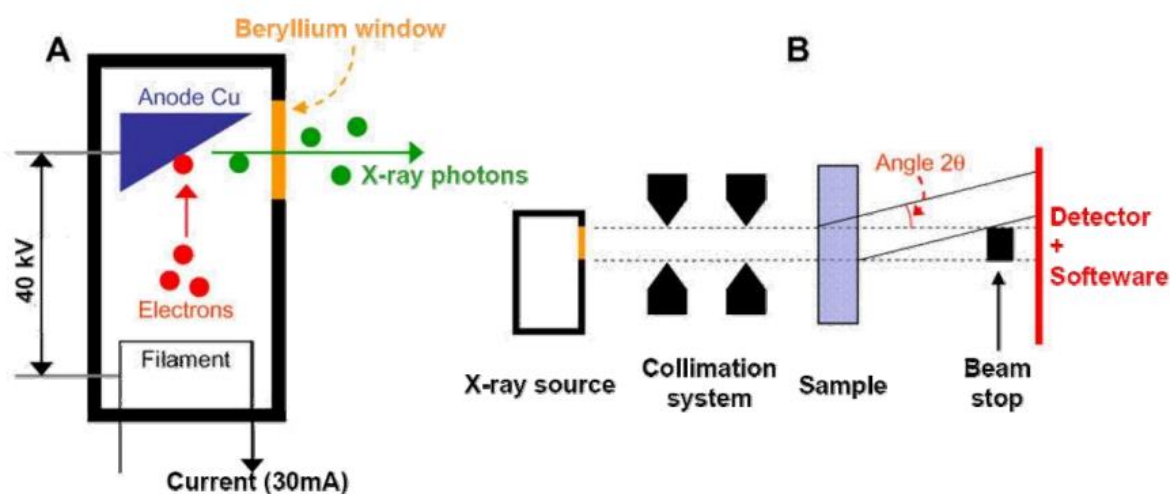


Figure 3-1: Schematic of an X-ray tube (A), and of a SAXS apparatus (B).

- An X-ray generator (PANalytical tube, $\lambda_{Cu} = 0.1542$ nm; $V_{max} = 40$ kV, $I_{max} = 50$ mA).

- A mirror to make the beam monochromatic and focalize it.
- A collimator bloc
- A vacuum chamber in which a sample holder is installed. The latter has its temperature stabilized with a Peltier temperature controller. The samples are inserted in capillary if it is fluid, and if it is powder it is fixed using a Kapton® tape.
- A CCD camera (charged-couple device) placed at a distance from the sample equal to 309 mm).

3.1.1 Lamellar phase

The X-ray diffraction on the parallel bilayer planes of a lamellar liquid crystal leads to the apparition of Bragg's peaks on decreasing intensities, whose positions are defined by q_0 , $q_1 = 2q_0$, $q_2 = 3q_0 \dots$ where q_0 is the position of the first peak.

The primary reflection comes from the repetition distance between two consecutive bilayers. The intensity and the width of this peak are a function of the regularity of the stacking. The secondary reflections which have lesser intensities are attributed to different diffractions orders (n) of Bragg's law.

The repetition distance "d" allows the calculation of the structural parameters that describe the studied lamellar phase, such as the surface per hydrophilic head (S), the hydrophilic thickness (d_A) and the hydrophobic one (d_B) as shown in Figure 3-2.

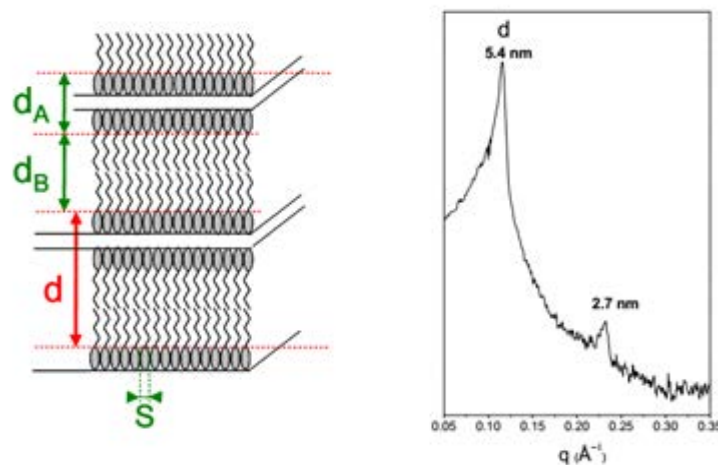


Figure 3-2: Schematic representation and a typical diffractogram of a lamellar liquid crystal.¹³

3.1.2 Hexagonal phase

The diffraction of the X-ray on a hexagonal liquid crystal phase, leads to the apparition of Bragg's peaks with decreasing intensities whose positions are defined by q_0 , $q_1 = \sqrt{3}q_0$, $q_2 = 2q_0$, $q_3 = \sqrt{7}q_0 \dots$

The primary and secondary reflections are due to the diffraction of the incident beam on the different planes of the two-dimensional hexagonal structure represented in Figure 3-3.

By taking geometrical considerations and knowing the partial volumes of the hydrophobic and hydrophilic moieties of the surfactant, it is possible to calculate the structural parameters defining the hexagonal phase like the hydrophobic radius R_H as well as the surface per hydrophilic head.

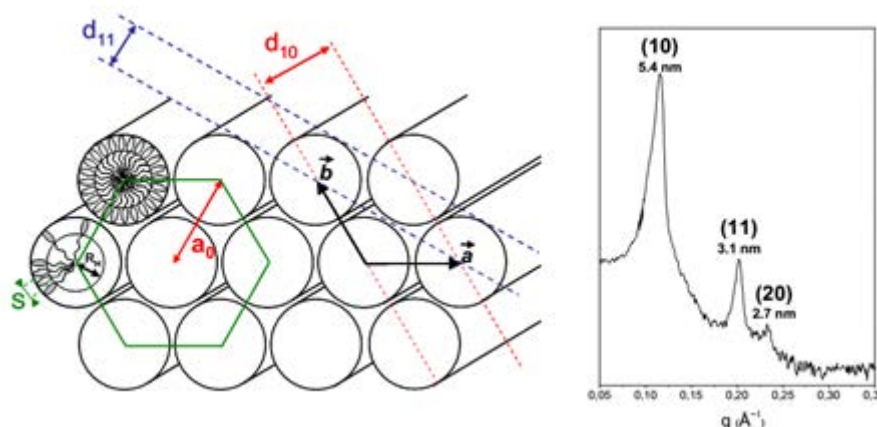


Figure 3-3: Schematic representation and a typical diffractogram of a hexagonal liquid crystal.¹³

3.1.3 Mesoporous material

The X-ray diffraction at small angles is also used to characterize the structure of mesoporous silica. The organized materials obtained in this study have a hexagonal structure. The diffractogram is similar to the one obtained from the hexagonal liquid crystal the liquid crystals (Figure 3-4A). The lattice parameter (a_0) corresponds to the sum of the diameter of a pore and the thickness of the silica wall. It is calculated from the repetition distance given by the first peak by the formula:

$$a_0 = \frac{2d_{10}}{\sqrt{3}}$$

The determination of the size of the pores is done by nitrogen sorption (section 3.2) and by a simple subtraction it allows the calculation of the silica wall thickness which is an important parameter in the material characterization of the material because it influences its stability. The thicker the walls the more stable the material is.

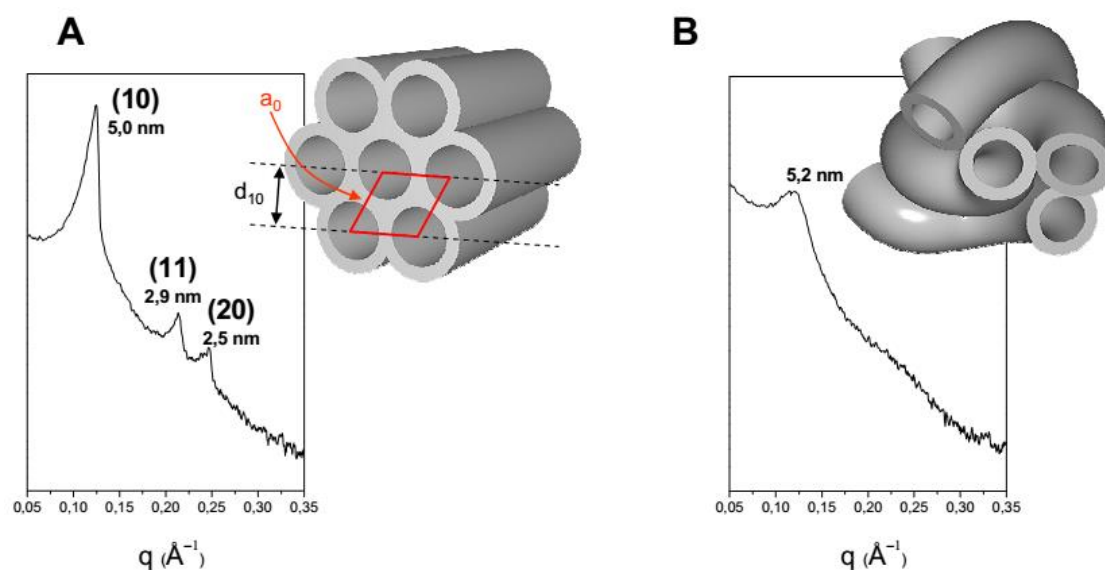


Figure 3-4: Schematic representation and typical diffractogram of a mesoporous material with a hexagonal structure (A) and wormlike structure (B).

The materials with a wormlike structure of the pores have characteristic diffractograms that have a single large peak (Figure 3-4B) and by the absence of secondary peaks. The position of this peak represents the average distance between pores.

3.2 Nitrogen sorption analysis

Organized porous material have alongside their structure a high specific area, a small pore size distribution. The textural properties are measured by nitrogen adsorption/desorption.

The adsorption corresponds to the adsorption of molecules on an adsorbent (a solid surface). The desorption corresponds to the release of the adsorbed molecules. There exists 2 types of adsorption, the physisorption or the physical adsorption and the chemisorption or chemical adsorption.

The characterization of porous material is done by physical adsorption and desorption of nitrogen at its liquefaction temperature (77 K) at the surface of the material. The gas quantity adsorbed on the surface of the solid depends on the nature of this surface, the gas pressure and the temperature. The equilibrium is established between the gaseous state and adsorbed of the adsorbable compound can be compared at equilibrium existing between a liquid and its vapor. At a given temperature, the quantity of the adsorbed species is plotted as a function of the equilibrium pressure (P/P_0) of the gas on the pressure domain between 0 and the saturating vapor pressure, forms the adsorption isotherm. The shape of the adsorption isotherm allows the qualitative determination of the textural properties of the studied material. The different isotherms are classified according to six distinct types. In this work, only two types of isotherms are detected, Type II, and Type IV.

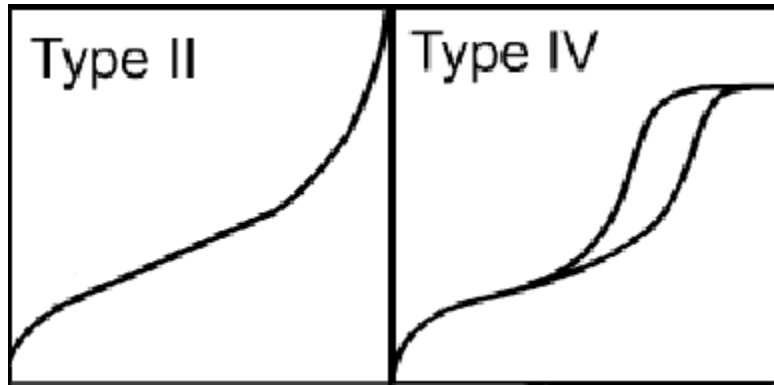


Figure 3-5: Type II and Type IV adsorption/desorption isotherms.

3.2.1 Type II isotherm

The Type II isotherm is shown in Figure 3-5. This type of isotherm indicates an indefinite multi-layer formation after completion of the monolayer and is found in adsorbents with a wide distribution of pore sizes.

3.2.2 Type IV isotherm

The type IV isotherm is shown in Figure 3-5. This types of isotherm is known by the fast increase of the adsorbed nitrogen quantity for relatively small pressures that corresponds to the adsorption of a monolayer. For higher pressures, the progressive increase of the adsorbed volume is translated by a capillary condensation phenomenon characteristic of the presence of mesopores (pores with a diameter between 2 and 5 nm) which is followed by the appearance of a plateau. A hysteresis loop appears when the nitrogen starts the desorption process, this loop is due to the irreversible nature of the capillary condensation inside the mesopores.

The analysis of this type of isotherms uses mathematical algorithms that allow the calculation of the surface area, the pore volume and the pore diameter of the studied material.

The surface area is calculated from the adsorbed volume of the monolayer (for lower pressure values) and the molecular cross-sectional area:

$$S_{BET} = \frac{V_m}{V_{mol}} N_a \sigma$$

σ = molecular cross-sectional area (16.2 Å² for N₂ at 77 K); V_m = molar gas volume; N_a = Avogadro number.

The volume of the monolayer V_m is calculated using the BET equation (Brunauer, Emmett, Teller¹⁴):

$$\frac{P}{V(P_0 - P)} = \frac{1}{V_m C} + \frac{(C - 1)P}{V_m C P_0}$$

V = adsorbed volume at a pressure P ; V_m = monolayer volume; P_0 = saturating vapor pressure of the adsorbent; C = constant.

The pore size distribution is calculated using the BJH method (Barrett, Jayne and Halenda¹⁵). This theory is based on the phenomenon of capillary condensation which appears in the mesopores, and by applying the Kelvin law, which links the pressure P at which the condensation happens to the curvature radius of the meniscus of the formed liquid.

$$\ln \frac{P}{P_0} = - \frac{\gamma V_m}{(r_p - t)RT}$$

γ = surface tension at a temperature T ; r_p = pore radius; t = thickness of the adsorbed layer.

This method is applied to the adsorption branch of the isotherm. Based on an iterative calculation, it allows the calculation of the quantity adsorbed in a defined pressure span. From the pore radius as a function of the relative pressure, it is possible to calculate the cumulated volume of all the pressure spans as a function of pore radius which gives by derivation the pore size distribution. However, this method may under-estimate the pore size by 20 %, which does not cause a major problem in this study, since the work in this study are limited to comparative purposes. The machine used is a Micromeritic Tristar 3000. The samples are degassed at least 12 hours prior to analysis in order to eliminate water and CO_2 physisorbed inside the pores of the material. The pore size range that can be detected by this technique is between 1.8 and 50 nm.

3.3 Mercury Porosimetry

This technique was used in order to determine the size of the macropores in the meso-macroporous materials in complementary to the nitrogen sorption analysis which allows the measurement of the size of the mesopores. This technique is based on the non-wetting properties of the mercury. When the mercury is in contact with a solid, it does not adsorb because of its high surface tension. This creates a resistance to the pore penetration which is overcome by applying a pressure. The smaller the pore size, the more pressure it requires to make the mercury go inside it. The relationship between the pore size and the pressure is given by the Washburn equation¹⁶:

$$\Delta P = \frac{2\gamma \cos \theta}{r}$$

where r is the pore radius, γ is the mercury surface tension, θ is the contact angle and ΔP is the applied pressure.

The apparatus used in this work is a Micromeritics' Autopore IV 9500 mercury porosimeter. It is equipped with two transducers, one for the low pressure analysis (0.1 – 15 psia) which is regulated by nitrogen gas after filling it with mercury, and one for the high pressure analysis

(15 – 60 000 psia) which is regulated by oil. The samples are inserted in the penetrometer adapted to powder samples and installed at first in the low pressure compartment. After this the system is switched to the high pressure compartment. The switchover effect is eliminated manually later from the result.

3.4 Electronic microscopy

The electronic microscopy methods are direct techniques that allows the visualization of the silica materials in real time, unlike the previous techniques that require further calculations in order to exploit the results. Two main techniques are used in this work: the Scanning Electronic Microscopy to study the morphology and the surface state of the materials, and the Transmission Electronic Microscopy to study the bulk of the materials on a different scale.

3.4.1 Scanning Electronic Microscopy – SEM

This technique consists of the scanning of the surface of the sample using a high energy electron beam. The interaction between the electrons and the sample's surface leads to the generation of backscattered electrons, X-rays and Auger electrons, UV/visible/IR cathodoluminescence and secondary electrons. The latter have low energy and are generated from the most superficial atoms of the sample, this makes them responsive to the sample's surface topography. Those electrons are collected point by point on the scanned area, and the resulting signals are normalized and converted to an image of the scanned surface.

The SEM used in this work is a HITACHI S-2500. The samples were dispersed in ethanol using ultrasound, then spread on an aluminum sample holder and dried at room temperature.

3.4.2 Transmission Electronic Microscopy – TEM

In this technique, the image obtained is the result of the interactions between the sample and the passing through electron beam. The intensity of the electron beam is controlled by the density and the thickness of the sample producing a fluctuation of the contrast analogous to the sample's texture. This technique was used to observe the organization and the general morphology of the mesopores. The TEM used in this study is a Philips CM20.

3.5 Fourier Transform Infrared spectroscopy – FTIR

The FTIR spectroscopy is a technique that identifies and detects the molecular groups for a material of a molecule. When a sample is irradiated with an infrared beam, inter-atomic bonds vibrates at a specific wavelength which leads to an absorption. The wavelength of the

absorbed wave depends on the location of the absorbing bond and on the environment in which they are situated.

Infrared spectra are collected using a Harrick DRA-2C1 and a Harrick HVC-DRP cell. For the analysis of the samples, the mesoporous material is mixed with KBr (10:90 ratio). The samples then are put under vacuum ($<10^{-4}$ mBar) to eliminate any physisorbed water. The spectra are acquired in reflection mode at a fixed spectral resolution of 8 cm^{-1} , the scans are repeated 50 times and the acquisition time is 5 minutes. The spectra are presented in a pseudo-absorbance mode $[-\log(R)]$ or R is the reflectance which is the ratio between the sample (R_s) and the reflectance of the KBr (R_r) ($R=R_s/R_r$).

4 References

- (1) Fiume, M. M.; Heldreth, B.; Bergfeld, W. F.; Belsito, D. V.; Hill, R. A.; Klaassen, C. D.; Liebler, D.; Marks, J. G.; Shank, R. C.; Slaga, T. J.; et al. Safety Assessment of Alkyl PEG Ethers as Used in Cosmetics. *Int. J. Toxicol.* **2012**, *31* (5 Suppl), 169S – 244S.
- (2) Singh-joy, S. D.; Valerie, C.; Review, C. I. Safety Assessment of Poloxamers 101, 105, 108, 122, 123, 124, 181, 182, 183, 184, 185, 188, 212, 215, 217, 231, 234, 235, 237, 238, 282, 284, 288, 331, 333, 334, 335, 338, 401, 402, 403, and 407, Poloxamer 105 Benzoate, and Poloxamer 182 Dibenzoate as Use. *Int. J. Toxicol.* **2008**, *27*, 93–128.
- (3) TOXNET <http://toxnet.nlm.nih.gov/cgi-bin/sis/htmlgen?CCRIS>.
- (4) Iler, R. K. *The Chemistry of Silica: Solubility, Polymerization, Colloid and Surface Properties, and Biochemistry*; John Wiley and Sons, Inc., 1979.
- (5) Abramowitz, M.; Parry-Hill, M. J.; Davidson, M. W. Polarized Light Microscopy <http://www.micro.magnet.fsu.edu/primer/virtual/polarizing/index.html>.
- (6) Murphy, D. B.; Spring, K. R.; Fellers, T. J.; Davidson, M. W. Introduction to Optical Birefringence <https://www.microscopyu.com/articles/polarized/birefringenceintro.html>.
- (7) Forgiarini, A.; Esquena, J.; González, C.; Solans, C. Formation of Nano-Emulsions by Low-Energy Emulsification Methods at Constant Temperature. *Langmuir* **2001**, *17* (7), 2076–2083.
- (8) May, A.; Stébé, M. J.; Gutiérrez, J. M.; Blin, J. L. Coexistence of Two Kinds of Fluorinated Hydrogenated Micelles as Building Blocks for the Design of Bimodal Mesoporous Silica with Two Ordered Mesopore Networks. *Langmuir* **2011**, *27* (23), 14000–14004.
- (9) Jacoby, J. Lipase Mucor Miehei Immobilisée Dans Des Matériaux Poreux Silicatés : Bioréacteurs Pour La Synthèse D'esters Méthyliques À Partir D'huiles Végétales, Thèse de l'Université de Lorraine, 2013.
- (10) Yin, P.; Chen, L.; Wang, Z.; Qu, R.; Liu, X.; Ren, S. Production of Biodiesel by Esterification of Oleic Acid with Ethanol over Organophosphonic Acid-Functionalized Silica. *Bioresour. Technol.* **2012**, *110*, 258–263.
- (11) Giraldo, L.; Moreno-Piraján, J. C. Lipase Supported on Mesoporous Materials as a Catalyst in the Synthesis of Biodiesel from Persea Americana Mill Oil. *J. Mol. Catal. B Enzym.* **2012**, *77*, 32–38.
- (12) Freedman, B.; Pryde, E. H.; Mounts, T. L. Variables Affecting the Yields of Fatty Esters from Transesterified Vegetable Oils. *J. Am. Oil Chem. Soc.* **1984**, *61* (10), 1638–1643.

- (13) Michaux, F. Contribution Des Tensioactifs Fluorés À La Synthèse de Matériaux Mésoporeux., Thèse de l'Université de Lorraine, 2009.
- (14) Brunauer, S.; Emmett, P. H.; Teller, E. Adsorption of Gases in Multimolecular Layers. *J. Am. Chem. Soc.* **1938**, *60* (2), 309–319.
- (15) Barrett, E. P.; Joyner, L. G.; Halenda, P. P. The Determination of Pore Volume and Area Distributions in Porous Substances. I. Computations from Nitrogen Isotherms. *J. Am. Chem. Soc.* **1951**, *73* (1), 373–380.
- (16) Giesche, H. Mercury Porosimetry: A General (Practical) Overview. *Part. Part. Syst. Charact.* **2006**, *23* (1), 9–19.

**Nano-emulsion/micelles based systems
for the preparation of a hierarchically
porous material: application as a new
drug delivery system**

Ce chapitre est consacré à l'élaboration de matériaux à porosité hiérarchisée à partir de nano-émulsions et de micelles. Ces matériaux ainsi que les matériaux hybrides, dans laquelle la phase organique n'a pas été éliminée ont été utilisés pour encapsuler un principe actif, le kétoprofène, et sa libération a été étudiée. L'étude commence par une investigation du comportement de phase du système Remcopal 4/décane/eau. Le Remcopal 4 est un tensioactif très voisin du $C_{12}(EO)_4$, mais son comportement dans l'eau ne présente pas exactement les mêmes propriétés de phase. Aucun point trouble, ni phase L_3 , détectés avec le $C_{12}(EO)_4$, n'ont été mis en évidence. L'addition de décane n'augmente pas le polymorphisme, la phase micellaire inverse (L_2) persiste ainsi que la phase lamellaire (L_α), qui peut incorporer jusqu'à 50% de décane pour un rapport massique eau/Remcopal 4 égal à 1 à température ambiante. En revanche, une phase hexagonale inverse (H_2) est détectée entre les phases L_α et L_2 . Les paramètres structuraux de la phase lamellaire gonflée de décane ont été déterminés. En se basant sur des considérations géométriques simples, la surface par tête polaire (S) et l'épaisseur hydrophobe (d_B) ont été calculées à partir de la distance de répétition (d_{100}), laquelle a été obtenue par SAXS. Les résultats montrent que d_B est une fonction linéaire du nombre de molécules de décane par molécule de tensioactif. La valeur de S varie entre 0.35 et $0.38 \pm 0.1 \text{ nm}^2$. Le caractère hydrophobe du tensioactif et la présence d'une phase lamellaire qui se gonfle considérablement en présence de décane, font que ce système est approprié à la préparation de nano-émulsion par deux méthodes qui sont liées à l'inversion de phase : température d'inversion de phase (PIT) et inversion de phase par changement de la composition (PIC).

Pour la méthode PIT, la connaissance de la température d'inversion de phase est nécessaire. Des mesures de conductivité en fonction de la température, en remplaçant l'eau par une solution de NaCl (10^{-2} mol/L), ont permis la détermination de la PIT en fonction de la concentration en tensioactif et des fractions massiques d'eau et de décane. Quatre rapports huile/tensioactif (H/TA) (2.3, 3, 4, 5.7) pour une fraction massique en eau (Φ_W) de 0.6, ainsi que quatre Φ_W (0.6, 0.7, 0.8, 0.9) pour un rapport H/TA de 3 ont été investis. Les résultats ont montré que la température d'inversion de phase augmente avec le rapport H/TA (de 23°C pour H/TA = 2.3 à 44°C pour H/TA = 5.7) et avec l'augmentation de la fraction massique d'eau (de 26°C pour $\Phi_W = 0.6$ à 31°C pour $\Phi_W = 0.9$). Cette méthode permet de visualiser sur les courbes de conductivité les différentes phases présentes en fonction de la température. C'est ainsi qu'on observe un épaulement ou un maximum, à l'exception de la courbe relative à la solution H/TA = 3 et $\Phi_W = 0.9$, qui est associée à des structures de type L_3 ou cristal liquide.

Pour mieux comprendre les structures qui entrent en jeu, un diagramme de phase de type pseudo-Shinoda a été établi pour H/TA = 3, et Φ_W variant entre 0.55 et 0.95. Ce diagramme de phase a montré qu'entre $\Phi_W = 0.6$ et 0.8, l'augmentation de la température entraîne le

passage d'une phase transparente bleutée et isotrope à une phase qui a le même aspect au repos, mais qui présente une biréfringence d'écoulement, caractéristique d'une phase bicontinue. Pour des températures plus élevées et sur une gamme de quelques degrés, une phase L_{α} est observée en équilibre avec une phase isotrope, et au-delà de 35°C une émulsion inverse est détectée. La corrélation de ce diagramme avec les courbes de conductivité correspondantes permet d'élucider les différentes structures. Au début, l'augmentation de la conductivité correspond à une émulsion directe (phase continue conductrice), ensuite la chute de conductivité correspond à la phase bicontinue, l'épaule ou le maximum étant associé à une phase L_{α} ou à une phase isotrope, et finalement les valeurs très faibles de la conductivité correspondent à une émulsion inverse (milieu continu non conducteur).

L'échantillon préparé avec un rapport H/TA de 3 et une fraction massique d'eau de 0.7 a été observé en fonction de la température en SAXS et les courbes ont pour les plus grandes valeurs du vecteur de diffusion (q) une loi en q^{-4} . Cette loi est caractéristique d'un changement abrupt de la densité de la longueur de diffusion et correspond ici à la présence d'une interface eau/décane qui est séparée par une monocouche de tensioactif. L'ensemble des courbes de diffusion SAXS corroborent les observations faites sur le diagramme pseudo-Shinoda. Les nano-émulsions sont formées à 5°C et le calcul de la taille, en utilisant la loi de Porod, donne une valeur voisine de 60 nm, qui est du même ordre que celle mesurée par DLS, qui est de 50 nm.

La taille des nano-émulsions préparées en utilisant les deux méthodes PIT et PIC ont été mesurées par DLS. Les résultats montrent que les nano-émulsions formées par la méthode PIC sont systématiquement plus grandes que celles formées par la méthode PIT, mais dans les deux cas la taille augmente avec le rapport H/TA et avec la fraction massique d'eau.

Les nano-émulsions ont été utilisées pour la préparation de matériaux poreux. Après traitement hydrothermal et élimination de la partie organique, la taille des pores est en moyenne de 2-3 μm . Cette taille est considérablement plus grande que celle des nano-émulsions. Ce phénomène est attribué à la coalescence des gouttelettes d'huile qui prend place durant la synthèse des matériaux.

Dans une deuxième étape, un système constitué de nano-émulsions et d'une solution micellaire de Pluronic P123 ont été utilisées pour la synthèse de matériaux silicatés à porosité hiérarchisée. Tout d'abord la concentration en P123 a été fixée à 2.5%, et on a étudié l'effet de la quantité de précurseur de silice (TMOS) sur la synthèse en faisant varier le rapport molaire $n_{\text{P123}}/n_{\text{TMOS}}$. Après traitement hydrothermal et élimination de la phase organique, on a trouvé que le rapport molaire optimal est de 0.0025. Pour ce rapport, le matériau obtenu donne des mésopores ayant un diamètre de 9.3 nm et qui sont organisés en réseau hexagonal. De

plus, des macropores, qui sont l’empreinte des nano-émulsions sont présents et leur taille est de 240 nm. La surface spécifique de ce matériau est de 780 m²/g et le volume poreux de 1.2 cm³/g. Ensuite, la concentration en P123 a été variée entre 0 et 10%, tout en utilisant le rapport molaire optimal (0.0025). Les résultats montrent que la taille des mésopores diminue de 10.2 à 8.6 nm en augmentant la concentration de P123 de 0.5 à 10%, alors que la surface spécifique et le volume poreux restent du même ordre de grandeur. Pour ce qui concerne les macropores, les photos MEB montrent que leur diamètre augmente avec la concentration en P123 en variant typiquement de 0.25 à 10 µm, sachant que la taille des gouttelettes de la nano-émulsion est de 100 nm. Pour mieux comprendre les facteurs qui influencent la taille des macropores on a étudié la stabilité des nano-émulsions en présence de méthanol (produit issu de l’hydrolyse du précurseur de silice) et, conjointement en présence de P123. Les résultats montrent que les nano-émulsions sont stables jusqu’à 10% de méthanol. Au-delà, une augmentation importante de la taille des gouttelettes est observée. D’un autre côté, la présence de micelles de P123 provoque une légère augmentation de la taille des nano-émulsions, de l’ordre de 40 nm, après quelques minutes de mélange, lorsque la solution contient 5% de P123. L’augmentation de taille des gouttelettes est plus prononcée si l’ajout de P123 est plus important. Par mesure de conductivité on a démontré que la PIT augmente avec la quantité de P123, ce qui a participé à l’augmentation de la déstabilisation des nano-émulsions. L’ajout de 18% méthanol (quantité qui correspond à l’alcool libéré lors de l’hydrolyse) au système nano-émulsion/solution micellaire (2.5% P123) engendre une légère augmentation de la taille des nano-émulsions. Le méthanol provoque de modifications de la structure des molécules d’eau, qui sont à proximité du film amphiphile, en favorisant la formation de liaisons hydrogènes et l’hydratation se propage jusque dans la partie hydrophobe du film. Finalement, on a pu conclure que la présence de P123 est cruciale dans cette synthèse à cause de son double rôle : rôle structurant dans la formation des mésopores et rôle stabilisant des gouttelettes des nano-émulsions.

A la suite, les matériaux à porosité hiérarchisée ont été utilisés pour encapsuler un principe actif hydrophobe modèle, le kétoprofène. Le profil de libération de cette molécule a été comparé à celui obtenu à partir des matériaux hybrides. Ces matériaux sont constitués de deux composantes : la première est organique et contient le kétoprofène, et la seconde est minérale, formée par la silice méso-structurée. La libération du kétoprofène à partir du matériau hybride a été étudiée dans des solutions réceptrices à différents valeurs de pH, et les résultats montrent que le kétoprofène est libéré préférentiellement en milieu acide, car il précipite localement dans la matrice. Durant la libération une faible partie du kétoprofène se dissout dans la solution réceptrice car l’équilibre ionique favorise la dissolution du kétoprofène,

qui est piégé dans la matrice, entraînant finalement la libération d'une quantité plus importante de kétoprofène.

Comme le matériau hybride contient du P123, l'effet de la présence du pluronic a été examiné avec des nano-émulsions chargées en kétoprofène, en présence ou non de micelles de P123 dans la solution réceptrice. Dans les deux cas le kétoprofène est libéré plus rapidement à partir des nano-émulsions qu'à partir des matériaux hybrides, mais dans la solution contenant les micelles de P123, le kétoprofène a tendance à se solubiliser au cœur des micelles, lesquelles agissant comme si une force d'aspiration était générée. La plus faible vitesse de libération de ce principe actif enregistrée avec les matériaux hybrides peut être justifiée, par le fait que le kétoprofène se solubilise au cœur des micelles de P123 durant la synthèse du matériau. Ces micelles sont piégées dans la matrice silicatée, inhibant alors la libération du kétoprofène. Pour mieux comprendre le mécanisme de libération, les profils ont été exploités avec les modèles de type : ordre zéro, premier ordre, Higuchi et Korsmeyer-Peppas. Le modèle le plus adapté étant celui de Korsmeyer-Peppas. Il permet d'en déduire que le mécanisme de libération est pseudo-Fickien. La libération est rapide dans un premier temps, puis devient plus lente et durable. Ce comportement rend le matériau hybride intéressant pour la vectorisation de principes actifs, laquelle requiert bien souvent un apport lent et durable de la substance active.

D'un autre côté, la libération kétoprofène à partir du matériau poreux silicaté, dans lequel le kétoprofène a été adsorbé est très limitée (de l'ordre de 8%) et rapide (quelques minutes). Ceci est dû à la faible solubilité du kétoprofène en milieu aqueux. En revanche la libération du kétoprofène en présence de micelles de P123 dans la solution réceptrice augmente le taux de kétoprofène libéré en fonction de la quantité de P123 présente, qui atteint 77% pour seulement 1% de P123. Ce taux est atteint en 40 minutes environ, quelle que soit la concentration en P123. Cette libération rapide est due au caractère hydrophile de la matrice silicatée. Comme pour les matériaux hybrides et les nano-émulsions, les courbes ont été modélisées. Le modèle de Korsmeyer-Peppas est à nouveau celui le plus adapté et suggère un mécanisme de libération pseudo-Fickien.

En conclusion, on a montré que pour tous les systèmes étudiés, la libération adopte un mécanisme pseudo-Fickien. La libération du kétoprofène à partir du matériau hybride est sensible au pH, et pour le matériau silicaté la libération est assistée par les micelles.



Contents lists available at ScienceDirect

Colloids and Surfaces A: Physicochemical and Engineering Aspects

journal homepage: www.elsevier.com/locate/colsurfa

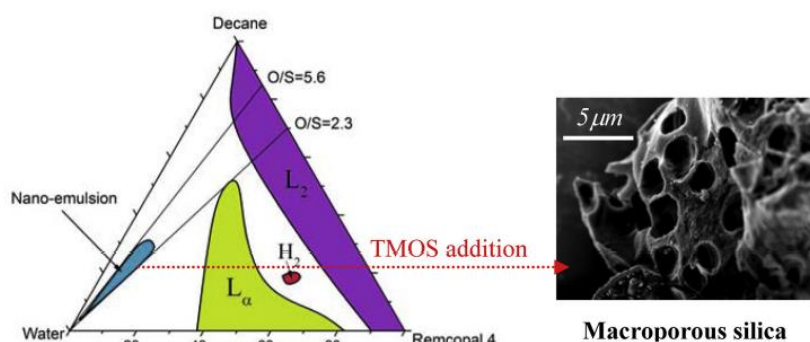
Detailed investigation of nano-emulsions obtained from the Remcopal 4/decane/water system

Philippe Riachy^a, Na Du^{a,b}, Marie-José Stébé^a, Jean-Luc Blin^{a,*}^a Université de Lorraine/CNRS, SRSMC, UMR7565, F-54506 Vandoeuvre-lès-Nancy cedex, France^b Key Laboratory for Colloid Science and Interface Chemistry of Ministry of Education, Shandong University, Jinan 250100, People's Republic of China

HIGHLIGHTS

- Nano-emulsions prepared by the PIT method.
- Structural study by SAXS of the nano-emulsions.
- Macroporous silica material from mineralization of nano-emulsions.

GRAPHICAL ABSTRACT



ARTICLE INFO

Article history:

Received 28 March 2015
 Received in revised form 3 May 2015
 Accepted 4 May 2015
 Available online 11 May 2015

Keywords:

Nano-emulsions
 SAXS investigation
 Phase inversion temperature
 Liquid crystals
 Mineralization

ABSTRACT

We have investigated the phase behavior of the Remcopal 4/decane/water system. Direct lamellar phase (L_{α}), reverse hexagonal (H_2) liquid crystals, and reverse micellar phase L_2 were identified. Then, nano-emulsions have been formulated by the phase inversion temperature (PIT) method and characterized by various techniques such as dynamic light scattering (DLS), nanoparticle tracking analysis (NTA), conductivity, and small angle X-ray scattering (SAXS). For oil/surfactant ratios comprising between 2.3 and 5.7, a domain of nano-emulsion, stable between 20 and 27 °C, which extend up to 95 wt.% of water, is formed. The size of nano-emulsions is around 100 nm of diameters. It increases with the oil/surfactant ratio. The conductivity and the SAXS analyzes show that there is a strong relation between the joint presence of a dispersion of the lamellar phase L_{α} , the sponge phase L_3 , and the formation of the nano-emulsions.

Finally, the obtained nano-emulsions have been used as building blocks to prepare porous silica. Surprisingly, materials with a pore size in the micrometer range have been recovered.

© 2015 Elsevier B.V. All rights reserved.

1. Introduction

Nano-emulsions are emulsions consisting of small mono-disperse droplets, typically in the 20–200 nm size range, which are

often referred to in the literature also as mini-emulsions, ultrafine emulsions, submicron emulsions [1–6]. Although they could have similar size like microemulsion droplets and appear transparent or translucent, they are in fact quite different from true microemulsions [7]. Nano-emulsions are thermodynamically unstable and their formation generally requires energy input. The properties of nano-emulsions depend not only on thermodynamic conditions (i.e., composition, temperature, and pressure), but also on

* Corresponding author. Tel.: +33 3 83 68 43 70.

E-mail address: Jean-Luc.Blin@univ-lorraine.fr (J.-L. Blin).

the preparation method and crucially, on the order of component addition. Among the different preparation methods, low-energy ones constitutes a field of growing interest [8–10]. These methods make use of accessible phase transitions occurring during the emulsification process as a result of changes in surfactant film spontaneous curvature. According to this process, the formation of nano-emulsions is obtained by the phase inversion temperature method (PIT) [11–13], phase inversion composition method (PIC) [14,15], or self-emulsification method [9,10,16]. To make use of these approaches, it is necessary to know in detail the phase behavior of the considered surfactant/oil/water system. Concerning the nano-emulsions formation with the PIT method, emulsions are obtained by increasing then lowering the temperature quickly to pass through the PIT, whereas for the PIC method, the continuous phase is added to the dispersed phase at constant temperature until phase inversion occurs and the intended emulsion type is formed. Concerning the self-emulsifying method, the dispersed phase is simply added to the continuous phase under intensive agitation. The kinetic stability of nano-emulsions and their transparent or translucent appearance due to the presence of nanometer-sized droplets makes these systems interesting for fundamental studies as well as for practical applications, such as the preparation of polymeric nanoparticles, agrochemical applications, food technology, pharmaceutical, and cosmetic fields [9,16–19]. Another application that may be considered for nano-emulsions is their use as imprints to prepare porous silica materials. Indeed, one way to design porous materials consists of combining the sol-gel chemistry and the use of surfactant molecule assemblies as templates to create the pore network. Depending on the structure of the initial system, microporous, mesoporous, or macroporous materials are recovered [20–26]. For example, by this way mesoporous and macroporous materials can be synthesized from micelles [20–22] and emulsions [24–26], respectively. Until now, the use of nano-emulsions to template porous materials has been barely reported in literature. Here in this study, we have investigated the ability of the Remcopal 4/decane/water system to form nano-emulsions that can be used as imprint for the synthesis of porous materials. First we have explored the system based on commercial surfactant Remcopal 4 and to better control the general conditions for obtaining nano-emulsions, we have in particular focused on the cosolubilization properties of water and decane in relation with the structural properties. The formulated nano-emulsions have been characterized in detail. Then, we have performed some experiments to prepare porous materials.

2. Materials and methods

Remcopal 4 (commercial name) was provided by CECA, a company that no longer exists nowadays. It is a technical grade surfactant, whose formula mainly consists of a hydrogenated carbon chain with 12 carbons and the average number of oxyethylene is 4. It is noted as $C_{12}(EO)_4$. The triblock copolymer P123 $(EO)_{20}(PO)_{70}(EO)_{20}$ and decane were purchased from Aldrich. Deionized water was used to prepare the various samples.

Phase diagram: The phase diagram has been established by preparing samples over the whole range of surfactant/water compositions. The required amounts of surfactant, decane, and water were introduced into well-closed glass vials to avoid evaporation. The homogenization of the samples was achieved by mixing with a vortex stirrer, combined with heat and ultrasounds, whenever necessary. The samples were placed in a thermostatic bath for several hours at 20 °C in order to reach equilibrium. The different phases were identified by visual inspection with a polarizing light microscope (Olympus BX 50). The boundaries lines of the liquid crystal

domains were delimited by Small Angle X-ray Scattering (SAXS) experiments.

2.1. Characterization of liquid crystals, nano-emulsions

SAXS measurements were carried out using a SAXSess mc2 (Anton Paar) apparatus. It is attached to a ID 3003 laboratory X-ray generator (General Electric), equipped with a sealed X-ray tube (PANalytical, $\lambda_{Cu(K\alpha)} = 0.1542$ nm, $V = 40$ kV, $I = 50$ mA). A multilayer mirror and a block collimator provide a monochromatic primary beam. A translucent beam stop allows the measurement of an attenuated primary beam at $q = 0$. Nano-emulsions are placed in a Quartz capillary, having a diameter of 1 mm, whereas liquid crystals are put in a paste cell, before being placed inside an evacuated chamber equipped with a temperature-controlled sample holder unit. Acquisition times are typically in the range of 20 min–1 h. Scattering of X-ray beam is recorded by a CCD detector (Princeton Instruments, 2084×2084 pixels array with $24 \times 24 \mu\text{m}^2$ pixel size) in the q range 0.03 – 5 nm⁻¹. The detector is placed at 309 mm from the sample holder. Concerning the nano-emulsions, the data were corrected for the background and the solvent (water) scattering. The scattering intensities were evaluated on an absolute scale using water as reference.

A Malvern zetasizer 3000HSA instrument was used to measure the size of the nano-emulsions in water by dynamic light scattering. The helium–neon laser, 5 mW operates at 633 nm, with the scatter angle fixed at 90°. The sample is contained in a flow-through cell kept at 25 °C. All the measurements were performed in the suitable conditions by systematically diluting three times the samples with water to validate the results. Water was first filtered with a mixed cellulose ester (surfactant free) filter (0.45 μm). The attenuator (diaphragm) of the photomultiplier was automatically adapted for each sample in order not to saturate the detector. The data were analyzed by the CONTIN method and the size was provided by an intensity distribution.

The sizes of the nano-emulsions were also determined by NTA (Nanoparticle Tracking Analysis). This technique combines laser light scattering microscopy with a CCD camera, which enables the visualization and recording of nanoparticles in solution. The NTA software is then able to identify and track individual particles moving under Brownian motion. NTA measurements were performed with a NanoSight NS300 of Malvern equipped with a sample chamber and a 635 nm laser. The microscope objective (x20 magnification) fitted to a conventional microscope onto which is mounted a CCD camera. The samples were diluted approximately 10^6 times and were injected in the sample chamber with syringes. The measurements are recorded for 90 s.

A radiometer analytical CDM210 conductivity meter apparatus equipped with a CDC641T conductivity cell was used to determine the phase inversion temperatures (PIT) using an electrolyte solution ($\text{NaCl } 10^{-2} \text{ mol L}^{-1}$) instead of pure water. The sample and the conductivity probe are placed in a thermostatic container. The conductivity was measured as a function of the temperature and depending on the recorded conductivity the temperature was varied by increment of 1–5 °C. For each increase of temperature, the conductivity was measured after stabilization of its value, indicating the equilibrium of the sample. According to the relevant phase, the equilibrium times varied from 10 to 30 min.

3. Results and discussion

3.1. The Remcopal 4/decane/water phase diagram

Remcopal 4 is a commercial surfactant mainly composed of $C_{12}(EO)_4$. However, its phase behavior in water (Fig. 1) is

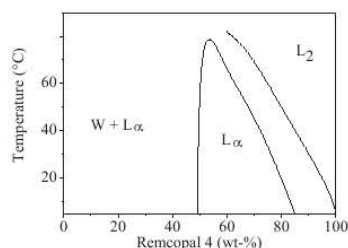


Fig. 1. Temperature-composition phase diagram of Remcopol 4 in water.

different from the pure $C_{12}(EO)_4$ [27]. The phase diagram of non-ionic surfactant is very sensitive to the presence of additives and to the molecular structure of the surfactant, so this result is not surprising since the number of the oxiethylene unit is not exactly 4, it can be represented by a Gaussian distribution centered on 4. Unlike the system with the pure $C_{12}(EO)_4$, whose phase diagram shows a lower consolute temperature of 4°C, in water the Remcopol 4 does not exhibit a cloud point curve. Moreover, the bicontinuous phase L_3 observed for the pure $C_{12}(EO)_4$ has not been detected in the Remcopol 4/water diagram. The addition of decane has not really increased the polymorphism. The ternary phase diagram, established at 20°C (Fig. 2), presents similarities with the one reported by Forgiarini et al. [14] for the Brij 30-based system. Brij 30 is also a technical grade surfactant, which according to the manufacturer is close to the pure $C_{12}(EO)_4$. For Remcopol 4, between the lamellar phase (L_α) and the isotropic phase L_2 we have also detected a reverse hexagonal phase (H_2), which is not detected when decane is solubilized in the Brij 30 or in the pure $C_{12}(EO)_4$ surfactants. The lamellar phase has incorporated up to 50.0 wt.% of decane for a water/Remcopol 4 weight ratio (R_w) of 1. No thermodynamically stable direct structure has been evidenced in the Remcopol 4/decane/water phase diagram. The structural parameters of the lamellar phase have been determined for various values of R_w as a function of the amount of solubilized oil. In a lamellar phase, the repetition distance (d_{001}) corresponds to the layer spacing between the water and oil films separated by the surfactant bilayer. As we can expect, an increase of the repetition distance is noted both with R_w and with the loading of decane (Fig. 3). The increase of R_w reflects the greater presence of water, which hydrates the polar head group and the excess forms a more and more dense film surrounding the surfactant head groups. Concerning decane, it forms a film of oil, which becomes thicker with decane loading, between the hydrophobic chains. Based on geometrical considerations the cross-sectional area (S) and the hydrophobic thickness (d_B) can be

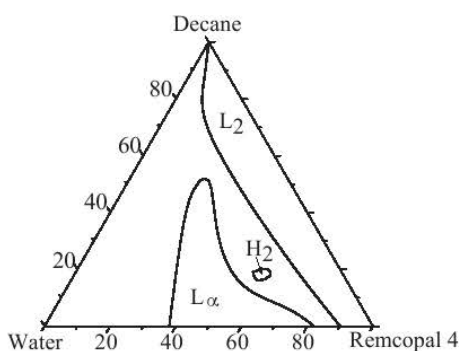


Fig. 2. Temperature-composition phase diagram (wt.%) of Remcopol 4/decane/water system at 20°C.

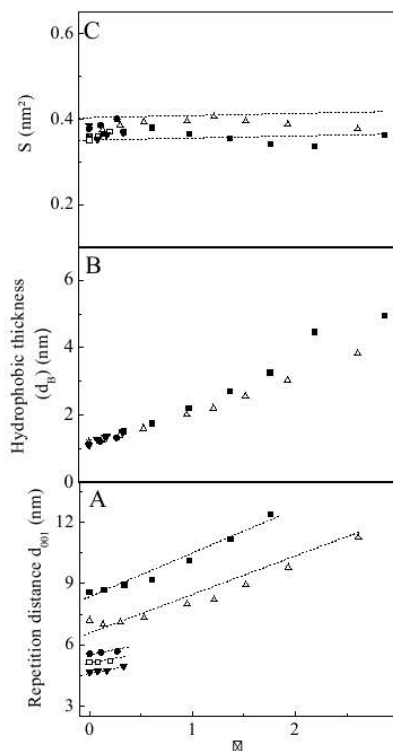


Fig. 3. Remcopol 4/decane/water system: Variation of the repetition distance (d_{001}) (A), the hydrophobic thickness (d_B) (B) and the cross-sectional area (S) (C) as a function of β , the number of decane molecules per surfactant molecule for different water/Remcopol 4 ratios (R_w) [■: $R_w = 1.5$; △: $R_w = 1$; ●: $R_w = 0.67$; □: $R_w = 0.43$ and ▼: $R_w = 0.25$].

calculated from the repetition distance (d_{001}), obtained by SAXS, according the following formulas [28]:

$$S = \frac{2(V_S + \alpha V_W + \beta V_O)}{N d_{001}} \quad d_B = \frac{2(V_B + \beta V_O)}{S}$$

where α stands for the number of water molecules per surfactant molecule and β stands for the number of oil molecules per surfactant molecule; V_B , V_S , V_W , and V_O , respectively stand for the molar volumes of the hydrophobic part of the surfactant ($V_B = 222.5 \text{ cm}^3/\text{mol}$), the surfactant ($V_S = 618.1 \text{ cm}^3/\text{mol}$), the water ($V_W = 18 \text{ cm}^3/\text{mol}$) and the decane ($V_O = 194 \text{ cm}^3/\text{mol}$). N is the number of Avogadro.

Results show that d_B is a linear function of the decane molecules per surfactant molecule (β) and within experimental error it is almost independent on the R_w ratio. The cross-sectional area is slightly sensitive to both decane incorporation and R_w ratio. S values range from 0.35 to $0.38 \pm 0.1 \text{ nm}^2$ (Fig. 3). The hydrophobic character, the formation of the lamellar phase, which can appreciably swell in the presence of decane make the Remcopol 4/decane/water system suitable for the preparation of nano-emulsions using either the phase inversion temperature (PIT) [11–13,29] or the phase inversion composition (PIC) methods. PIT is based on the changes in surfactant spontaneous curvature induced by the temperature, whereas for PIC, the phase transitions are induced by changes in the composition during emulsification, at constant temperature [15,30].

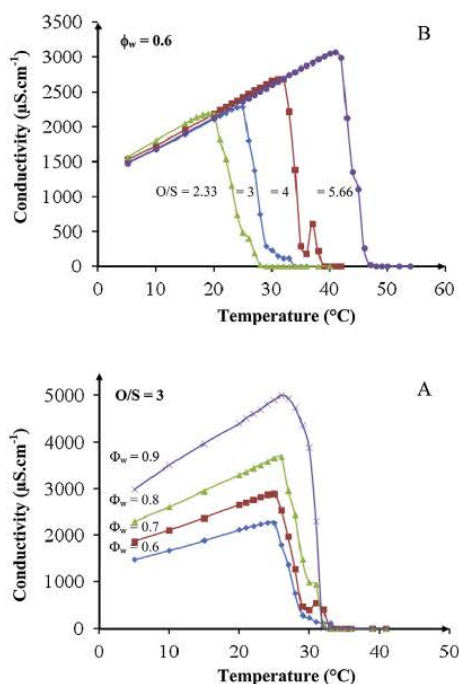


Fig. 4. Conductivity of the emulsion as a function of the temperature at different salt water weight fractions (ϕ_w) for a constant $O/S = 3$ (A) and at different O/S ratios for a constant $\phi_w = 0.6$ (B).

3.2. Formation and characterization of the nano-emulsions

Nano-emulsions have been prepared according to the PIT and the PIC methods. For the PIT method, the phase inversion temperature has to be known. To determine the domain of the emulsion phase inversion, conductivity measurements have been performed as a function of the temperature by substituting water with a $10^{-2} \text{ molL}^{-1}$ sodium chloride solution. As the phase inversion depends on the surfactant concentration and on the volume fractions of both oil and water [31], the experiments have been performed for several oil/surfactant ratios (O/S) and for 4 water weight fractions. Samples have been prepared by mixing at room temperature the oil, the surfactant and the salt water with a vortex to get a homogeneous solution. Then samples have been placed at 5°C to start the conductivity measurements and increased up to temperatures in the range of $40\text{--}55^\circ\text{C}$, depending on the O/S ratio. Results are depicted in Fig. 4. All the curves present the same trend and the Remcopal 4/decane/water system behaves in a similar way as other systems reported in literature [11,12,14]. At low temperature, the conductivity is high, meaning that the continuous phase is aqueous. As expected by applying the Bruggeman law [32], the starting values increase from 1500 to $3000 \mu\text{S cm}^{-1}$ when the water weight fractions (ϕ_w) vary from 0.6 to 0.9 . When the temperature increases the conductivity also increases until a maximum, which depends more strongly on the O/S ratio than on ϕ_w . However, before reaching the maximum, the conductivity values are not significantly affected by the O/S ratio. Then over a range of $4\text{--}5^\circ\text{C}$, the conductivity sharply drops to attain few $\mu\text{S cm}^{-1}$, indicating that the continuous phase is oily. This phenomenon is characteristic of the phase inversion and the related temperature is the phase inversion temperature (PIT), which is usually determined at the inflection point. Except the curve corresponding to $\phi_w = 0.9$ and $O/S = 3$, which presents a typical phase inversion around 31°C , it should be noted that other curves exhibit either a shoulder or

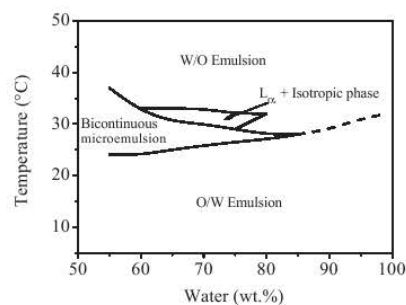


Fig. 5. Pseudo-Shinoda phase diagram established according to the temperature and to the weight fraction of water for the sample prepared with a O/S ratio of 3.

a true maximum. This phenomenon has already been observed by other groups [11,14,33]. These discontinuous variations of the conductivity are associated with the existence of different structures (bicontinuous L_3 phase and liquid crystals) formed by changing the temperature.

To map the possible structures for the investigated system, pseudo-Shinoda type diagrams [34] have been established. This method consists in looking at the solubilization of water at a function of temperature for a given O/S ratio. As an example, the diagram obtained for an O/S ratio of 3 and for weight fraction of water is comprised between 0.55 and 0.95 is reported in Fig. 5. At low temperatures and up to 25°C oil in water (O/W) emulsions are formed. Then, increasing the temperature on a range of about 5°C and for water weight fraction from 0.60 to 0.80 the solutions become transparent and are optically isotropic at rest, but they exhibit flow birefringence upon shaking, reflecting the presence of a bicontinuous system that we labeled bicontinuous microemulsion, for which the two continuous mediums are the water and the oil. This label allows differentiating with the L_3 phases, where the system is assumed to be comprising an interconnected infinite bilayer sheet, separating the space into two regions of the same nature (either water or oil) [35]. At higher temperatures but only on a span of a few degrees, the solutions are birefringent and some Maltese crosses are detected by polarized optical microscopy. The texture observed is characteristic of the defects of the lamellar phase, the latter being in equilibrium with an isotropic phase. This area is transitional to the reverse emulsion domain observed above about 35°C .

The Shinoda's diagrams can be correlated to the obtained conductivity curves. For example, for the system prepared with $\phi_w = 0.7$ and $O/S = 3$ (Fig. 6A), the variation of the conductivity can be associated with the appearance of different structures. Indeed, the high conductivity between 5 and 25°C corresponds to oil in water emulsion. Above 25°C , the conductivity starts to decrease until 29°C and a bicontinuous microemulsion is evidenced in this range of temperature. Then at 30°C , a slight increase of the conductivity is noted until 31°C and coincides with a domain where an isotropic phase is in equilibrium with the lamellar phase. Above 33°C , the very low conductivity and the milky aspect of the solution are in accordance with the presence of reverse water-in oil-emulsions.

The evolution of the structures with the temperature has also been followed by SAXS. The scattering curves evaluated on an absolute scale and plotted on a log-log scale in Fig. 6B have been reordered in function of temperature with $\phi_w = 0.7$ and $O/S = 3$. At high q , the intensity is sensitive to scattering from local interfaces. From $q = 0.1 \text{ nm}^{-1}$, the overall curves shown a q^{-4} decay over one decade, characteristic of an abrupt change of scattering length density. The nano-emulsions obtained at low temperature (from 22 to 26°C) fulfill this criterion, since the interface between oil and water is formed by only one layer of surfactant. This q^{-4} variation for nano-emulsions has previously been evidenced from SANS (small

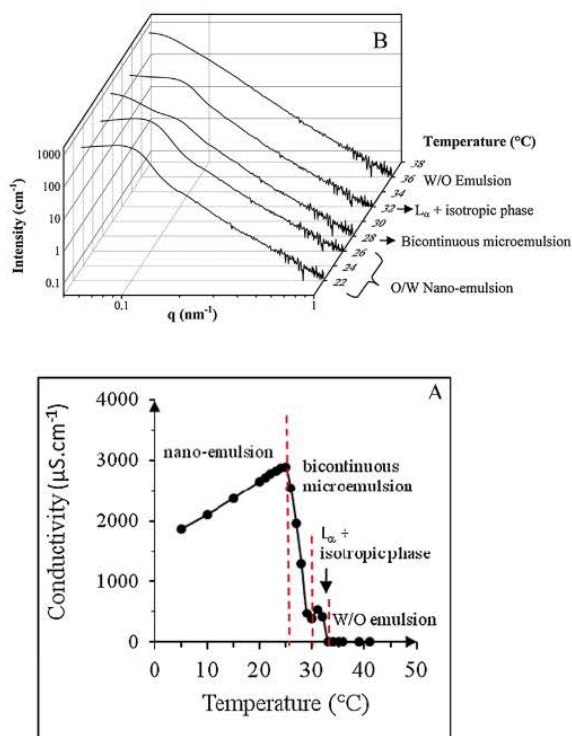


Fig. 6. Conductivity (A) and SAXS pattern (B) as a function of temperature. The sample has been prepared with an O/S ratio of 3 and $\phi_w = 0.7$.

angle neutron scattering) by Dong et al. [10] and Mason et al. [2]. The increase of temperature involves a change in the SAXS spectrum at low q values, corresponding to the formation of the bicontinuous microemulsion. As aforementioned, these kinds of systems are constituted of intertwining water and oil channels, which are separated by a surfactant film. As reported by Strey et al. in 1991 [36], the SAXS intensity varies as q^{-4} , since the interface of the bicontinuous microemulsions, separating the aqueous and oily domains, which have different scattering lengths, consisting in a monolayer. By contrast, in the L_3 phase, the interface between the two aqueous domains, which have the same scattering length, is constituted of a surfactant bilayer and the SAXS intensity varies as q^{-2} . A broad peak centered at $q_c = 0.083$ is evidenced on a plot in a linear scale of the intensity of the bicontinuous microemulsions. The characteristic length $L = 2\pi/q_c$ represents the size between the centers of two adjacent channels. The L value is found to be equal to 70 nm. Further increasing the temperature, the profile of the spectrum recorded at 32 °C changes again and it corresponds to the system for which a lamellar phase is in equilibrium with an isotropic phase. Finally, since 36 °C a coarse water-in-oil emulsion is formed and the intensity monotonically decreases as a function of q^{-4} .

The droplets size of nano-emulsions can be determined using the Porod law [37]:

$$I(q) = \frac{2\pi S_V (Q_{ext} - Q_{int})^2}{q^4}$$

where S_V is the area per unit volume of dispersion, Q_{ext} and Q_{int} are the scattering length densities of the continuous phase (water) and internal phase (decane), respectively. From S_V a mean value of the radius (R) of the droplets can be derived from the following formula $R = 3\Phi/S_V$ where Φ is the dispersed volume fraction. For example, applying the above equation, the radius of the oil droplets

Table 1

PIT values in function of oil/surfactant ratio (O/S) for $\phi_w = 0.6$ and the water weight fraction (ϕ_w) for O/S = 3.

O/S	2.3	3.0	4.0	5.7
PIT (°C)	23	26	34	44
ϕ_w	0.6	0.7	0.8	0.9
PIT (°C)	26	27	29	31

of the nano-emulsions prepared with O/S = 3 and $\phi_w = 0.7$ is equal to 62 nm. By comparison, the size obtained by DLS, given below in Fig. 8, is in the same order, since the radius for this formulation is found equal to 50 nm.

The PIT values, gathered in Table 1 as a function of both the O/S ratio and ϕ_w , have been determined from the conductivity curves (Fig. 4). The phase inversion is delayed when the quantity of surfactant decreases (higher O/S ratio). For example, the PIT value is 26 °C for O/S = 3 against 44 °C for O/S = 5.7. The phase inversion phenomenon of the emulsions prepared with a O/S ratio of 3 and water weight fraction comprised between 0.6 and 0.9 starts in a limited range of temperature (between 26 and 31 °C) and the PIT values, deduced from the graph in Fig. 4A, increase from 27 to 32 °C with ϕ_w .

The nano-emulsions domain, as a function of temperature, has first been determined by the PIT method. Knowing the PIT values, samples have been prepared with different O/S ratios (from 2.3 to 9.0) and starting with a water weight fraction of 0.55. The samples are placed at temperature of 10 degrees above the PIT and then they are quenched at 5 °C. The bluish or gray aspect of the isotropic solution is a characteristic of the presence of the nano-emulsions. The limit of the nano-emulsion existence is found by increasing of temperature. Similar experiments are performed with higher quantities of water to cover the overall water-rich zone of the diagram. Fig. 7 shows that nano-emulsion exist between 20 and 27 °C and that the domain is bordered by oil/surfactant ratios 2.3 and 5.7 and can extend from 65 to 95 wt.% of water, depending on temperature. It should be noted that the nano-emulsions region corresponds to the oil in water emulsions domain on the pseudo-Shinoda diagram (Fig. 5). The PIC method has also been used to prepare the nano-emulsions at a constant temperature (20 °C). In this case, reverse micellar phase L_2 are prepared by mixing decane with the Remco-pal 4. Successively, a reverse microemulsion, an anisotropic viscous phase, a white emulsion and finally bluish solutions appear with the progressive addition of water. O/S ratios comprised between 2.3 and 9.0 have been investigated, but the nano-emulsion region detected by using the PIC method is limited to O/S ratio in the range 2.3–4.0 and to water weight fraction higher than 0.75.

The size of the nano-emulsions has been determined by DLS. A first series of nano-emulsions have been prepared at constant $\phi_w = 0.85$ by varying the O/S ratio from 2.3 to 5.7, when the PIT method has been used or from 2.3 to 4.0 when nano-emulsions have been obtained from the PIC method. Before DLS experiments, each

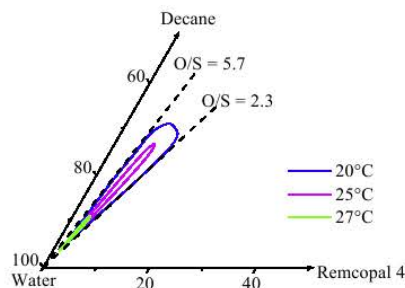


Fig. 7. Existence domain of the nano-emulsions.

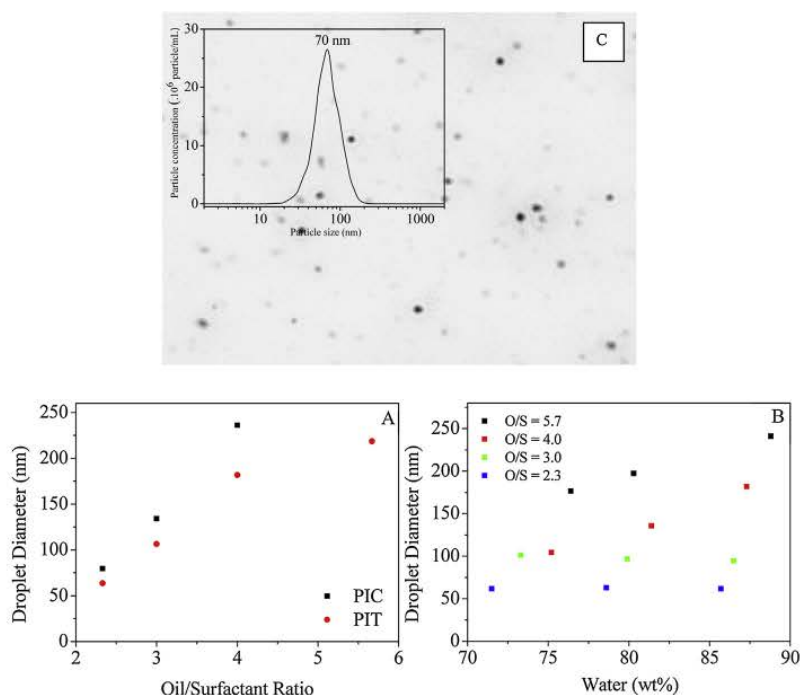


Fig. 8. Size of the nano-emulsions obtained at 25 °C by DLS as a function of both the O/S ratio (A) and of the water weight fraction (B) and by NTA size (C). The nano-emulsions have been prepared by the PIT method (B and C).

sample has been diluted with water to get system for which the inter-particle interactions are negligible. The sizes of the nano-emulsions obtained from PIC are systematically higher than the ones obtained from the PIT method (Fig. 8A); however, in the two cases the size increases with the oil/surfactant ratio. The minimum size reached is around 50 nm. In a second time, nano-emulsions have been prepared only from the PIT method. The water weight fraction has been varied from 0.73 to 0.88 and several O/S ratios have been considered. The DLS measurements have been performed after simple dilution with water, as made for the first set of experiments. Results indicate that the size of the nano-emulsions might depend on the quantity of water used for their preparation, in particular for the highest ratios (Fig. 8B). Nonetheless, once prepared their sizes remain unchanged with dilution. We again see that the size of the nano-emulsions increases with the O/S ratio. The size of the nano-emulsions was also determined by nanoparticle tracking analysis. By this technique, the particles size is around

70 nm for the sample prepared with an O/S ratio equal to 3 and 74.3 wt.% of water (Fig. 8C). It should be noted that contrary to DLS, which provides a repartition in intensity, NTA gives a number size distribution. As a consequence, in comparison with DLS, NTA size distributions were usually shifted toward smaller sizes.

3.3. Mineralization

The detailed investigation of the structural properties of the Remcopal 4-based system, shows that the proximity of the bicontinuous microemulsions and a dispersion of the lamellar phase participates to the oil in water (O/W) nano-emulsions formation. These structural characterizations support the suggestion made by the Solans' group based on the phase equilibrium in nano-emulsions in relation with the hydrophilic–hydrophobic balance (HLB) temperature. The authors suggest that the mean requirement for O/W nano-emulsions formation is the complete

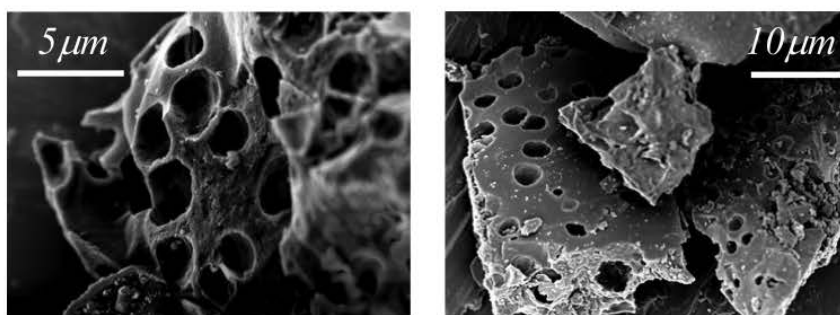


Fig. 9. SEM images of the obtained porous material.

solubilization of the oil component in a bicontinuous microemulsion [38]. Nonetheless, it is still difficult to make a difference between the domain of the bicontinuous microemulsion and the one of the nano-emulsions, since both have a bluish aspect. The conductivity results associated with the SAXS experiments allow distinguishing these two types of systems and to be sure of the presence of nano-emulsions, which have been used as imprints to synthesize porous materials. First, we have prepared nano-emulsions containing 80 wt.% of water with a Remcopal 4/decane ratio equals to 0.25. Then, tetramethoxysilane (TMOS), used as the silica source, has been added to the mixture at 25 °C at pH=2. The Remcopal 4/TMOS molar ratio is fixed to 0.5. The obtained mixture was sealed in Teflon autoclaves and allowed to undergo hydrothermal treatment at 80 °C for 48 h. The final material was recovered after ethanol extraction with a Soxhlet apparatus for 48 h. SEM images recorded with a HITACHI S-2500 at 15 keV shows that the pores have diameters in the range of few microns (Fig. 9). It should be noted that the size of the pores is higher than one of the droplets of the nano-emulsion. This can be attributed to a coalescence of the droplets that can take place during the material synthesis. This phenomenon is in accordance with what it is observed during the mineralization of others imprints such a solid lipid nanoparticles, emulsions or double emulsions [39–41].

4. Conclusion

In this study, we have investigated the Remcopal 4/decane/water system. First, we have delimited the domains of the various phases and we have shown that the hydrophobic thickness and the cross section of the lamellar liquid crystal phase increase with the addition of decane. The phase inversion temperature has been determined by conductivity measurements and the values of PIT varying from 23 to 44 °C, depending on both the oil/surfactant ratio and water fraction considered. The nano-emulsions have been prepared from the Remcopal 4/decane/water system according to the PIT and PIC methods. The nano-emulsions exist between 20 and 27 °C and the domain is bordered by oil/surfactant ratios 2.3–5.7 for water weight fractions that can extend from 0.65 to 0.95. The conductivity measurements performed in parallel with SAXS analysis show that the presence of the bicontinuous microemulsion phase as well as the dispersion of the lamellar phase are associated to the nano-emulsions formation. The SAXS spectra show for all of these systems q^{-4} decay over one decade but the diffusion at the lower q is distinct. The radius of the nano-emulsion determined by SAXS, 62 nm, is in the same order of value than the one obtained from DLS analysis (50 nm). Nanoparticle tracking analysis allows visualizing the nano-emulsions and gives a number size distribution of 70 nm. Finally, the nano-emulsions have been used as imprints to prepare macroporous silica.

References

- [1] C. Solans, P. Izquierdo, J. Nolla, N. Azemar, M.J. García-Celma, Nano-emulsions, *Curr. Opin. Colloid Interface Sci.* 10 (2005) 102–110.
- [2] T.G. Mason, J.N. Wilking, K. Meleson, C.B. Chang, S.M. Graves, Nanoemulsions: formation, structure, and physical properties, *J. Phys.: Condens. Matter* 18 (2006) R635–R666.
- [3] M.Y. Koroleva, E.V. Yurtov, Nanoemulsions: the properties, methods of preparation and promising applications, *Russ. Chem. Rev.* 81 (2012) 21–43.
- [4] R. Pons, I. Carrera, J. Caelles, J. Rouch, P. Panizza, Formation and properties of miniemulsions formed by microemulsions dilution, *Adv. Colloid Interface Sci.* 106 (2003) 129–146.
- [5] S. Sajjadi, Effect of mixing protocol on formation of fine emulsions, *Chem. Eng. Sci.* 61 (2006) 3009–3017.
- [6] D.J. McClements, Nanoemulsions versus microemulsions: terminology, differences, and similarities, *Soft Matter* 8 (2012) 1719–1729.
- [7] K. Landfester, Polyreactions in miniemulsions, *macromol. Rapid Commun.* 22 (2001) 896–936.
- [8] C. Solans, I. Solé, Nano-emulsions. Formation by low-energy methods, *Curr. Opin. Colloid Interface Sci.* 17 (2012) 246–254.
- [9] L. Wang, X. Li, G. Zhang, J. Dong, J. Eastoe, Oil-in-water nanoemulsions for pesticide formulations, *J. Colloid Interface Sci.* 314 (2007) 230–235.
- [10] L. Wang, K.J. Mutch, J. Eastoe, R.K. Heenan, J. Dong, Nanoemulsions prepared by a two-step low-energy process, *Langmuir* 24 (2008) 6092–6099.
- [11] P. Izquierdo, J. Esquena, Th.F. Tadros, C. Dederen, M.J. Garcia, N. Azemar, C. Solans, Formation and stability of nano-emulsions prepared using the phase inversion temperature method, *Langmuir* 18 (2002) 26–30.
- [12] N. Anton, P. Gayet, J.P. Benoit, P. Saulnier, Nano-emulsions and nanocapsules by the PIT method: an investigation on the role of the temperature cycling on the emulsion phase inversion, *Int. J. Pharm.* 344 (2007) 44–52.
- [13] S.L. Ee, X. Duan, J. Liew, Q.D. Nguyen, Droplet size and stability of nano-emulsions produced by the temperature phase inversion method, *Chem. Eng. J.* 140 (2008) 626–631.
- [14] A. Forgiarini, J. Esquena, C. González, C. Solans, Formation of nano-emulsions by low-energy emulsification methods at constant temperature, *Langmuir* 17 (2001) 2076–2083.
- [15] A. Maestro, I. Solé, C. González, C. Solans, J.M. Gutiérrez, Influence of the phase behavior on the properties of ionic nanoemulsions prepared by the phase inversion composition method, *J. Colloid Interface Sci.* 327 (2008) 433–439.
- [16] L. Wang, J. Dong, J. Chen, J. Eastoe, X. Li, Design and optimization of a new self-nanoemulsifying drug delivery system, *J. Colloid Interface Sci.* 330 (2009) 443–448.
- [17] N. Sadurni, C. Solans, N. Azemara, M.J. Garcia-Celma, Studies on the formation of O/W nano-emulsions, by low-energy emulsification methods, suitable for pharmaceutical applications, *Eur. J. Pharm. Sci.* 26 (2005) 438–445.
- [18] M. Jaworska, E. Sikora, M. Zielina, J. Ogonowski, Studies on the formation of O/W nano-emulsions, by low-energy emulsification method suitable for cosmetic applications, *Acta Biochim. Pol.* 60 (2013) 779–782.
- [19] N. Anton, J.P. Benoit, P. Saulnier, Design and Production of Nanoparticles Formulated from Nano-Emulsion Templates—A Review, *J. Controlled Release* 128 (2008) 185–199.
- [20] Y. Wan, D. Zhao, On the controllable soft-templating approach to mesoporous silicates, *Chem. Rev.* 107 (2007) 2821–2860.
- [21] J.L. Blin, M.J. Stébé, Effect of fluorocarbon addition on the structure and pore diameter of mesoporous materials prepared with a fluorinated surfactant, *Microporous Mesoporous Mater.* 87 (2005) 67–76.
- [22] J.L. Blin, A. Léonard, B.L. Su, Well-ordered spherical mesoporous materials CMI-1 synthesized via an assembly of decaoxyethylene cetyl ether and TMOS, *Chem. Mater.* 13 (2001) 3542–3553.
- [23] J.L. Blin, A. Léonard, Z.Y. Yuan, L. Gigot, A. Vantomme, A.K. Cheetham, B.L. Su, Hierarchically mesoporous/macroporous metal oxides templated from polyethylene oxide surfactant assemblies, *Angew. Chem. Int. Ed.* 42 (2003) 2872–2875.
- [24] B.P. Binks, Macroporous silica from solids-stabilized emulsion templates, *Adv. Mater.* 14 (2002) 1824–1827.
- [25] C. Zhao, E. Danish, N.R. Cameron, R. Katak, Emulsion-templated porous materials (polyHIPEs) for selective ion and molecular recognition and transport: applications in electrochemical sensing, *J. Mater. Chem.* 17 (2007) 2446–2453.
- [26] S. Zhang, J. Chen, Synthesis of open porous emulsion-templated monoliths using cetyltrimethylammonium bromide, *Polymer* 48 (2007) 3021–3025.
- [27] J. Mitchell, G.J.T. Tiddy, L. Waring, T. Bostock, M.P. McDonald, Phase Behaviour of polyoxyethylene surfactants with water mesophase structures and partial miscibility (cloud points), *J. Chem. Soc.: Faraday Trans. 1* 79 (1983) 975–1000.
- [28] M. Alibrahim, M.J. Stébé, G. Dupont, J.C. Ravey, Effect of an ionic surfactant on the phase behavior of a nonionic surfactant-based system, *J. Chim. Phys. Phys. Chim. Biol.* 94 (1997) 1614–1633.
- [29] T. Tadros, P. Izquierdo, J. Esquena, C. Solans, Formation and stability of nano-emulsions, *Adv. Colloid Interface Sci.* 108–109 (2004) 303–318.
- [30] N. Usón, M.J. Garcia, C. Solans, Formation of water-in-oil (W/O) nano-emulsions in a water/mixed non-ionic surfactant/oil systems prepared by a low-energy emulsification method, *Colloids Surf. A: Physicochem. Eng. Aspects* 25 (2004) 415–421.
- [31] K. Shinoda, S. Friberg (Eds.), *Emulsions and Solubilization*, John Wiley & Sons, New York, 1986.
- [32] V.D.A.G. Bruggeman, Calculation of various physical constants from heterogeneous substances, *Ann. Phys.* 24 (1935) 636–679.
- [33] P.L. Klassen, Z. George, J. Warwick, S. Georgiadou, PIT tuning effects of hydrophobic co-surfactants and drugs, *Colloids Surf. A: Physicochem. Eng. Aspects* 455 (2014) 1–10.
- [34] K. Shinoda, T. Ogawa, The solubilization of water in nonaqueous solutions of nonionic surfactants, *J. Colloid Interface Sci.* 24 (1967) 56–60.
- [35] N. Lei, C.R. Safinya, D. Roux, K.S. Liang, Synchrotron X-ray studies on the dodecyl sulfate-water-pentanol-dodecane L_3 sponge phase, *Phys. Rev. E* 56 (1997) 608–613.
- [36] R. Strey, J. Winkler, L. Magid, Small angle neutron scattering from diffuse interfaces. 1. mono- and bilayers in the water-octane- $C_{12}E_5$ system, *J. Phys. Chem.* 95 (1991) 7502–7507.
- [37] G. Porod, in: O. Glatter, O. Kratky (Eds.), *Small Angle X-ray Scattering*, Academic Press, 1982, pp. 17–51.
- [38] D. Morales, J.M. Gutiérrez, M.J. Garcia-Celma, Y.C. Solans, A Study of the relation between bicontinuous microemulsions and oil/water nano-emulsion formation, *Langmuir* 19 (2003) 7196–7200.
- [39] R. Ravetti-Duran, J.L. Blin, M.J. Stébé, C. Castel, A. Pasc, Tuning the morphology and the structure of hierarchical meso-macroporous silica by dual templating with micelles and solid lipid nanoparticles (SLN), *J. Mater. Chem.* 22 (2012) 21540–21548.

- [40] J.L. Blin, J. Jacoby, S. Kim, M.J. Stébé, N. Canilho, A. Pasc, A meso-macro compartmentalized bioreactor obtained through silicalization of “green” double emulsions. W/O/W and W/SLNs/W, *Chem. Commun.* 50 (2014) 11871–11874.
- [41] J.L. Blin, R. Bleta, J. Ghanbaja, M.J. Stébé, Fluorinated emulsions: templates for the direct preparation of macroporous–mesoporous silica with a highly ordered array of large mesopores, *Microporous Mesoporous Mater.* 94 (2006) 74–80.



Nano-emulsions as imprints for the design of hierarchical porous silica through a dual templating mechanism



Philippe Riachy^a, Marie-José Stébé^a, Bénédicte Lebeau^b, Andreea Pasc^a, Loïc Vidal^b, Jean-Luc Blin^{a,*}

^a Université de Lorraine/CNRS, SRSMC, UMR7565, F-54506 Vandoeuvre-lès-Nancy cedex, France

^b Université de Haute Alsace (UHA)/CNRS, Equipe Matériaux à Porosité Contrôlée (MPC), Institut de Science des Matériaux de Mulhouse (IS2M), UMR 7361, F-68093 Mulhouse cedex, France

ARTICLE INFO

Article history:

Received 1 September 2015
Received in revised form
27 September 2015
Accepted 28 September 2015
Available online xxx

Keywords:

Nano-emulsions
Micelles
Hierarchical porosity
Silica
Dual templating mechanism

ABSTRACT

Due to their properties nano-emulsions are excellent candidates to be used as imprints to create a macropore network. In this study nano-emulsions have been formulated from the Remcopal 4/decane/water system and mineralized by a dual templating mechanism in the presence of Pluronic P123 micelles. After removing the organic matter, macro-mesostructured silica materials are obtained. Small angle X-ray scattering patterns of the materials and transmission electronic microscopy experiments show that the mesoporous network (mesopore size around 9 nm) adopts a hexagonal arrangement.

Macropores have been characterized by transmission electron microscopy, scanning electron microscopy and mercury porosity. As determined by mercury porosimetry, the size of the macropores imprinted by the nano-emulsions is of about 240 nm. A second macroporosity is also detected in the micrometer range and could be related to the further fusion of nano-emulsions during the hydrothermal process and to interparticular porosity. To better address the formation mechanism of the hierarchical structure of the silica material, the stability of nano-emulsions in the presence of methanol, P123 and both of them has been investigated.

We have also evidenced the dual role played by the Pluronic micelles. They do not only induce the mesopore network through the cooperative templating mechanism, but their presence also avoids the total destruction of the nano-emulsion by methanol, released during the hydrolysis of the silica precursor.

© 2015 Elsevier Inc. All rights reserved.

1. Introduction

One way to design porous materials consists of combining the sol–gel chemistry and the use of surfactant molecules assemblies as framework templates. Depending on the structure of the initial system either mesostructures, i.e. materials having a pore diameter between 2 and 50 nm or macroporous materials, i.e. compounds with pore size larger than 50 nm are recovered. By this way mesoporous and macroporous materials can be synthesized from micelles and emulsions, respectively. However, practical applications require porous materials having hierarchical pore structures at different length scales, since the limited diffusion of substrates through confined nano-channels can be a problem [1–3]. In

catalysis [4,5] for example, the hierarchical combination of pores reduces transport limitations resulting in higher activities and better control over selectivity [5]. Therefore, over the past few years the development of these hierarchically ordered structures at multiple length scales has attracted much attention and many papers are focused on the synthesis of meso-macro, micro-macro or micro-mesoporous materials [6–11]. Materials with a macroporous structure have been synthesized using multiple templates, such as latex spheres [12,13], solid lipid nanoparticles [14] and emulsions [15–20] using either soft or hard templating methods. For example, these techniques were employed to design a new class of three-dimensional ordered macrostructures (3DOM) [21–23], which have applications in catalysis [22] or photonics [23]. However, emulsions templating is perhaps most general and has been used to produce macroporous silica, titania and zirconia [15]. Although systems having two types of mesopores are rarely investigated, some interesting strategies have been developed to prepare this

* Corresponding author. Tel.: +33 3 83 68 43 70.

E-mail address: Jean-Luc.Blin@univ-lorraine.fr (J.-L. Blin).

kind of hierarchical materials. One of them consists of using mixture of surfactants [24–27]. For example Morris et al. employed mixtures of micellar solutions of nonionic surfactants, including Pluronic, Brij and Tetronic types, as templates for synthesizing porous silica materials having several pore sizes [26]. Depending on the surfactant mixture, ordered uniform pore size arrangements, partially ordered complex bimodal structures or totally disordered non-mesoporous structures were obtained. As mentioned above various building blocks such as micelles, liquid crystals, micro-emulsions or emulsions can be used to induce and to tune the porosity to the targeted application. Due to their unique properties, nano-emulsions [28–30] make excellent candidates for the design of such materials. Indeed, nano-emulsions are emulsions consisting of small mono-disperse droplets, typically in the 20–200 nm size range, which are often referred to in the literature also as mini-emulsions, ultrafine emulsions, submicron emulsions [31–33]. Although they could have similar size like microemulsion droplets and appear transparent or translucent, they are in fact quite different [34]. Nano-emulsions are thermodynamically unstable and their formation generally requires energy input. The properties of nano-emulsions depend not only on thermodynamic conditions (i.e., composition, temperature and pressure), but also on the preparation method and crucially, on the order of component addition. Among the different preparation methods low-energy ones constitutes a field of growing interest [35–38]. These methods make use of accessible phase transitions occurring during the emulsification process as a result of changes in surfactant film spontaneous curvature. According to this process the formation of nano-emulsions is obtained by the phase inversion temperature method (PIT) [39–41], phase inversion composition method (PIC) [38,42], or self-emulsification method [36,37,43]. Due to their properties these systems are used for different kinds of applications [36,43–46]. For example in the pharmaceuticals field, nano-emulsions emerge as a promising drug delivery technique [43,44,47,48]. Recently, nano-emulsions have been employed as templates for the preparation of porous silica [49,50]. However, to the best of our knowledge only very few papers address this topic. For example Prouzet et al. have reported the synthesis of porous silica from phase inversion composition O/W nano-emulsions [49]. Authors have used the oil phase of the nanoemulsion as a nano-reactor for the preparation of magnetic gamma-Fe₂O₃ nanoparticles. Mou et al. have also used the nanoemulsion-templating approach for the synthesis of silica nanoparticles with compartmentalized hollow structure *via* ultrasound-assisted sol–gel method [50].

Taking advantage of the monodispersity of nano-emulsions in this paper we are interested in combining the cooperative templating mechanism (CTM) with the nano-emulsions templating to design hierarchical porous silica using tetramethoxysilane (TMOS) as the silica precursor. Nano-emulsions have been prepared from the Remcopol 4/decane/water system according to the PIT method. Since both the methanol, released during the hydrolysis of TMOS, and the presence of micelles, required for the CTM mechanism, can modify the Remcopol 4/decane/water phase behavior and thus disturb the domain of nano-emulsions we have also investigated the effect of the presence of these two additives on the stability of the nano-emulsions. This allows to shed some lights on the formation of the hierarchical porous silica.

2. Materials and methods

Remcopol 4 (commercial name) was provided by CECA. It is a technical grade surfactant, which formula mainly consists of a hydrogenated carbon chain with 12 carbons and the average number of oxyethylene is 4. It is noted as C₁₂(EO)₄. The triblock copolymer

P123 (EO)₂₀(PPO)₇₀(EO)₂₀ and decane were purchased from Aldrich. Deionized water was used to prepare the various samples.

Preparation and stability of the nano-emulsions: Nano-emulsions have been formulated from the Remcopol 4/decane/water system using the PIT method, according to a procedure previously reported [51]. Here the oil to surfactant ratio and the weight fraction of water have been fixed to 3 and 0.74, respectively. These conditions lead to formation of nano-emulsions with a size, determined by SAXS and DLS, of around 100 nm in diameter [51]. The stability of the nano-emulsions in the presence of methanol, P123 micelles and both of them has been investigated by visual observations and by DLS. The quantity of methanol has been varied from 0 to 40%, this corresponds to the maximum amount of methanol released during the hydrolysis of the silica precursor. The concentration of the P123 micellar solution has been changed from 0 to 10 wt.%.

Porous materials preparation: First a solution of nano-emulsions and a micellar solution of Pluronic P123, at various concentrations, are separately prepared. Then 50% in volume of each solution are mixed and in the final mixture the content of the Pluronic P123 varied between 0 and 10 wt.%. The pH of the mixture was kept at value of 0.3. After that tetramethoxysilane (TMOS), used as the silica source was added. The quantity of TMOS is calculated according to the P123/TMOS molar ratio (R), which was varied between 0.0075 and 0.0015. The mixture was stirred at ambient temperature for 1 h using a magnetic stirrer. Then it was transferred and sealed in a Teflon autoclave. The autoclave was heated at 40 °C for 24 h, afterward at 100 °C for 24 h. The final products were recovered after ethanol extraction with a Soxhlet apparatus for 48 h. Before characterization samples are dried at room temperature.

Characterization: A Malvern zetasizer 3000HSA instrument was used to measure the size of the nano-emulsions in water by dynamic light scattering. The Helium–Neon laser, 5 mW operates at 633 nm, with the scatter angle fixed at 90°. The sample is contained in a flow-through cell kept at 25 °C. All the measurements were performed in the suitable conditions by systematically diluting three time the samples with water to validate the results. Water was first filtered with a mixed cellulose ester (surfactant free) filter (0.45 μm). The attenuator (diaphragm) of the photomultiplier was automatically adapted for each sample in order not to saturate the detector. The data were analyzed by the CONTIN method and the size was provided by an intensity distribution.

SAXS measurements were carried out using a SAXSess mc2 (Anton Paar) apparatus. It is attached to a ID 3003 laboratory X-Ray generator (General Electric), equipped with a sealed X-ray tube (PANalytical, λ_{Cu (Kα)} = 0.1542 nm, V = 40 kV, I = 50 mA). A multilayer mirror and a block collimator provide a monochromatic primary beam. A translucent beam stop allows the measurement of an attenuated primary beam at q = 0. Porous materials are introduced into a powder cell before being placed inside an evacuated chamber equipped with a temperature controlled sample holder unit. Acquisition times are typically in the range of 1–5 min. Scattering of X-ray beam is recorded by a CCD detector (Princeton Instruments, 2084 × 2084 pixels array with 24 × 24 μm² pixel size) in the q range 0.3–5 nm⁻¹. The detector is placed at 309 mm from the sample holder.

N₂ adsorption and desorption isotherms were determined on a Micromeritics TRISTAR 3000 sorptometer at –196 °C. The pore diameter and the pore size distribution were determined by the BJH (Barret, Joyner, Halenda) method applied to the adsorption branch of the isotherm [52].

Macropores were detected using mercury porosimetry on a Micromeritics Autopore IV 9500. The penetrometer (stem volume = 0.412 ml, penetrometer volume = 1 ml) was filled with 0.1 g of the sample. A low pressure (0.1–15 psia) followed by a high

pressure analysis (15–60 000 psia) were done in order to detect pores down to 5 nm in diameter, the equilibration time is 10 s.

Transmission Electron Microscopy (TEM) images of the samples were acquired using a Philips CM200 microscope working at 200 kV. Prior to the observation, the powder was dispersed into chloroform with ultrasounds and a few drops of the suspension were deposited at the surface of a copper observation grid covered with a formvar/amorphous carbon film.

The morphology of the samples was observed by Scanning Electron Microscopy (SEM) using a Philips FEI XL30 FEG microscope with an accelerating voltage = 7 kV. The samples were first metallized by a thin gold layer (<10 nm).

3. Results and discussion

In a previous study [51] the nano-emulsions domain as a function of temperature has been determined by the PIT method. We have shown that the stable nano-emulsion domain exists between 20 and 27 °C, which is bordered by oil/surfactant weight ratios 2.3 and 5.7 and can extend beyond 95 wt.% of water [51]. In order to design the porous silica, various parameters should be taken into account. In particular, the quantity of TMOS and the P123

concentration, which may affect the organization and the size of the mesopores.

3.1. Effect of the silica amount

In this study the concentration of the Pluronic micellar solution is fixed at 2.5 wt.%. The quantity of silica has been expressed as the P123/TMOS molar ratio (R). Looking at Fig. 1A, there is an optimum ratio to get a mesopore ordering. Indeed, for $R = 0.0025$ in addition to a sharp peak at 10.6 nm, two other peaks are detected on the SAXS pattern (Fig. 1Ab). The presence of these last two peaks is characteristic of a hexagonal organization of the channels. The unit cell a_0 , which is the sum of the pore diameter and of the thickness of the pore wall, can be deduced from the following relation: $a_0 = 2d_{100}/(3)^{1/2}$, and its value is found to be equal to 12.3 nm. The hexagonal arrangement of the channels is further confirmed by the TEM micrographs. Indeed, the hexagonal stacking of the channels is clearly evidenced (Fig. 1Bd–f). In addition, two light spots are present (Fig. 1Bd,e) on the Fourier transform pictures of TEM images, indicating the parallelism of well oriented channels.

If a lower quantity of the silica precursor is introduced, only a single broad reflection at 10.6 nm is observed on the SAXS pattern. Its intensity decreases with the increase of R (Fig. 1Ac,d). The

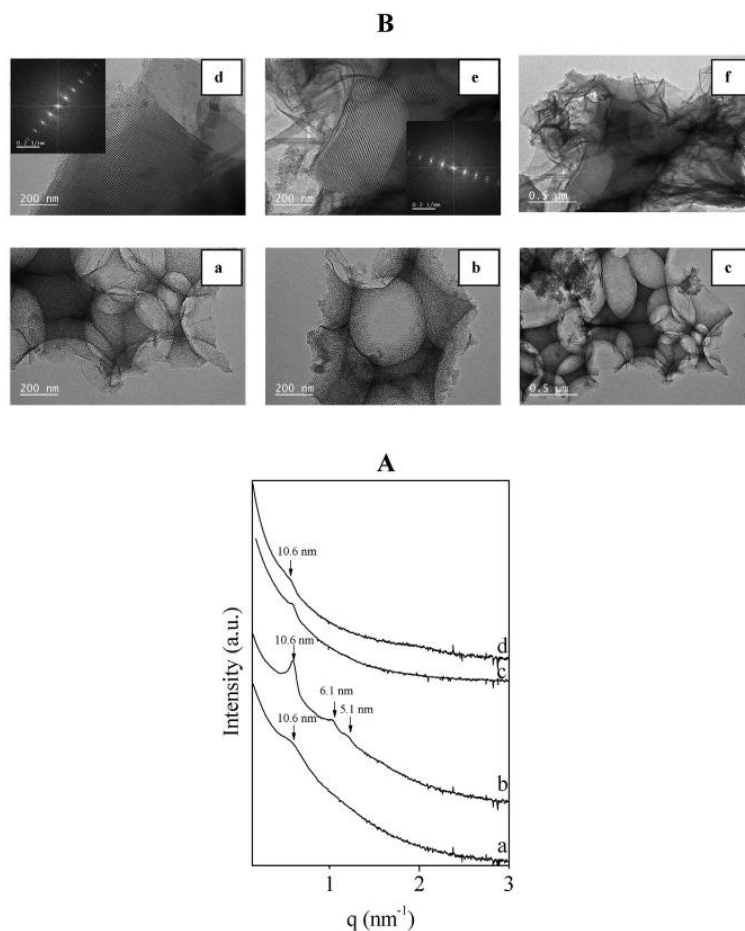


Fig. 1. SAXS patterns (A) of the materials prepared with a P123/TMOS molar ratio equal to a: 0.0015, b: 0.0025, c: 0.005 and d: 0.0075. TEM micrographs (B) of the material prepared with a P123/TMOS molar ratio equal to 0.0015 (a–c) and 0.0025 (d–f).

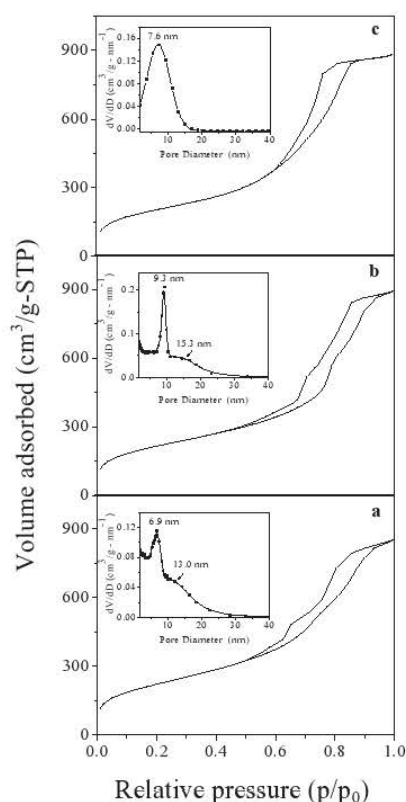


Fig. 2. Nitrogen adsorption–desorption isotherm with the corresponding pore size distribution of the materials prepared with a P123/TMOS molar ratio equal to a: 0.0015, b: 0.0025 and c: 0.0075.

Table 1

Specific surface area (S_{BET}), pore volume (V_p) and pore diameter (\emptyset) as a function of R. The P123 micellar concentration is equal to 2.5 wt.%.

R	S_{BET} (m^2/g)	V_p (cm^3/g)	\emptyset (nm)
0.0075	740	1.3	7.6
0.005	750	1.2	7.6
0.0025	780	1.2	9.3
0.0015	810	1.1	6.9

materials adopt a wormhole-like mesostructure. The same tendency is noted when R is decreased to 0.0015 (Fig. 1Aa). Neither the honeycomb like structure nor the stacking of the channel is detected by TEM (Fig. 1Ba–c). TEM images show that in this case materials have a disordered structure with a large number of wormhole-like and interconnected channels lacking a long range packing order as observed in MSU (Michigan State University) compounds.

Porous materials are prepared by combining both the CTM and the nano-emulsions templating mechanisms. So, at low silica content (higher value of R), it is possible that the micelles are not well-covered by the hydrolyzed silica precursor and that the intermicellar condensation is not complete, leading to a less ordered mesopore network. On the other hand, for a high amount of TMOS, we can assume that only a part of the silica interacts with the surfactant to form the channel arrangement and that another part precipitates to form an amorphous silica phase. Thus, the ordered

pore network is diluted in a non-structured silica phase and the SAXS patterns exhibit weaker and larger diffraction peaks [53–55]. For instance, Schulz-Ekloff et al. [53] attributed the poor hexagonal long range order of their particles obtained at surfactant/silica ratio higher than 0.66 to the polymerization of the silica source into solid amorphous silica due to the excess of surfactant. In the present study, similar arguments can be taken into account to explain the transition from a well ordered mesopore ordering to a randomly oriented pore structure when the value of R is diminished.

The samples exhibit a type IV isotherm (Fig. 2), characteristic of mesoporous materials according to the IUPAC classification [56]. The values of the specific surface area and pore volume are rather high (Table 1). The mesopore diameter is centered on 7.6 nm for materials prepared with $R = 0.0075$ and $R = 0.005$ (Insert Fig. 2 and Table 1). Concerning the materials prepared with a higher amount of silica, it seems that a very weak proportion of mesopores having a higher diameter (between 13 and 20 nm) are present for the materials prepared with $R = 0.0025$ and $R = 0.0015$. As the Remcpol 4 is used to formulate the nano-emulsions, this second contribution in the mesopore size distribution could arise from mixed micelles (P123 + Remcpol 4). However these micelles, present in a very low proportion, has not been detected by dynamic light scattering experiments. The main mesopore diameter varies from 9.3 to 6.9 nm when R is changed from 0.0025 to 0.0015.

The presence of macropores has been evidenced by TEM (Fig. 1B), SEM (Fig. 3A) and mercury porosity (Fig. 3B). Indeed TEM allows not only characterizing the mesopore arrangement but it also reveals the existence of macropores with a size either in the nanometer or in the micrometer range (Fig. 1B). In addition from these TEM photos we can see that the mesopores network with the hexagonal or the wormhole-like structure, depending on the quantity of silica, constitutes the walls of the macropore. A macroporous network arising from the mineralization of nano-emulsions in presence of P123 is also shown Fig. 3A, which depicts several representatives scanning electron micrographs of the synthesized silica. Indeed, highly porous particles are clearly observed by SEM. In any case, the macropores are not well-ordered and the pore size varies from a few hundred nanometers to a few microns. Fig. 3B shows the macropore size distribution determined by mercury intrusion porosimetry measurements. It exhibits the presence of two macropores size distributions centered at 240 nm and 6 μm , confirming the observations made from the SEM and TEM images. The first one is compatible with the size of the nano-emulsions and likely arises from their mineralization. By contrast, the second one corresponds to macropores having a size clearly above the diameters of the oil droplets. It is due to bigger size pores but probably also to interparticular porosity.

3.2. Variation of the P123 micellar concentration

Keeping $R = 0.0025$, which is the optimum ratio to get a hexagonal mesopore ordering, the mesoporosity has been tuned by changing the concentration of P123. From Fig. 4A it can be seen that the mesopore ordering is not deeply modified by the variation of the P123 content. Indeed, whatever the concentration of the Pluronic micellar solution is, the 3 reflections characteristic of the hexagonal systems are detected on the SAXS pattern (Fig. 4A). This fact is also supported by the TEM pictures (Fig. 5A), which show the honeycomb like hexagonal arrangement of the hexagonal structure and the fast Fourier transform images, given as inserts, exhibit the typical 6-fold symmetry. For all the samples a type IV isotherm (Fig. 4B) is obtained by nitrogen adsorption–desorption analysis, confirming the presence of mesopores. Whatever the concentration of the micellar solution, the mesopore size distribution is quite narrow (Fig. 6A). However, while, the specific surface area and the

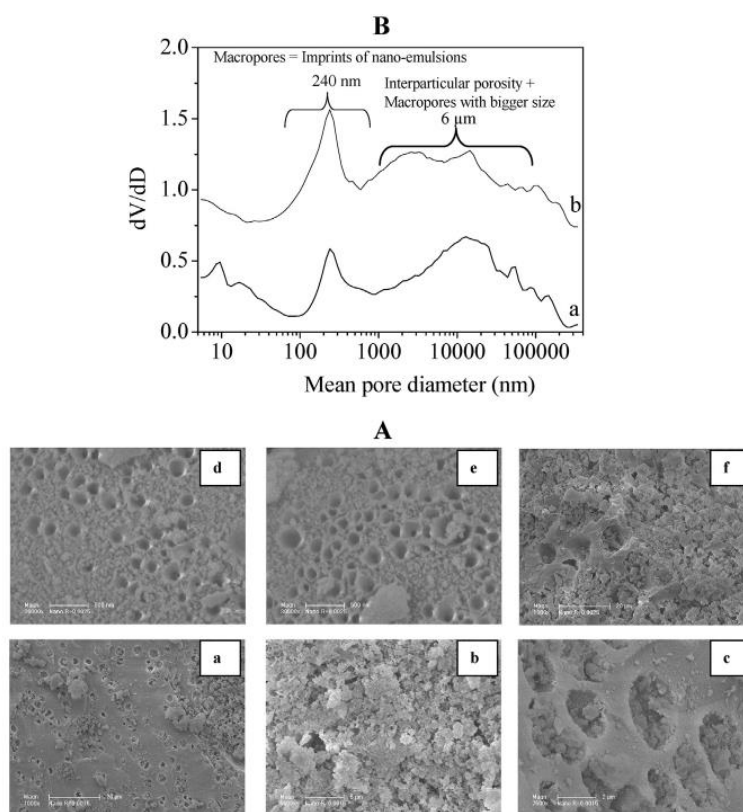


Fig. 3. SEM micrographs (A) of samples prepared with a P123/TMOS molar ratio equal to 0.0015 (a–c) and 0.0025 (d–f). Pore size distributions, determined by mercury intrusion (B) of the samples prepared with a P123/TMOS molar ratio equal to a = 0.0015 and b = 0.0025.

pore volume are in the same range of order for all the synthesized samples (Table 2), the mesopore diameter can be tailored from 8.6 to 10.2 nm by decreasing the P123 concentration from 10 to 0.5 wt.% (Fig. 6B).

The morphology of the materials can be described as porous particles with irregular shape. Macropores in the nanometers domain are detected by both TEM (Fig. 5A) and SEM (Fig. 5B), but on the different photos macropores having a size in the micrometer range are also visible. In addition with the increase of the P123 concentration it seems that the latter predominate. The presence of macropores in the samples was further confirmed by mercury intrusion experiments and it appears that the macropore size distributions are not significantly affected by the variation of the P123 content as long as its concentration remains higher than 1 wt.% (Fig. 7). Indeed, unexpectedly Fig. 7 reveals that except for the macropores with a size in the micrometer domain, no size is detected in the nanometer range when the materials are prepared either in the absence of P123 or with a Pluronic concentration lower than 1 wt.%.

3.3. Discussion

The above results show that dual porous materials having a well ordered mesopore network (9.3 nm) and a macroporosity in the range of few hundred nanometers (240 nm), attributed to the mineralization of the nano-emulsion, can be synthesized. Nevertheless, it should be noted that the size of the pores is higher than

the one of the droplets of the nano-emulsions (around 100 nm in diameters). However, the macropore size distribution is not homogeneous and components in the micrometer range are also detected. The proportion of these macropores increases with the concentration of the P123 micellar solution. In addition, no macropore in the nanometer range is observed for P123 concentration lower than 1wt.%. To better understand these phenomenons we have investigated the effect of P123 addition on the stability of the nano-emulsions. We have also taken into account the possible influence of methanol, released during the hydrolysis of the silica precursor.

The stability of the nano-emulsions in the presence of P123, methanol and both of them has been evaluated by optical observation but also by determining the size of the nano-emulsions by DLS. Before DLS experiments, each sample has been diluted with water to get a system in which the inter-particle interactions are negligible. Fig. 8A depicts the effect of the progressive addition of methanol, in the absence of P123, on the size of nano-emulsions. It appears that until 10 wt.% of CH₃OH the nano-emulsions retain their size and up to 72 h no modification is noted. Beyond 10 wt.%, the size of the oil droplets sharply increases to reach 1150 nm for 20wt.% of CH₃OH after 3 h of preparation. So the nano-emulsions are not stable any longer. This is why no macropores in the nanometer range are detected without P123. Indeed, considering the amount of TMOS used to mineralize the nano-emulsions we can evaluate that in that case 18 wt.% of methanol are released during the hydrolysis of the silica precursor.

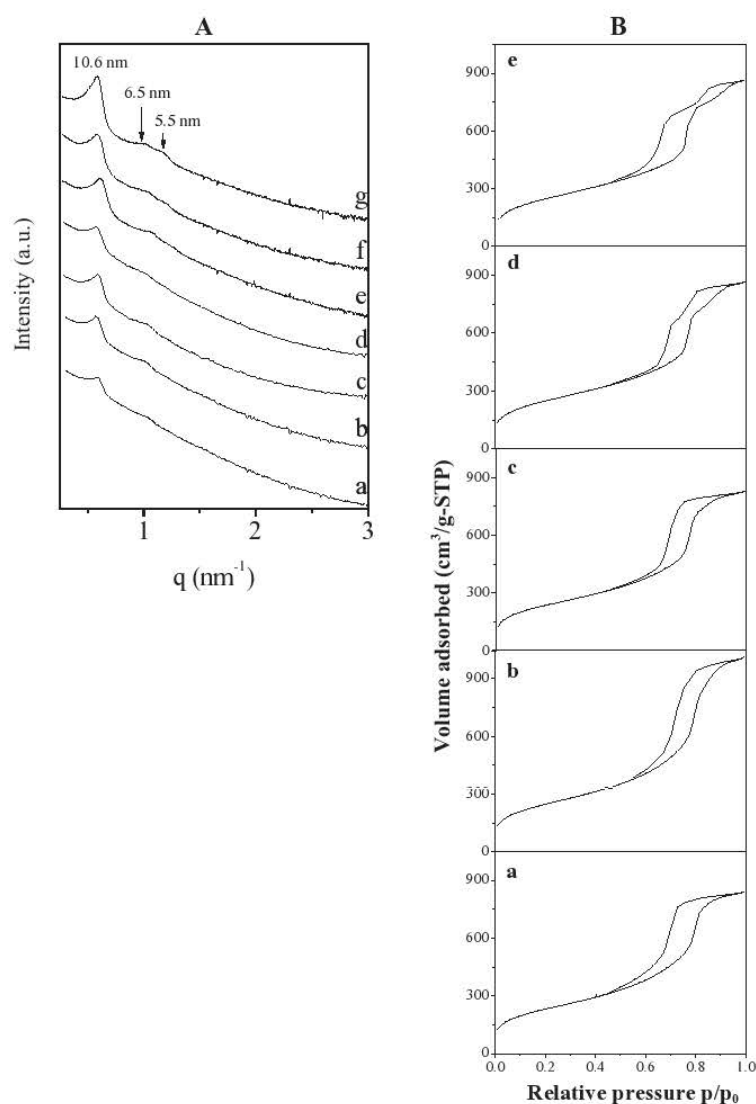


Fig. 4. SAXS patterns (A) of the materials prepared with a P123 content of a: 0.5, b: 0.75, c: 1, d: 1.25, e: 2.5, f: 5 and g: 10 wt.%. Nitrogen adsorption–desorption isotherm (B) of materials synthesized in the presence of a: 0.75, b: 1.25, c: 2.5, d: 5 and e: 10 wt.% of P123.

The effect of Pluronic micelles is quite different (Fig. 8B). Their presence involves an increase of the oil droplets' size. For example at the initial time, that means a few minutes after mixing the nano-emulsions and the micellar solution, the diameter of the nano-emulsions' droplets varies from 75 to 110 nm when the P123 concentration is changed from 0 to 5 wt.%. It should be noted that under these conditions P123 micelles are not observed in the presence of the nano-emulsions. Until 80 h the nano-emulsions are quite stable. We can note a slight increase from 110 (after 24 h) to 180 nm (after 72 h) for the nano-emulsions prepared in the presence of 5 wt.% of P123. For 10 wt.% of Pluronic the increase of the oil droplets' size is more pronounced. The addition of P123 has another drawback for the nano-emulsions since the PIT of the Remcopal 4/decane/water system increases and this situation does not favor the formation of the nano-emulsions. The conductivity curves given in

Fig. 9A show the effect of the P123 presence in the system on the PIT. In the absence of P123, at low temperature the conductivity is high (Fig. 9A), meaning that the continuous phase is aqueous. When the temperature increases the conductivity also increases until a maximum at around 26 °C. The PIT of the system is slightly higher at around 27–28 °C (inflection point). The decrease of the conductivity is discontinuous and according to literature this phenomenon is associated with the existence of different structures (bicontinuous L_3 phase and liquid crystals) formed by changing the temperature [38,41,57]. In a previous paper dealing with the detailed characterization of nano-emulsions prepared from the Remcopal 4/decane/water system we have identified these various structures [51]. In the presence of P123 micelles the system behaves in a different way. Indeed, in the considered range of temperature neither a maximum nor a discontinuous variation of the

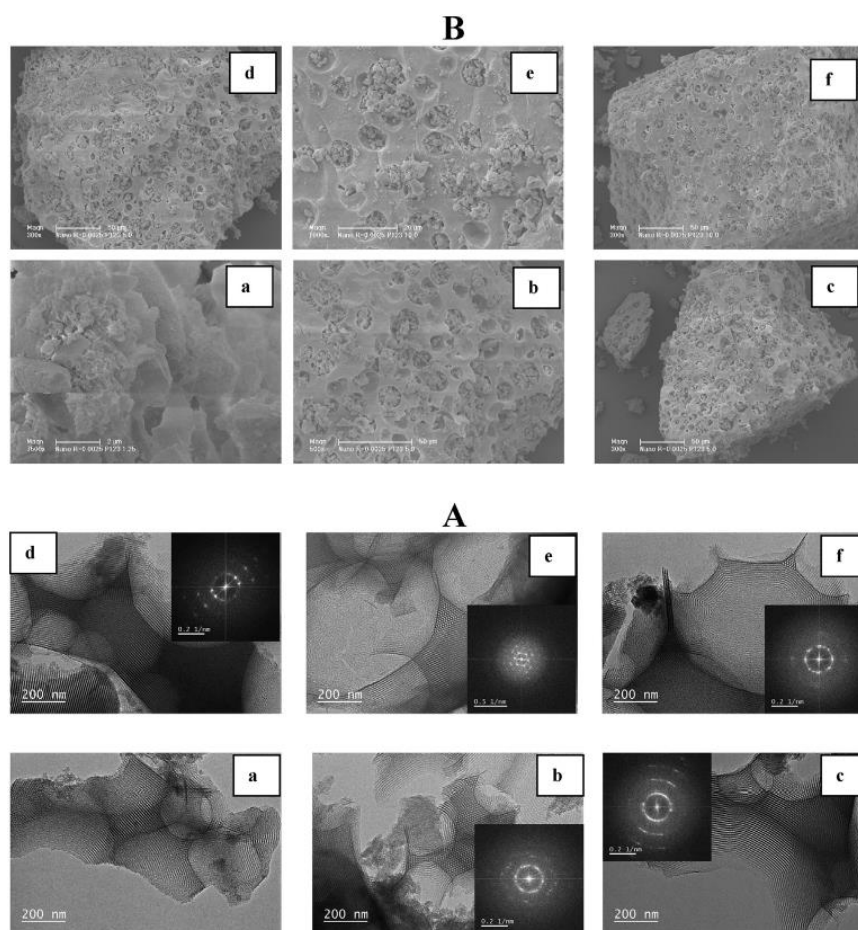


Fig. 5. TEM (A) micrographs of f the materials prepared with a P123 content of 5 (a–c) and 10 wt.% (d–f). SEM images (B) of the samples prepared in the presence of 1.25 (a), 5 (b–d) and 10 wt.% (e–f) of Pluronic.

conductivity is noted. This means that the PIT is significantly increased, the system becomes more hydrophilic and the phase behavior is modified. The existence of the nano-emulsions is not favored in the presence of the Pluronic micelles and looking at the diameter of the oil droplets it seems that emulsions, which size remains small, are rather formed. This can explain why the size of the macropores, detected in the nanometer range is slightly higher than the one of the nano-emulsions. A partial coalescence of the droplets during the material synthesis might also be the cause of that. This phenomenon has already been reported for the mineralization of others imprints such a Solid Lipid Nanoparticles, emulsions or double emulsions [18,58,59].

We have also considered the effect of methanol addition on the size of the Pluronic micelles. Fig. 9B shows that whatever the P123 concentration, a slight increase of the micelles size is noted with the methanol content. For example for a P123 concentration of 2.5 wt.%, the hydrodynamic diameter of the micelles varies from 19 to 25 nm when the methanol amount is changed from 0 to 18 wt.%. This behavior can be explained by the fact that short chain alcohols like methanol rather acts as a co-solvent, whereas longer chain of the alcohol, behaves more like real oil [60]. So, short chain alcohols mainly remain in the aqueous phase and change the water structure and as a consequence the volume of the aggregates increases.

This involves an increase of the hydrodynamic diameter [61,62]. For example Parekh et al. have reported that alcohol such as methanol, ethanol or 1-propanol induce micellisation of triblock copolymers (PEO-PPO-PEO), the cloud point (CP) and the critical micellisation temperature (CMT) are increased. These alcohols enhance the hydrogen bonding and hydrophobic hydration [62]. It should also be noted from Fig. 9B that the hydration of the polar heads is not limited to the oxyethylene units in contact with water but it also reaches the hydrophobic core and that the modification of the P123 micelles' size by the addition of methanol is instantaneous. No change in the size is noted with time.

The combined effect of methanol and P123 on the size of the nano-emulsions' oil droplets is reported in Fig. 10. In a general way an increase of the diameter is observed with time. It is interesting to point out that comparing with nano-emulsions prepared without P123, the stability of the oil droplets in presence of methanol is enhanced when Pluronic micelles are added. Indeed, focusing on the initial step ($t = 0$) no variation of the hydrodynamic diameters occurs up to 30 wt.% of methanol when 2.5 (Fig. 10A) or 5 wt.% (Fig. 10B) of P123 are added. This value falls to 20 wt.% of CH_3OH for 10wt.% of P123. It should be reminded that in the absence of micelles, the size of oil droplets is modified after the addition of 10 wt.% of alcohol (Fig. 8B). Therefore P123 plays a dual role. Firstly

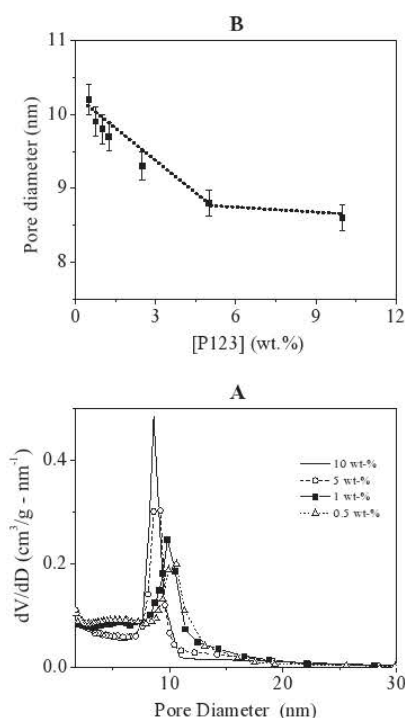


Fig. 6. Mesopore size distribution (A) and variation of the mesopore diameter (B) as a function of the P123 content (wt.%).

it induces the mesopore network according to the cooperative templating mechanism and secondly, at least at the initial step, thanks to the affinity of methanol for P123 micelles, it stabilizes the size of the oil droplets. After 3 h its protective effect is not efficient anymore. However P123 has also some drawbacks since it makes the system more hydrophilic, which is less favorable to the existence of nano-emulsions. In addition it involves an increase of the oil droplets' diameter. As a function of time when Pluronic micelles are added, the system evolves from nano-emulsions to emulsions. The higher the micellar concentration, the more pronounced this phenomenon is. Based on the different observations reported above some light can be shed on the formation mechanism of the hierarchical silica materials. After mixing the nano-emulsions and the P123 micellar solutions TMOS is immediately added and its hydrolysis occurs involving the release of methanol. According to Brinker this process occurs very rapidly under acidic conditions [63]. For example, using HCl as acid, Chen et al. [64] have evaluated that 95% completion of the hydrolysis process are less than 10 min. In the study reported here strong acidic conditions are used to

Table 2
Specific surface area (S_{BET}), pore volume (V_p) and pore diameter (\emptyset) as a function of the P123 content (wt.%). R is equal to 0.0025.

P123 (wt.%)	S_{BET} (m ² /g)	V_p (cm ³ /g)	\emptyset (nm)
10	890	1.1	8.6
5	890	1.2	8.8
2.5	850	1.1	9.3
1.25	890	1.4	9.7
1	860	1.4	9.8
0.75	830	1.1	9.9
0.5	870	1.2	10.2

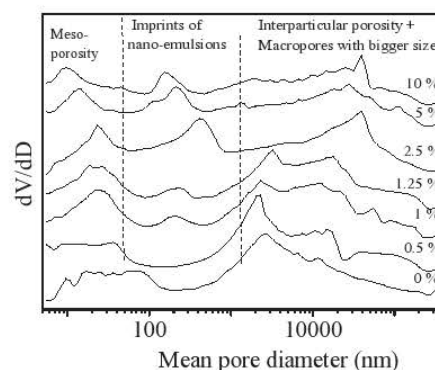


Fig. 7. Macropore size distribution as a function of the P123 content (wt.%).

prepare the hierarchical materials and we can also consider a fast hydrolysis of TMOS and that this step is almost completed within the first 10 min of the material preparation, this corresponds to $t = 0$. As demonstrated above Pluronic makes the system more hydrophilic and involves the transformation from nano-emulsions to emulsions with small size. However since TMOS is immediately incorporated to the mixture the system does not reach an equilibrium state and nano-emulsions are still present. The P123 micelles protect the nano-emulsions against the adverse effect of methanol. Hydrogen-bonds between hydrogen atoms of hydrolyzed TMOS and of the oxygen atoms of the oxyethylene groups of the surfactant of both the P123 micelles, nano-emulsions and/or emulsions are formed, leading to the formation of a hybrid-silica. After the hydrothermal treatment and surfactant removal by ethanol extraction, hierarchical silicas are recovered. It should be noted that less than 1 h elapses before performing the hydrothermal treatment at higher temperature to complete the polymerization of the silica source. In such a mechanism, the highly ordered array of mesopores is templated by the P123 micelles and induced via the CTM mechanism, whereas the macropore network is generated by the nano-emulsions and/or small-size emulsions. When the proportion of P123 in the starting mixture is increased since the P123/TMOS molar ratio has been fixed to 0.0025 the effect of methanol is more pronounced. Indeed, the quantity of methanol released varies from 18 to 40%, depending on the concentration of the micellar solution and the small-size emulsions predominate. As a consequence more macropores having a size in the micrometer range are detected on the SEM and TEM images.

4. Conclusion

Among the different templates used to design porous materials, until now nano-emulsions have been barely considered. Moreover, the reported studies do not focus on the possible influence of the alcohol released during the hydrolysis of the inorganic precursor on the system phase behavior and on the stability of the nano-emulsions. Although it is well known that the presence of additives such as alcohol can strongly modify the features of the system, in particular its phase behavior. In this study we have investigated the mineralization of nano-emulsions, prepared from the Remcopal 4/decane/water system, in the presence of Pluronic P123 micelles. By this way we have succeeded to synthesize materials with a hexagonally ordered mesopores of 9 nm and macropores of 240 nm, as well as a surface area of 800 m²/g and a pore volume of 1 cm³/g. To the best of our knowledge this is the first example of hierarchical porous materials obtained by this way

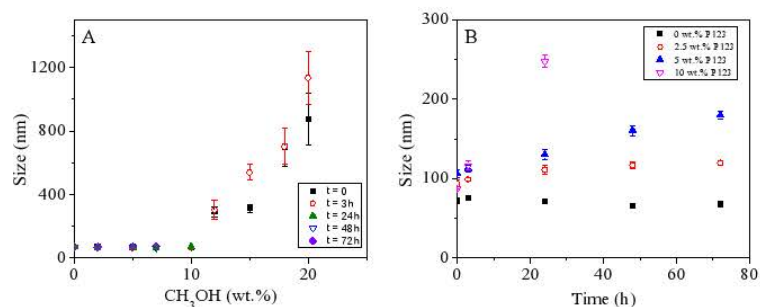


Fig. 8. Hydrodynamic diameter of the nano-emulsions' oil droplets as a function of time in the presence of methanol (A) or Pluronic micelles (B).

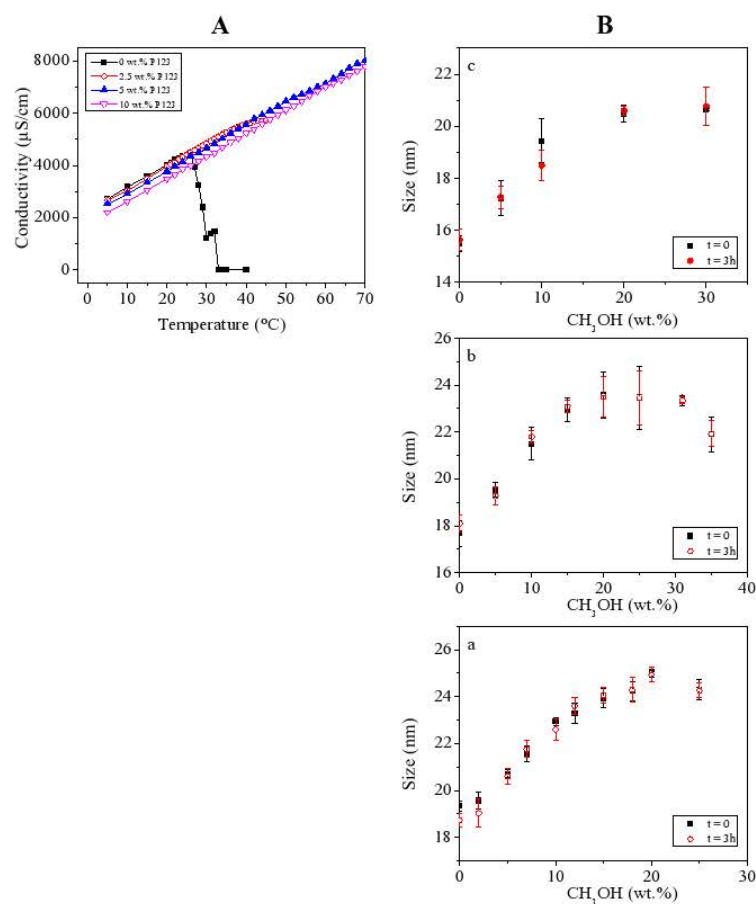


Fig. 9. Conductivity as a function of the temperature in the presence of P123 micelles (A) and effect of methanol on the hydrodynamic diameter of the P123 micelles (B). The P123 micellar concentration is a : 2.5, b : 5 and c : 10 wt.%.

combining nano-emulsions and micelles. We have also shown that Pluronic micelles not only involve the formation of the mesopore ordering *via* the cooperative templating mechanisms, but they also avoid the complete destructuration of the nano-emulsions. Indeed without P123 or at low P123 concentration no size is observed in the nanometer range by mercury porosity. To better address the formation mechanism of the hierarchical silica materials, we have

investigated in detail the effect of P123, methanol which is released during the hydrolysis of the silica precursor and both on them on the nano-emulsions stability. The approach described herein will open a new way to prepare hierarchical meso-macroporous silica or hybrid organic–inorganic materials and straightforward applications for example in drug delivery. In our group, work is underway to encapsulate a pharmaceutical

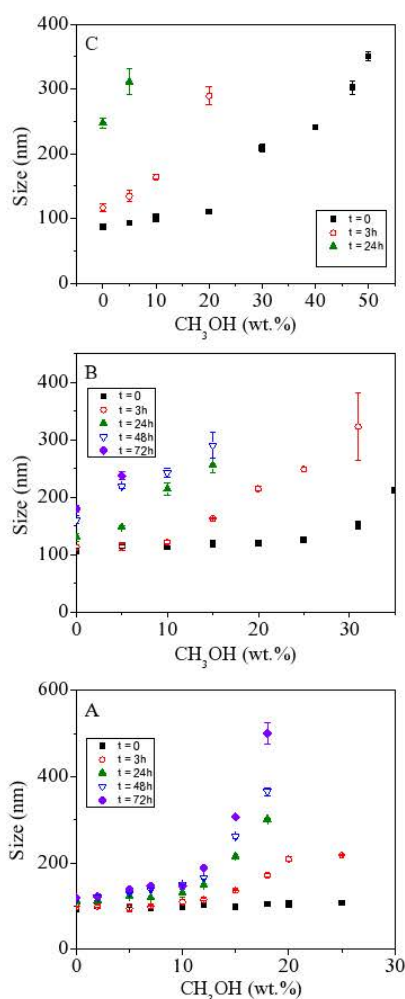


Fig. 10. Hydrodynamic diameter of the oil droplets as a function of time in the presence of both methanol and P123 micelles. The P123 micellar concentration is A: 2.5, B: 5 and C: 10 wt.%.

ingredient, ketoprofen, into nano-emulsions, hybrid materials and bare hierarchical silica.

References

- [1] R.J. Wackeman, Z.G. Bhungara, G. Akay, *Chem. Eng. J.* 70 (1998) 133–141.
- [2] J.F. Brown, P. Krajnc, N.R. Cameron, *Ind. Eng. Chem. Res.* 44 (2005) 8565–8572.
- [3] G. Akay, M.A. Birch, M.A. Bokhari, *Biomaterials* 25 (2004) 3991–4000.
- [4] M.A. Parlett, K. Wilson, A.F. Lee, *Chem. Soc. Rev.* 42 (2013) 3876–3893.
- [5] M.O. Coppens, G.F. Froment, *Fractals* 5 (1997) 493–505.
- [6] B.T. Holland, L. Abrams, A. Stein, *J. Am. Chem. Soc.* 121 (1999) 4308–4309.
- [7] T. Sen, G.J.T. Tiddy, J.L. Casci, M.W. Anderson, *Chem. Commun.* 17 (2003) 2182–2183.
- [8] K. Nakanishi, Y. Kobayashi, T. Amatani, K. Hirato, T. Kodaira, *Chem. Mater.* 16 (2004) 3652–3658.
- [9] J. Nestor, A. Vilchez, C. Solans, J. Esquena, *Langmuir* 29 (2013) 432–440.
- [10] H. Mori, M. Uota, D. Fujikawa, T. Yoshimura, T. Kuwahara, G. Sakai, T. Kijima, *Microporous Mesoporous Mater.* 91 (2006) 172–180.
- [11] O. Sel, D. Kuang, M. Thommes, B. Smarsly, *Langmuir* 22 (2006) 2311–2322.
- [12] B.T. Holland, C.F. Blanford, T. Do, A. Stein, *Chem. Mater.* 11 (1999) 795–805.
- [13] T. Sen, G.J.T. Tiddy, J.L. Casci, M.W. Anderson, *Chem. Mater.* 16 (2004) 2044–2054.
- [14] R. Ravetti-Duran, J.L. Blin, M.J. Stébé, C. Castel, A. Pasc, *J. Mater. Chem.* 22 (2012) 21540–21548.
- [15] A. Imhof, D.J. Pine, *Nature* 389 (1997) 948–951.
- [16] H. Zhang, G.C. Hardy, M.J. Rosseinsky, A.L. Copper, *Adv. Mater.* 15 (2003) 78–81.
- [17] B.P. Binks, *Adv. Mater.* 14 (2002) 1824–1827.
- [18] C. Oh, S.C. Chung, S.I. Shin, Y.C. Kim, S.S. Im, S.G. Oh, *J. Colloids Interface Sci.* 254 (2002) 79–86.
- [19] C. Zhao, E. Danish, N.R. Cameron, R. Katak, *J. Mater. Chem.* 17 (2007) 2446–2453.
- [20] S. Zhang, J. Chen, *Polymer* 48 (2007) 3021–3025.
- [21] B.T. Holland, C.F. Blanford, A. Stein, *Science* 281 (1998) 538–540.
- [22] Y. Wei, J. Liu, Z. Zhao, Y. Chen, C. Xu, A. Duan, G. Jiang, H. He, *Angew. Chem. Int. Ed.* 50 (2011) 2326–2329.
- [23] L. Han, D. Xu, Y. Liu, T. Ohsuna, Y. Yao, C. Jiang, Y. Mai, Y. Cao, Y. Duan, S. Che, *Chem. Mater.* 26 (2014) 7020–7028.
- [24] M. Groenewolt, M. Antonietti, S. Polarz, *Langmuir* 20 (2004) 7811–7819.
- [25] R. Xing, H.J. Lehmler, B. Knutson, S.E. Rankin, *Langmuir* 25 (2009) 6486–6492.
- [26] L. Chen, J. Xu, W.H. Zhang, J.D. Holmes, M.A. Morris, *J. Colloid Interface Sci.* 353 (2011) 169–180.
- [27] A. May, M.J. Stébé, J.M. Gutiérrez, J.L. Blin, *Langmuir* 27 (2011) 14000–14004.
- [28] C. Solans, P. Izquierdo, J. Nolla, N. Azemar, M.J. Garcia-Celma, *Curr. Opin. Colloid Interface Sci.* 10 (2005) 102–110.
- [29] T.G. Mason, J.N. Wilking, K. Meleson, C.B. Changn, S.M. Graves, *J. Phys. Condens. Matter* 18 (2006) R635–R666.
- [30] M.Y. Koroleva, E.V. Yurtov, *Russ. Chem. Rev.* 81 (2012) 21–43.
- [31] R. Pons, I. Carrera, J. Caelles, J. Rouch, P. Panizza, *Adv. Colloid Interface Sci.* 106 (2003) 129–146.
- [32] S. Sajjadi, *Chem. Eng. Sci.* 61 (2006) 3009–3017.
- [33] D.J. McClements, *Soft Matter* 8 (2012) 1719–1729.
- [34] K. Landfester, *Macromol. Rapid Commun.* 22 (2001) 896–936.
- [35] C. Solans, I. Solé, *Curr. Opin. Colloid Interface Sci.* 17 (2012) 246–254.
- [36] L. Wang, X. Li, G. Zhang, J. Dong, J. Eastoe, *J. Colloid Interface Sci.* 314 (2007) 230–235.
- [37] L. Wang, K.J. Mutch, J. Eastoe, R.K. Heenan, J. Dong, *Langmuir* 24 (2008) 6092–6099.
- [38] A. Forgiarini, J. Esquena, C. González, C. Solans, *Langmuir* 17 (2001) 2076–2083.
- [39] P. Izquierdo, J. Esquena, ThF. Tadros, C. Dederen, M.J. Garcia, N. Azemar, C. Solans, *Langmuir* 18 (2002) 26–30.
- [40] N. Anton, P. Gayet, J.P. Benoit, P. Saulnier, *Int. J. Pharm.* 344 (2007) 44–52.
- [41] S.L. Ee, X. Duan, J. Liew, Q.D. Nguyen, *Chem. Eng. J.* 140 (2008) 626–631.
- [42] A. Maestro, I. Solé, C. González, C. Solans, J.M. Gutiérrez, *J. Colloid Interface Sci.* 327 (2008) 433–439.
- [43] L. Wang, J. Dong, J. Chen, J. Eastoe, X. Li, *J. Colloid Interface Sci.* 330 (2009) 443–448.
- [44] N. Sadurni, C. Solans, N. Azemara, M.J. Garcia-Celma, *Eur. J. Pharm. Sci.* 26 (2005) 438–445.
- [45] M. Jaworska, E. Sikora, M. Zielina, J. Ogonowski, *Acta Biochim. Pol.* 60 (2013) 779–782.
- [46] N. Anton, J.P. Benoit, P. Saulnier, *J. Control. Release* 128 (2008) 185–199.
- [47] N. Ahmad, R. Ramsch, M. Llinàs, C. Solans, R. Hashim, H.A. Tajuddin, *Colloids Surf. B* 115 (2014) 267–274.
- [48] C. Fornaguer, A. Dols-Perez, G. Calderó, M.J. Garcia-Celma, J. Camarasa, C. Solans, *J. Control. Release* 211 (2015) 134–143.
- [49] M. Hessian, P. Léone, M. Suchaud, B. Lebeau, H. Nouali, Y. Guarid, E. Prouzet, *Chem. Commun.* 48 (2012) 10022–10024.
- [50] S.H. Wu, Y. Hung, C.Y. Mou, *Chem. Mater.* 25 (2013) 352–364.
- [51] P. Riachy, N. Du, M.J. Stébé, J.L. Blin, *Colloids Surfaces A Physicochem. Eng. Aspects* 481 (2015) 207–214.
- [52] E.P. Barret, L.G. Joyner, P.P. Halenda, *J. Am. Chem. Soc.* 73 (1951) 373–380.
- [53] G. Schulz-Ekloff, J. Rathouský, A. Zukal, *Microporous Mesoporous Mater.* 27 (1999) 273–285.
- [54] A. Leonard, J.L. Blin, M. Robert, P. Jacobs, A.K. Cheetham, B.L. Su, *Langmuir* 19 (2003) 5484–5490.
- [55] F. Michaux, M.J. Stébé, J.L. Blin, *Microporous Mesoporous Mater.* 151 (2012) 201–210.
- [56] K.S.W. Sing, D.H. Everett, R.A.W. Haul, L. Moscou, R.A. Pierotti, J. Rouquerol, T. Siemieniewska, *IUPAC Pure Appl. Chem.* 57 (1985) 603–619.
- [57] P.L. Klassen, Z. George, J. Warwick, S. Georgiadou, *Colloids Surfaces A Physicochem. Eng. Asp.* 455 (2014) 1–10.
- [58] J.L. Blin, J. Jacoby, S. Kim, M.J. Stébé, N. Canilho, A. Pasc, *Chem. Commun.* 50 (2014) 11871–11874.
- [59] J.L. Blin, R. Bleta, J. Ghanbaja, M.J. Stébé, *Microporous Mesoporous Mater.* 94 (2006) 74–80.
- [60] M. Tomsic, M. Bester-Rogac, A. Jamnik, W. Kunz, D. Touraud, A. Bergmann, O. Glatter, *J. Colloid Interface Sci.* 294 (2006) 194–211.
- [61] R.K. Mahajan, J. Chawla, M.S. Bakshi, *Colloids Surfaces A Physicochem. Eng. Asp.* 237 (2004) 119–124.
- [62] P. Parekh, K. Singh, D.G. Marangoni, P. Bahadur, *J. Mol. Liq.* 165 (2012) 49–54.
- [63] C.J. Brinker, *J. Non-Cryst. Solids* 100 (1988) 31–50.
- [64] K.C. Chen, T. Tsuchiya, J.D. Mackenzie, *J. Non-Cryst. Solids* 81 (1986) 227–237.

Hybrid hierarchical porous silica templated in nano-emulsions for drug release

In press

Keywords: Nano-emulsions, Hierarchical porous silica, Hybrid material, Drug release, ketoprofen, Korsmeyer–Peppas model

Abstract

A new nanocarrier for loading and releasing of drugs is reported and ketoprofen was used as a model drug. More precisely, the carrier is a hybrid material prepared by combining O/W nano-emulsions, into which the drug has been solubilized, with mesostructured silica. This organic-inorganic hybrid material shows a controlled release of the drug, depending on pH. If the drug is impregnated into the bare hierarchical meso/macroporous dual silica material, obtained after removal of organic components by extraction, only 8 wt.% of ketoprofen is released in a phosphate buffer media (pH 7.4), probably due to its low solubility in the aqueous phase. The drug solubility and the release strongly increase by adding Pluronic micelles in the receptor phase, suggesting a micelle-promoted and assisted release mechanism. Whatever the vehicle, release profiles of ketoprofen always follow the Korsmeyer–Peppas model with a diffusional release exponent value lower than 0.5, characteristic of a pseudo-Fickian release mechanism. Moreover, the release of ketoprofen is better controlled from the hybrid nanocarrier than from the hierarchical bare porous silica.

Introduction

The growing demand of more efficient medicines forces to adapt drug delivery systems, and efficient production techniques in particular, because of the low solubility of many active pharmaceutical ingredients in biocompatible solvents. For example, the water solubility of ketoprofen, which is effective and well-tolerated in the treatment of acute and chronic pain of both rheumatic and traumatic origin as well as postoperative pain^[1,2], is only 0.0213 mg.mL⁻¹. Different strategies have been developed to overcome this drawback and one of the most popular approaches is the entrapment of a drug molecule into inert vehicles. Various systems based on micelles, microemulsions, emulsions or inorganic materials, have been formulated for this purpose. In particular, Pluronic block copolymers micelles are interesting^[3-5] as they in addition to increase the solubility, the metabolic stability and the circulation of the drugs, they also inhibit drug efflux transporters in both blood-brain barrier and in the small intestines^[3]. Wei et al.^[5] used P123/F127 micelles to encapsulate paclitaxel (PTX), which is a poorly soluble anticancer drug and investigated the in vitro antitumoral activity of the PTX-load mixed micelles. The results show an increased in vitro cytotoxicity compared to injection of the only available commercial preparation of PTX (Taxol) and free PTX in human lung adenocarcinoma cell line A-549^[5]. Microemulsions can also serve as reservoirs for bioactive molecules^[6-9]. For example in a paper dealing with the comparison of emulsion and microemulsion for the encapsulation of hydroxytyrosol (HT), Xenakis et al. show that emulsion provides a better HT release than microemulsions, whereas the opposite effect is noted for the storage ability^[7]. Among the different carriers, nano-emulsions emerge as a promising drug delivery approach^[10-15]. Nano-emulsions are emulsions consisting of small droplets, typically in the 20-200 nm size range^[16,17]. Although their size in the lower range may overlap that of microemulsion droplets and also appear transparent or translucent, nano-emulsions are in fact quite different from true microemulsions^[18] Nano-emulsions, being

emulsions, can possess kinetic stability and they do not form spontaneously, since their free energy of formation is positive, and consequently, have a limited lifespan and their preparation generally requires an energy input. The properties of nano-emulsions depend not only on thermodynamic conditions (i.e., composition, temperature and pressure), but also on the preparation method and crucially, on the order of component addition. The formation of nano-emulsions can be achieved by low-energy methods, in which external input energy might not be required and in contrast to high-energy methods, it does not control droplet size. The most common low-energy methods are those based on phase inversion (phase inversion temperature method, PIT^[19,20], or phase inversion composition method, PIC^[21]), and the so-called self-emulsification methods^[22,23], that are usually based on dilution and/or diffusion processes. Their need for small amounts of surfactants, their stability towards dilution and the ease of formulation make nano-emulsions low-cost drug delivery systems and favors their mass production. Their mechanical, optical properties and droplet size can be controlled; many water insoluble drug molecules can be incorporated into these droplets, and their small size gives them the advantage of penetrating deep into tissues, thus fulfilling the criteria of many drug administration routes.

Another promising drug delivery approach is the adsorption of the drug molecules on the surface of porous silica materials. Thanks to their properties such as a high specific surface area and a narrow pore size distribution, the ordered mesoporous silica, mainly MCM-41 or SBA-15, and the mesoporous silica nanoparticles (MSN) have been widely considered for this application^[24-30]. In 2001, Vallet-Regí et al. first reported^[24] the use of MCM-41 with different pore diameters as a carrier for ibuprofen. Authors showed that due to the small size of ibuprofen molecules, there is no influence of the mesopore diameter on its release^[24]. Since this date, various pharmaceutical active components have been entrapped within mesoporous materials, by adsorption or impregnation, and released through a diffusion-controlled

mechanism^[25,27]. The synthesis of these materials is performed through a templating method. Either chemical^[31-33] or biological^[34-36] templating approaches can be used. When using the chemical one, their preparation combines the sol-gel chemistry and the use of assemblies of surfactant molecules as framework templates^[31-33]. By this way, ordered mesoporous silica or MSN are obtained after surfactant removal, either by extraction or by calcination. So, one alternative method, to develop the carriers, consists in incorporating the active ingredient during the material synthesis^[37-40]. Following this strategy, the use of micelles has the advantage of playing a dual role; first they allow the solubilization of the active ingredient, and second, they act as templates for the formation of the mesopore network. This approach allows entrapping a higher amount of hydrophobic drugs^[39]. For example, in a study dealing with silica capsules enclosing P123 triblock copolymer micelles for flurbiprofen storage and release, Martens et al. have shown that the molecular environment of flurbiprofen in P123 filled silica capsules is different from ordered mesoporous silica materials synthesized using P123 as template having the drug molecules adsorbed on the silica surface^[37]. Besides mesoporous materials, more recently macroporous and hierarchical macro-mesoporous silica have also been used for drug delivery^[41-43]. The main advantage of these carriers deals with the increased mass transport due to the macroporosity, while maintaining a large surface area due to the mesoporosity. This allows a better adsorption of a wide array of drug molecules, while maintaining good diffusion pathways for the drug, thanks to the presence of larger macropores.

Here, we have investigated the ability of nano-emulsions, of hierarchical bare silica obtained after the mineralization of the nano-emulsions and of the hybrid material, to be used as matrix for loading and releasing of a model hydrophobic drug, ketoprofen. We have characterized in detail the various carriers and, for each of them, we have also shed some light on the ketoprofen release mechanism.

Results and discussion

Characterization of the carriers

Nano-emulsions, prepared according to the PIT method have been visualized by NTA (Fig. 1A and 1B). They have been characterized by SAXS and DLS. From $q = 0.1 \text{ nm}^{-1}$, a q^{-4} decay over one decade, characteristic of an abrupt change of scattering length density over a large interfacial area, is detected on the SAXS pattern (Fig 1C).

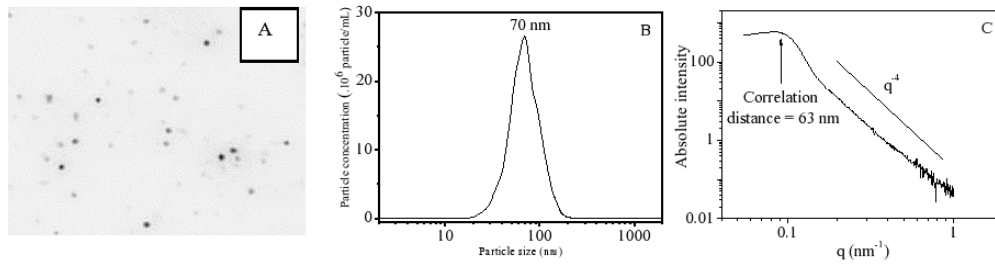


Figure 1 : NTA picture (A), particle size distribution profile from NTA (B) and SAXS pattern (C) of the nano-emulsion.

The droplets size of nano-emulsions can be determined using the Porod law^[44]:

$$I(q) = \frac{2 \pi S_V (Q_{\text{ext}} - Q_{\text{int}})^2}{q^4}$$

where S_V is the area per unit volume of dispersion, Q_{ext} and Q_{int} are the scattering length densities of the continuous phase (water) and internal phase (decane), respectively. From S_V a mean value of the radius (R) of the droplets can be derived from the following formula $R = 3\Phi / S_V$ where Φ is the dispersed volume fraction. According to this equation, the radius of the nano-emulsions is 62 nm. For the 50/50 mixture of both the nano-emulsions and the P123 solutions, the DLS measurements give an average nano-emulsions droplet radius of 74 nm. This value is slightly higher than the one obtained from SAXS. Indeed, DLS gives the hydrodynamic size which is higher than that obtained by SAXS which give hard sphere size. We noticed that the micelles were not detected in the nano-emulsions/micelle mixture; it is

likely due to the intensity masking effect that the large droplet sizes (the nano-emulsions) have on the smaller ones (the micelles). Indeed, the micellar solutions have an average micelles radius of 19.1 nm measured by DLS.

After mineralization of the nano-emulsions in the presence of the P123 micelles, in addition to a sharp peak at 11.2 nm, two peaks at 6.5 nm and 5.6 nm are also detected on the SAXS pattern of the recovered bare porous silica (Fig. 2A). The presence of the latter peaks reveals a hexagonal organization of the mesopore in the material, since the peak position ratio is $1:\sqrt{3}:2$. Indeed, these peaks are attributed to the (110) and (200) reflections of the hexagonal structure. A type IV isotherm, characteristic of mesoporous material is obtained by nitrogen adsorption-desorption analysis (Fig. 2B).

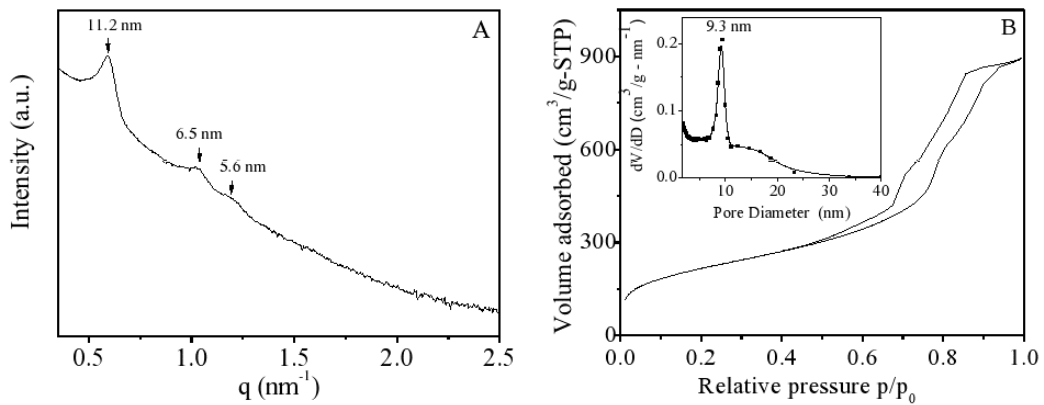


Figure 2 : SAXS patterns (A) and nitrogen adsorption-desorption isotherm (B) with the corresponding mesopore size distribution (insert B) of the bare porous silica.

The specific surface area and pore volume values are $782 \text{ m}^2/\text{g}$ and $1.2 \text{ cm}^3/\text{g}$, respectively. The pore diameter distribution calculated by the BJH method is quite narrow and centered at 9.3 nm (Fig. 2B, insert). As shown by both TEM and SEM micrographs, the silica particles exhibit a macroscopic network structure with a size of few hundred nanometers (Fig. 3A and 3B). The macropore size distribution, determined by mercury intrusion porosimetry

measurements, reveals the presence of macropores with two different size distributions centered at 240 nm and 6 μm (Fig. 3C). The first one can be attributed to the fingerprint of the oil droplets of the nano-emulsions and the second peak (6 μm) might arise from inter-particle porosity induced by aggregation of particles.

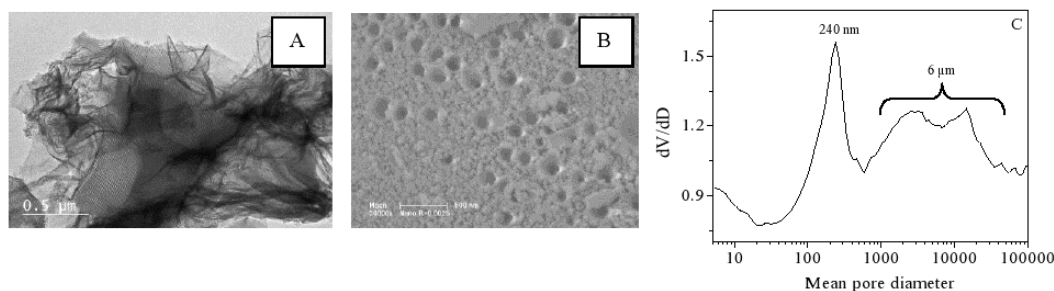


Figure 3 : TEM (A), SEM (B) micrographs and macropore size distribution, determined by mercury intrusion (C) of the hierarchical bare porous silica.

After impregnation the presence of the drug has been determined by infrared spectroscopy. In the 400-2000 cm^{-1} domain, the bare silica material exhibits bands located at 1217, 1056, 954 and 795 cm^{-1} (Fig. 4a). The most intensive band, centered at 1056 and the shoulder at 1217 cm^{-1} are associated with the $\text{SiO}_4 \nu_3(\text{F}_2)$ stretching vibration. The band at 795 cm^{-1} corresponds to the

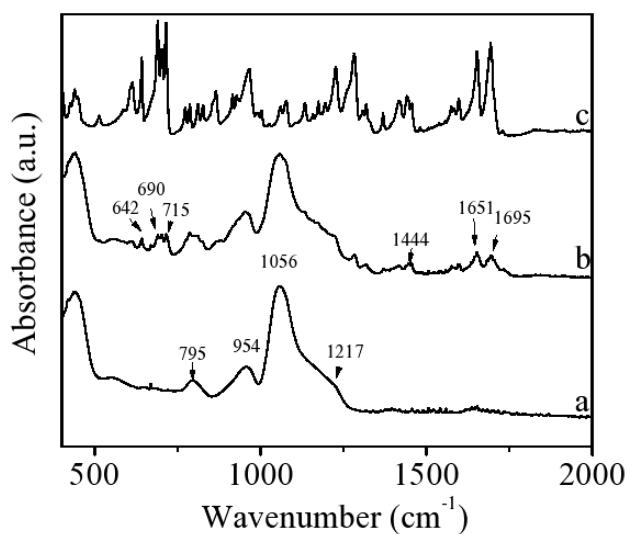


Figure 4 : Infrared spectra of bare silica (a), ketoprofen-loaded silica (b) and pure ketoprofen (c).

$\text{SiO}_4 \nu_1(\text{A})$ stretching vibration. The band at 954 cm^{-1} is related to the Si-(OH) stretching of terminal silanol. By comparison of the spectrum of the spectra of the silica-loaded ketoprofen

(Fig. 4b) with the ones of the pure ketoprofen (Fig. 4c) and the bare silica (Fig. 4a), the presence of adsorbed ketoprofen can be unambiguously confirmed. Indeed, in the investigated wavenumber range and by comparing with the spectrum of bare silica, the supplementary vibrations detected in Figure 4b can be attributed to ketoprofen. In particular, the bands at 1695 and 1651 cm^{-1} are due to the symmetric carbonyl vibration and to both the dimeric carboxylic and ketonic group stretching vibrations^[45]. The peak at 1444 cm^{-1} can be attributed to the presence of CH-CH₃ deformation and the C-H peaks, corresponding to out of plane deformation for substituted aromatics, are observed between 640 and 860 cm^{-1} .

In vitro release of ketoprofen from the hybrid material

The cumulative release profiles of ketoprofen from the hybrid material, determined at four pH values of the receptor solution, are depicted in Figure 5A.

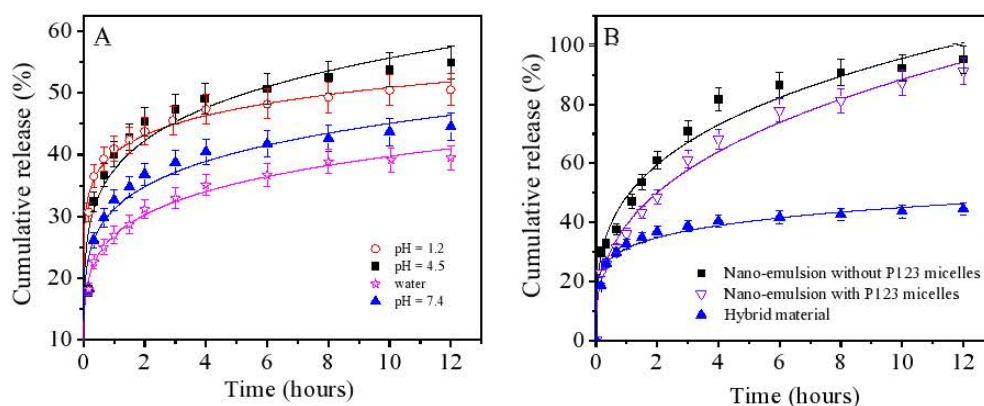


Figure 5 : Profiles of the cumulative release of ketoprofen from the hybrid material as a function of receptor solution pH (A) and from both the nano-emulsion and the hybrid material in PBS solution at pH = 7.4 (B). The scatters correspond to the experimental data and the solid lines to the fitted curves obtained with the Korsmeyer-Peppas model.

From this figure it appears that ketoprofen release is favored under acidic conditions. Indeed, after 5 hours the quantity of discharged drug varies from 43 to 53% when the pH is decreased from 7.4 to 4.5. The lowest value, 39%, is obtained in deionized water. This behavior is quite unexpected, since taking into account the pKa of ketoprofen, which is around 4.2-4.4^[46], the opposite would be expected as observed for ketoprofen loaded in pure mesoporous silica SBA-15 material^[26] or ibuprofen in MCM-41^[47]. Indeed, for a carboxylic acid drug, it has been shown previously that increasing pH would enhance the solubility and consequently the release amount, particularly at $\text{pH} > \text{pKa}$ of the acid. When pH increases, carboxylic acid groups become deprotonated, which should lead to an increase of the ketoprofen solubility and as a consequence, a higher released amount would be expected. However, our experiments show the opposite trend. This surprising phenomenon has already been reported in literature by Laniecki et al.^[26] or by Van Speybroeck et al.^[48] for SBA-15. The authors explained that in the matrix, under acidic conditions ketoprofen can locally precipitate. Since, some ketoprofen molecules, which have not precipitated, have migrated into the receptor solution, the ionic equilibrium is shifted and the precipitated ketoprofen can dissolve. As a consequence, further amounts of drug are released from the pores of the support. The enhancement of the ketoprofen release under acidic conditions thus results from shifted ionic equilibrium in acidic medium and from precipitation of acidic ketoprofen.

Here, we can assume that such behavior also occurs for the hybrid material, since the pH used in the synthesis is very low (0.3), and also because the silicic acid species produced by TMOS hydrolysis^[49] and the subsequent oligomerization of these species also contributes to maintain strong acidic conditions. The effect of the generated silicic acid species on pH has already been reported for the synthesis of the ordered mesoporous materials^[50]. For example, when the synthesis occurs through the cooperative templating mechanism using $\text{C}_{16}(\text{EO})_{10}$ micellar solutions, at 10 wt.% surfactant, it has been shown that under acidic conditions ($\text{pH} <$

5) no variation of pH was observed, but a decrease of pH was found upon addition of the inorganic precursor when the initial pH value is higher than 5. After the addition of TMOS, the pH of the solutions decreases to 5.5, 6.5 and 7 if the initial values are 7, 8.5 and 10, respectively. In the study reported here, we can therefore assume that when in contact with surface acidic groups of the hybrid material, the pH in the vicinity around the surface will also be locally modified, in particular for PBS solution at pH 7 and 7.4, affecting the solubility of ketoprofen and its release rate.

As the nanocarrier is synthesized and mineralization occurs around the nano-emulsion droplets that contain the drug, in the presence of Pluronic micelles, for comparison we have also looked at the release of ketoprofen from the nano-emulsions with and without P123 micelles in a PBS solution (Fig. 5B). To avoid any precipitation due to acidic conditions, the pH of the receptor solution has been fixed to 7.4. A fast release of ketoprofen, around 80% after 5 hours, from nano-emulsions without P123 micelles is observed. It should be noted that in the presence of P123 micelles a rapid burst release occurs, even if comparing with the hybrid material. For example after 4 hours, 82% and 68% of ketoprofen are released from the nano-emulsions without and with Pluronic micelles, respectively. Since both experiments have been performed under the same conditions (same loading of drug in the nano-emulsions and same pH of the receptor solution) this indicates that after being released from the oil droplets, a fraction of the drug molecules is solubilized in the P123 micelles. Therefore, in both cases ketoprofen release is faster than in the hybrid material (Fig. 5B). For example, 71 and 61% of active agent are released from nano-emulsions after 3 hours, in absence and presence of Pluronic, respectively, whereas only 39% of the drug is released from the hybrid material within the same period. Therefore, it can be concluded that the hybrid material is a promising drug delivery system for a sustained and slow release, in contrast to nano-emulsions, which could be appropriate when a fast response is required, like in oral or topical

administration of drugs. By contrast, the hybrid material will be a better candidate, for example, for the treatment of osteoporosis and osteoarthritis, in which the release rate of the drug should be as slow as the bone reconstruction. Another potential application concerns the use of nanocarriers in cancer therapy by chosen mitochondria as target sites. Indeed in literature there are only few reports dealing with nanoparticle-based delivery platforms to target and deliver therapeutic drugs to mitochondria^[51]. For example Zhao et al.^[51] have reported the use of mesoporous nanoparticles to deliver the anticancer drug doxorubicin (DOX) to mitochondria.

Based on the above observations, we propose the following scheme for the release of ketoprofen from the hybrid material. After mixing the nano-emulsions loaded with ketoprofen and the P123 micellar solutions, TMOS is immediately added and its hydrolysis occurs. Hydrogen-bonds between hydrogen atoms of hydrolyzed TMOS and both of the oxygen atoms of the oxyethylene groups of the $C_{12}(EO)_4$ and P123 surfactants are formed, leading to the formation of a hybrid-silica containing the drug, also labeled as the nanocarrier. The oil droplets are the imprints of the macropores and the micelles involve the formation of the mesopores network, which constitutes the macropore walls. During the release experiments, the receptor solution penetrates into the nanocarrier and the ketoprofen, entrapped into the oil droplets, dissolves into the receptor medium. Consecutively, due to the connection between the macro and the mesopore networks, a part of the ketoprofen molecules can diffuse and solubilize in the core of the Pluronic micelles, which act as a stabilizing cage. So they remain entrapped in the hybrid material. Since the micelles are embedded in the silica, release of ketoprofen from the micelles is more difficult. Silica behaves as a barrier for the diffusion of the drug molecules. This can explain why under the same conditions a lower amount of drug is released from the hybrid material than from the nano-emulsions.

To go further with the release mechanism, the experimental data can be fitted to different kinetic models. The commonly used mathematical models for evaluating drug release kinetics are zero order or first order, or Higuchi or Korsmeyer–Peppas models^[52]. The equation corresponding to the latter model is $Q_t = k t^n$, where Q_t , k and n stand for the fraction of drug released at time t ; the kinetic and the diffusional release exponent, respectively. The value of n provides information about the diffusion modes. The Korsmeyer–Peppas model provides acceptable fits for the ketoprofen release from the hybrid material in the receptor solution at various pHs and from the nano-emulsions, in the presence or absence of Pluronic micelles, as shown in Figure 5 (straight lines). By plotting Q_t versus $\log(t)$, the values of n and k as well as the correlation coefficient (R^2), can be calculated. Results are gathered in Table 1.

Table 1 : Release kinetic parameters, calculated by fitting the Korsmeyer-Peppas model, to ketoprofen release from both the hybrid materials and the nano-emulsions

Sample	Korsmeyer-Peppas model: $Q_t = k t^n$		
	R^2	k ($\text{mg}\cdot\text{h}^{-1}$)	n
Nano-emulsion without P123	0.97	0.20	0.36
Nano-emulsion in the presence of P123	0.97	0.15	0.40
Hybrid release at pH 7.4	0.94	1.65	0.24
Hybrid release at pH 7	0.98	1.40	0.20
Hybrid release at pH 4.5	0.94	2.00	0.28
Hybrid release at pH 1.2	0.86	2.10	0.13

Whatever the vehicles or the pH of the receptor solution, the value of n is lower than 0.5, showing a pseudo-Fickian release mechanism. This means a fast release in the beginning, followed by a sustained slow release. Looking at the k values (Table 1), it can be also noticed that the release from the hybrid material is faster than from nano-emulsions. For release at pH 7.4 of the receptor solution, k values are 1.65, 0.19 and 0.15 for the hybrid material and the nano-emulsions without and with P123 micelles, respectively. Concerning the variation of the

pH of the receptor solution, a higher release rate from the hybrid material is obtained with decreasing the pH.

To go further into the release mechanism, the release profiles have also been fitted considering the alternative models mentioned above: Higuchi, first-order and second-order release models (Table 2). Considering the correlation coefficient, R^2 , obtained from fitting the different kinetic equations, ketoprofen release from the hybrid material could follow the Higuchi model, suggesting that the drug releases by diffusion and that process is controlled by the vehicle. From Table 2 it appears also that the first order release model can also be applied for the release of ketoprofen in the case of nano-emulsions, meaning that the drug is released by diffusion controlled mechanism, and that its released rate depends greatly on the concentration of loaded drug during the loading stage.

Table 2 : Different kinetic models fitted to the release profiles of ketoprofen, from the hybrid material and from nano-emulsions, to the receptor solutions.

Sample	Higuchi		Zero-order		First-order	
	R^2	k_H ($\text{mg.h}^{-1/2}$)	R^2	k_0 (mg.h^{-1})	R^2	k_1 (h^{-1})
Nano-emulsion	0.94	0.17	0.94	0.11	0.97	0.068
Nano-emulsion + P123	0.96	0.14	0.94	0.084	0.98	0.054
Hybrid – pH 7.4	0.99	2.35	0.92	1.58	0.86	0.058
Hybrid – water	0.98	2.13	0.90	1.06	0.90	0.027
Hybrid – pH 4.5	0.96	2.70	0.88	1.56	0.85	0.021
Hybrid – pH 1.2	0.98	3.50	0.92	1.54	0.80	0.071

Higuchi : This model describes drug release as a diffusion process based in the Fick's law, square root time dependent. $Q_t = k_H t^{1/2}$ where Q_t is the amount of drug released in time t and k_H Higuchi's release rate constant.

Zero-order : It describes a system where the drug release is controlled by the diffusion across the membrane, while it is independent of the vehicle. $Q_t = Q_0 + k_0 t$ where Q_t is the amount of drug released in time t , Q_0 is the initial amount of drug in the solution and k_0 is the zero order release constant.

First-order : This model describes the release of drug from a system where the release rate is concentration dependent. $Q_t = Q_0 e^{-k_1 t}$ where Q_t is the amount of drug released in time t , Q_0 is the initial amount of drug in the solution and k_1 is the first order release constant.

In vitro release of ketoprofen from the bare hierarchical porous silica

The release profile from the hybrid material was compared to the one from the hierarchical bare silica (Fig. 6) in which the ketoprofen was impregnated. In that case, the results showed that the release of ketoprofen is very limited and did not exceed 8%, which was reached within few minutes. This is probably due to the low solubility of ketoprofen in the aqueous phase. The solubilization rate of poorly soluble acid drugs can be improved by the presence of surfactants in the release medium^[53,54], for example Choi et al^[54] have reported that the solubility of ibuprofen (pKa = 4.4) in a buffer solution at pH = 1.2 is increased from 11.0 to 1415 $\mu\text{g}\cdot\text{mL}^{-1}$ when 1% (w/v) of polysorbate 80 is added.

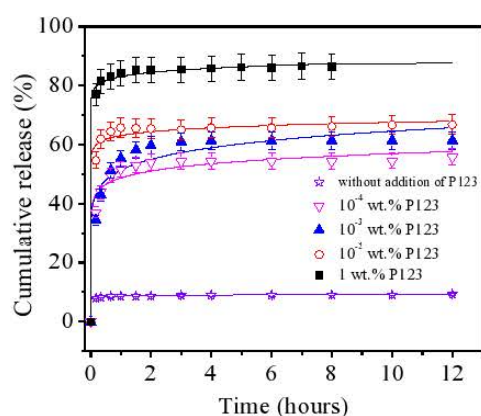


Figure 6 : Profiles of the cumulative release of ketoprofen from the hierarchical bare silica. The scatters correspond to the experimental data and the solid lines to the fitted curves obtained with the Korsmeyer-Peppas model. The receptor solution is PBS at pH = 7.4 and various concentration of P123 surfactant have been added in the receptor solution.

Here, we have investigated the effect of the addition of Pluronic P123 in the PBS solution on the release of ketoprofen from the bare porous silica. The concentration of the Pluronic in the receptor solution was varied from 10^{-4} to 1 wt.% in order to be above the CMC value ($4.4 \cdot 10^{-6}$ mol.L⁻¹, i.e. $2.5 \cdot 10^{-5}$ wt.%)^[55]. Indeed, in such dissolution process, it is assumed that

solubilization occurs by partitioning of the drug into surfactant micelles. Both the free and ionized acid forms of ketoprofen molecule should be considered. From Figure 6, a beneficial effect of the presence of the Pluronic micelles in the PBS solution on the ketoprofen release is noted. Indeed, after 10 minutes the amount of the released drug is increased from 8 to 77%, when the P123 concentration varies from 0 to 1 wt.%. The release medium penetrates into the silica matrix through pores and ketoprofen dissolves into it, allowing its diffusion from the system along with the solvent filling pore channels. The solubility of ketoprofen in the release medium increases with Pluronic content in the PBS solution. And consequently the amount of released drug increased. Therefore, in any case a burst release of ketoprofen is noted and a plateau is reached after 40 minutes. This is due to weak interactions between the drug and the silica. This rapid release is usually observed when poorly soluble drug are adsorbed on unmodified bare silica material, which is a rather hydrophilic substrate^[26,43,47]. Similarly to hybrid materials and nano-emulsions, the profiles of cumulative release of ketoprofen from the hierarchical bare silica have been fitted to the Korsmeyer-Peppas model (straight line in Fig. 6). The values of n , given in Table 3, are lower than 0.5, suggesting also a pseudo-Fickian release mechanism. The calculated k constants confirmed faster release when the P123 concentration is increased.

Table 3 : Release characteristics obtained from the Korsmeyer-Peppas model of ketoprofen from the bare hierarchical porous silica

Sample	Korsmeyer-Peppas		
	R^2	K ($\text{mg}\cdot\text{h}^{-1}$)	n
Bare silica – 0% P123	0.94	0.35	0.04
Bare silica – 10^{-5} % P123	0.96	2.10	0.18
Bare silica – 10^{-3} % P123	0.98	2.25	0.25
Bare silica – 10^{-2} % P123	0.86	2.70	0.09
Bare silica – 1% P123	0.90	3.40	0.04

Conclusions

O/W Nano-emulsions of 100 nm diameters are prepared by the Phase Inversion Temperature (PIT) method in the Remcopal 4 /decane /water system. These nano-emulsions are mixed to silica precursor solutions, and mineralization was performed in the emulsion external phase, obtaining meso/macroporous dual silica materials, by a dual templating mechanism with micelles and nano-emulsions. The material has hexagonally ordered mesopores of 9.3 nm and macropores around 240 nm, as well as a high surface area of 782 m²/g and a large pore volume of 1.2 cm³/g. Without removing the organic components, the hybrid organic/inorganic nanocomposite can perform as a nanocarrier, by pre-dissolving ketoprofen in the nano-emulsions. The results show that such nanocarrier can release up to 43 wt.% of the drug in a phosphate buffer at pH 7.4. The release reaches 53 wt.% at pH 4.5, indicating a pH responsive system for the release of ketoprofen. In addition, during the release process a fraction of the ketoprofen molecules solubilize into the P123 micelles, added to induce the mesostructure. The Pluronic micelles act as a stabilizing cage, whereas the silica shell performs as a barrier against diffusion of the drug molecules. In any case, the organic/inorganic hybrid materials allow to achieve a slow and sustained drug release.

By contrast, due to its low solubility in the aqueous phase, only a weak fraction of ketoprofen can be released to the PBS solution at pH = 7.4, after impregnation of this drug in the bare meso/macrostructured silica. The solubility of ketoprofen is increased by the addition of Pluronic micelles in the receptor solution and a maximum of 87 wt.% of release can be reached when 1 wt.% of P123 is added in the PBS solution. Therefore, in the case of bare meso/macrostructured silica, the release is surfactant-assisted.

Release profiles from the different vehicles have been fitted to commonly used mathematical models, for evaluating the release kinetics of the drug. In all cases a pseudo-Fickian release mechanism is observed.

Experimental section

Remcopal 4 (commercial name) it is a technical grade nonionic ethoxylated surfactant, which mainly consists of a hydrogenated carbon chain with 12 carbons and the average number of polyoxyethylene is 4. It is noted as $C_{12}(EO)_4$. This surfactant was provided by CECA. The triblock copolymer P123 $[(EO)_{20}(PO)_{70}(EO)_{20}]$ and decane were purchased from Aldrich. Deionized water, obtained using a Milli-Q water purification system, was used to prepare the various samples.

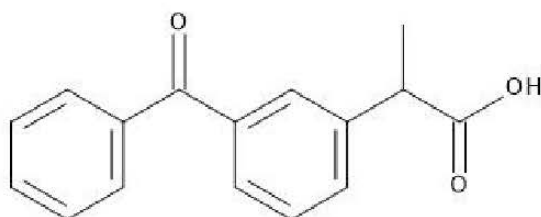
Carriers preparation and ketoprofen loading : The O/W nano-emulsions were formulated from the system: water, Remcopal 4 ($C_{12}EO_4$) and decane ($C_{10}H_{22}$) using the PIT method. A mixture of 6.6 wt.% of Remcopal, 73.4 wt.% of deionised water acidified with HCl (pH 0.3), and 20 wt.% of decane was prepared in a glass tube and stirred using a vortex. The mixture was heated to 40°C, then quickly cooled to 5°C, forming O/W nano-emulsions, which were stored at room temperature (25°C).

Hierarchical porous silica was synthesized according a dual templating mechanism, using previously prepared nano-emulsions as imprints for the macropore network, and P123 micelles to induce the formation of mesoporosity. In a typical synthesis, 50% in volume of both the nano-emulsions and aqueous Pluronic micellar solutions were mixed. In the final mixture the content of Remcopal, Pluronic P123 and decane were 3.3, 10 and 2.5 wt.%, respectively, and the pH was kept at 0.3. After homogenization of the sample, 2.6 g of tetramethoxysilane (TMOS), the silica source, were added. The mixture was stirred at room temperature for 1 hour, using a magnetic stirrer. Then, it was transferred and sealed in a Teflon autoclave, which was heated at 40°C for 24 hours and afterwards at 70°C for 24 hours. To eliminate surfactants, oil and methanol (generated by TMOS hydrolysis), Soxhlet extraction with ethanol for 48 hours was then performed. After this extraction and the

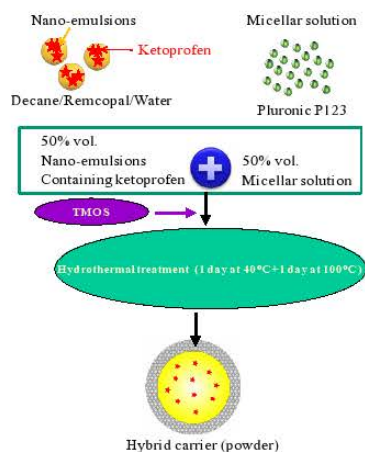
subsequent drying at room conditions, a white silica powder was obtained, which was designated to be the bare hierarchical silica.

Using nano-emulsions as carriers, ketoprofen (scheme 1) was incorporated into the oil, Remcopal 4 mixture and fully dissolved before the addition of water and the nano-emulsions are formed via the PIT method as described above. The samples were kept in a water bath at 25.0°C. To use the hybrid materials as carriers, ketoprofen was first loaded in the nano-emulsions. Second, 50% in volume of both the nano-emulsions containing the drug and aqueous Pluronic micellar solutions were mixed prior the addition of TMOS. Then, the mixture was transferred and sealed in a Teflon autoclave, which was heated at 40°C for 24 hours and afterwards at 70°C for 24 hours. After this step a powder material was obtained, which was designated to be the hybrid material loaded with ketoprofen (Scheme 2).

For comparison, ketoprofen was also encapsulated in the bare silica material using the impregnation method. In that case 50 mg of the drug was dissolved in 5 ml of hydro-alcoholic solution (1:1), and then the solution was dispersed homogeneously on 2 g silica particles. The whole mixture is heated at 60°C for 24 hours. The sample was considered dry when its weight became constant.



Scheme 1 : Chemical structure of ketoprofen.



Scheme 2 : Preparation of the hybrid material loaded with ketoprofen.

In any case, the quantity of encapsulated drug was calculated to make 2.5 wt.% of the final product. This ratio corresponds to the typical dosage embedded in commercial formulations^[2].

Characterization : SAXS measurements were carried out using a SAXSess mc2 (Anton Paar) apparatus. It is attached to a ID 3003 laboratory X-Ray generator (General Electric), equipped with a sealed X-ray tube (PANalytical, $\lambda_{Cu (K\alpha)} = 0.154$ nm, V = 40 kV, I = 50 mA). A multilayer mirror and a block collimator provide a monochromatic primary beam. A translucent beam stop allows the alignment of an attenuated primary beam at $q = 0$. Porous materials are introduced into a powder cell, whereas nano-emulsions are placed in a Quartz capillary having a diameter of 1 mm, before being placed inside an evacuated chamber equipped with a temperature controlled sample holder unit. Acquisition times are typically in the range of 1 to 5 minutes for porous materials, of 20 minutes to 1 hour for nano-emulsions. Scattering of X-ray beam is recorded by a CCD detector (Princeton Instruments, 2084 x 2084 pixels array with 24 x 24 μm^2 pixel size) in the q range 0.3 to 5 nm^{-1} . The detector is placed at 309 mm from the sample holder. Concerning the nano-emulsions, the data were corrected for the background and the solvent (water) scattering. The scattering intensities were evaluated on an absolute scale using water as reference. A Malvern zetasizer 3000HSa instrument was used to measure the size of the nano-emulsions in water by dynamic light scattering. The Helium-Neon laser, 5mW operates at 633nm, with the scattering angle fixed at 90°. The sample is contained in a flow-through cell kept at 25°C. All the measurements were performed in suitable conditions by systematically diluting three times the samples with water to validate the results. Water was first filtered with a mixed cellulose ester (surfactant free) filter (0.45 μm). The attenuator (diaphragm) of the photomultiplier was automatically adapted for each sample to prevent detector saturation. The data were analyzed by the CONTIN method and the size was provided by an intensity distribution. Nanoparticle tracking analysis (NTA) measurement was performed with a NanoSight NS300 of Malvern equipped with a sample chamber and a

635 nm laser. Samples for transmission electron microscopy (TEM) analysis were prepared by crushing some material in Chloroform. Afterwards a drop of this suspension was placed on a holey carbon coated copper grid. A Philips FEI XL30 FEG microscope with an accelerating voltage = 7 kV was used to record the scanning electron microscopy images. The infrared spectra were recorded on the Fourier transform infrared spectrometer SHIMADZU IRAffinity-1, equipped with a PIKE diamond GladiATR. To perform the analysis, the sample is spread directly on the diamond window and stabilized with a stainless steel handle. The measurements were made in absorbance mode and a resolution of 2 cm^{-1} . N_2 adsorption and desorption isotherms were determined on a Micromeritics TRISTAR 3000 sorptometer at $-196\text{ }^\circ\text{C}$. The pore diameter, the pore size distribution and the cumulative pore volume were determined by the BJH (Barret, Joyner, Halenda) method applied to the adsorption branch of the isotherm^[56]. Macropores were detected using mercury porosimetry on a Micromeritics Autopore IV 9500. The penetrometer (stem volume = 0.412ml, penetrometer volume = 1ml) was filled with 0.1g of the sample. A low pressure (0.1 to 15 psia) followed by a high pressure analysis (15 to 60 000 psia) were done in order to detect pores down to 5 nm in diameter, the equilibration time is 10 seconds.

In vitro release experiments : 0.2 g of nano-emulsions, hybrid material or silica containing ketoprofen was filled in a dialysis bag (Molecular Weight Cut Off 12000 - 14000 Da) and immersed in a beaker containing a receptor solution consisting, in most cases, of a phosphate buffer solution at pH 7.4. The solution was stirred at 150 rpm with a magnetic stirrer. The beakers contained 150 ml of buffer solution to insure sink conditions, i.e. the concentration of the drug in the receptor solution was always lower than 10% of its solubility in this medium. All experiments were carried at room temperature. To assist the release of ketoprofen from the bare silica material, micelles of P123 were eventually added in the PBS solution. In the case of the hybrid material, the pH of the receptor solution was varied from 1.2 (pH of the

gastric fluid) to 7.4 (considered to be the pH of blood and of intestinal fluid). This allows simulating the behavior of the material after oral administration. Acidic medium (pH = 1.2 hydrochloric acid buffer, pH = 4.5 acetic buffer), deionized water (pH \approx 6.5) and PBS (pH = 7.4) have been considered as receptor solutions. Aliquots of 4 ml were taken at regular time intervals and replaced with 4 ml of fresh solution; the dilution effect was taken into account in the calculations. The samples were analyzed using a LAMBDA 1050 UV/Vis/NIR Spectrophotometer at 260 nm. In all cases, the release experiments were conducted in three replicas to confirm the results. The error between the three measurements should not exceed 5 %.

References

- [1] P. Sarzi-Puttini, F. Atzeni, L.Lanata, M. Bagnasco, M. Colombo, F. Fischer, M. D'Imporzano, *Reumatismo* **2010**, *62*, 172-188.
- [2] S. Coaccioli, *Eur. Rev. Med. Pharmacol. Sci.* **2011**, *15*, 943-949.
- [3] A.V. Kabanov, E. Batrakova, V.Y. Alakhov, *J. Controlled Release* **2002**, *82*, 189-2012.
- [4] Y. Zhang, P. Lundberg, M. Diether, C. Porsch, C. Janson, N. A. Lynd, C. Ducani, M. Malkoch, E. Malmström, C.J. Hawker, A. M. Nyström, *J. Mater. Chem. B.* **2015**, *3*, 2472-2486.
- [5] Z. Wei, J. Hao, S. Yuan, Y. Li, W. Juan, X. Sha, X. Fang, *Int. J. Pharm.* **2009**, *376*, 176-185.
- [6] M.J. Lawrence, G.D. Rees, *Adv. Drug Delivery Rev.* **2009**, *45*, 89-121.
- [7] M.D. Chatzidaki, N. Arik, J. Monteil, V. Papadimitriou, F. Leal-Calderon, A. Xenakis, *Colloids Surf. B*, <http://dx.doi.org/10.1016/j.colsurfb.2015.04.053>.
- [8] D.H. oh, J.H. Kang, D.W. Kim, B.J. Lee, J.O. Kim, C.S. Yong, H.G. Choi, *Int. J. Pharm.* **2011**, *420*, 412-418.
- [9] S. Setthacheewakul, S. Mahattanadul, N. Phadoongsombut, W. Pichayakorn, R. Wiwattanapatapee, *Eur. J. Pharm. Biopharm.* **2010**, *76*, 475-485.
- [10] N. Sadurní, C. Solans, N. Azemar, M.J. García-Celma, *Eur. J. Pharm. Sci.* **2005**, *26*, 438-445.
- [11] D. Mou, H. Chen, D. Du, C. Mao, J. Wan, H. Xu, X. Yang, *Int. J. Pharm.* **2008**, *353*, 270-276.
- [12] N. Ahmad, R. Ramsch, M. Llinàs, C. Solans, R. Hashim, H.A. Tajuddin, *Colloids Surf. B* **2014**, *115*, 267-274.

- [13] C. Fornaguera, A. Dols-Perez, G. Calderó, M.J. García-Celma, J. Camarasa, C. Solans, *J. Controlled Release* **2015**, *211*, 134-143.
- [14] S. Calligaris, P. Comuzzo, F. Bot, G. Lippe, R. Zironi, M. Anese, M.C. Nicoli, *LWT-Food Sci. Technol.* **2015**, *63*, 77-84.
- [15] S.M. Dordević, N.D. Cekić, M.M. Savić, T.M. Isailović, D.V. Randelović, B.D. Marković, Saša R. Savić, T. T. Stamenić, R.Daniels, S.D. Savić, *Int. J. Pharm.* **2015**, *493*, 40-54.
- [16] C. Solans, P. Izquierdo, J. Nolla, N. Azemar, M.J. García-Celma, *Curr. Opin. Colloid Interface Sci.* **2005**, *10*, 102-110.
- [17] T.G.Mason, J.N. Wilking, K. Meleson, C.B. Chang, S.M. Graves, *J. Phys. : Condens. Matter.* **2006**, *18*, R635–R666.
- [18] K. Landfester, *Macromol. Rapid Commun.* **2001**, *22*, 896-936.
- [19] P. Izquierdo, J. Esquena, Th.F. Tadros, C. Dederen, M.J. Garcia, N. Azemar, C. Solans, *Langmuir* **2002**, *18*, 26-30.
- [20] S.L. Ee, X. Duan, J. Liew, Q.D. Nguyen, *Chem. Eng. J.* **2008**, *140*, 626-631.
- [21] A. Forgiarini, J. Esquena, C. González, C. Solans, *Langmuir* **2001**, *17*, 2076-2083.
- [22] L. Wang, X. Li, G. Zhang, J. Dong, J. Eastoe, *J. Colloid Interface Sci.* **2007**, *314*, 230-235
- [23] L. Wang, J. Dong, J. Chen, J. Eastoe, X. Li, *J. Colloid Interface Sci.* **2009**, *330*, 443-448.
- [24] M. Vallet-Regi, A. Rámila, R.P. del Real, J. Pérez-Pariente, *Chem. Mater.* **2001**, *13*, 308-311.
- [25] W. Xu, J. Riikonen, V.P. Lehto, *Int. J. Pharm.* **2013**, *453*, 181-197.
- [26] M. Moritz, M. Laniecki, *Appl. Surf. Sci.* **2012**, *258*, 7523-7529.
- [27] S. Wang, *Microporous Mesoporous Mater.* **2009**, *117*, 1-9.

- [28] L. Gao, J. Sun, L. Zhang, J. Wang, B. Ren, *Mater. Chem. Phys.* **2012**, *135* 786-797.
- [29] V. Mamaeva, C. Sahlgren, M. Lindén, *Adv. Drug Deliver. Rev.* **2013**, *65*, 689-702.
- [30] P. Botella, A. Corma, M. Quesada, *J. Mater. Chem.* **2012**, *22*, 6394-6401.
- [31] C. T. Kresge, W. J. Roth, *Chem. Soc. Rev.* **2013**, *42*, 3663-3670.
- [32] Y. Wan, D. Zhao, *Chem. Rev.* **2007**, *107*, 2821-2860
- [33] J. L. Blin, M. Impérator-Clerc, *Chem. Soc. Rev.* **2013**, *42*, 4071-4082.
- [34] F. Wang, S.L. Nimmo, B. Cao, M. Chuanbin, *Chem. Sci.*, **2012**, *3*, 2639-2645.
- [35] E. Kasotakis, A. Mitraki, *Biopolymers (Pept Sci)*, **2012**, *98*, 501-509.
- [36] C. Mao, F. Wang, B. Cao, *Angew. Chem.*, **2012**, *124*, 6517-6521.
- [37] S. Kerkhofs, F. Saïdi, N. Vandervoort, G. Van den Mooter, C. Martineau, F. Taulelle, J.A. Martens, *J. Mater. Chem. B* **2015**, *3*, 3054-3061.
- [38] M. Manzano, M. Vallet-Regi, *J. Mater. Chem.* **2010**, *20* 5593-5604.
- [39] T. Fontecave, C. Boissiere, N. Baccile, F.J. Ploun C. Sanchez, *Chem. Mater.* **2013**, *25*, 4671-4678.
- [40] Y.H. Son, M. Park, Y.B. Choy, H.R. Choi, D.S. Kim, K.C. Park, J.H. Choy, *Chem. Commun.* **2007**, *27*, 2799-2801.
- [41] L.Y. Xu, Y.Y. Huang, T. Long, Z.G. Shi, *Mater. Manuf. Processes* **2013**, *28*, 626-630.
- [42] F. Qu, H. Lin, X. Wu, X. Li, S. Qiu, G. Zhu, *Solid State Sci.* **2010**, *12*, 851-856.
- [43] E. Santamaría, A. Maestro, M. Porras, J.M. Gutiérrez, C. González, *J. Solid State Chem.* **2014**, *210*, 242-250.
- [44] G. Porod, in *Small Angle X-ray Scattering*, O Glatter, O. Kratky (Eds.), Academic Press, 1982, pp 17-51.
- [45] P. Sancin, O. Caputo, C. Cavallari, M. Passerini, L. Rodriguez, M. Cini, A Fini, *Eur. J. pharm. Sci.* **1999**, *7*, 207-213.
- [46] T.X. Bui, V.H. Pham, S.T. Le, H. Choi, *J. Hazard. Mater.* **2013**, *254-255*, 345-353.

- [47] C. Charnay, S. Bégu, C. Tourné-Péteilh, L. Nicole, D.A. Lerner, J.M. Devoisselle, *Eur. J. Pharm. Biopharm.* **2004**, *57*, 533-540.
- [48] M. Van Speybroeck, R. Mols, R. Mellaerts, T.D. Thi, J.A. Martens, J. Van Humbeeck, P. Annaert, G. Van den Mooter, P. Augustijns, *Eur. J. Pharm. Biopharm.* **2010**, *75*, 354-365.
- [49] C.J. Brinker, G.W. Scherer, *The physics and chemistry of sol-gel processing*, Academic Press Inc., San Diego, **1990**, p 97.
- [50] A. Léonard, J.L. Blin, P.A. Jacobs, P. Grange, B.L. Su, *Microporous Mesoporous Mater.* **2003**, *63*, 59-73.
- [51] Q. Qu, X. Ma, Y. Zhao, *Nanoscale*, **2015**, *7*, 16677-16686.
- [52] P. Costa, J.M.S. Lobo, *Eur. J. Pharm. Biopharm.* **2001**, *13*, 123-133.
- [53] J.J. Sheng, N.A. Kasim, R. Chandrasekharan, G.L. Amidon, *Eur. J. pharm. Sci.* **2006**, *29*, 306-314.
- [54] S.H. Park, H. K. Choi, *Int. J. Pharm.* **2006**, *321*, 35-41.
- [55] M. Y. Kozlov, N.S. Melik-Nubarov, E. V. Batrakova, A. V. Kabanov, *Macromolecules* **2000**, *33*, 3305-3313.
- [56] E.P. Barrett, L.G. Joyner, P.P. Halenda, *J. Am. Chem. Soc.* **1951**, *73*, 373-380.

1 Biocompatible nano-emulsions

In this work we have used the system Remcopal 4/decane/water which proved to be a very useful system for the formation of nano-emulsions and the preparation of silica materials and hybrid materials in the presence of P123 micelles, but this systems major drawback is its toxicity. Its incompatibility with the biological processes makes further investigation of its efficiency as a drug carrier impossible, thus arises the need for a biocompatible system with similar properties. For this, in a collaboration with the CSIC – IQAC and the Faculty of Pharmacy in Barcelona, the system consisting of Kolliphor EL, isopropyl Myristate and water which are all biocompatible components and for its capacity to form nano-emulsions using phase inversion composition is suggested as a replacement for the current system.

This system has been investigated by Solans *et al.*¹ and yielded the ternary phase diagram presented in Figure 1-1.

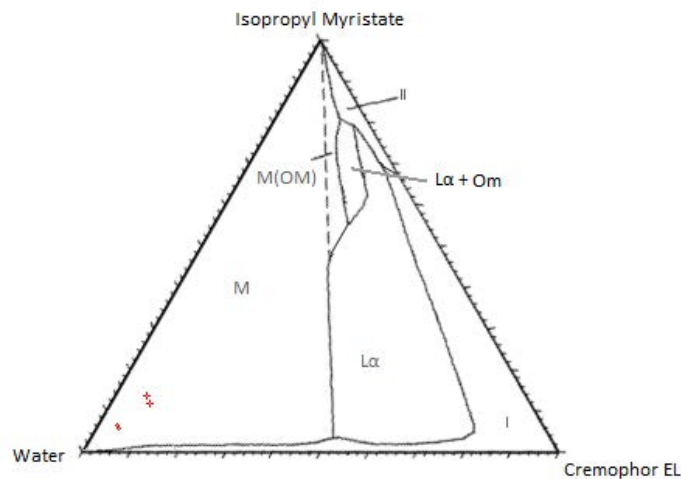


Figure 1-1: Ternary phase diagram of the Water/Cremophor EL/Isopropyl Myristate at 30°C. I: monophasic isotropic liquid phase; O_m : reverse micellar solution or W/O microemulsion; L_α : lamellar liquid crystalline phase; II: two-liquid isotropic phases; M: multiphase region; M(Om): multiphase region with an upper W/O microemulsion phase.¹

1.1 Formulation

The nano-emulsions were prepared using the Phase Inversion Concentration (PIC). At first, a mixture of Isopropyl Myristate and Kolliphor EL (previously known as Cremophor EL) was prepared. For the samples with Ketoprofen; the drug was added to the oil-surfactant mixture and dissolved completely before proceeding to the next step. Water was added slowly to the mixture, which was stirred using a magnetic stirrer at 700 rpm. 16 samples were prepared for the parameters given below.

Temperature = 25°C and 60°C,

Water content = 80 wt-% and 90 wt-%,

Oil/Surfactant ratio = 4/6 and 3/7.

The ratio of the encapsulated Ketoprofen was 1.2 wt-%.

The nano-emulsions were formed in a water bath with controlled temperature, and the final products were stored at 25°C.

1.2 Characterization

All freshly prepared nano-emulsions are optically transparent. The nano-emulsions were stored at 25°C for 7 days and the aspects of the solutions after this period were noted in the Table 1-1.

Table 1-1: Visual aspects of the nano-emulsions formed at 25°C and 60°C after 7 days at 25°C.

		Water 80%		Water 90%	
		25°C	60°C	25°C	60°C
Ketoprofen-free nano-emulsions	O/S = 4/6	Turbid	Creaming	Turbid	Creaming
	O/S = 3/7	Creaming	Creaming	Creaming	Turbid
1.2 wt% Ketoprofen-loaded nano-emulsions	O/S = 4/6	Transparent	Transparent	Demixing	Demixing
	O/S = 3/7	Transparent	Transparent	Demixing	Demixing

Those observations show that the nano-emulsions with 1.2 wt-% Ketoprofen were more stable than the nano-emulsions without Ketoprofen (Table 1-1). The samples that did not show any creaming were analyzed using the DLS technique (3D LS Spectrometer – LS Instruments) at a scattering angle of 90°C (Table 1-2 and Table 1-3) and ambient temperature (25°C).

The DLS measurements showed that there is a slight increase in the mean droplet radius (Cumulant analysis) with the decrease of the formulation temperature. The samples without Ketoprofen showed a mean droplet radius 10 to 20 times bigger than the samples with 1.2 wt-% Ketoprofen.

Table 1-2: Nano-emulsion droplet diameter measured by DLS (Cumulant analysis).

		Water 80%		Water 90 %	
		25°C	60°C	25°C	60°C
Ketoprofen-free nano-emulsions	O/S = 4/6	247.3	-	110.2	-
	O/S = 3/7	-	-	-	204
1.2 wt% Ketoprofen-loaded nano-emulsions	O/S = 4/6	14.57	12.96	9.17	8.89
	O/S = 3/7	13.68	13.07	8.91	10.08

Table 1-3: Nano-emulsion droplet diameter measured by DLS (Contin analysis).

		Water 80%						Water 90 %					
		25°C			60°C			25°C			60°C		
		O/S = 4/6	O/S = 3/7	O/S = 2/3	O/S = 4/6	O/S = 3/7	O/S = 2/3	O/S = 4/6	O/S = 3/7	O/S = 2/3	O/S = 4/6	O/S = 3/7	O/S = 2/3
Ketoprofen-free nano-emulsions	O/S = 4/6	28.5	163.5	489.7	-	-	-	18.2	140	855.5	-	-	-
	O/S = 3/7	-	-	-	-	-	-	-	-	-	56	282.3	135.4
1.2 wt% Ketoprofen-loaded nano-emulsions	O/S = 4/6	-	9.6	90.8	1.7	13.6	81.6	-	9.9	61.7	-	11.8	-
	O/S = 3/7	4.1	9.9	157.7	3.1	11.6	133.9	-	7.4	76.9	-	8	79.6

1.3 Release Experiment of the Ketoprofen from the Biocompatible Nano-emulsions

The release experiment was performed using nano-emulsions prepared at 25°C for 80 wt-% water, O/S = 3/7 and 1.2 wt-% Ketoprofen. Three ointment cells were loaded with the nano-emulsion ($\approx 0.8\text{g}/\text{cell}$), the release medium is the PBS (150 ml, pH = 7.4). The release profile of the Ketoprofen from the biocompatible nano-emulsions is plotted in Figure 1-2. The release reached 70 wt-% of the total Ketoprofen in 25 hours. The nano-emulsions exhibit a fast release rate making them more suitable for fast medical treatments.

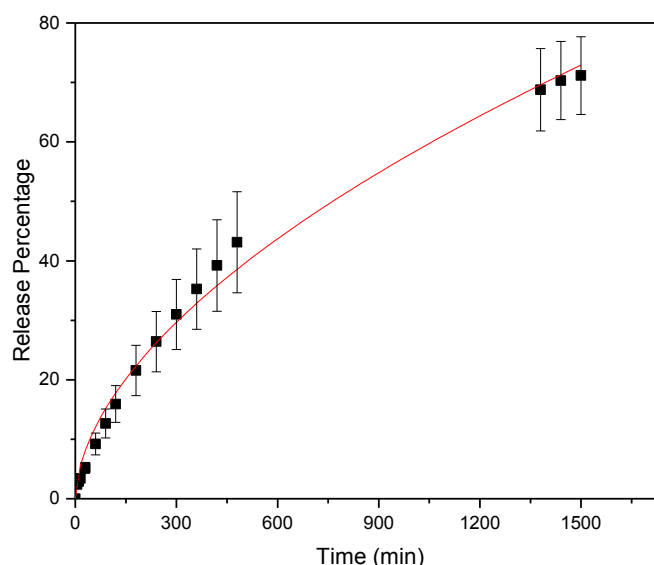


Figure 1-2: The release profile of ketoprofen from the nano-emulsion.

1.4 Silica materials templating

Furthermore, the nano-emulsions prepared for an O/S ratio of 3, a water content of 0.8 by PIC were used in the synthesis of hierarchical porous material. The preparation method is similar to the one described in Chapter III where the nano-emulsion is mixed with a micellar solution of P123 (5%) for a 1:1 ratio. The molar ratio of the surfactant and the silica precursor is also equal to 0.0025. The precursor is added dropwise to the nano-emulsion/micelle mixture and then transferred to an autoclave where it is heated at 40°C for 24 hours followed by a heating

at 100°C for 24 hours. The organic phase is extracted by ethanol using a Soxhlet for 48 hours. The resulting material is dried at room temperature.

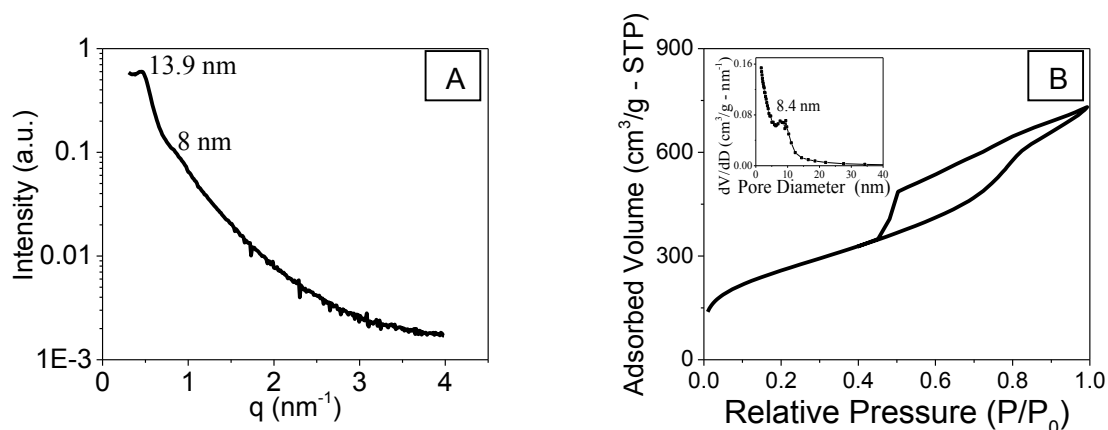


Figure 1-3: A) SAXS diffractogram for the silica material and B) the nitrogen sorption isotherm and pore size distribution.

The SAXS analysis of the material in Figure 1-3-A shows two peaks that are characteristic of a hexagonal organization of the channels. And Figure 1-3-B shows a type IV isotherm characteristic of mesopores. The pore size distribution indicate the presence of pores having a size centered at 8.4 nm. Moreover, this material shows a surface area of 930 m²/g and a pore volume of 0.9 cm³/g.

In conclusion, the initial results obtained for this system shows that it can be considered as a viable candidate for the elaboration of a new and innovative type of drug delivery system, nonetheless further studies and optimization are still required in order for this system to become a fully functional drug carrier.

2 References

- (1) Usón, N.; Garcia, M. J.; Solans, C. Formation of Water-in-Oil (W/O) Nano-Emulsions in a Water/mixed Non-Ionic Surfactant/oil Systems Prepared by a Low-Energy Emulsification Method. *Colloids Surfaces A Physicochem. Eng. Asp.* **2004**, 250 (1-3 SPEC. ISS.), 415–421.

**Lipase immobilization onto meso-
macroporous and dual mesoporous silica
materials**

Il existe une large gamme de supports pour les enzymes qui présentent des propriétés et des caractéristiques différentes. Dans le but de choisir le meilleur couple enzyme/support, la première étape consiste à rassembler le plus de renseignements possible sur les caractéristiques de l'enzyme comme sa taille, sa forme, sa structure sur les propriétés physico-chimiques, comme le point isoélectrique et sur propriétés de surface, comme la description des acides aminés de surface. Les applications industrielles des enzymes sont limitées car leur stabilité est fragile et la récupération est difficile. Alors dans le but d'ajuster ces problèmes, les enzymes peuvent être immobilisées sur un support solide. Dans cette étude, deux matériaux ayant chacun deux tailles de pores distinctes ont été utilisés comme matrice pour l'immobilisation d'un enzyme, la *Mucor miehei* lipase Mml. Cette enzyme permet la méthanolyse de l'huile de colza pour la transformer en biodiesel. L'immobilisation de cette enzyme requiert l'immersion de la matrice silicatée dans un milieu aqueux, ce qui met en question la stabilité des matrices dans ce milieu.

Le matériau silicaté est formé de tétraèdre de SiO_4 . A la surface il y a des groupes siloxanes avec l'oxygène orienté vers la surface ou bien différents types de silanols. Les matériaux silicatés sont donc sensibles à l'eau et les propriétés comme la stabilité thermique, hydrothermale et mécanique peut avoir un impact important pour les applications visées. Les chercheurs ont mis en évidence que la stabilité thermique est liée à l'épaisseur des parois des pores. D'un autre côté, la stabilité hydrothermale dépend de 3 facteurs, le degré de polymérisation ou la condensation, l'épaisseur des parois des pores ainsi que la structuration des pores.

Dans ce chapitre, tout d'abord sont comparées la stabilité thermique et hydrothermale de 2 types de matériaux silicatés ayant chacun 2 tailles de pores distinctes, le premier est méso-macroporeux et le second possède une double-mésoporosité.

La stabilité thermique des matériaux est évaluée en les chauffant dans un four tubulaire. La montée de température est réalisée sous air jusqu'à 550°C et pendant 1 heures un flux oxygène. La calcination du matériau méso-macroporeux cause une légère déstructuration du réseau de mésopores. De plus, la surface spécifique diminue de 780 à $630 \text{ m}^2/\text{g}$, le volume poreux de 1.2 à $0.8 \text{ cm}^3/\text{g}$, le diamètre des mésopores de 8.7 à 7.7 nm et le diamètre des macropores de 250 nm à 150 nm. Ceci indique que la calcination cause une contraction et une restructuration de la surface. D'un autre coté la calcination du matériau à double mésoporosité à plusieurs températures conduit à une déstructuration complète de la matrice ayant des petits pores alors que la matrice ayant des grands pores montre n'est quasiment pas déstructurée. La surface spécifique diminue de 11 à 15% et le volume poreux de 50%. Concernant la taille des pores, la distribution qui était initialement centrée sur 3.6 nm disparaît

quelle que soit la température de calcination, la distribution qui est centrée sur 9.4 nm persiste, mais avec une diminution de l'intensité dV/dD . Cette différence de stabilité entre les deux matrices du même matériau est attribuée à l'épaisseur de la paroi des pores, la matrice ayant des grands pores à une épaisseur 3.2 nm, alors que la matrice ayant des petits pores à une épaisseur de 2.4 nm.

Dans un deuxième temps, la stabilité hydrothermale a été évaluée en submergeant le matériau dans l'eau bouillante pendant 24 heures. Des échantillons sont prélevés à intervalle régulier pour étudier l'évolution de la structure et de la texture en fonction du temps d'immersion. La stabilité hydrothermale des matériaux méso-macroporeux calciné et non-calciné a été comparés. La caractérisation SAXS des échantillons prélevés à intervalle régulier montre que le matériau non calciné est déstructuré après 30 minutes, alors que le matériau calciné reste stable pendant 1 heure. La distribution de la taille des pores en fonction du temps d'immersion se comporte de façon similaire. De plus, la surface spécifique et le volume poreux du matériau non-calciné chutent brutalement durant les premières 90 minutes et après 24 heures 40% de la surface est perdue. Concernant le matériau calciné, la diminution du volume et de la surface est lente, après 24 heures la surface spécifique a chuté de 65% et le volume poreux de 30%. Les macropores résistant à l'eau bouillante et leur taille est maintenue durant toute la durée de l'expérience. L'analyse par FTIR des échantillons montre que le matériau non-calciné a une surface riche en silanols isolés qui sous l'effet de l'eau bouillante s'appauvrit légèrement après 24 heures, alors que pour le matériau calciné, on note une forte diminution de l'intensité du pic des silanols isolés qui disparaît après 24 heures. La faible teneur de silanols isolés dans le matériau calciné permet d'expliquer sa meilleure stabilité hydrothermale, car il y a moins de possibilité d'attaque de la surface par l'eau. Concernant le matériau à double mésoporosité, l'évaluation de sa stabilité hydrothermale montre que la matrice ayant des petits pores est déstructurée complètement après 3 heures et la matrice ayant des grands pores résiste mieux puisqu'elle est déstructurée seulement après 8 heures d'immersion dans l'eau bouillante. La surface spécifique diminue de 90% et le volume poreux de 80% après 24 heures d'immersion, indiquant une forte altération de la surface, ceci étant confirmé par analyse FTIR. La différence de comportement des deux matrices est due à l'épaisseur des parois, plus la paroi est épaisse plus la matrice est stable.

Ensuite, l'immobilisation de l'enzyme Mml par physisorption sur différents supports a été étudiée pour réaliser des réactions de transestérification sur le matériau méso-macroporeux calciné et sur le matériau à double mésoporosité. Les isothermes d'adsorption ont été établies pour déterminer le taux d'adsorption maximale de la Mml. Pour ce faire, le matériau est plongé dans un solution tampon de tris(hydroxyméthyl)aminométhane à pH 6 contenant la lipase à

différentes concentrations. Les échantillons sont ensuite analysés par FTIR pour quantifier la lipase adsorbée sur la silice. Le modèle de Langmuir permet d'obtenir des informations quantitatives comme les valeurs d'adsorption maximales (Γ_{max}) et les constantes de Langmuir (K_L) qui sont pour le matériau méso-macroporeux de 0.76 mg_{Mml}/mg_{Silice} et 3.81 mg/ml respectivement, et de 0.94 mg_{Mml}/mg_{Silice} et 12.7 mg/ml pour le matériau à double mésoporosité. Les propriétés texturales du matériau méso-macroporeux après adsorption de la Mml sont modifiées, la surface spécifique diminue légèrement de 630 à 600 m²/g et le volume poreux est fortement abaissé de 0.8 à 0.3 cm³/g. D'un autre côté la taille des mésopores et des macropores est restée inchangée. Concernant le matériau à double mésoporosité, les pores de petite taille ne sont plus détectables, et la taille des larges pores diminue de 9.6 à 7.6 nm, la surface spécifique est abaissée de 880 à 530 m²/g et le volume poreux de 0.94 à 0.38 cm³/g. Après l'immobilisation de l'enzyme, les réactions de transestérification ont été faites à partir des 2 types de matériaux dans les conditions optimales déterminées auparavant au laboratoire par J. Jacoby¹. Les échantillons sont analysés par spectrométrie de masse pour quantifier les esters méthylés produits. La vitesse initiale de la réaction pour le catalyseur méso-macroporeux est de 12.1 μmol/h, alors que pour le catalyseur à double mésoporosité la vitesse est de 7.6 μmol/h. Le nombre de "turnover" qui correspond au nombre de moles transformées pour une mole d'enzyme est de 3700 moles de substrat pour la matrice méso-macroporeuse, et pour la matrice à double mésoporosité de 3000 moles de substrats. Un autre point important est la recyclabilité du catalyseur, et les expériences montrent que la matrice méso-macroporeuse est recyclable 3 fois, tandis que la matrice à double mésoporosité est recyclable 4 fois.

La comparaison avec les résultats obtenus au laboratoire avec d'autres matrices mésoporeuses de type SBA-15 et méso-macroporeuses montre que plus le volume poreux est important plus la quantité d'enzyme immobilisée est importante. D'autre part, la présence d'une deuxième porosité améliore le transfert de masse et augmente la probabilité d'adsorption de l'enzyme. La plus faible adsorption maximale est d'ailleurs enregistrée pour le matériau de type SBA-15. Concernant l'activité enzymatique, la SBA-15 atteint 100% de conversion après 30 heures, le matériau méso-macroporeux après 50 heures, le matériau méso-macroporeux synthétisé à partir d'émulsions concentrées fluorées, et 75 heures pour le matériau à double mésoporosité. La vitesse initiale la plus élevée est celle du SBA-15 et la plus faible est pour le matériau à double mésoporosité. L'activité enzymatique croît avec l'augmentation de la taille des pores ; ce qui peut être expliqué par la facilitation de l'ouverture du couvercle de l'enzyme quand l'espace est suffisamment grand, aussi le large diamètre des pores facilite le transfert de masse et diminue le risque de blocage. Ainsi plus le diamètre poreux est grand plus ce processus est amélioré. Concernant la matrice à double

mésoporosité, l'activité enzymatique est la plus faible même si la taille des mésopores est la plus large, car lorsque les molécules d'enzyme sont dans les pores de petite taille l'ouverture du couvercle est inhibé, et empêche la réaction d'avoir lieu. De façon étonnante cette matrice est la plus performante en termes de recyclabilité car l'utilisation de cette matrice est prolongée grâce au transfert de l'enzyme des pores de petite taille vers les pores de grande taille.

1 Introduction

A wide array of carriers for enzyme immobilization exists with different properties and characteristics. So in order to choose the best enzyme/support couple, the first step consists of knowing the features of the enzyme such as its size, shape, structure and other characteristics such as the isoelectric point, and the amino acids on its surface. The applications in the industry of the enzymes is limited by their low stability and difficulty to be recovered, so in order to overcome those drawbacks the enzymes can be immobilized on solid materials². Ravindra *et al.* showed that enzymes immobilized on a support have increased stability and their denaturation is inhibited³. In this study two materials with two distinct pore sizes were used as matrixes for the immobilization of an enzyme, *Mucor miehei* Lipase. This enzyme allows the methanolysis of the Colza oil in order to transform it into biodiesel, and for this biocatalyst to be made, it must be submerged in an aqueous solution for long times which raises the question of the stability of those matrixes in aqueous solutions.

The silica material is made from interlinked SiO_4 tetrahedra. At the surface, there are either siloxane groups ($\equiv\text{Si-O-Si}\equiv$) with the oxygen on the surface, or one of several forms of silanol groups ($\equiv\text{Si-OH}$). The several types of surface silanols are isolated groups (or free silanols), where the surface silicon atom has three bonds into the bulk structure and the fourth bond attached to a single -OH group, vicinal silanols (or bridged silanols), where two single silanol groups, attached to different silicon atoms, are close enough to hydrogen bond. And finally, a third type of silanols, germinal silanols, consist of two hydroxyl groups that are attached to one silicon atom. The germinal silanols are too close to hydrogen bond each other, whereas the free hydroxyl groups are too far separated⁴.

The different applications impose some critical conditions on those materials, and properties such as thermal, hydrothermal and mechanical stability can have a high impact. Materials like the M41S have a poor hydrothermal stability in boiling water and steam which is the consequence of silicate hydrolysis due to the relatively thin amorphous silica walls^{5,6}. In fact, the thermal stability was found to be strongly related to the wall thickness and the silica precursor⁷. The hydrothermal stability is influenced by three factors. First of all, it was shown

that materials with very polymerized or condensed silica are less affected in boiling water conditions. Secondly, the thicker the pore wall thickness, the more stable the material. The third factor is the pore structure and affinity. It has been shown that the cubic MCM-48 has a lower structural degradation than that of the hexagonal mesoporous materials MCM-41⁸. In this section, a comparison of the thermal and the hydrothermal stability of two types of porous silica materials having two distinct pore sizes. The first one is the meso-macroporous silica described in the previous chapter. The second material is a dual-mesoporous silica developed in our group⁹. It consists of a silica material having two ordered interconnected pore networks templated by a mixture of hydrogenated micelles (Pluronic P123) and micelles of $C_8F_{17}C_2H_4(OC_2H_4)_9OH$ ($R^F_8(EO)_9$) via a self-assembly mechanism. This material have two pore sizes one at 9.4 nm and the second at 3.6 nm. In the second section, the immobilization of the *Mucor miehei* Lipase is studied and then in the third section the materials efficiency as catalysts is assessed by determining the kinetics of the transesterification reaction and the recyclability of the catalyst. Finally, the catalysts investigated here are compared to other catalysts studied in a previous work done in our group¹.

2 Thermal stability of the hierarchically porous the silica material

The thermal treatment of the silica material is employed to eliminate totally the organic phase, since the ethanol extraction can leave up to 9% of the surfactant in the silica matrix^{10,11}.

2.1 Thermal stability of the meso-macroporous silica material

The meso-macroporous silica material are subjected to heat in a tubular oven. The temperature profile is presented in Figure 2-1.

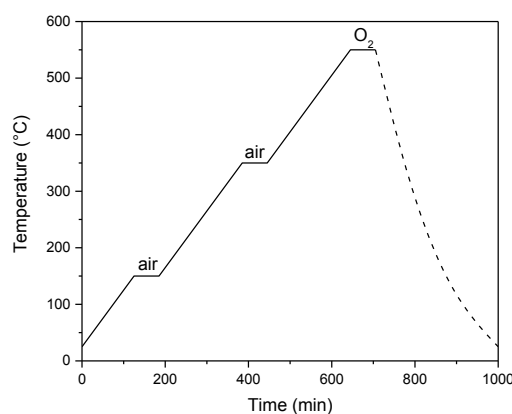


Figure 2-1: Calcination profile of the meso-macroporous silica materials.

SAXS patterns of the calcined meso-macroporous materials according to the profile of temperature presented in Figure 2-1 exhibit 3 peaks characteristic of the hexagonally ordered structure (Figure 2-2A), but those peaks are weaker than those of the un-calcined material. The calcination caused a decrease of the parameters of the hexagonal unit cell from 11 to 9.5 nm, this is linked to the shrinkage of the pores, this is generally due to an enhancement of the cross-linking¹². Nitrogen sorption isotherms for these material are similar to the isotherms of the un-calcined materials (Figure 2-2C), but the surface area decreases from 780 m²/g to 630 m²/g and the pore volume decreases from 1.2 cm³/g to 0.8 cm³/g

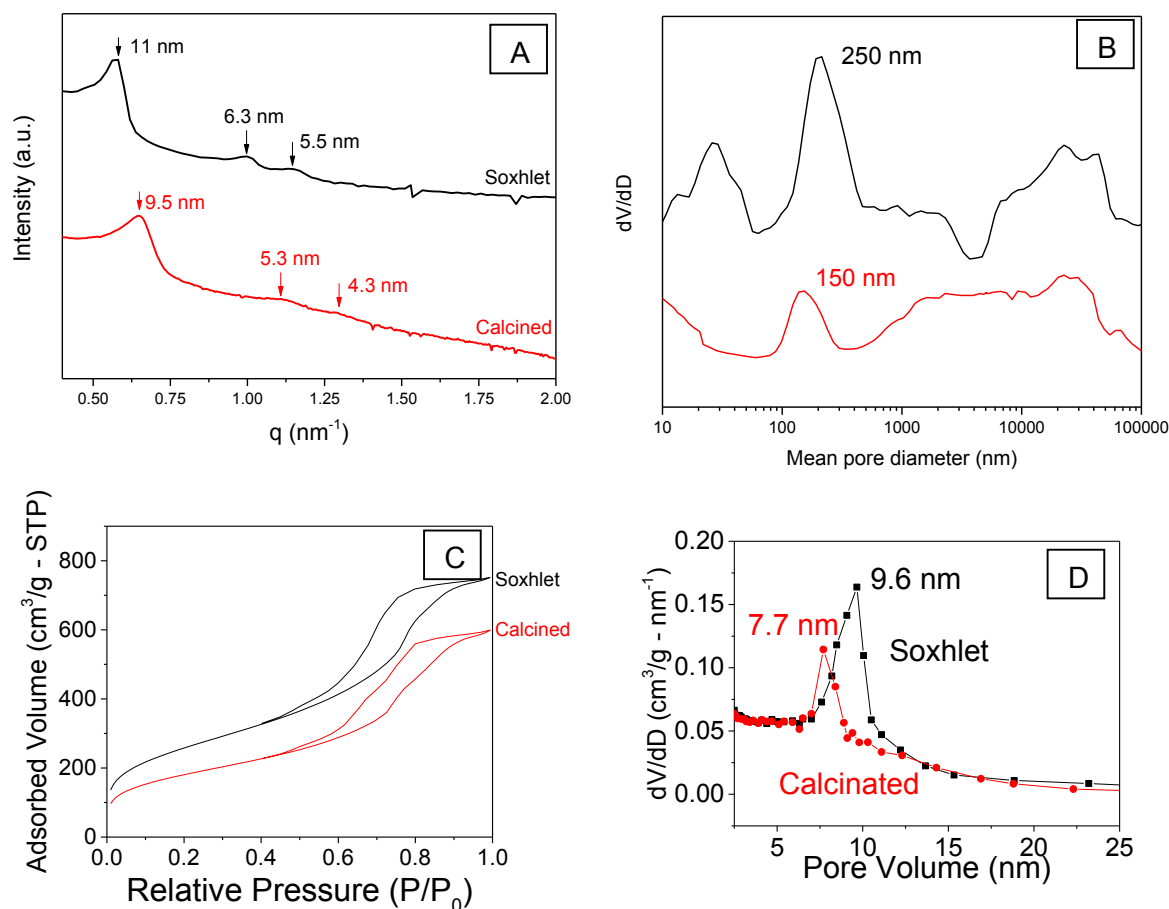


Figure 2-2: Comparison between the ethanol cleaned material and the calcined material, A) SAXS pattern, B) mercury intrusion porosimetry, C) nitrogen sorption isotherm and D) pore size distribution.

. The pore size distribution showed that after calcination the pore size decreased from 8.7 to 7.7 nm (Figure 2-2D), as well as the values of dV/dD. Mercury intrusion showed that the calcined material has a macropore size of 150 nm while the un-calcined material has a macropore size of 250 nm (Figure 2-2B). This shows that the thermal treatment of the meso-macroporous silica material causes the contraction of the mesopores as well as the macropores and a partial damage to the mesostructure. The decrease of the surface area and the pore volume indicate that not only contraction, but also surface reconstruction occurred

significantly on the pore walls of the calcined meso-macroporous material¹³. Furthermore, the pore wall thickness equal to 3.1 nm, remained unchanged after the calcination.

The calcination of the silica materials causes the reduction of the pores. The partial damage for the mesostructure can be attributed to the elimination of the surfactant, particularly by the purging of the ethylene oxide blocks from the silica walls. In turn void spaces in the walls promote structural collapse¹⁴. Moreover Gallarneau *et al.*¹⁵ determined a formula that allows the calculation of the mesoporous volume (V_{mes}) as well as the secondary porosity (micropores and interparticular porosity) volume (V_{sec}):

$$V_{mes} = \left(\frac{d}{1.05a_0} \right)^2 \times \left(V_p + \frac{1}{\rho_{SiO_2}} \right)$$

where d is the pore diameter (nm), a_0 is the lattice parameter (nm), V_p is the pore volume (cm^3/g) and ρ_{SiO_2} is the silica density ($2.2 \text{ g}/\text{cm}^3$). The secondary porosity volume is:

$$V_{sec} = V_p - V_{mes}$$

Those formulas has been applied to the calcined and non-calcined meso-macroporous materials and gave a value of $0.05 \text{ cm}^3/\text{g}$ and $0.26 \text{ cm}^3/\text{g}$ respectively. This further corroborates the fact that the calcination eliminates the micropores which is reflected here by an 80% decrease of the secondary porosity volume.

2.2 Thermal stability of the dual-mesoporous silica materials

In a previous work done in our laboratory, May *et al.*⁹ used a mixture of $R^F_8(\text{EO})_9$ and P123 as building blocks for the synthesis of a dual-mesoporous silica material with two hexagonally ordered mesoporous networks through the self-assembly mechanism. The mixture of those two surfactants in water (> 85%) yield a micellar solution where two kinds of micelles coexist, one having a size of 8 nm and corresponds to the pure $R^F_8(\text{EO})_9$ micelles, and the second having a size of 27 nm and corresponds to the size of $R^F_8(\text{EO})_9$ micelles that have accommodated P123. The final material shows two distinct pore size distributions, the largest one is centered on 9.4 nm and is attributed to the $R^F_8(\text{EO})_9/\text{P123}$ micelles and the smallest pore size is centered on 3.6 nm and is attributed to the pure $R^F_8(\text{EO})_9$ micelles

The thermal stability of the dual-mesoporous silica materials was evaluated at 350, 400 and 450°C. The samples were heated in a tubular oven at 1°C/min, and then maintained at the maximum temperature for 1 hour under oxygen atmosphere.

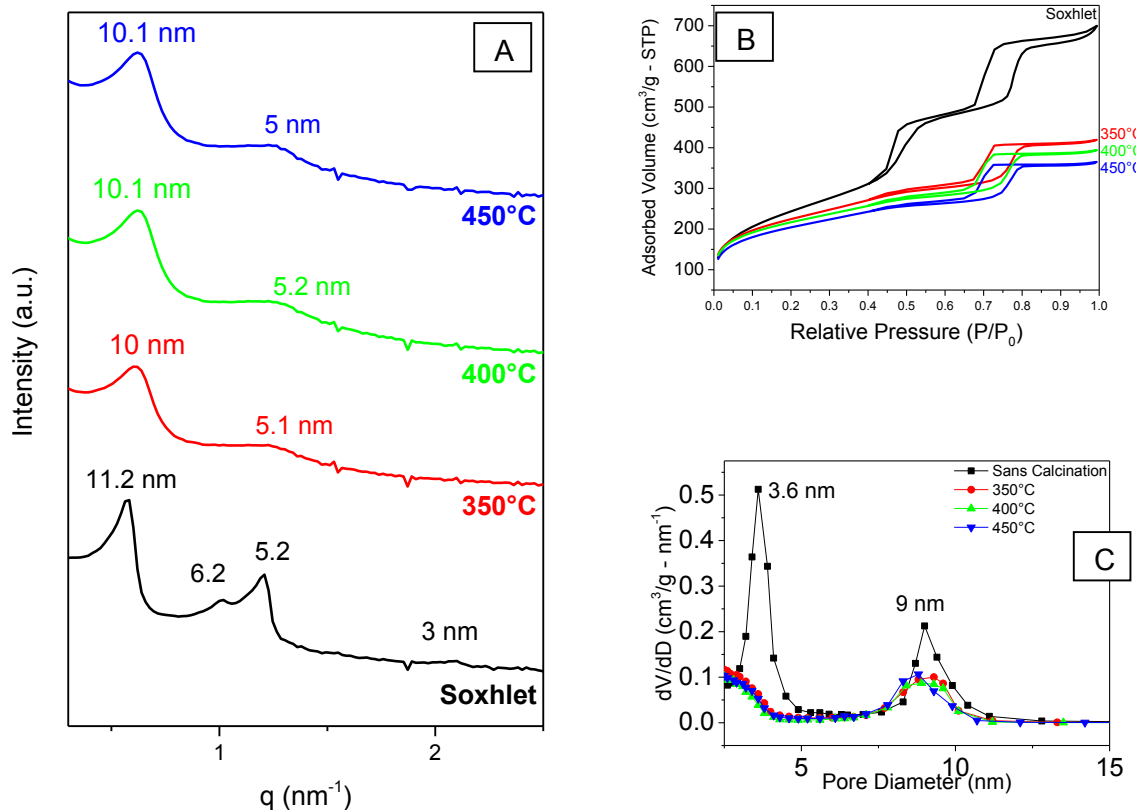


Figure 2-3: Comparison of the materials calcined at different temperatures and the initial material, A) SAXS pattern, B) Nitrogen sorption isotherm and C) Mean pore size distribution.

The SAXS patterns shows the presence of 3 peaks for the un-calcined dual-mesoporous material, the first and second peaks correspond to the (100) and (110) reflections respectively of the hexagonal structure of the matrix that is templated by the $R^F_8(EO)_9/P123$ micelles and the third peak corresponds to the (100) reflection of the hexagonal structure of the matrix templated by the pure $R^F_8(EO)_9$ micelles (Figure 2-3). After the thermal treatment, only two peaks remain corresponding to the (100) and (200) reflections of the matrix templated by $R^F_8(EO)_9/P123$ (Figure 2-3A). This is further confirmed by the nitrogen sorption isotherms which show that the capillary condensation at 0.45 disappears after the thermal treatment (Figure 2-3B), while the capillary condensation at 0.75 remains.

Table 2-1: S_{BET} and V_P for as a function of the calcination temperature of the silica materials.

	S_{BET} (m^2/g)	V_P (cm^3/g)
Initial material	880	1
350°C	780	0.5
400°C	760	0.48
450°C	750	0.45

The pore size distribution in Figure 2-3C shows that the pore size at 3.6 nm disappears, and the pore size at 9.4 nm remains, but its dV/dD value decreases by half. The surface area decreases by 11% to 15%, and the pore volume decreases by 50% for the thermal treatments at all the temperatures.

This shows that the thermal treatment of the dual-mesoporous silica material have a damaging effect. The matrix with the smaller pore size collapses when the temperature is applied while the matrix with the larger pore size is slightly damaged. This difference in the behavior of the two matrices is attributed to the variations in the pore wall thickness. The pore wall size is calculated from the SAXS pattern and the nitrogen isotherm of the initial material:

$$a_0 = 2d/\sqrt{3}$$

$$t = D - a_0$$

Using the formulas presented above, the pore wall thickness of the matrix with the smaller pore size is equal to 2.4 nm, while the pore wall thickness of the matrix with the larger pore size is equal to 3.2 nm. The thinner pore wall of the matrix with the small pore size renders it prone to collapse under high temperatures^{8,16}, and explains its faster decay compared with the matrix with the larger pore size.

3 Hydrothermal stability of the hierarchically porous silica material

The assessment of the thermal stability of those materials is not enough, it is necessary to study their behavior in aqueous conditions in order to understand the effects of water on their structure and physico-chemical properties for potential applications. Vansant *et al.*⁸ suggested that this stability is influenced by three important factors: pore wall thickness, condensation ratio and the mesostructure of the matrix.

The assessment of the hydrothermal stability of mesoporous silica material is usually done by two methods, the first one consists of placing the sample under steam at 800°C and the second one consists of submerging the sample in boiling water. Since the second method is easier to realize, it was adopted in this study.

3.1 Hydrothermal stability of the meso-macroporous silica material

The SAXS pattern of the initial and the calcined materials showed three peaks of the hexagonal ordering of the mesostructure (Figure 3-1A-B). After 30 minutes in boiling water the un-calcined material lost its mesostructure, while the calcined material collapsed after 60 minutes.

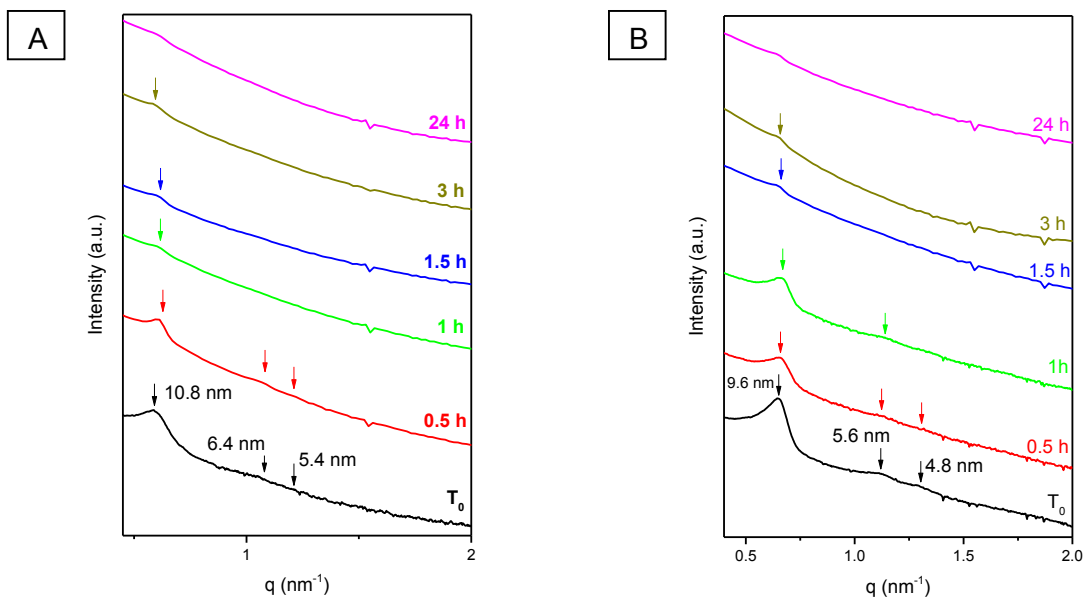


Figure 3-1: SAXS patterns evolution as a function of time in boiling water of A) the meso-macroporous material and B) the calcined meso-macroporous material.

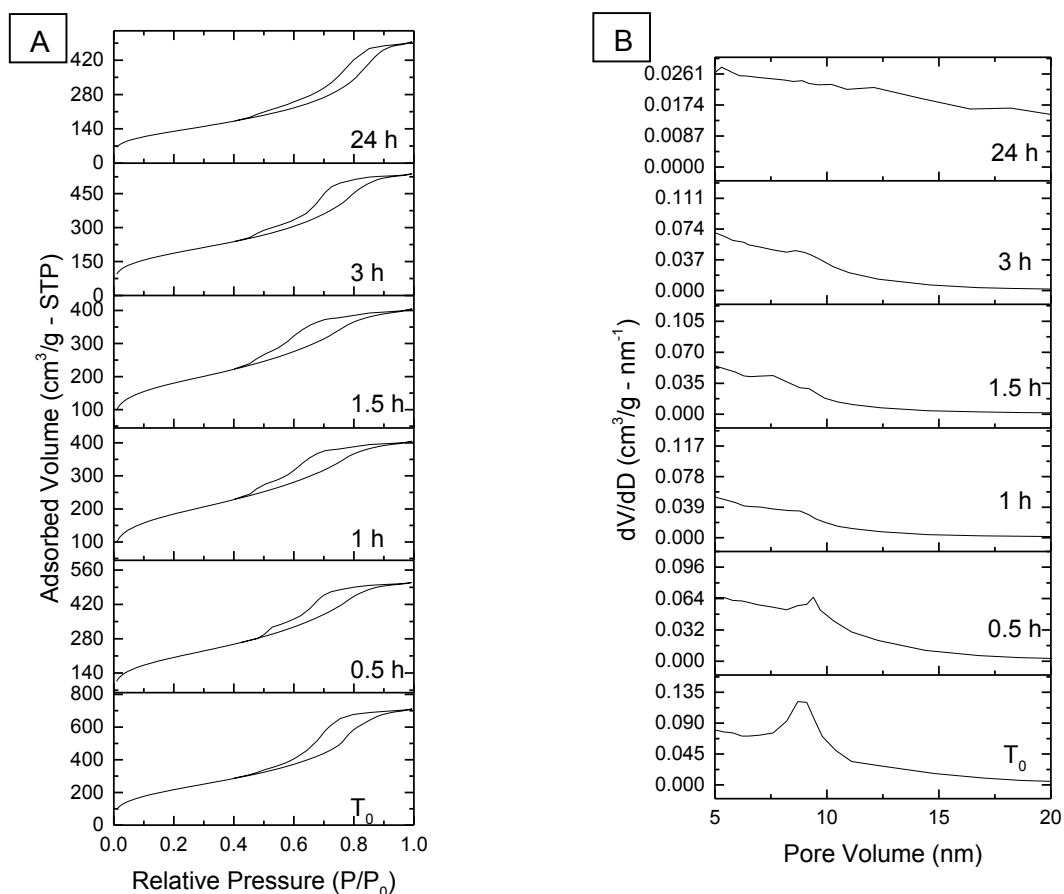


Figure 3-2: Nitrogen sorption analysis as a function of time in boiling water of the initial meso-macroporous material, A) isotherms and B) pore size distribution of the samples taken at regular intervals.

As for the texture, the nitrogen sorption isotherms of both materials showed a sharp capillary condensation initially and this sharpness decayed and disappeared after 30 minutes for the un-calcined material (Figure 3-2A) versus 60 minutes for the calcined material (Figure 3-3A). The pore size distribution showed a gradual decrease in the dV/dD value and the peak disappeared after 30 minutes for the un-calcined material (Figure 3-2B) and after 60 minutes for the calcined material (Figure 3-3). Furthermore, the surface area and pore volume of the un-calcined material showed a fast decrease in the first 90 minutes and then the decrease is slower (Figure 3-4A). After 24 hours they sustained a loss of 40% is recorded. On the other hand, the surface area and the pore volume of the calcined material showed a relatively slower decrease (Figure 3-4B), and after 24 hours the surface area lost 65% of its initial value and whilst the pore volume loses 30%.

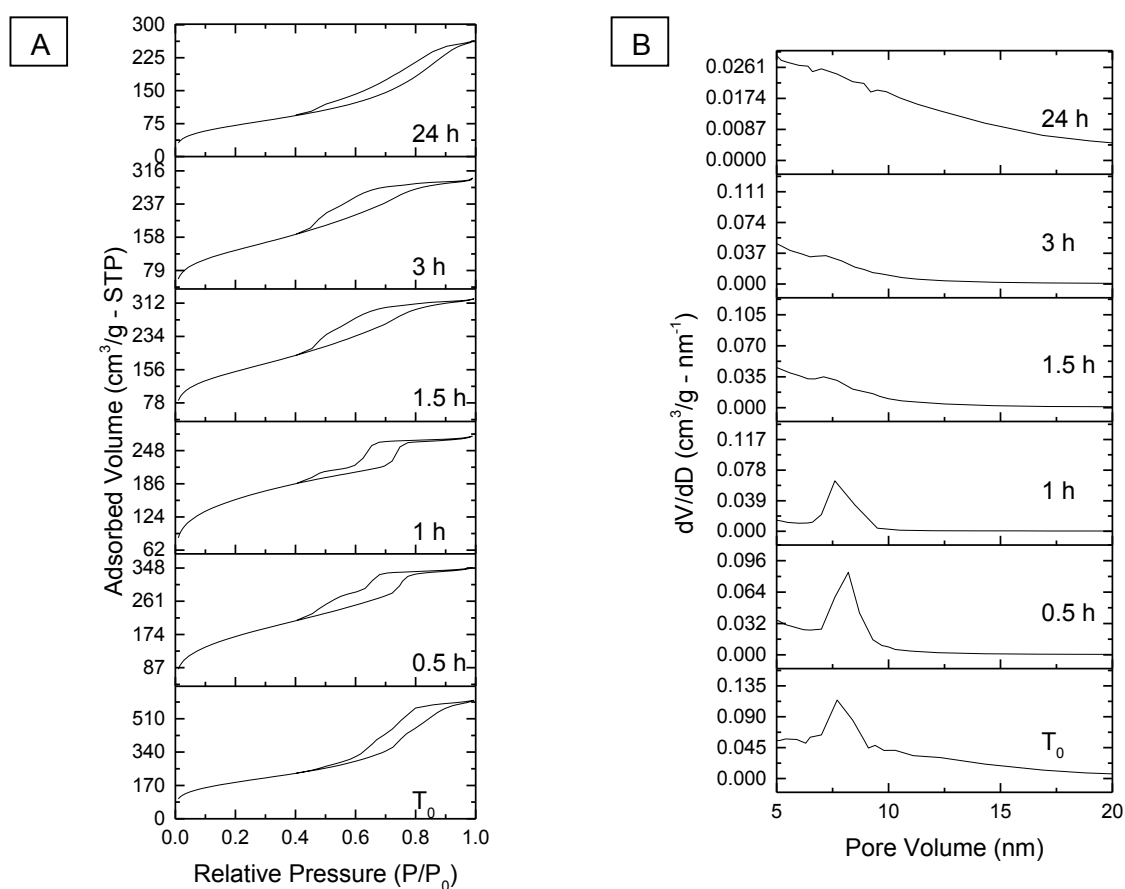


Figure 3-3: Evolution of nitrogen sorption analysis as a function of time in boiling water of the calcined meso-macroporous material, A) isotherm and B) pore size distribution of the samples taken at regular intervals.

The mercury intrusion porosimetry (Figure 3-5) showed that the macropores remained after 24 hours in boiling water with a slight decrease in their dV/dD values for both materials. This shows that the macropores are much more stable than the mesopores in the materials.

Figure 3-6 shows the vibrations of the silica matrix detected on the infrared spectrum below 1800 cm^{-1} . The broad and intense band with a maximum at 1080 cm^{-1} as well as the shoulder

at 1200 cm^{-1} are characteristic of the antisymmetric stretching vibrational mode of the Si-O-Si siloxane bridges.

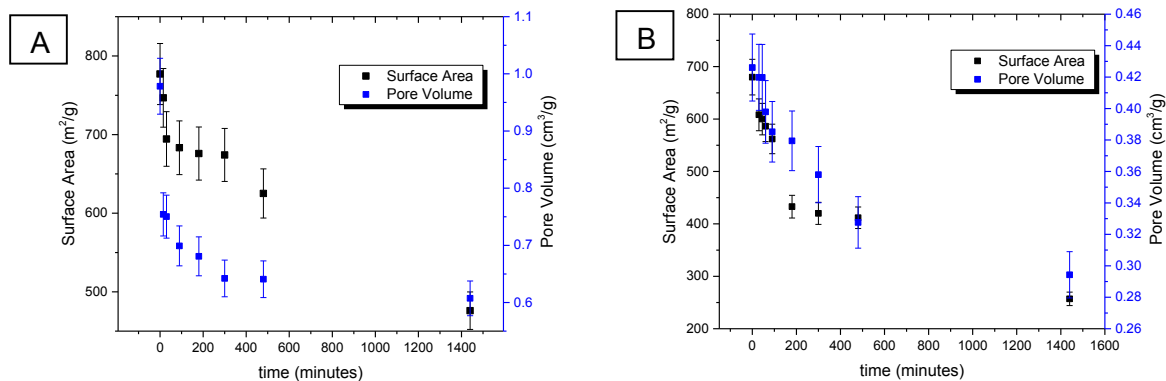


Figure 3-4: Graphs showing the evolution of the surface area and pore volume as a function of time in boiling water for A) the initial meso-macroporous material and B) for the calcined meso-macroporous material

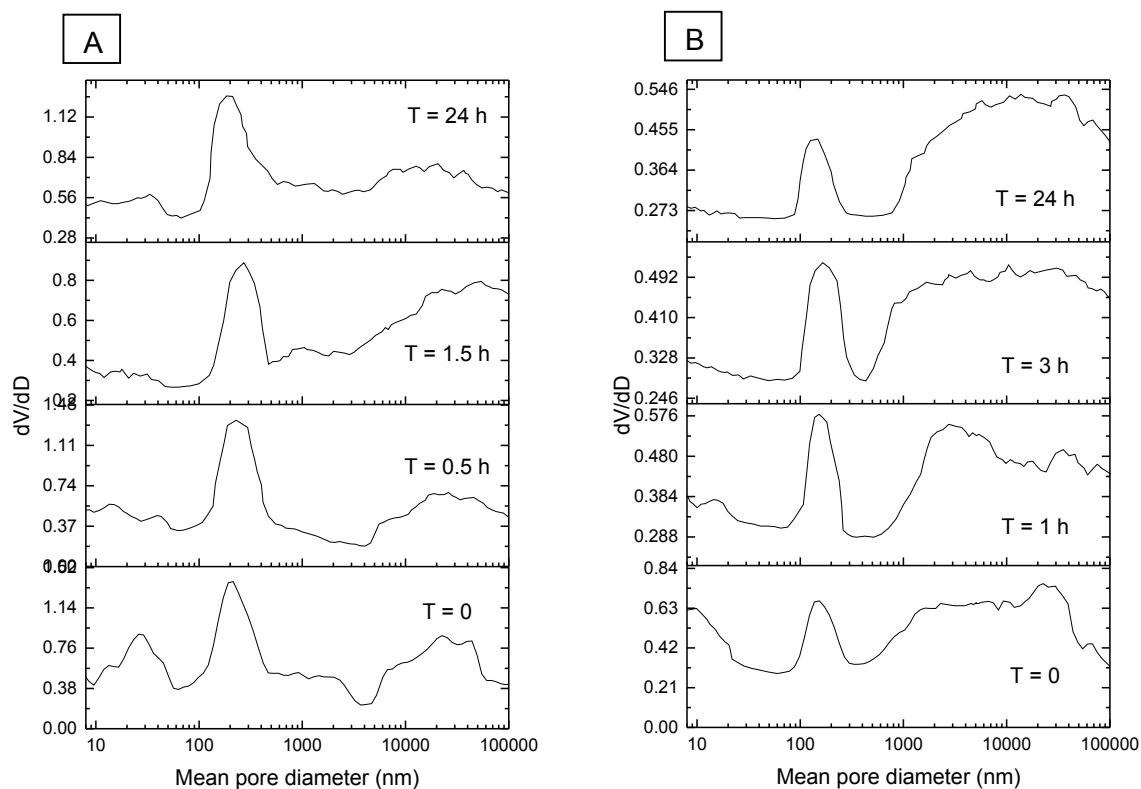


Figure 3-5: Evolution of mercury intrusion porosimetry as a function of time in boiling water of (A) the initial material and of (B) the calcined material.

The less intense absorption at 970 cm^{-1} is assigned to the Si-O stretching of silanols. Bands detected at 2978 and 2907 cm^{-1} are assigned to the stretching vibrations of the CH groups of the surfactant and hydrocarbons, which was not completely removed for the initial material by the ethanol extraction, but are not present in the calcined material. The H-bonded, OH- groups with various OH...H distances are responsible for the intense absorption below 3700 cm^{-1} ,

whereas the sharp band at 3740 cm^{-1} is due to the isolated silanols. The combination of stretching OH and bending Si-OH $[(\nu+\delta)\text{OH}]$ at 4370 cm^{-1} characterize these silanols. As this combination mode is not overlapped by vibration due to other groups, its intensity can be used to follow the amount of silanols. The peak of the isolated silanols decreased after 24 hours in boiling water (Figure 3-6A-B).

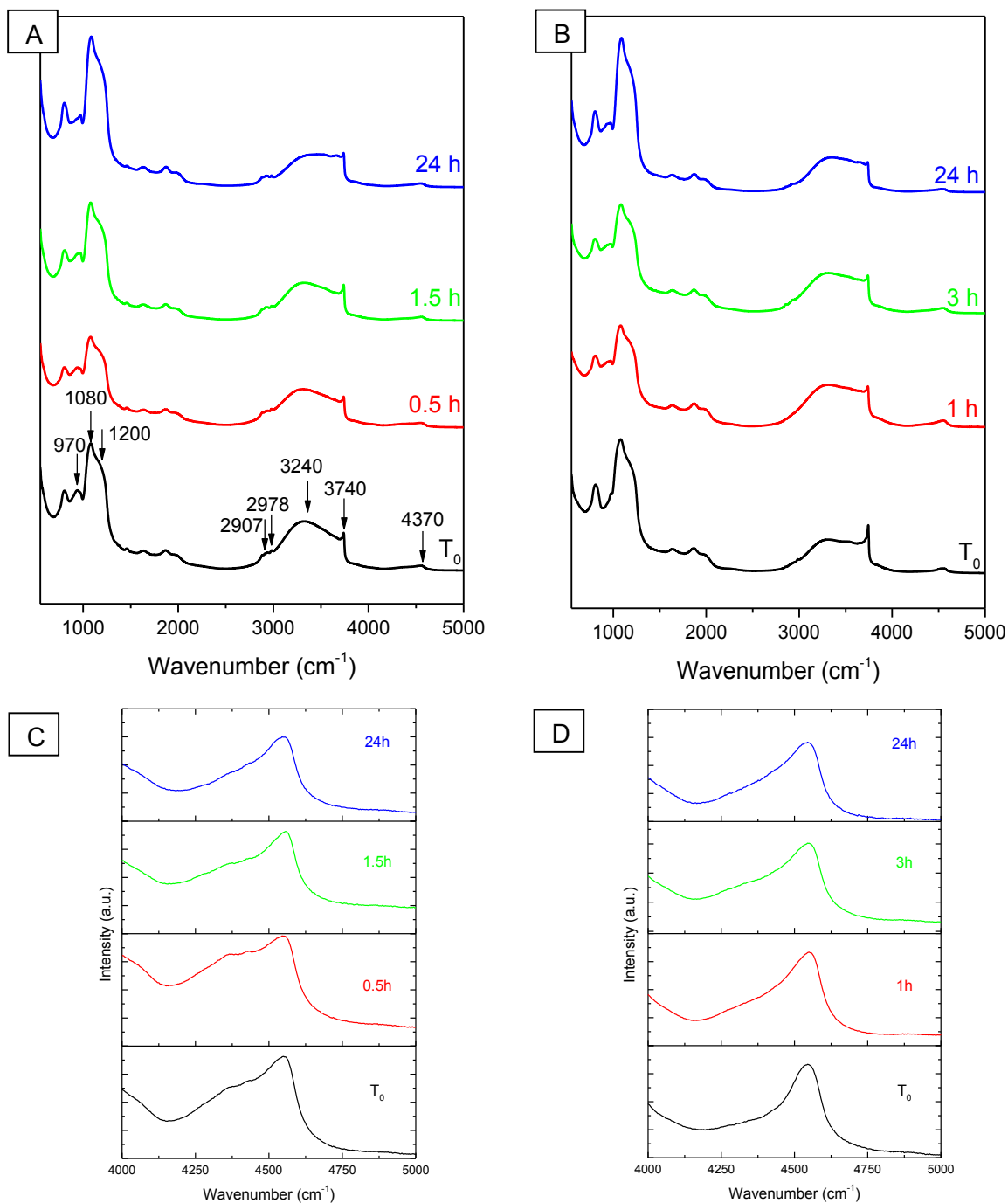
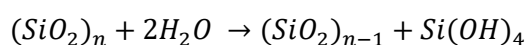


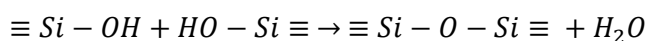
Figure 3-6: Evolution of the FTIR spectra as a function of time in boiling water of A) the initial meso-macroporous material and B) the calcined material and C,D) the peaks at 4370 cm^{-1} for the materials, respectively.

The quantification by measuring the ratio of the surface area of isolated silanols peak over the Si-O peak at 970 cm^{-1} shows that at the end of the experiment the silanol quantity of the uncalcined material is reduced by 20% whereas for the calcined material it is reduced by 92%. The FTIR spectra show that the uncalcined material has a silanol rich surface compared to the calcined material. The calcination process alters the textural properties of the material as it has been shown in Section 2.1 and reduces the silanol density on the surface. During the assessment in boiling water, the hydrolysis process can break many siloxane bridges (Si-O-Si) to yield more or less branched (Si-O)_n chains.

When the hydrolysis process breaks enough siloxane bridges, dissolution processes start to take place with the formation of orthosilicic acid molecules and small oligomers according to the reaction:



Then the dissolved molecules and oligomers are re-precipitated according to the reaction:



The collapse of the structure is mainly caused by those processes. Several authors agree that this mechanism is behind the collapse of the structure^{5,17,18}.

3.2 Hydrothermal stability of dual-mesoporous silica material

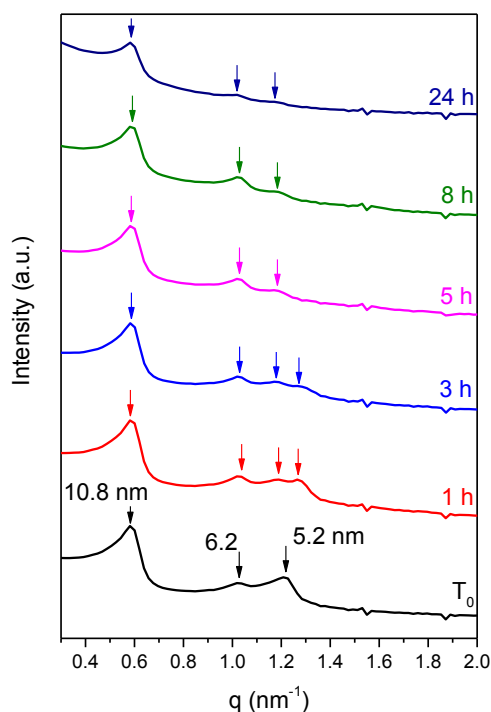


Figure 3-7: SAXS pattern evolution as a function of time in boiling water of the dual mesoporous silica material.

The SAXS patterns in Figure 3-7 shows that the structure of the matrix with the small pore collapses after 3 hours, while the structure of the matrix with the large pore remains stable even after 24 hours in boiling water, although the intensity of the peaks decreases with time.

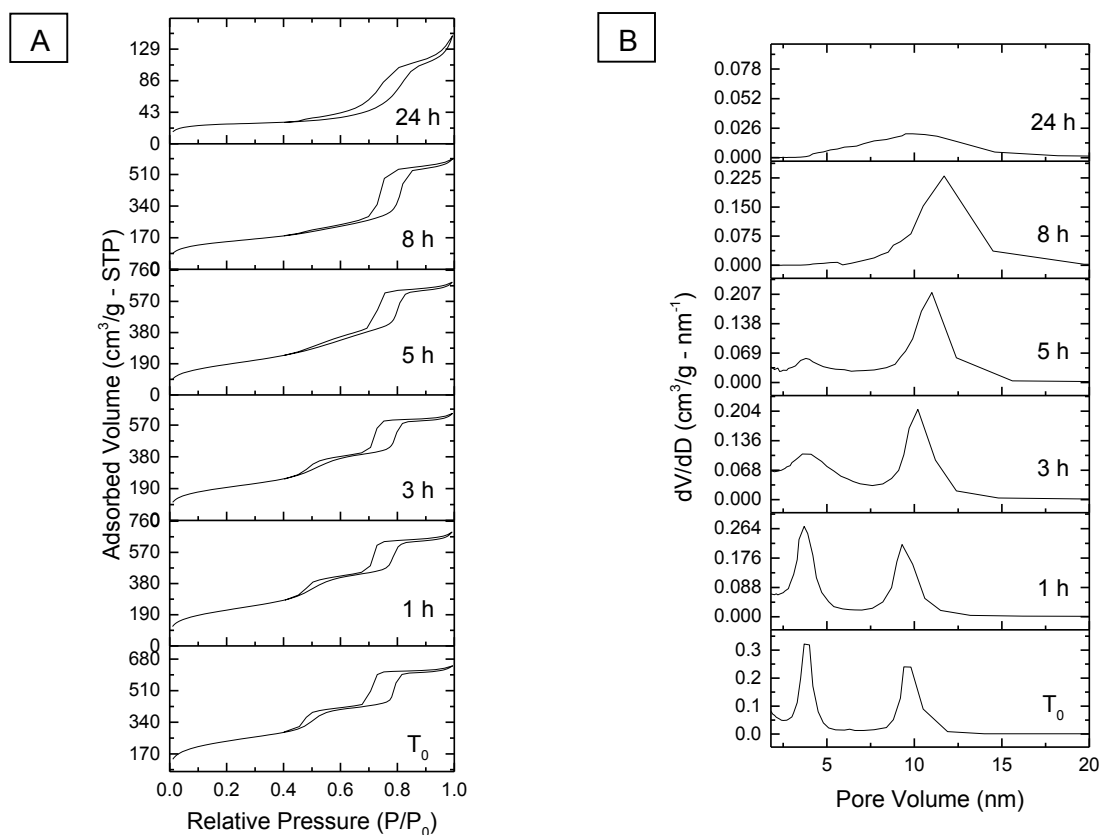


Figure 3-8: Nitrogen sorption analysis as a function of time in boiling water (A) isotherms and (B) pore size distribution of the dual-mesoporous silica material.

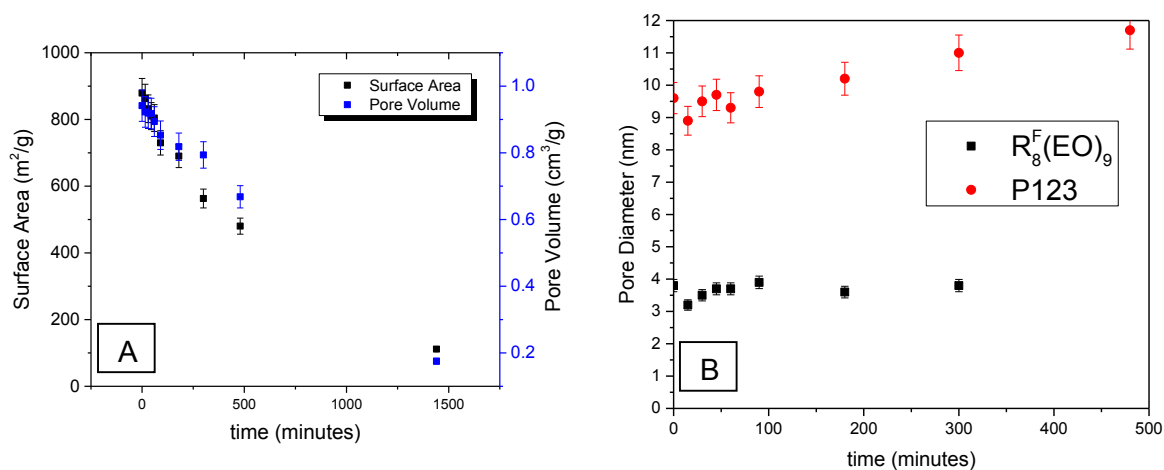


Figure 3-9: (A) surface area and pore volume evolution as a function of time in boiling water, and (B) the pore size evolution of the dual-mesoporous silica material.

The hydrothermal stability assessment for the dual-mesoporous silica material was realized on the material after ethanol extraction and drying only, since the thermal treatment collapses the matrix with the small pore.

Concerning the texture of those materials, the nitrogen sorption analysis (Figure 3-8A) showed that the capillary condensation at 0.45 disappears after 3 hours in boiling water, while the capillary condensation at 0.75 loses its sharpness after 8 hours. On the other hand the pore size distribution (Figure 3-8B) shows a fast decrease of the dV/dD values for the peak at 3.6 nm, while the peak at 9.4 nm decreases in a relatively slower manner. At 24 hours both peaks have disappeared.

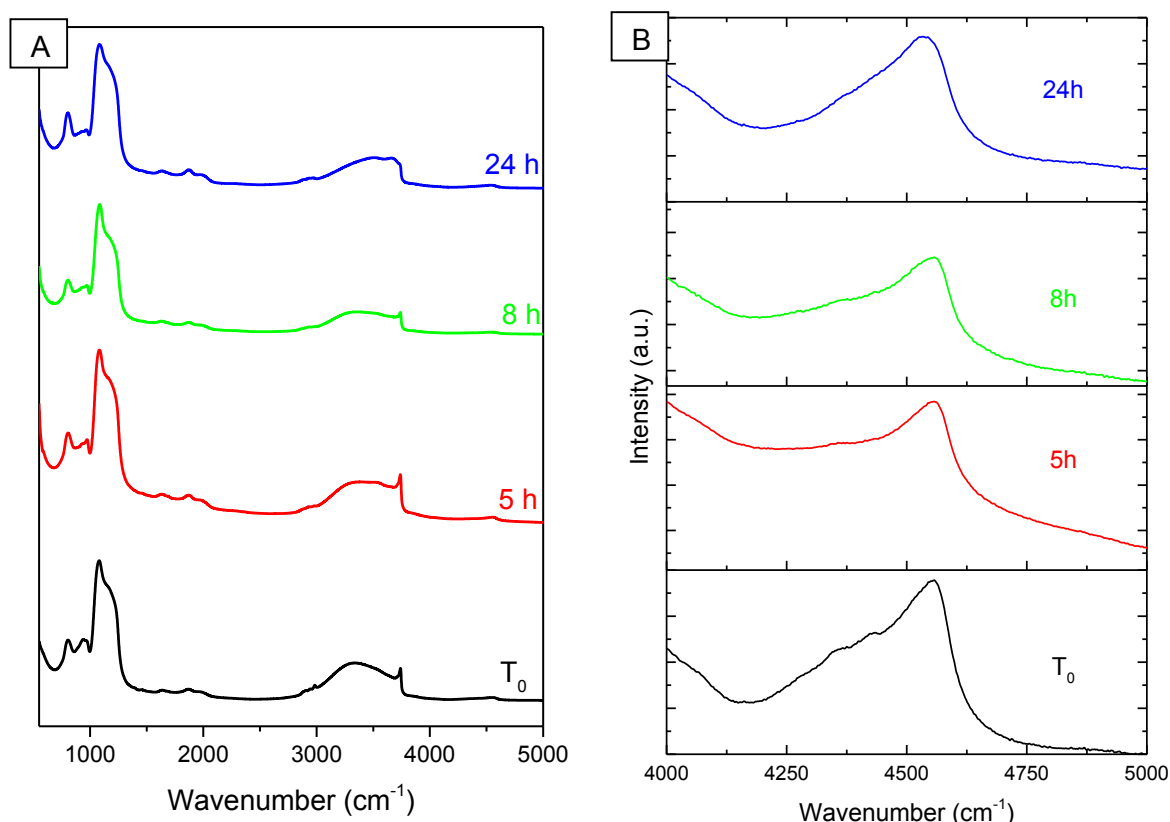


Figure 3-10: A) FTIR analysis of the dual-mesoporous silica material and B) the peak at 4370 cm^{-1} as a function of time in boiling water.

Furthermore, the surface area and pore volume decreased drastically, after 24 hours in boiling water, the surface area lost 90% of its initial value, while the pore volume lost 80%. This reflects an important surface alteration in the presence of boiling water.

The FTIR analysis in Figure 3-10 showed a fast decrease in the intensity of the peak at 3740 cm^{-1} characteristic of the isolated silanols. This observation further corroborates the fact that the surface is heavily modified during this process.

Even though the decay mechanism is the same as the one described in section 3.1, it is not enough to explain the difference in the decay kinetics of the two matrices forming the material.

In the case of the dual-mesoporous material, both its constituting matrices show a hexagonal mesostructure, the only difference resides in the pore wall thickness. The matrix with the large pores has thicker walls than the matrix with the smaller pores, which makes the latter less hydrothermally resistant.

3.3 Comparison and discussion

The comparison of the thermal stability of the meso-macroporous silica material and the dual-mesoporous silica material shows that the mesopores sustain mainly two types of damages they shrink or collapse. The mesopores of the meso-macroporous material sustained a shrinkage from 9.6 to 7.7 nm, and the secondary porosity volume constitute initially 21% of the pore volume, and after calcination it reduced to 6%. This shrinkage is due to the consolidation of the micropores and the enhancement of the cross-linking¹⁴. While the dual-mesoporous silica material showed a total collapse of the matrix with the smaller pore and a damage for the matrix with the larger pore, and this phenomena can be attributed to the pore wall thickness. The lack of shrinkage of the pores of the matrix with the large pores can be explained by the absence of micropores which in the walls and enhances its stability.

The comparison between the hydrothermal stability of the meso-macroporous silica material, the calcined meso-macroporous silica material and the dual-mesoporous silica material shows that each type of material display a different decay kinetic. The meso-macroporous silica material collapsed entirely after 30 minutes in boiling water, while its calcined counterpart remained stable for 1 hour. This increased stability is caused by two factors, the enhanced cross-linking and the decrease in the surface density of the isolated silanols which makes the material more resistant to water attacks. On the other hand, the dual-mesoporous material showed a much better hydrothermal stability, since the total collapse of the matrix with the small pore size happened after 3 hours in boiling water, while the matrix with the larger pore size remained stable for 8 hours. Since pore wall thickness of the matrix with the large pores is thinner for the matrix with the small pores. It has been shown by Mokaya *et al.*⁷ that MCM-41 materials with thicker pore walls have a much enhanced thermal and hydrothermal stability and they proposed a mechanism where silicate units crystallize and grow without interacting with surfactant molecules. Those crystals will improve long range ordering, which in turn enhances the stability of the material. Many methods has been suggested in order to inhibit those reactions from taking place and reducing the damages, such as in the synthesis of the materials¹⁹, or post-synthesis treatment in the presence of salts²⁰, and by silylating the surface in order to eliminate the silanol groups⁵.

4 *Mucor miehei* Lipase immobilization

We have studied the capacity of adsorption of the *Mucor miehei* Lipase (Mml) on the silica material. The immobilization protocol is presented in Chapter 2, it has been optimized by our group in a previous work¹.

The immobilization consists of the submerging of the material in a buffer solution for a considerable amount of time. So in order to determine the optimal conditions for the enzyme immobilization, we started by establishing the adsorption isotherm, the experimental protocol has been described in Chapter 2.

4.1 Meso-macroporous biocatalyst

The calcined meso-macroporous silica material has been chosen because of its better hydrothermal stability over its non-calcined counterpart.

4.1.1 Adsorption isotherm

The adsorption isotherm is presented in Figure 4-1. The isotherm have been fitted using the Langmuir model:

$$\Gamma = \frac{\Gamma_{max}[C]_{eq}}{[C]_{eq} + K_L}$$

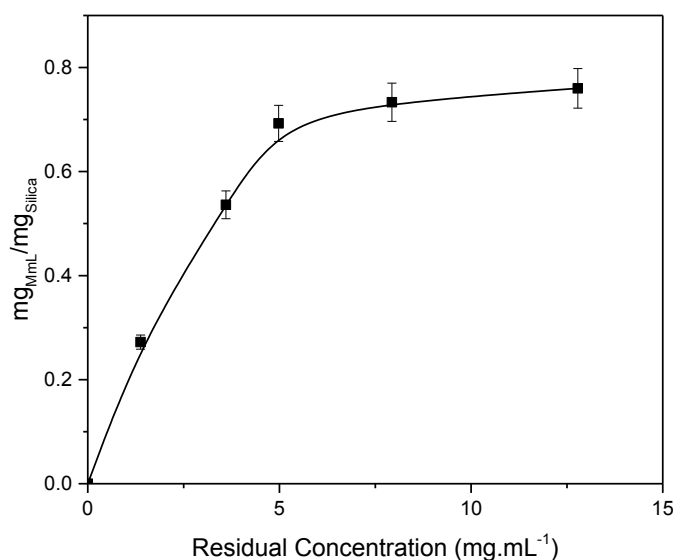


Figure 4-1: Adsorption isotherm of the Mml immobilized at pH6 on the calcined meso-macroporous material.

Using this model the best fit compared to the experimental data points revealed that the maximal adsorption capacity (Γ_{\max}) of this material is $0.76 \text{ mg}_{\text{Mml}}/\text{mg}_{\text{Silica}}$, and $K_L = 3.81 \text{ mg/ml}$. The pore volume of the material is $0.8 \text{ cm}^3/\text{g}$, and supposedly the Mml adopts a spherical shape with a 4 nm diameter, it is possible to calculate the theoretical adsorption capacity of the mesopores. An enzyme molecule has a volume of 33.5 nm^3 . So the theoretical maximal adsorption is $1.25 \text{ mg}_{\text{Mml}}/\text{mg}_{\text{Silica}}$. This value is obtained by calculating how many enzyme molecules can be fitted in the pore volume of 1 g of silica material then converting this number into the theoretical weight of the enzymes. Furthermore, the presence of the enzymes has been evidenced by FTIR spectroscopy, which was also used to quantify the quantity of adsorbed enzymes and establish the adsorption isotherm.

The FTIR spectra in Figure 3-6 show the characteristic bands of the Mml as a function of the initial Mml concentration in the TRIS solution. The peak at 1528 cm^{-1} corresponds to the amide II, the peak at 1460 cm^{-1} corresponds to the amide III, also the peak at 3333 cm^{-1} corresponds to the amide A, the whole of the absorptions is characteristic of the lipase molecule. On the other hand the peak at 3740 cm^{-1} corresponds to isolated silanols and its decrease in intensity is in agreement with the presence of the enzyme in the material.

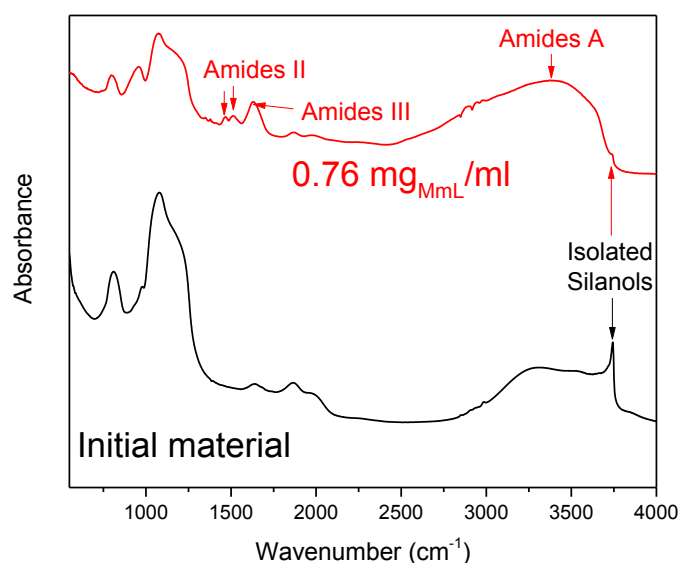


Figure 4-2: FTIR spectra of the adsorbed Mml on the meso-macroporous material (red) and the initial material (black).

4.1.2 Characterization of the meso-macroporous biocatalyst

The calcined material has been prepared at its maximal loading capacity, and characterized in order to assess the damage sustained during the immobilization of the enzyme in aqueous solution.

The physicochemical properties of meso-macroporous material after the adsorption of the enzyme has sustained slight modifications to its. The SAXS patterns in Figure 4-3A show that the hexagonal structure is still maintained, but the intensity of the peaks decreased and the (200) peak became undetectable. The nitrogen sorption in Figure 4-3B revealed an important decrease in the sharpness of the capillary condensation, this is also reflected in the mesopore size distribution in Figure 4-3C, which displayed a constant pore size with a significant decrease in the dV/dD value reflecting the filling of the mesopores with Mml. Likewise, the surface area decreased slightly from 630 to 600 m^2/g and the pore volume from 0.8 to 0.3 cm^3/g . This confirms that the enzymes are adsorbed mainly in the mesopores. The macropores in Figure 4-3D are not influenced by the enzyme immobilization.

4.2 Dual-mesoporous biocatalyst

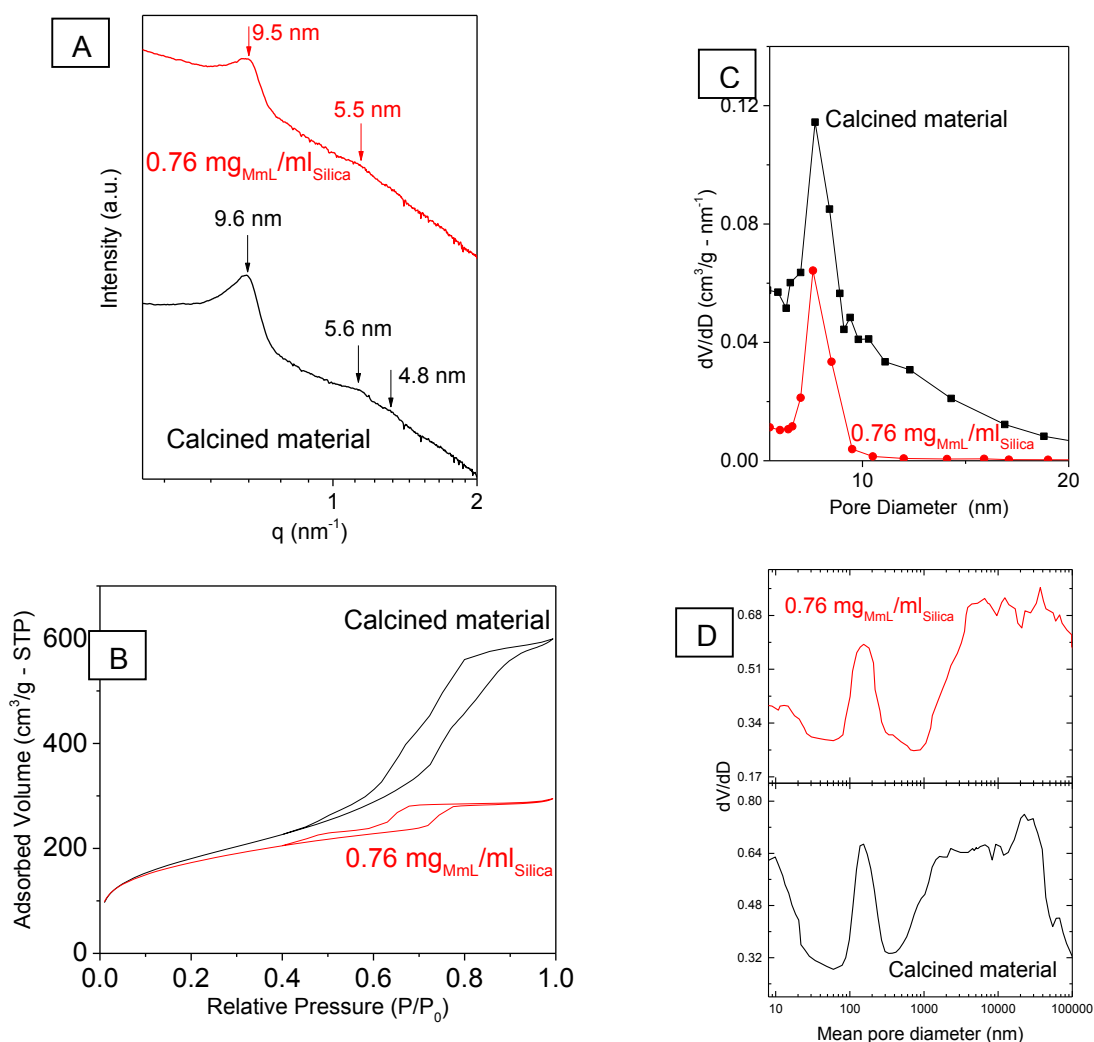


Figure 4-3: Meso-macroporous biocatalyst characterization before and after enzyme adsorption. A) SAXS pattern, B) pore size distribution, C) Nitrogen sorption isotherm and D) Mercury intrusion porosimetry.

In this work, the initial un-calcined material has been used because of its better hydrothermal stability which is necessary in this work since the enzyme immobilization will be done by submerging the material in an aqueous solution containing the enzyme.

4.2.1 Adsorption isotherm

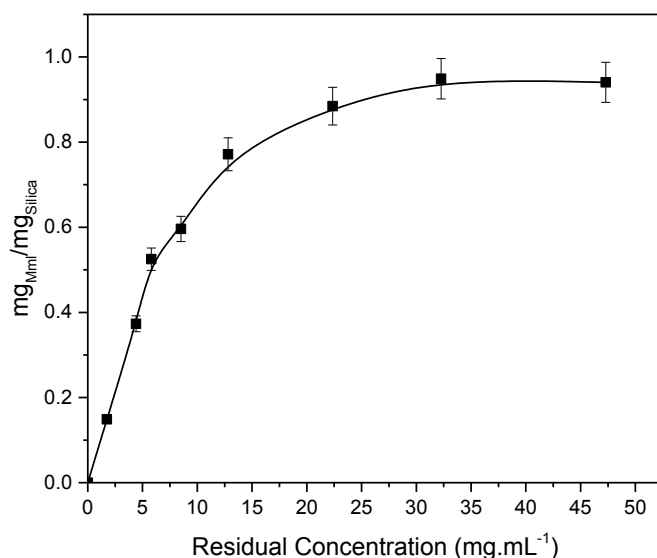


Figure 4-4: Adsorption isotherm of the Mml immobilized at pH6 on the dual meso-porous material.

The adsorption isotherm for this material is presented in Figure 4-4. The experimental points have been fitted using the Langmuir model, and it revealed that the maximal adsorption capacity is $0.94 \text{ mg}_{\text{Mml}}/\text{mg}_{\text{Silica}}$ and $K_L = 12.7 \text{ mg/ml}$.

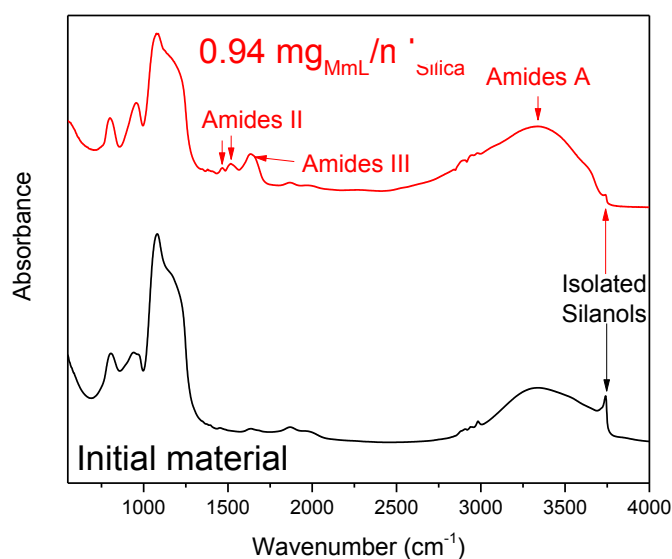


Figure 4-5: FTIR spectra of the dual-mesoporous biocatalyst (red) and the initial material (black).

The pore volume of this material is $0.94 \text{ cm}^3/\text{g}$, so the theoretical maximal loading capacity is equal to $1.47 \text{ mg}_{\text{MmL}}/\text{mg}_{\text{Silica}}$. This maximal adsorption value is overestimated because it represents the global pore volume of the mesopores, but also because the enzyme molecule has a diameter of 4 nm , which is slightly larger than the mesopore diameter of the matrix with the small pore size (3.6 nm), which indicates that the enzyme is mainly adsorbed in the matrix with the larger pore size.

The FTIR spectra in Figure 4-5 exhibit the same behavior such the meso-macroporous silica material and evidence the presence of MmL.

4.2.2 Characterization of the dual-mesoporous biocatalyst

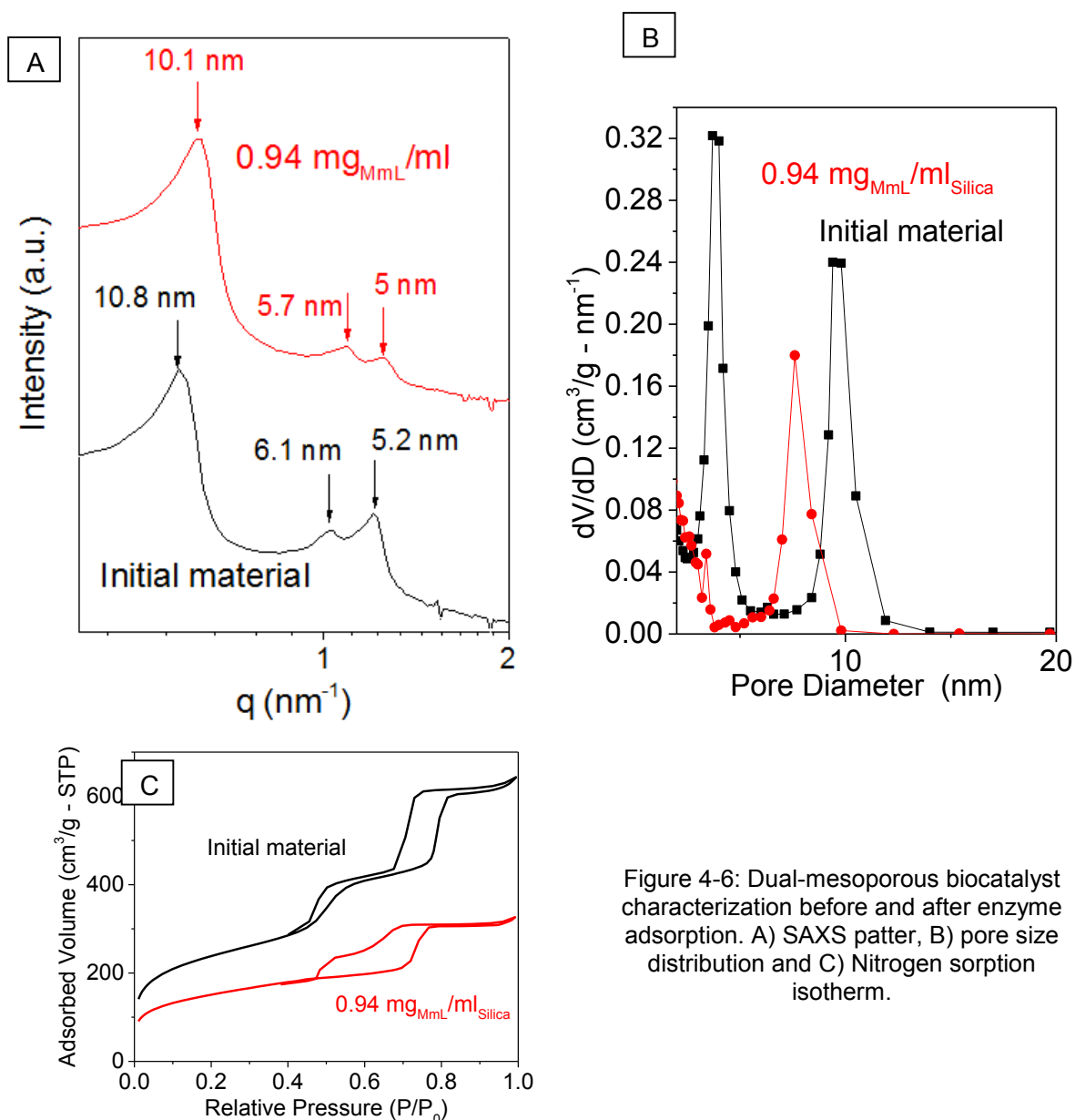


Figure 4-6: Dual-mesoporous biocatalyst characterization before and after enzyme adsorption. A) SAXS pattern, B) pore size distribution and C) Nitrogen sorption isotherm.

The dual-mesoporous material has been prepared at its maximal loading capacity, and characterized in order to assess the damage sustained during the immobilization of the enzyme in aqueous solution.

SAXS patterns in Figure 4-6A show that the peaks corresponding to the matrix with the small pore size seems to decrease in intensity after the enzyme immobilization. On the other hand, the nitrogen sorption isotherm in Figure 4-6B show that the capillary condensation at 0.45 has disappeared and the capillary condensation at 0.75 became less sharp, this is also observable for the pore size distribution (Figure 4-6C), which exhibits a decrease in the large pore size from 9.6 nm to 7.6 nm. On the other hand the small pore size remains unchanged but its dV/dD value decreases 5 folds. The surface area decreases also from 880 m^2/g to 530 m^2/g , and the pore volume from 0.94 cm^3/g to 0.38 cm^3/g . Since the Mml size (4 nm) is very close to the pore diameter of the matrix with the small pore (3.6 nm), the adsorption of Mml may suppress nitrogen penetration into the interior part of the mesopores, thus causing an underestimation of the textural properties of the dual-mesoporous material.

5 Transesterification reaction of colza oil

After the immobilization of the *Mucor miehei* Lipase in the calcined meso-macroporous material and the dual-mesoporous material, they were used for the methanolysis of colza oil.

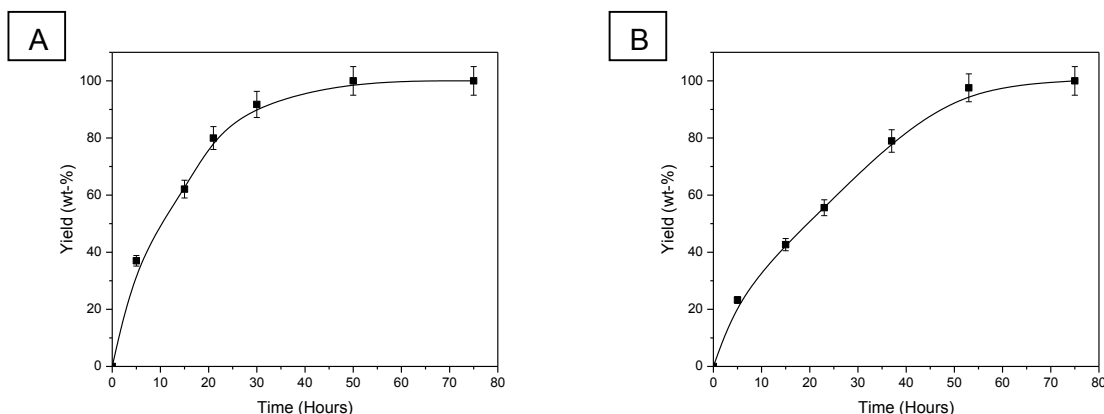


Figure 5-1: Methyl esters yield as a function of time for the A) meso-macroporous catalyst, and B) for the dual-mesoporous catalyst.

The immobilization of the enzyme on the meso-macroporous was done in an Mml buffer solution (pH6) having a concentration of 5 mg/ml, whilst for the dual-mesoporous materials the Mml concentration has a concentration of 15 mg/ml, those concentrations correspond to the beginning of the plateau on the Langmuir isotherm. Figure 5-1 shows the production of the methyl ester as a function of time.

Table 5-1: Comparison of the initial speed between the meso-macroporous and the dual-mesoporous catalysts.

Catalyst Matrix	Methyl ester formation	
	Initial speed ($\mu\text{mol/h}$)	Initial speed ($\mu\text{mol/h/mg}_{\text{Mml}}$)
Meso-macroporous	12.1	1.6
Dual-mesoporous	7.6	0.8

The initial speed of the formation of methyl esters for the different catalysts are given in Table 5-1. The performance of the catalyst does not depend only on the yield of the reaction, but also on the “turnover number”. This number is the ratio of the mole number of the transformed substrate over the mole number of the enzyme in the reaction. Figure 5-2 shows the evolution of the turnover number of the reaction catalyzed by the meso-macroporous and dual-mesoporous catalysts.

That of the meso-macroporous catalyst is higher than the one for the dual-mesoporous catalyst. One mole of enzyme present on the meso-macroporous matrix is capable of the methanolysis of 3700 moles of substrate, whilst for the dual-mesoporous matrix, it is capable of the methanolysis of 3000 moles of substrate.

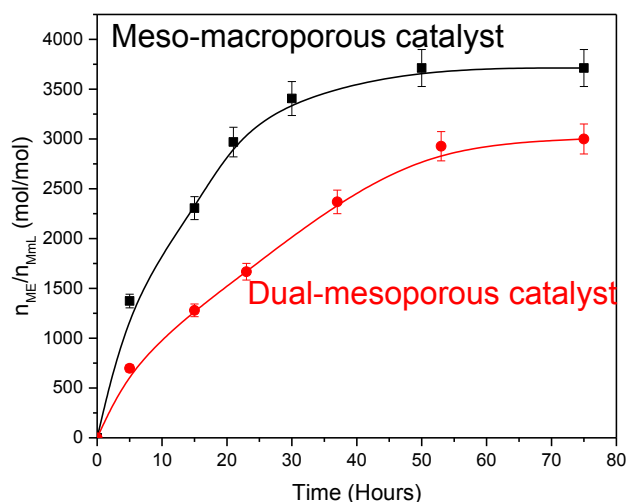


Figure 5-2: “Turnover number” of the two types of catalysts.

The catalyst with the macropores seems to facilitate the diffusion of the substrate, this is shown by the more important initial speed of the meso-macroporous catalyst. Even though the dual-mesoporous silica has a higher immobilization capacity, its activity is lower.

5.1 Recycling of the catalysts

The recyclability of the catalysts is an important feature, especially for industrial applications. In this section, we present the effects of consecutive reactions using the same catalyst. For the evaluation of the efficiency, the production of methyl esters of the first transesterification will be used as a reference. After each use, the catalyst is recuperated by centrifugation, then washed with water in order to eliminate the glycerol. After drying, it is reused. The recycling of the catalyst is stopped after the catalytic activity is below 10%.

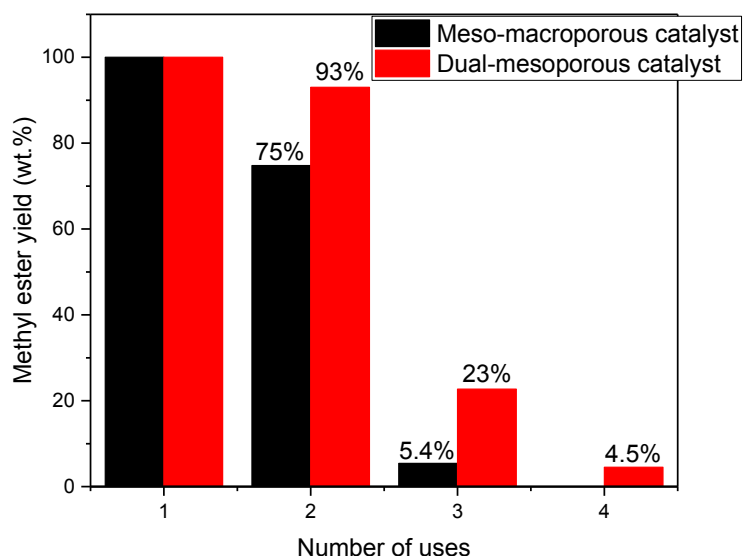


Figure 5-3: Recyclability of the meso-macroporous and the dual-mesoporous catalysts.

Figure 5-3 shows that the meso-macroporous catalyst decays after 2 reuses, on the third the production of methyl esters decreases to 5.4% while the dual-mesoporous material remains active for a fourth reuse with a production of 4.5% of methyl esters.

6 Discussion

In this section, we present a comparison between those results and the ones obtained previously by our group^{1,21-23} concerning the use of a mesoporous material SBA-15 having a pore size of 8.5 nm and a biocatalyst prepared from a meso-macroporous matrix obtained by using a concentrated fluorinated emulsion as a template. So I start with a summary of all the results. The materials used previously were an SBA-15 and a meso-macroporous silica material synthesized from a mixture of 30% $C_8F_{17}C_2H_4(OC_2H_4)_9$ and 70% $C_7F_{15}C_2H_4(OC_2H_4)_8$. The addition of oil creates direct swelled micelles alongside a direct concentrated emulsion. After the addition of TMOS, hydrothermal treatment and elimination of the organic component, the final material shows a combination of mesopores in a hexagonal ordering and macropores²⁴. To avoid any confusion with the meso-macroporous silica material used in this

work, this material will be called MMMTE for Meso-Macroporous Materials Templated by Emulsion. The SBA-15 material is used without any treatment, while the MMMTE was calcinated at 550°C for 3 hours under air. The calcination step proved to be crucial, since the enzyme immobilization on the non-calcined MMMTE caused a total collapse of the structure. The properties of all the materials are summarized in the Table 6-1.

Table 6-1: Summary of the properties of the materials. a_0 = repetition distance of the first SAXS peak, d_p = mesopore diameter, S_{BET} = surface area, V_P = pore volume and D_P = macropore diameter.

Material	a_0 (nm)	d_p (nm)	S_{BET} (m ² /g)	V_P (cm ³ /g)	D_P (μm)
Meso-macro	9.6	7.7	630	0.8	0.15
Dual-meso	10.8	9.4/3.6	880	0.94	-
SBA-15	11.3	8.5	700	0.72	-
MMMTE	8.2	7.1	820	1.57	4.8

The enzyme immobilization has been done by putting the materials in an enzyme solution at 10 mg/ml. The effects of the enzyme immobilization of the materials are summarized in Table 6-2.

Table 6-2: Summary of the properties of the materials after the immobilization of Mml. a_0 = repetition distance of the first SAXS peak, d_p = mesopore diameter, S_{BET} = surface area, V_P = pore volume and D_P = macropore diameter.

Material	a_0 (nm)	d_p (nm)	S_{BET} (m ² /g)	V_P (cm ³ /g)	D_P (μm)
Meso-macro	9.5	7.7	600	0.3	0.15
Dual-meso	10.1	7.1	530	0.38	-
SBA-15	11.3	8.5	420	0.65	-
MMMTE	8.1	6.5	540	0.67	4.8

Table 6-3: The Langmuir formula parameters of the materials.

Material	K_L (mg/ml)	Γ_{max} (mg/mg)	$\Gamma_{theoretical}$ (mg/mg)
Meso-macro	3.81	0.76	1.25
Dual-meso	12.7	0.94	1.47
SBA-15	1.02	0.5	1.44
MMMTE	2.57	1.1	2.47

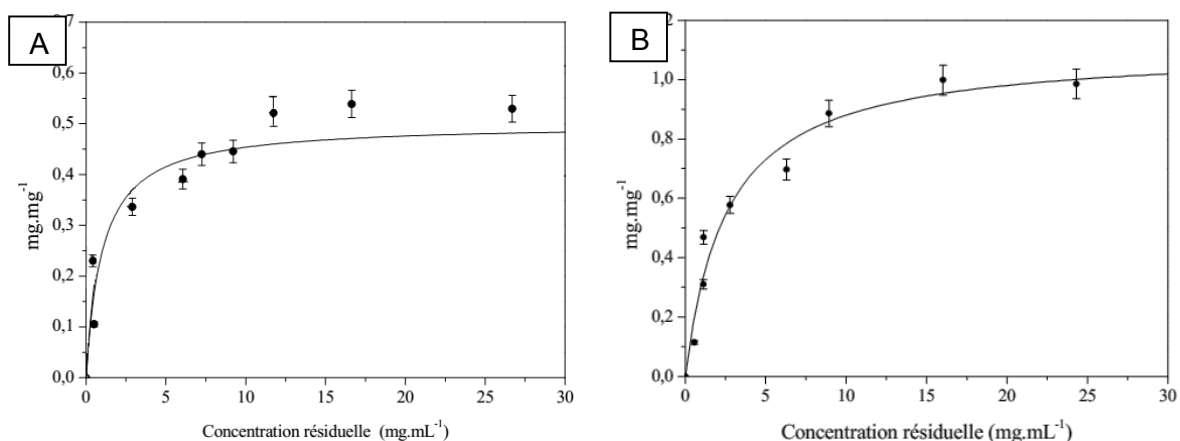


Figure 6-1: Adsorption isotherms of Mml on A) SBA-15 and B) MMMTE

Table 6-4: Adsorption rates and immobilization efficiency of the Mml of the different matrices.

Material	Adsorption rate ($\text{mg}_{\text{Mml}}/\text{mg}_{\text{Silica}}$)	Immobilization efficiency
Meso-macro	0.76	76%
Dual-meso	0.94	31%
SBA-15	0.42	26%
MMMTE	0.57	36%

The adsorption isotherms were fitted the Langmuir model. The resulting adsorption isotherms are shown in Figure 6-1.

The Table 6-3 summarizes the parameters of the fit, and Table 6-4 the adsorption rate and immobilization efficiency.

All the catalysts have been used in the transesterification of colza oil. For each one the reaction has been done using the optimal conditions the parameters in the different reaction kinetics are summarized in Table 6-5:

Table 6-5: Comparison of the initial speeds and the turnover number of the different matrixes.

Catalyst Matrix	Methyl ester formation		Reaction time (Hours)	Turnover number (mol/mol)
	Initial speed ($\mu\text{mol}/\text{h}$)	Initial speed ($\mu\text{mol}/\text{h}/\text{mg}_{\text{Mml}}$)		
Meso-macro	12.1	1.6	50	3700
Dual-meso	7.6	0.8	75	3000
SBA-15	18.5	4.4	30	4900
MMMTE	8.3	1.45	72	3600

The recyclability of the materials has also been evaluated and it has been summarized in the Figure 6-2.

The comparison of the maximal adsorption ratio of the materials and of the pore volume is illustrated in Figure 6-3 finds that the higher the pore volume, the more the matrix is able to immobilize the lipase. This correlated is further corroborated with the study made by Hartmann *et al.*²⁵, in which they immobilized the lysozyme on several types of silica materials having each a distinct pore volume, they noticed that the loading capacity of the material increased with the increase of the pore volume. The relatively high loading capacity obtained in this study can be attributed to the presence of a second porosity which can improve the mass transfer and increase the probability of the adsorption of the enzyme. As for the SBA-15 catalyst in this study, the lack of a second porosity leads to a low maximal adsorption value.

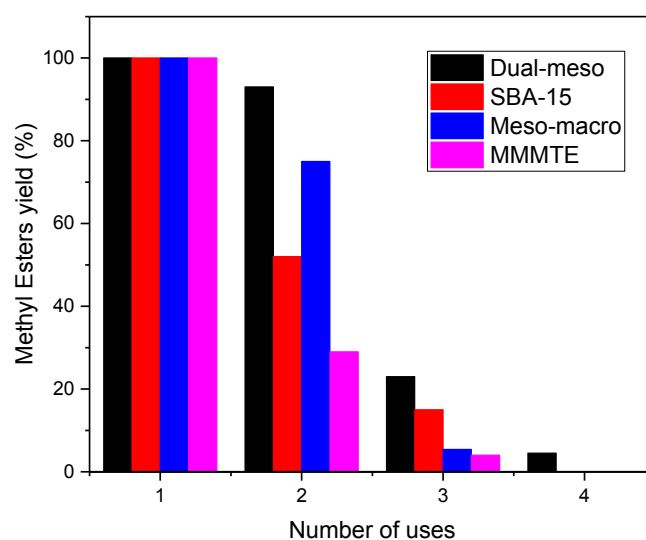


Figure 6-2: Recyclability of the SBA-15, MMMTE, meso-macroporous and dual-mesoporous catalysts.

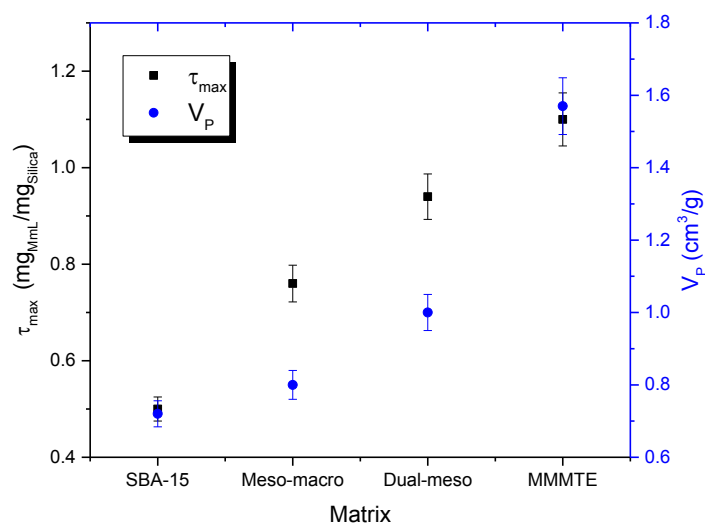


Figure 6-3: The Γ_{\max} evolution of the different matrixes in correlation with the pore volume of the matrixes.

Concerning the enzyme activity, the SBA-15 reached 100% conversion rate after 30 hours, the meso-macroporous catalyst after 50 hours, the MMMTE after 72 hours and the dual-mesoporous catalyst after 75 hours. The highest initial speed for formation of methyl esters is recorded for the SBA-15 catalyst, while the lowest initial speed is for the dual-mesoporous catalyst (Figure 6-4A). The same observation is made when the turnover number is compared to the mesopore size of the different matrixes (Figure 6-4B).

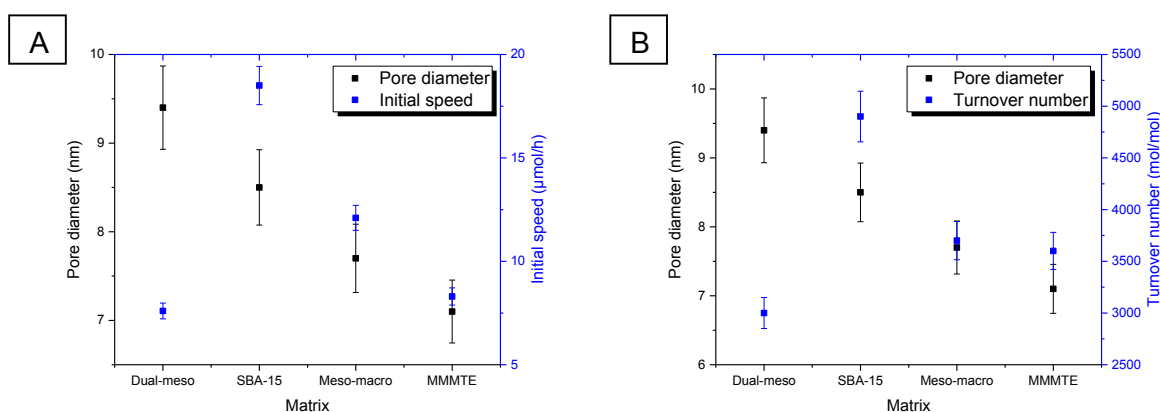


Figure 6-4: the correlation between the mesopore size and A) the initial speed of the formation of methyl esters and B) the turnover number.

Figure 6-4 shows that the best enzymatic activity is observed for a pore size of 8.5 nm. This observation is in agreement with the results obtained by Gustafsson *et al.*²⁶ where they show that the best enzymatic activity is obtained for SBA-15 matrix that have a mesopore size around 8.9 nm, and when the pore size is decreased, the enzymatic activity decreases as well.

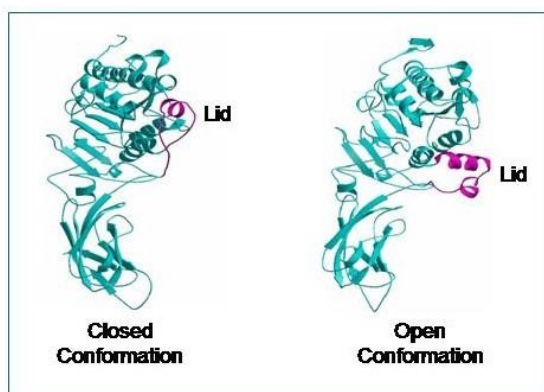


Figure 6-5: The closed and open conformation of the lipase molecule²⁸.

Even though the SBA-15 matrix has the lowest loading ratio, the other matrices were not able to match its catalytic activity, even in the presence of macropores enhances the mass transfer. This phenomena was also observed by Verger *et al.*²⁷ and explained it by the fact that the Mml possesses by a lid that covers the active site and which folds open when approaching a hydrophobic environment. Such a conformational change requires some space. A very narrow space in the mesopores is unsuitable for the lipase²⁶.

Those explanations are not suitable for the dual-mesoporous catalyst which has the lowest initial speed and turnover number. In fact, the pore size of the matrix with the large pores is equal to 9.4 nm, which is more than enough for the lipase conformation change. This can be due partly to the frustration of the enzyme molecules inside the pores of the matrix with the smaller pores. The overly small size of the pores has a tendency to inhibit the activity of the enzyme in the matrix with the larger pores. On the other hand, the recyclability of the dual-mesoporous materials, which showed an activity for 4 uses, unlike the other matrices that lost their enzymatic activity totally after 3 uses (Figure 6-2). This difference in the behavior may be attributed to the transference of the enzyme from the matrix with the small pores to the matrix with the large pores, thus sustaining its catalytic activity for more uses.

7 Conclusion

In this study, we have shown that the dual-mesoporous silica material has two different decay kinetics, whether during the heat treatment, or in boiling water. This difference has been attributed to the pore wall thickness of the different matrices. It revealed that the thinner the pore wall is, the less stable against heat and boiling water.

Concerning the immobilization of the lipase enzyme, the dual-mesoporous silica matrix can immobilize a higher quantity of enzymes than the meso-macroporous matrix, but the highest immobilization ratio was for the MMMTE matrix. For all matrices, the surface area and pore volume decreased mainly because of the loading of the enzyme inside the mesopores.

Finally, the catalytic activity of the different catalysts revealed that the best activity was for the meso-macroporous matrix, because it had the highest initial speed, the highest turnover number and reached a yield of 100% the most rapidly among the catalysts that have two pore sizes in this study. Moreover, we acknowledged that the presence of macropores along with mesopores improves the overall performance of the catalyst.

8 References

- (1) Jacoby, J. Lipase Mucor Miehei Immobilisée Dans Des Matériaux Poreux Silicatés : Bioréacteurs Pour La Synthèse D'esters Méthyliques À Partir D'huiles Végétales, Université de Lorraine, 2013.
- (2) Zhou, Z.; Hartmann, M. Progress in Enzyme Immobilization in Ordered Mesoporous Materials and Related Applications. *Chem. Soc. Rev.* **2013**, *42* (9), 3894.
- (3) Ravindra, R.; Zhao, S.; Gies, H.; Winter, R. Protein Encapsulation in Mesoporous Silicate: The Effects of Confinement on Protein Stability, Hydration, and Volumetric Properties. *J. Am. Chem. Soc.* **2004**, *126* (39), 12224–12225.
- (4) Vansant, E. F.; Voort, P. Van Der; Vrancken, K. C. *Characterization and Chemical Modification of the Silica Surface*; 1995.
- (5) Van Der Voort, P.; Baltes, M.; Vansant, E. F. Stabilized MCM-48/VOx Catalysts: Synthesis, Characterization and Catalytic Activity. *Catal. Today* **2001**, *68* (1-3), 119–128.
- (6) Kawi, S.; Shen, S.-C. Effects of Structural and Non-Structural Al Species on the Stability of MCM-41 Materials in Boiling Water. *Mater. Lett.* **2000**, *42* (1-2), 108–112.
- (7) Mokaya, R. Improving the Stability of Mesoporous MCM-41 Silica via Thicker More Highly Condensed Pore Walls. *J. Phys. Chem. B* **1999**, *103* (46), 10204–10208.
- (8) Linssen, T.; Cassiers, K.; Cool, P.; Vansant, E. . Mesoporous Templated Silicates: An Overview of Their Synthesis, Catalytic Activation and Evaluation of the Stability. *Adv. Colloid Interface Sci.* **2003**, *103* (2), 121–147.
- (9) May, A.; Stébé, M. J.; Gutiérrez, J. M.; Blin, J. L. Coexistence of Two Kinds of Fluorinated Hydrogenated Micelles as Building Blocks for the Design of Bimodal Mesoporous Silica with Two Ordered Mesopore Networks. *Langmuir* **2011**, *27* (23), 14000–14004.
- (10) Bae, Y. K.; Han, O. H. Removal of Copolymer Template from SBA-15 Studied by ¹H MAS NMR. *Microporous Mesoporous Mater.* **2007**, *106* (1-3), 304–307.
- (11) Tian, B.; Liu, X.; Yu, C.; Gao, F.; Luo, Q.; Xie, S.; Tu, B.; Zhao, D. Microwave Assisted Template Removal of Siliceous Porous materials Electronic Supplementary Information (ESI) Available: Syntheses, XRD Patterns, SEM Image, Pb²⁺ Extraction Images, ²⁹Si MAS NMR and TG Curves. *Chem. Commun.* **2002**, No. 11, 1186–1187.
- (12) Esquena, J.; Rodríguez, C.; Solans, C.; Kunieda, H. Formation of Mesostructured Silica in Nonionic Fluorinated Surfactant Systems. *Microporous Mesoporous Mater.* **2006**, *92* (1-3), 212–219.
- (13) Inaki, Y.; Yoshida, H.; Kimura, K.; Inagaki, S.; Fukushima, Y.; Hattori, T. Photometathesis Activity and Thermal Stability of Two Types of Mesoporous Silica Materials, FSM-16 and MCM-41. *Phys. Chem. Chem. Phys.* **2000**, *2* (22), 5293–5297.
- (14) Kruk, M.; Jaroniec, M.; Ko, C. H.; Ryoo, R. Characterization of the Porous Structure of SBA-15. *Chem. Mater.* **2000**, *12* (7), 1961–1968.

- (15) Galarneau, A.; Cambon, H.; Di Renzo, F.; Fajula, F. True Microporosity and Surface Area of Mesoporous SBA-15 Silicas as a Function of Synthesis Temperature. *Langmuir* **2001**, *17* (26), 8328–8335.
- (16) Zhao, D.; Feng, J.; Huo, Q.; Melosh, N.; Fredrickson, G.; Chmelka, B.; Stucky, G. Triblock Copolymer Syntheses of Mesoporous Silica with Periodic 50 to 300 Angstrom Pores. *Science* **1998**, *279* (5350), 548–552.
- (17) Blin, J. L.; Carteret, C. Investigation of the Silanols Groups of Mesostructured Silica Prepared Using a Fluorinated Surfactant: Influence of the Hydrothermal Temperature. *J. Phys. Chem. C* **2007**, *111* (39), 14380–14388.
- (18) Zhao, D.; Huo, Q.; Feng, J.; Chmelka, B. F.; Stucky, G. D. Nonionic Triblock and Star Diblock Copolymer and Oligomeric Surfactant Syntheses of Highly Ordered, Hydrothermally Stable, Mesoporous Silica Structures. *J. Am. Chem. Soc.* **1998**, *120* (24), 6024–6036.
- (19) Michaux, F.; Carteret, C.; Stébé, M. J.; Blin, J. L. Hydrothermal Stability of Mesostructured Silica Prepared Using a Nonionic Fluorinated Surfactant. *Microporous Mesoporous Mater.* **2008**, *116* (1-3), 308–317.
- (20) Jun, S.; Kim, J. M.; Ryoo, R.; Ahn, Y.-S.; Han, M.-H. Hydrothermal Stability of MCM-48 Improved by Post-Synthesis Restructuring in Salt Solution. *Microporous Mesoporous Mater.* **2000**, *41* (1-3), 119–127.
- (21) Jacoby, J.; Pasc, a.; Carteret, C.; Dupire, F.; Stébé, M. J.; Coupard, V.; Blin, J. L. Ordered Mesoporous Materials Containing Mucor Miehei Lipase as Biocatalyst for Transesterification Reaction. *Process Biochem.* **2013**, *48* (5-6), 831–837.
- (22) Canilho, N.; Jacoby, J.; Pasc, A.; Carteret, C.; Dupire, F.; Stébé, M. J.; Blin, J. L. Isocyanate-Mediated Covalent Immobilization of Mucor Miehei Lipase onto SBA-15 for Transesterification Reaction. *Colloids Surfaces B Biointerfaces* **2013**, *112*, 139–145.
- (23) Blin, J.-L.; Jacoby, J.; Kim, S.; Stébé, M.-J.; Canilho, N.; Pasc, A. A Meso-Macro Compartmentalized Bioreactor Obtained through Silicalization of “green” Double Emulsions: W/O/W and W/SLNs/W. *Chem. Commun.* **2014**, *50* (80), 11871–11874.
- (24) Blin, J. L.; Bleta, R.; Ghanbaja, J.; Stébé, M. J. Fluorinated Emulsions: Templates for the Direct Preparation of Macroporous-Mesoporous Silica with a Highly Ordered Array of Large Mesopores. *Microporous Mesoporous Mater.* **2006**, *94* (1-3), 74–80.
- (25) Vinu, a.; Murugesan, V.; Tangermann, O.; Hartmann, M. Adsorption of Cytochrome c on Mesoporous Molecular Sieves: Influence of pH, Pore Diameter, and Aluminum Incorporation. *Chem. Mater.* **2004**, *16* (16), 3056–3065.
- (26) Gustafsson, H.; Thörn, C.; Holmberg, K. A Comparison of Lipase and Trypsin Encapsulated in Mesoporous Materials with Varying Pore Sizes and pH Conditions. *Colloids Surfaces B Biointerfaces* **2011**, *87* (2), 464–471.
- (27) Verger, R. “Interfacial Activation” of Lipases: Facts and Artifacts. *Trends Biotechnol.* **1997**, *15* (1), 32–38.
- (28) Lipase conformation
<http://www.icp.csic.es/biocatalisis/web3/Palomoweb/uusframe/lipases.html>.

Conclusion

Dans ce travail nous avons préparé des matériaux silicatés à porosité hiérarchisée comme support pour l'adsorption de molécules d'intérêts dans le domaine pharmaceutique et comme catalyseur pour la production de biodiesel. Les matériaux ont été synthétisés à partir d'un mélange de micelles et de nano-émulsions, qui ont servi d'empreinte pour créer des mésopores et des macropores. La première partie est consacrée à l'étude détaillée du système Remcopal 4/décane/eau. Le diagramme de phase a été établi et les paramètres structuraux du film de tensioactif pour les différentes structures ont été déterminés. Nous avons montré que ce système est adapté à la formation de nano-émulsions. En effet, des nano-émulsions ont été préparées par température d'inversion de phase (PIT) et par composition d'inversion de phase (PIC). La température d'inversion de phase augmente avec le rapport huile/tensioactif ainsi qu'avec la quantité d'eau. Les nano-émulsions obtenues par température d'inversion de phase ont montré une meilleure stabilité temporelle et leur taille est systématiquement plus petite que celle obtenue par composition d'inversion de phase.

Les matériaux à porosité hiérarchisée ont été préparés par "dual templating". Ce mécanisme combinant les mécanismes Liquid Crystal Templating (LCT) et Cooperative Templating Mechanism (CTM) a permis l'obtention d'un matériau ayant une macroporosité dont la taille des pores est de 250 nm, qui correspond à l'empreinte des nano-émulsions ainsi qu'une mésoporosité dont la taille des pores est de 9 nm, qui est générée par mécanisme coopératif entre les micelles de P123 et le précurseur de silice. En plus des micelles qui permettent la formation des mésopores, la présence du P123 contribue à stabiliser les nano-émulsions et en même temps les protège contre les effets du méthanol (démixtion) qui est produit par l'hydrolyse du précurseur de silice.

Ensuite matériaux poreux et matériaux hybrides ont été dopés avec une molécule hydrophobe, le kétoprofène. Les matériaux hybrides sont constitués des nano-émulsions chargés en kétoprofène et des micelles de P123, lesquelles sont recouvertes de silice. La libération du kétoprofène à partir de ces matériaux hybrides est sensible au pH. D'un autre côté, la libération du kétoprofène adsorbé sur le matériau silicaté méso-macroporeux est très limitée, mais en présence de micelles de P123 dans la solution réceptrice, la libération est améliorée. Nous avons montré que la quantité de kétoprofène libérée à partir du matériau méso-macroporeux dépend de la concentration en P123 dans la solution réceptrice. Dans ce cas la libération est assistée par les micelles.

Les stabilités thermique et hydrothermale de ces matériaux silicatés ont été examinées avant de les utiliser comme biocatalyseur. Pour effectuer une étude comparative, des matériaux à

double mésoporosité ont été préparés à partir d'une solution micellaire dans laquelle deux types de micelles coexistent, des micelles riches en tensioactif fluorées et des micelles riches en P123. Les matériaux méso-macroporeux sont stables jusqu'à 550°C, la structure n'étant que faiblement endommagée, mais une contraction de la taille des pores est observée. D'un autre côté, la matrice ayant des petits pores du matériau à double mésoporosité est complètement dégradée, mais la matrice ayant des plus grands pores n'est que faiblement endommagée quelle que soit la température de calcination. Pour ce qui concerne la stabilité hydrothermale, le matériau méso-macroporeux calciné est stable pendant une heure dans l'eau bouillante, alors que le matériau non-calciné n'est stable que pendant 30 minutes. La déstructuration n'atteint que les mésopores, les macropores restent intacts. Le matériau à double mésoporosité, est également sensible à l'eau bouillante, mais deux cinétiques, qui correspondent à chaque matrice, sont observées, la matrice ayant de petits pores se déstructure après 3 heures, tandis que la matrice ayant des grands pores est détruite après 8 heures.

Ensuite l'immobilisation de la *Mucor miehei* lipase (Mml) sur le matériau méso-macroporeux calciné et le matériau à double mésoporosité a été étudiée. Le matériau à double mésoporosité a une capacité d'immobilisation de la lipase plus importante que le matériau méso-macroporeux calciné. Quant à l'activité catalytique, le catalyseur méso-macroporeux est plus performant que le catalyseur à double mésoporosité. En revanche ce dernier peut être recyclé 4 fois contrairement au premier qui n'est recyclable que 3 fois.

La comparaison avec des catalyseurs préparés auparavant au laboratoire a montré que le matériau méso-macroporeux calciné est le meilleur catalyseur. Il a une relativement faible capacité d'immobilisation de l'enzyme, mais la vitesse initiale est la plus grande et le turnover number est le plus important..

Outlooks

9 Acylases immobilization

The immobilization of an enzyme on a silica support has a lot of advantages for industrial applications, but one major downside still persists, the cost the enzymes. So enzymes produced by bacteria emerge as a promising and low cost technique. One particular type of enzymes piqued our interest, the acylases¹, because of the increasing demand for peptide acylation via enzymatic routes and the lack of proper bioreactors. So in collaboration with the BioProMo group of the LRGP laboratory who were able to produce acylases using bacteria of the *Streptomyces* species and the optimization of the acylation process using those enzymes², we suggested their initial immobilization on an SBA-15 material via physisorption in order to investigate the effects of their immobilization on the acylation reaction.

9.1 Immobilization of the acylases

The physisorption of the acylases was done on two types of SBA-15 materials, non-calcined and calcined in order to understand the effect of the calcination on the adsorption and the acylation reaction. For this an enzymatic solution was diluted in TRIS buffer at pH6 followed by the addition of the material to the solution. The mixture is stirred at 150 rpm for 3 and for 6 hours. The final step consists of the filtration of the material using a surfactant-free filtering paper with a mean pore size of 2 μm followed by three additions of fresh TRIS solutions in order to eliminate the poorly adsorbed molecules and the molecules adsorbed on the external surface. The filtrated solution was recuperated and analyzed using a UV-Vis spectrophotometer in order to quantify the remaining enzymes in the solution and calculate the adsorbed quantity on the SBA-15. The recuperated material is dried in the fridge for 24 hours. Then the catalytic activity was estimated by studying the kinetics of the hydrolysis of N- α -acétyl-L-lysine using the different catalysts prepared. The results are shown in Table 9-1 and Table 9-2.

Table 9-1: Summary of the adsorption rates of the acylases on the silica materials and the thin film chromatography analysis of the N- α -acétyl-L-lysine reaction kinetics.

Immobilized acylases	
Calcination	
Yes	No

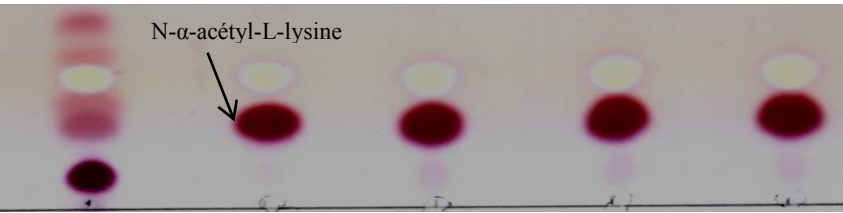
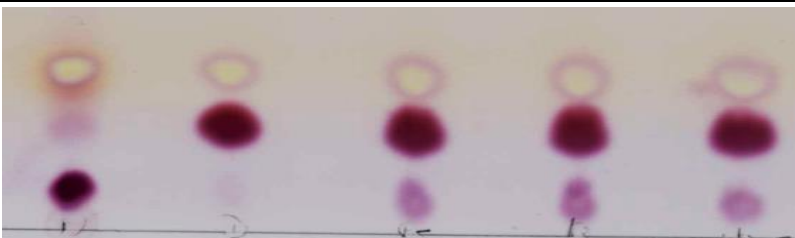
	3h	6h	3h	6h
Enzyme concentration (g/L)	0,069	0,053	0,026	0,058
Adsorption %	17,66%	15,16%	7,13%	15,25%
Hydrolytic activity of N- α -acétyl-L-lysine				
Time	24 h			
Hydrolytic activity of N- α -acétyl-L-lysine				
Time	48 h			

Table 9-2: Enzymatic activity of the different bioreactors estimated from the HPLC analysis of the N- α -acétyl-L-lysine.

	Calcination	Immobilization time (h)	Enzyme concentration (g/L)	Initial Speed (mmol _{lysine} /L/h)	Specific enzymatic activity (mmol/h/g _{enzyme})
Immobilized acylases	Yes	3	0,069	0,001	0,012
		6	0,053	0,006	0,113
	No	3	0,026	0,006	0,212
		6	0,058	0,010	0,175
Acylases					0,112

Those measurements show that the specific enzymatic activity for the enzymes immobilized for 3 hours on the non-calcined SBA-15 in a TRIS buffer solution at a pH6 is the best one.

9.2 Adsorption isotherm

Using the optimal experimental conditions determined in the previous paragraph, the adsorption isotherm has been established by mixing the materials with enzyme solutions at different concentrations and quantifying the adsorbed quantity using FTIR.

For the FTIR quantification, a calibration curve has been done by mixing silica with the appropriate amount of enzymes and drying them under vacuum for 12 hours. The quantification was done using the ratio of the surface of the peaks at 800 cm^{-1} (Si-O) and at 1535 cm^{-1} (Amides II). The results are shown in Figure 9-1.

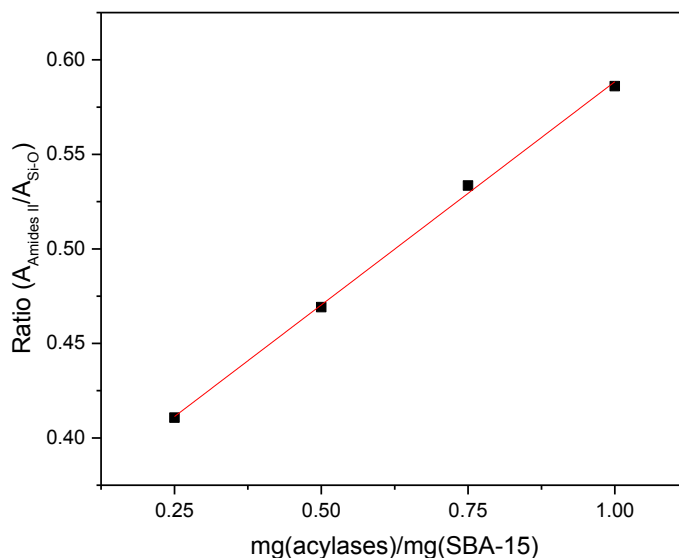
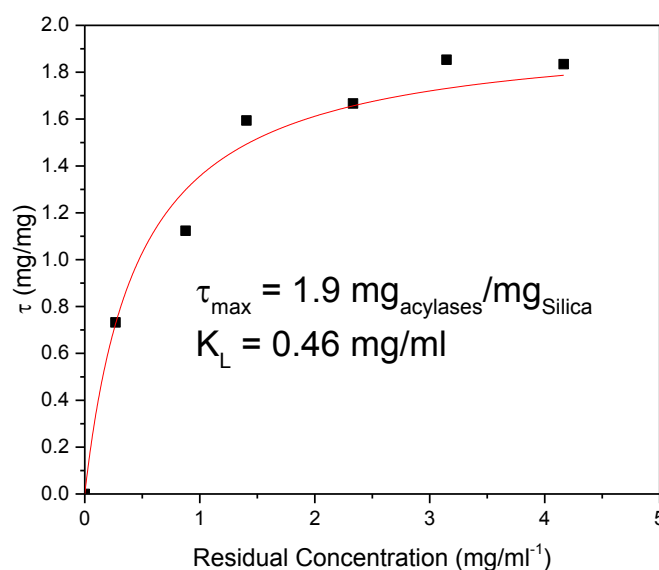


Figure 9-1: Calibration curve for the acylases immobilized on the SBA-15 material. The slope is equal to 0.2362 and the $R^2 = 0.9993$.

Using this calibration curve, the adsorption isotherm is shown in Figure 9-2.



Model	Langmuir (User)		
Equation	$(Tm \cdot x)/(x + K_L)$		
Reduced Chi-Sqr	0.00968		
Adj. R-Square	0.97957		
B	Tm	Value	Standar
	KL	1.98654	
		0.46489	

Figure 9-2: Adsorption isotherm of the acylases on the SBA-15 material.

The experimental points were fitted using the Langmuir model. The model showed a maximal adsorption capacity (Γ_{max}) of $2.13\text{ mg}_{\text{acylases}}/\text{mg}_{\text{SBA-15}}$ and a Langmuir constant (K_L) of 0.59 mg/ml .

9.3 Conclusion

In summary, we have shown that the immobilization of the proper support of the acylases increases the specific enzymatic activity. Further investigation is required to fully understand the effects of the immobilization on the enzymatic activity.

10 References

- (1) Schmid, a; Dordick, J. S.; Hauer, B.; Kiener, A.; Wubbolts, M.; Witholt, B. Industrial Biocatalysis Today and Tomorrow. *Nature* **2001**, *409* (6817), 258–268.
- (2) Ferrari, F. Étude de La Sélectivité D'acylation Enzymatique de Peptides : Prédiction de La Sélectivité de La Lipase B de Candida Antarctica Par Modélisation Moléculaire et Recherche de Nouvelles Enzymes Spécifiques de Type Aminoacylases, Université de Lorraine, 2014.

Résumé :

Ce travail porte sur la préparation de matériaux silicatés à porosité hiérarchisée pour l'encapsulation de molécules d'intérêt dans le domaine de la pharmacie et en tant que biocatalyseur. Afin d'atteindre cet objectif, les nano-émulsions sont choisies comme empreinte pour créer les macropores du matériau en raison de la taille homogène et réduite des gouttelettes de l'émulsion (inférieure à 100 nm). Pour cela le système Remcopal 4/décane/eau est investi en déterminant les conditions les plus optimales de formation de nano-émulsion, via les méthodes d'inversion de phases. L'ajout de micelles aux nano-émulsions ne déstabilise pas les émulsions et permet la formation d'un réseau de mésopores organisés selon une symétrie hexagonale. Les matériaux hybrides issus des matériaux poreux contenant encore la phase organique sont dopés par le ketoprofène en vue d'étudier la libération de ce dernier. Celle-ci se révèle sensible au pH. De plus, cette étude de la libération du ketoprofène à partir du matériau méso-macroporeux indique qu'elle est assistée par les micelles qui sont solubilisées dans la solution réceptrice. Le deuxième objectif de ce travail est d'utiliser ces matériaux poreux en tant que biocatalyseur pour la synthèse de biodiesel à partir d'huile de colza. Pour cette application, il est nécessaire que les matériaux résistent à l'immersion dans des milieux aqueux. L'étude de la stabilité hydrothermale a montré que le matériau calciné présente la meilleure stabilité dans l'eau bouillante. Par ailleurs, le matériau peut résister jusqu'à 550°C, la structure ne subissant que des dégradations mineures. Nous avons également utilisé un matériau silicaté à double mésoporosité préparé à partir de micelles fluorées et hydrogénées coexistant dans une même solution. L'évaluation thermique et hydrothermale indique que ces matériaux présentent deux cinétiques de déstructuration qui correspondent à chacune des deux matrices ayant deux tailles de pores différents. L'immobilisation de la lipase Mml est étudiée sur le matériau méso-macroporeux calciné et sur le matériau à double mésoporosité. Les isothermes d'adsorption ont permis de mettre en évidence que le matériau à double mésoporosité peut encapsuler plus d'enzymes que son homologue méso-macroporeux. L'activité enzymatique, au regard des réactions de transestérification, est de façon inverse plus importante avec le matériau méso-macroporeux calciné.

Mots clés : Nano-émulsions, matériaux silicatés, porosité hiérarchique, biocatalyseur, immobilisation.

Summary :

This work concerns the preparation of silica materials with hierarchical porosity for the encapsulation of molecules of interest in the field of drug delivery and as biocatalysts. In order to reach this goal, the nano-emulsions were chosen as templates for the macropores of the material because of the homogeneous and small size of the emulsion droplets (less than 100 nm). The system Remcopal 4/decane/water was investigated and the optimal conditions for which nano-emulsion is formed via the phase inversion methods were determined. Adding micelles to the nano-emulsions does not affect its stability and can form a network of mesopores organized with a hexagonal symmetry. Hybrid materials which are hierarchically porous materials where the organic phase is still present, were doped with ketoprofen to study its release, which proved to be pH sensitive. Moreover, the study of the release of ketoprofen from the meso-macroporous material indicates that it is assisted by the micelles which are solubilized in the release medium. The second objective of this work was to use these porous materials as a biocatalyst for biodiesel synthesis from colza oil. For this application it was necessary that the materials are resistant to immersion in aqueous media. The study of the hydrothermal stability shows that the calcined material has the best stability in boiling water. Moreover, the material can withstand up to 550 ° C, the structure undergoes only minor damages. We also used a dual-mesoporous silica material prepared from hydrogenated and fluorinated micelles coexisting in the same solution. Thermal and hydrothermal evaluation indicates that these materials have two different decay kinetics corresponding to each of the two matrices having different pore sizes. The immobilization of lipase Mml was studied on the meso-macroporous calcined material and the dual-mesoporous material. The adsorption isotherms were used to demonstrate that the dual-mesoporous material can encapsulate more enzymes than its meso-macroporous counterpart. On the other hand, the enzyme activity, evaluated by the transesterification reactions, is more important for the calcined meso-macroporous material.

Key words: Nano-emulsions, silica materials, hierarchical porosity, biocatalyst, immobilization.

